Artificial engineered materials for novel accelerator applications

Emmy Sharples

e.sharples@lancaster.ac.uk

The EMIT group

Department of Engineering

Lanacster University

Thesis submitted in fulfilment of the requirements for the degree of

Doctor of Philosophy at Lancaster University

November 7, 2016

Abstract

This thesis presents the design of a metamaterial loaded waveguide for accelerator applications, the metamaterial comprises of sheets of Complementary Split Ring Resonators (CSRRs). These CSRRs act as a left handed medium at certain frequencies allowing the structure to be used for the generation of reverse Cherenkov radiation. The proposed initial design exhibits a left handed TM_{31}-like mode at 5.5 GHz with a R/Q of 6.6 kΩ/m and a shunt impedance of 10.9 MΩ/m, indicating strong beam coupling, this is verified by the strong longitudinal wake impedance of 13 kΩ. Design considerations are discussed to alleviate typical issues of metamaterials in high-power environments and make the structure more suitable for a proof-of-concept beam test at the Cockcroft Institute. The objectives of this study have been to increase fabrication suitability, reduce the number of hybrid modes and improve resistance to damage from high power, while maintaining the electromagnetic performance. Designs with increased sheet thickness, ring spacing and curvature are discussed via electromagnetic and wakefield analysis. The final chosen design with 1mm thick metasurfaces exhibits a suitable TM_{31}-like mode at 5.86 GHz. This mode exhibits a R/Q of 4.5 kΩ/m, a shunt impedance of 22.6 MΩ/m and a longitudinal wake impedance of 10.6 kΩ, indicating that the modified geometry does not significantly affect the electromagnetic interaction of the structure with charged particles. To understand the wave-beam interactions in the structure, particle in cell simulations were performed for a commercial beam, a very high intensity beam and the current beam available on the Versatile Electron Linear Accelerator (VELA) which the structure is designed for. Through these studies the VELA beam is confirmed as the most suitable for reverse Cherenkov applications. The CSRR loaded structure can lead to novel designs of particle detectors, coherent sources and acceleration schemes, leading to compact novel accelerator applications.

Declaration of originality

I hereby declare that I am the sole author of this thesis and that this work has not been submitted in substantially the same form towards the award of a degree or other qualification at any other University or Institution.

I certify to the best of my knowledge that my thesis does not infringe upon anyone's copyright and all major sources of information are properly referenced. I confirm that I have read and understood the publication Guidance on Writing Technical Reports published by the Department.

Signed

Emmy Sharples

Date

Dedicated to Brian Whitaker, my Granddad,
for all the inspiration and encouragement you gave me growing up.

Acknowledgements

First and foremost, I would like to thank my supervisors Dr Rosa Letizia and Dr Graeme Burt for all the help and guidance they provided through the course of my thesis, without their help I would not have been able to bring together all my ideas into a cohesive project. My work with CST would not have been possible without help from Dr Ben Hall and Dr Mike Jenkins from Lancaster University and Louise Cowie and Dr Philippe Goudket from ASTeC who helped me get to grips with the software at the start of my PhD and put up with my obvious and not so obvious questions. I extend my thanks to the AP group for all their input on the beams and systems available at Daresbury, and for letting me join their Christmas dinners.

I am grateful to my work colleagues who have kept me sane over the past few years especially Dr Ben Hall for his cake breaks, Thomas Pacey and Alisa Healy for their well-timed coffee breaks and all the snacks they provided for motivations. I would like to thank everyone at the Cockcroft Institute for making me feel so welcome, especially the members of cake club who made Tuesdays the best day of the week, the usual Friday lunch group, and everyone from the climbing group for creating a friendly community outside of the office.

I extend my thanks to office mates Lee Devlin and Alexandra Alexandrova who have become close and valued friends; for being there through the highs and lows of my PhD, putting up with my crazy antics and introducing me to John. I want to thank Paolo and Monia for being fantastic friends and providing me with a home away from home, and many fantastic meals when I was living on my own in the middle of my PhD. A huge thank you to John Milne for putting up with my work based rambles and providing love and support when it was needed. Finally a big thank you to my Mum and Dad, my sister Laura and my Grandparents, for all their love, support and encouragement through my research endeavours.

Contents

List of Figures

List of Tables

Glossary

Glossary of terms

Asymmetrically Inhomogeneous material	A material which does not have uniform composition throughout and the inhomogeneity occurs in such a way that the composition encountered is different for different directions. See figure 2.22
Backward propagation	When waves or an electromagnetic phenomena propagate in the opposite direction to the one they usually do, this occurs in left handed media.
Bragg Reflector	A reflector made from alternating layers of high and low permittivity dielectric material, where the ratio of permittivity enhances constructive interference to form a perfect reflector.
Carrier concentration	The number of electrons in a doped material.
Cherenkov radiation	Radiation emitted by an electron travelling through a medium at a speed faster than light within that medium.
Chiral metamaterials	Metamaterials that rely on twisted structures to generate their unique electromagnetic response.
Complement	One of two parts that make up a whole or complete each other.
Complementary split ring resonator	The complement of the split ring resonator, two concentric split rings are cut out of metal, this gives rise to negative permittivity at resonance.
Effective parameters	The new or effective parameters generated by a metamaterial, that are different to the parameters of the constituent materials.
Epsilon near zero	Permittivity close to zero, a factor often used in metamaterials and dispersion engineering.

Homogeneous material	A material with uniform composition throughout.
Hybrid mode	Non zero electric and magnetic fields in the direction of propagation.
Infinite metamaterial	A metamaterial with periodic boundaries in all directions meaning it repeats on infinitely. Sometimes referred to as the unbounded form.
Inhomogeneous material	A material which does not have uniform composition throughout.
Intermetallics	A type of new plasmonic materials, formed by reducing the carrier concentration of metals by mixing them with non-metals, these materials have higher carrier concentrations than transparent conducting oxides.
LC resonator	A resonator that depends on both inductance and capacitance to drive a resonance.
Left handed medium	A material in which **E**, **H** and **k** form a left handed triplet, creating a material in which backward propagation occurs and the refractive index is negative.
Longitudinal direction	The direction of propagation, in this work it is taken to be the z direction, therefore the longitudinal electric field is E_z and the longitudinal wake impedance is the z component.
Metamaterials	An artificially engineered material comprising of periodic sub-wavelength elements, that when excited by external radiation gives rise to unique electromagnetic effects not associated the the material used to fabricate them.
Metasurface	A surface comprising of repeating metamaterial elements, sometimes referred to as a two dimensional metamaterial.
Mie resonance	Resonance of dielectric or plasmonic materials that gives rise to unique electromagnetic effects that can be quantified by Mie theory.
Mode order	The order in which modes are found in an eigen mode simulation, mode order increases with increasing frequency.
Negative index	A negative index of refraction, where permittivity and permeability are simultaneously negative.

Negative index mode	A mode with a negative dispersion gradient, indicating a negative refractive index.
New plasmonic materials	Materials engineered to bridge the gap between metals and dielectrics, by tailoring the carrier concentration of the material. These often take the form of doped semiconductors, transparent conducting oxides or intermetallics.
Photonic Band Gap structures	Three dimensional dielectric structures which have a frequency band in which electromagnetic waves are forbidden irrespective of the propagation direction in space.
Positive index mode	A mode with a positive dispersion gradient, indicating a normal refractive index.
R/Q	A proportionality factor relating the accelerating voltage to the stored energy in an resonant RF system.
Right handed medium	A material in which **E**, **H** and **k** form a right handed triplet, as in most known materials.
Rutile form	A common form of Titanium dioxide TiO_2.
Scattering coefficients	The reflected and transmitted waves when radiation is incident on either side of an object, system or slab of material, including S_{11}, S_{12}, S_{21} and S_{22}
Shunt impedance	A measure of the strength with which an eigenmode of a resonant RF structure interacts with charged particles on a given straight line.
Smith-Purcell Grating	A periodic metallic grating which generates crescents of radiation when an electron propagates just above the surface of the grating, with one crescent of radiation for every grating period passed.
Split ring resonator	A type of metamaterial made from two concentric split rings on a substrate, that gives rise to negative permeability.
Subwavelength	Less than one tenth of a wavelength.
Synchrotron	A type of cylindrical accelerator, known as a light source.
Symmetrically Inhomogeneous material	A material which does not have uniform composition throughout, however the inhomogeneity of the materiel is symmetric meaning that the change in composition will appear the same if viewed from left to right or right to left. See figure 2.22

TE-like mode	A mode with strong transverse electric field components similar to a TE mode but with a small non zero longitudinal component.
TM-like mode	A mode with a strong longitudinal electric field component similar to a TM mode but with small non zero transverse components.
Transparent Conducting Oxides	A type of new plasmonic materials where the plasma frequency can be tuned by doping.
Transverse electric mode	Magnetic field in the direction of propagation and no electric field in the direction of propagation.
Transverse magnetic mode	Electric field in the direction of propagation and no magnetic field in the direction of propagation.
WR-284 waveguide	American terminology for an S-band waveguide 34 mm by 72 mm.

Acronyms

ASR	Asymmetrically Split Rings.
ASTeC	Accelerator Science and Technology Centre.
AWAKE	Advanced Wakefield Experiment.
CCR	Coherent Cherenkov Radiation.
CERN	Conseil Europeen pour la Recherche Nucleaire.
CLARA	Compact Linear Accelerator for Research and Applications.
CMOS	Complementary Metal Oxide Semiconductor.
CSRR	Complementary Split Ring Resonator.
DBW	Dielectric Bragg Waveguide.
DLA	Dielectric Laser Accelerator.
DLW	Dielectric Lined Waveguide.
ENZ	Epsilon Near Zero.
FAcET	Facility for Advanced accelerator Experimental Tests.

FEL	Free Electron Laser.
GZO	Gallium doped Zinc Oxide.
InSb	Indium antimonide.
IR	Infra Red.
ITO	Indium Tin Oxide.
LHM	Left Handed Medium.
MTM	Short hand for metamaterial.
NIM	Negative Index Mode.
NIR	Near Infra Red.
PBG	Photonic Band Gap.
PEC	Perfect Electric Conductor.
PIC	Particle In Cell.
PIM	Positive Index Mode.
RHM	Right Handed Medium.
RF	Radio Frequency.
SLAC	Stanford Linear Accelerator Centre.
SRR	Split Ring Resonator.
STFC	Science and Technology Faculties Council.
TCO	Transparent Conducting Oxide.
TE	Transverse Electric.
TiN	Titanium Nitride.
TM	Transverse Magnetic.
UHV	Ultra High Vacuum.
VELA	Versatile Electron Linear Accelerator.
X-FEL	X-ray Free Electron Laser.
ZrN	Zirconium Nitride.
ZTA	Zirconia-Toughened-Alumina.

Symbol list

a	The length of a ray.
a'	The length of the ray in the medium.
$\mathbf{B}$	The magnetic field vector.
b	The length of a second ray.
b'	The length of the second ray in a medium.
c	The speed of light in a vacuum defined as 2.99792458×10^8 ms^{-1}.
C	Capacitance.
C_c	The capacitance of a CSRR.
C_{pul}	Capacitance per unit length.
c_1	The ratio of relative permittivity and permeability.
c_2	The product of relative permittivity and permeability.
c_{eff}	The effective speed of light within a material.
$\mathbf{D}$	The displacement field.
d	The thickness of a slab.
d_i	Thickness of the ith layer.
d_{di}	Thickness of the diamond layer.
d_m	Thickness of the matching layer.
d_{ZTA}	Thickness of the ZTA layer.
$\mathbf{E}$	The electric field vector.
F	The focal point of a ray.
F_0	The fraction of the unit cell not inside the rings.
F_i	Fractional volume of a unit cell occupied by the resonator.
f	Frequency.
f_{mp}	The non angular magnetic plasma frequency.
$\mathbf{H}$	The Magnetizing field vector.
H_{red}	Normalised magnetic field incident on a slab.
h	Grating height.
I	Current flowing in a system.

$\mathbf{k}$	The wave vector.
L	The self inductance in a system.
L_0	Inductance on both rings.
L_{pul}	Inductance per unit length.
L_s	Inductance of a SRR.
l	length.
M	Distance of a source from a focal point.
m	An integer.
n	The refractive index of a medium.
P	Propagating factor.
P_s	Power lost.
p	The period of a metamaterial unit cell.
Q	Quality Factor.
q	Charge.
R	Resistance.
R_{int}	Inner radius.
R_{SH}	Shunt impedance.
r	The radius of a ring or circle.
r_0	Radius of the inner ring.
$\mathbf{S}$	The Poynting vector which gives the direction of energy flux.
s	The spectral order.
t	Denotes a time.
U	Stored energy.
V	Accelerating voltage.
V_1	The sum of the scattering coefficients.
V_2	The difference of the scattering coefficients.
V_B	Voltage in section B of a signal flow graph.
V_{inc}	Incident voltage in a signal flow graph.
v	The velocity of a moving object.

v_b	Beam velocity.
v_p	The phase velocity.
w	The width of a spacing in metamaterial or dispersion engineering designs.
X	An integer number of layers.
z	The impedance of a material.
z_0	The impedance of free space.
z_{red}	Impedance for a homogeneous material.
α	The phase advance per unit cell in a metamaterial.
β	Ratio of velocity to speed of light.
Γ	Reflection coefficient of a wave incident on a slab of material.
γ	Damping frequency.
ε	The permittivity.
ε_0	The permittivity of free space, defined as $8.5418782\times10^{-12}\mathrm{m}^{-3}\mathrm{kg}^{-1}\mathrm{s}^4\mathrm{A}^2$.
ε_i	Permittivity of the ith layer.
$\varepsilon_{\mathrm{di}}$	Permittivity of the diamond layer.
ε_r	Relative permittivity of a material.
$\varepsilon_{\mathrm{ZTA}}$	Permittivity of the ZTA layer.
ε_∞	Dielectric constant at infinite frequency.
η	Phase constant.
θ	Denotes an angle.
Λ	Ratio of complex relative permittivity and permeability.
λ	The wavelength of the incident radiation.
λ_0	Free space wavelength.
λ_c	Cut off wavelength.
λ_g	Guide wavelength.
μ	The permeability.
μ_0	The permeability of free space defined as $1.25663706 \times 10^{-6}\mathrm{kg}\ \mathrm{s}^{-2}\mathrm{A}^{-2}$.
μ_{eff}	The effective permittivity of a medium.

μ_r	Relative permeability of a material.
ρ	The conductivity of a material.
Σ	An external excitation incident on a system.
σ	Standard deviation bunch length.
τ	Transmission coefficient.
τ'	Normalised transmission coefficient.
Φ_m	Magnetic flux.
ϕ	Denotes a second angle if two are present.
χ	Relates the sum and difference of the scattering coefficients.
ψ	The propagating constant.
ω	The angular frequency, determined by $2\pi f$.
ω_0	Initial angular frequency.
ω_{mp}	The magnetic plasma frequency.
ω_p	The plasma frequency, when waves propagate below this frequency they can generate a negative permittivity response.

Chapter 1

Introduction

In this Chapter a brief introduction to the thesis is provided to give background and insight into the motivation behind the work done. First a brief review of the most promising concepts proposed for novel accelerators is provided. In the next section, potential uses of metamaterials in accelerators are discussed, with a brief introduction to metamaterials, the motivation behind incorporating metamaterials into accelerators, recent design proposals in the field and how these can be improved upon. Finally, the aims of this research project are given and an outline of the content of the thesis is provided.

1.1 Beyond Conventional accelerators

Physicists have been inventing new types of particle accelerators to propel charged particles to higher and higher energies for more than 80 years. There are more than 17,000 accelerators in operation worldwide, operating in industry, healthcare, and at research institutions. This growth in energy can be represented by a Livingston plot [1] [2], which plots the energy of the accelerator against the construction year on a semi-log scale as seen in Figure 1.1. Livingston noted that advances in accelerator technology increase the energy by a factor of 10 every six years. However in recent years this growth has reached saturation with both hadron and electron-positron colliders no longer reaching the predicted energies, creating an energy limit. To overcome this energy limit, new accelerator technology is required.

In addition to reaching higher energies, new accelerator technology is required to reduce the size of accelerator systems, achieving high accelerating gradients at affordable costs to enable widespread applications in medicine, industry and

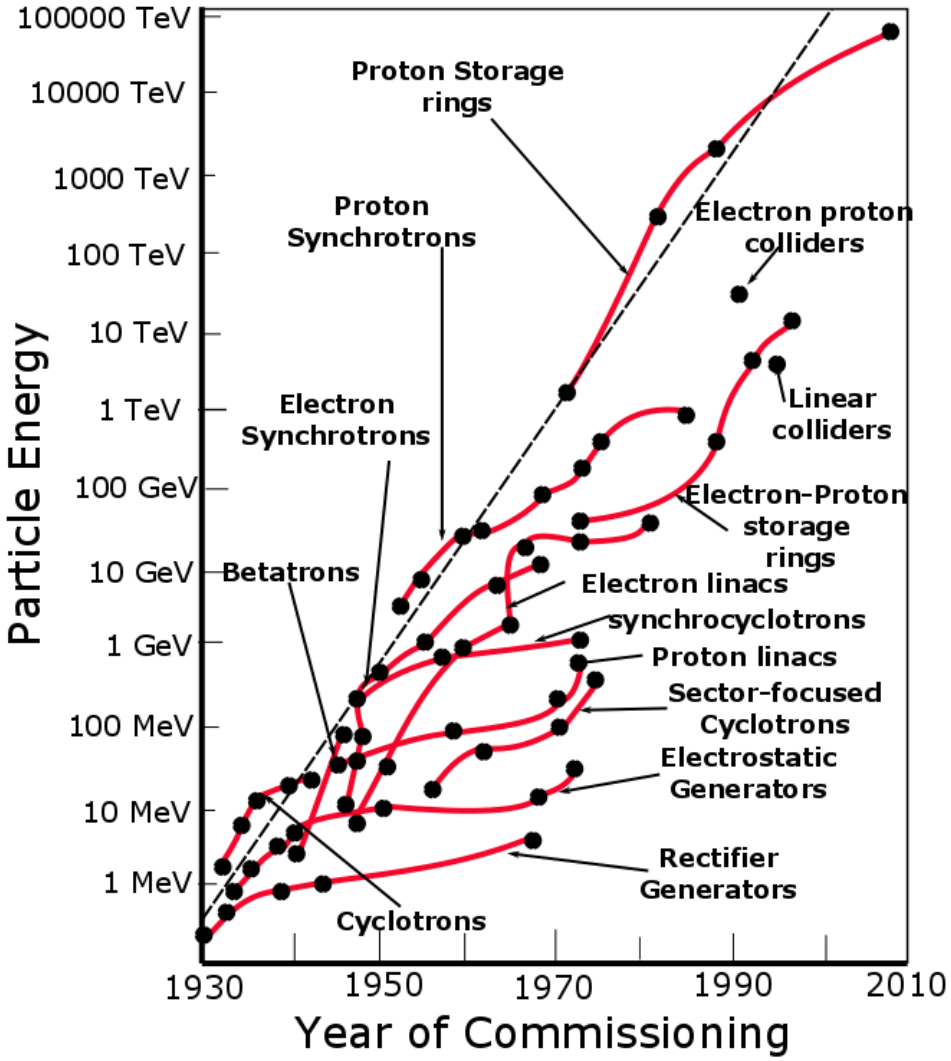

Figure 1.1: A Livingston plot showing the growth of accelerators from the 1930's to 2010, the energy increase can be seen to be roughly linear on the semi log graph, indicating an exponential increase in energy.

research. In current Radio-Frequency (RF) driven accelerator systems, the accelerating gradients have reached their physical limit at around 0.15 GeV/m [3], thus novel technological solutions that go above this are desirable. Dielectric laser accelerators [4] aim to reach gradients of over 0.25 GeV/m and plasma wakefield acceleration could achieve higher gradients approaching 4 GeV/m for beam driven systems [5] and 100 GeV/m using laser driven systems [6], however these gradients have only been obtained for short scales. Metamaterials provide another interesting alternative to conventional accelerator structures for high gradient acceleration.

1.1.1 Microwave linear accelerators

Microwave accelerators use RF electric fields to deliver energy to a beam of particles, by synchronously switching the fields it is possible to ensure that the beam always sees an accelerating voltage. In 1928 Windroe [7], demonstrated that electrons could be accelerated through a tube by applying an RF voltage to separate sections of the tube such that electrons passing the gaps between these sections experienced an accelerating voltage. By ensuring that the electrons arrived at the next gap when the RF voltage was at a maximum the electrons were accelerated again. Linear accelerators are an extension of this idea, using an array of "Cells" powered by RF to accelerate the particle, the acceleration can be optimised by shaping the waveguide cavities of the accelerator so the phase velocity of the electromagnetic field matches the particle speed at the points where acceleration is to occur.

Linear accelerators are often single pass machines with the charged particle traversing each section once, thus the overall energy gain is limited by the length of the machine. Therefore strong accelerating fields are desirable to increase the accelerating gradient and make sure the maximum energy possible is transferred to the particle over the shortest length. With output being limited by length it is clear that linear structures cannot compete with cylindrical machines in terms of energy however they have significant advantages over their cylindrical counter parts. The geometry makes injection and extraction simple, high flux beams are better handled due to the increased number of option for high power RF and beam handling and the duty cycle is high meaning it takes less time for the machine to produce an output beam. Thus they are a more desirable option for applications in industry and healthcare, where they have direct applications to radiation therapy, and other health care applications that rely on the production of short lived isotopes.

High energy electrons have numerous applications including the generation of synchrotron radiation for materials research and photon beam generation through the free electron laser process. The acceleration is performed using RF resonant cavities that are coupled together, and the beam is confined by quadrupole magnets. The cavity shape is optimised to accelerate the particles at the frequency with the highest energy transfer and lowest cost. The choice of the accelerating field mode is a compromise between the linac length reduction and the power dissipation. In cavity based accelerators there is a toss-up between operating at the π mode which has a high shunt impedance and high gradient but low stability and the $\pi/2$ mode which is stable, but less efficient as it results in unfilled cells. There are two

solutions; use the $\pi/2$ mode in a side coupled cavity or in a bi-periodic structure [8].

Conventional RF linacs are a popular way to create low cost accelerating structures however these structures can quickly become high in cost as higher energies require longer structures. By using superconducting RF the accelerating gradient can be increased and hence the length of the structure can be reduced, however this is significantly more costly. Linear accelerators also face further challenges relating to the disruption caused by higher order modes and wakefields generated by the beam. Thus alternative methods beyond the conventional microwave linear accelerator need to be explored to reach higher energies and higher gradients.

1.1.2 Plasma Wakefield Accelerators

Plasma wakefield acceleration is an attractive novel method of acceleration, with the advantage that the plasma supports much higher field gradients than a conventional RF accelerator, and is limited by only mechanical factors and not the dielectric breakdown threshold. There are two main types of plasma wakefield acceleration; beam driven and laser driven. These accelerating structures use plasmas of charged electrons and ions, they propagate a laser pulse or particle bunch through the plasma creating a charge separation in the electrons of the plasma and the electrons moving away from the front and back of the pulse or particle bunch form a wake. Subsequently injected particles can the ride the wake and gain energy. Plasma accelerators use the high electric fields formed within plasma waves to accelerate particles to very high energies in a fraction of the distance needed in conventional accelerators, resulting in accelerating gradients as high as 100 GeV/m [9].

Laser driven plasma wakefield acceleration uses an intense laser pulse to push the electrons away from the front and back of the pulse which then rush back in and cause plasma oscillations which drive the wakefield which accelerates a subsequent electron bunch [10]. Laser plasma wakefield acceleration is particularly promising for generating short pulses of high-energy electrons for applications in femtosecond electron diffraction, medical imaging, and miniature free-electron X-ray lasers. For laser plasma acceleration to be successful the driving laser pulse must be guided over a distance of mm, either using a plasma channel [11], or through self guidance [12].

In beam driven plasma wakefield acceleration a high-gradient wakefield is driven

by an intense, high-energy charged particle beam as it passes through the plasma, and this wakefield is then used to accelerate a trailing witness bunch of particles. The wakefield can be driven by either electrons or protons, in the electron beam driven case the space-charge of the electron bunch pushes out the plasma electrons, which then rush back and overshoot creating plasma oscillations. In the case of a protons beam, the plasma electrons are pulled in towards the proton bunch, and then flow outwards once the bunch has passed causing the plasma oscillations and wakes for acceleration. Particle driven plasma wakefield acceleration has been experimentally researched by several American laboratories [13] and KEK in Japan [14], and more recently SLAC [15] and AWAKE [16] have been exploring proton driven plasma wakefield acceleration as a means to reach even higher energies.

Challenges facing plasma wakefield acceleration are the generation of stable wakefields, controlled synchronous injection of particles into the wave buckets, and the generation of mono-energetic beams. Plasma wakefield acceleration has only been demonstrated to work over very small distances, so though high gradients have been demonstrated they can only accelerate particles for very short periods of time.

1.1.3 Direct laser acceleration structures

Acceleration using a laser and no plasma is analogous to the microwave driven particle acceleration, using electromagnetic waves to drive acceleration of a bunch of particles. There are some distinct differences between RF and laser driven acceleration though; lasers produce very short pulses of radiation which allow for much larger electric fields without causing breakdown. The short wavelengths of laser radiation leads to the production of very short bunches (approximately 30 nm or 100 attoseconds) [17] which leads to applications in ultra-fast science. One key attraction is that much of the core technology required to create laser driven accelerators, such as the lasers themselves, the optics, and the fibres have already been developed by industry and the strong semiconductor chip manufacturing industry will allow for new elements to be created swiftly. This method is also very compact, moving much closer to the accelerator on a bench or an accelerator on a chip designs, that are put forward as ultimate goals.

These structures still face their own challenges though, the lasers produce radiation with transverse electromagnetic fields, thus the structures used must be able

to transform and guide the modes to produce strong longitudinal electric fields. These structures include Photonic Band Gap (PBG) structures [18] such as the woodpile structures [19], and dielectric grating structures [4]. In PBG structures, a central defect is used to trap the field within the core, and this field is suitable for accelerating the beam. The appeal of PBG structures is that they damp higher order modes thus eliminating the wakefield effects that limit conventional accelerating structures.

The dielectric grating structure [4] consists of two gratings on either side of a confined vacuum channel, which are excited by laser light which creates an accelerating field between the two gratings. This design eliminates the pulse-slippage problem of conventional waveguide-based accelerators by optically pumping the structure perpendicular to the beam channel. Since the laser light traverses a relatively small amount of medium there are minimal dispersion effects allowing the structure to be driven by ultra-short high-power laser beams. Since the incident fields are not confined within the vacuum gap, the structure is non resonant and thus there is no energy storage, allowing the structure to maintain high gradients. Like the cavities of a conventional RF accelerator the grating synchronises the phase velocity of the field with the beam to minimize exposure to the decelerating phase of the field, so the beam experiences net acceleration for every period. This has been shown to reach accelerating gradients of 300 MeV/m.

These designs offer interesting opportunities for obtaining high gradient acceleration at compact scales, however many demonstrations have been over very short distances and structures have been shown to sustain these gradients for only for a small amount of particles, therefore alternative routes to develop novel accelerating structures are under investigation.

1.2 Metamaterials in Accelerators

Metamaterials are a novel approach to tackling the challenges that limit conventional accelerators. The compact nature, easy integration and unique electromagnetic effects that allow for the manipulation of the dispersion make metamaterials an attractive alternative to plasma and laser wakefield devices, especially if they can sustain high gradients over longer periods. Metamaterials that have simultaneously negative permittivity ε and permeability μ and are hence left handed also have significant applications as sources of coherent radiation or for particle detectors using backward propagating Cherenkov radiation.

1.2.1 A brief introduction to metamaterials

Definition: *A metamaterial is an artificially engineered material comprising of periodic elements, the period of which is subwavelength ($p \ll \frac{\lambda}{10}$), that when excited by external radiation gives rise to unique electromagnetic effects not associated with the material used to fabricate them.*

The term metamaterial as defined above became common in the late 90's after Pendry's [20] work on the split ring resonator, in which the size of the unit cell was constrained by

$$a \ll \lambda, \tag{1.1}$$

Therefore the unit cell is much smaller than the wavelength and the microstructures that form them can be considered like the atoms in a conventional material, so the unit cells form meta-atoms and the full structure forms a metamaterial. These metamaterials exhibit unique electromagnetic effects, which relate to the effective permittivity and permeability, some effects can be seen in Figure 1.2

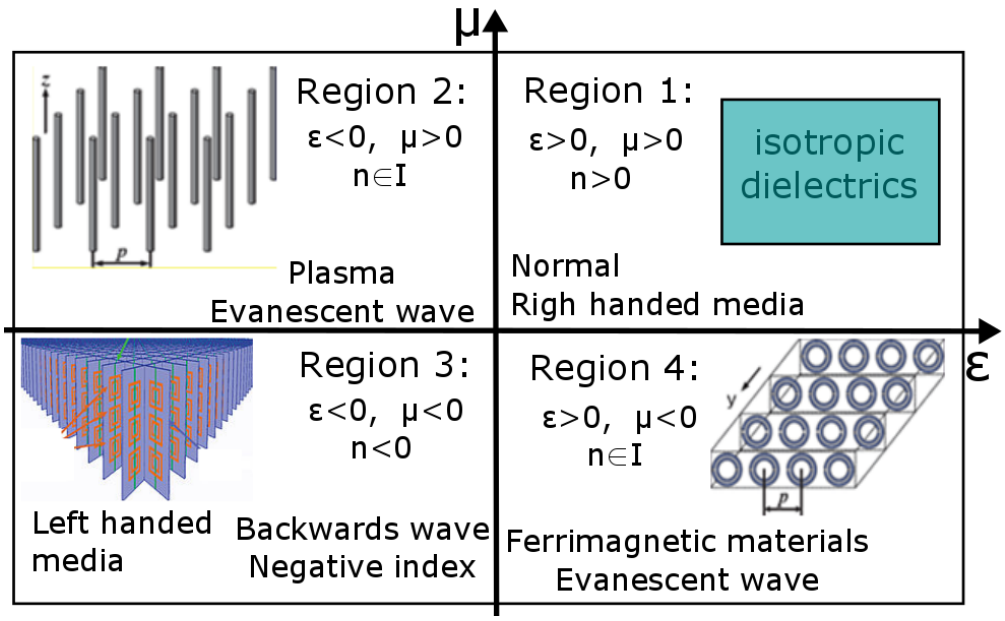

Figure 1.2: A graph showing the possible combinations of permittivity and permeability achievable with metamaterials. Right handed media [21], negative permittivity media [22], left handed media [23] and negative permeability media [20].

Metamaterial research has focused on left handed or negative index media, in which the permittivity and permeability are simultaneously negative, a concept that was discussed at length by Veselago in 1968 [24]. The term left handed media is used as simultaneously negative values of ε and μ lead to $\mathbf{k}$, $\mathbf{H}$ and $\mathbf{E}$ forming a left handed triple of vectors. In such a medium, the backward propagation of electromagnetic

waves is observed where the wave vector and Poynting vector propagate antiparallel, which implies the phase and group velocities are of opposite signs. In such a media a number of interesting electromagnetic phenomena can occur, notably the backward propagation of electromagnetic effects such as Cherenkov radiation, where the shock-wave propagates behind the moving particle not in front of it. A more in depth discussion of the phenomena behind left handed materials and the unique properties they possess can be found in Section 2 of Chapter 2.

Materials with simultaneously negative ε and μ are not found in nature, and though a negative permittivity can be obtained by most metals below the plasma frequency, negative permeability is less common only occurring for some ferrites. Thus materials need to be engineered with these properties, achieving negative permittivity is relatively straight forward, and can be done with an array of wires operating below the plasma frequency. Negative permeability is more complex, and it wasn't until 1999 that a method for obtaining negative permeability was found. This was the Split Ring Resonator (SRR) [20], an LC resonator that gives rise to negative value of permeability just above its resonant frequency. The SRR in its most common form comprises of two metallic concentric rings, each with a small gap in the ring at opposite sides, on a substrate, as shown in Figure 1.3. An in depth analysis of the SRR and the mechanisms that govern its behaviour are given in Chapter 2 Section 3.

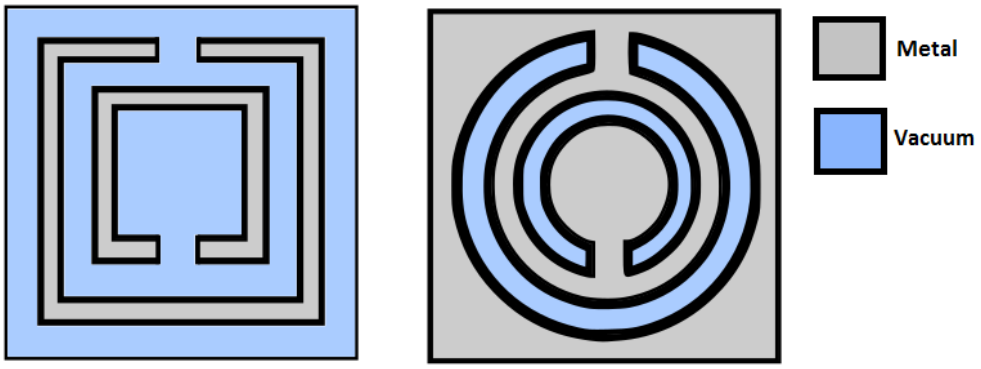

Figure 1.3: The unit cell for a square split ring resonator with the split rings on substrate, and a circular complementary split ring resonator where the rings are cut out of the metal.

With a material now able to produce negative permeability all that was needed was to combine two materials, one with $\varepsilon < 0$ and the other with $\mu < 0$ to form a left handed medium. In 2000 a composite material comprising of a periodic array of SRRs with inter spaced continuous wires [23] was designed as an LHM, where the SRRs contribute the $\mu < 0$ effect and the wires realise the $\varepsilon < 0$ effect. Left

handed media can be used for a number of interesting applications, most notably the design of invisibility cloaks [25] [26], and applications to subwavelength imaging via the creation of hyper lenses [27] [28]. Though the combination of wires and SRRs is the most common method of forming a left handed media, numerous other schemes exist using different resonator elements, some rely on metallic elements whereas other use mie resonant dielectrics, more details on the different types of metamaterial elements can be found in Chapter 2 Section 3.

The complementary form of the SRR is the Complementary Split Ring Resonator (CSRR) [29] which comprises of two concentric rings cut out of metal as shown in Figure 1.3. As this is the complement to the SRR it gives rise to negative permittivity not permeability and interestingly when formed into stacked metasurface sheets can be used to create a left handed medium by confining transverse magnetic modes [30]. This application is explored at length within the thesis as it is this metamaterial that is chosen for the metamaterial loaded waveguide discussed in Chapters 3-5. Analysis of the CSRR, its properties and its applications are given in Chapter 2 Section 3.

1.2.2 Motivation for metamaterials in accelerators

Conventional accelerator technology is close to its physical limits, where once the energy of accelerators was growing exponentially, it has now begun to plateau and an energy limit has been reached. To overcome this energy limit new accelerator technologies need to be explored. In addition to the energy limit, these large scale accelerators are becoming increasing costly and thus to increase the applications of accelerators, compact accelerators with high accelerating gradients are needed. Metamaterials pose an interesting avenue for exploring compact accelerating technologies as they are easy to fabricate, relatively simple to integrate and provide control over the dispersion of electromagnetic waves.

Metamaterials also provide a compact option for the generation of coherent radiation, by driving a left handed media with an electron beam, to generate backward propagating Cherenkov radiation which has interesting applications in accelerators, such as the creation of a non-destructive detector, strong coherent sources and the possibility of acceleration. Conventional electron-beam driven coherent sources include large scale facilities like synchrotrons [31], free-electron lasers (FELs) [32], and small scale options like dielectric loaded waveguides [33], which have been shown to create coherent radiation and support the acceleration of particles. Di-

electric loaded waveguides use the Cherenkov effect to generate coherent radiation like left handed metamaterials, however though useful to support high frequency operation, dielectrics can suffer from accumulation of charge, breakdown [34] at the vacuum/dielectric gaps where the fields are enhanced and thermal management issues can occur. By using all metallic metamaterial structures these issues can be prevented while providing an effective means for dispersion engineering, to mimic the behaviour of dielectrics. The typical dispersion of a metallic rectangular waveguide can be modified by loading it with a metamaterial. The composite structure can be tailored to support both forward and backward propagating Cherenkov radiation, which can then be used as a radiation source or to detect propagating particles.

1.2.3 Review of proposed metamaterial designs

Metamaterials play an important part in research into advanced and novel acceleration techniques, where novel methods, materials and accelerating structures can be developed through their integration. There is a small growing field researching the integration of metamaterials into particle accelerators worldwide, though a lot of the work still focuses on the theory rather than the practicalities. The unique metamaterial effect most commonly utilised by these schemes is that of the left handed media to generate backward propagating Cherenkov radiation. As well as applications with reverse Cherenkov radiation, metamaterials pose a strong avenue for alleviating problems such as higher order mode excitation in accelerating structures. A brief overview of schemes will be given here, with a more in-depth discussion is available in Section 4 of Chapter 2.

Early designs to integrate metamaterials into accelerators focussed on the use of SRRs and wires to generate a left handed media [35], these structures developed from a metamaterial where the wires ran along the back of the SRRs [36], to a metamaterial where the wires penetrated the SRRs [37]. The metamaterial was deigned to be loaded into a waveguide and then have a beam propagate down the centre of the waveguide, exciting a left handed mode and generating backward propagating Cherenkov radiation [38] [39]. In addition to the backward propagation of Cherenkov radiation the left handed structure created unique dispersion characteristics within the waveguide including the appearance of several slow-backward wave bands, which indicate a possibility of applications in acceleration as well as detection.

More recent designs have focused on using repetitions of only one type metamaterial element to reduce the complexity of the structure and improve clearance for the beam. These design focus on the use of CSRRs [40], this is advantageous as they generate an LHM [30] on their own, are all metallic thus more vacuum compatible, provide greater beam clearance and are compatible with modern planar fabrication techniques. Initial CSRR designs focussed on infinite stack of CSRR metasurface sheets [41] and showed that a beam propagating parallel to the metasurface sheets between the central two layers will excite a left handed mode. A secondary design where a modified CSRR metasurface formed the inner surfaces of a cross shaped waveguide [42] was also proposed showing consideration was put on the effect of loading the material into a waveguide.

Very recently new designs for volumetric metamaterials formed from a metallic cube with modified resonators cut from the sides [43] of the cube have been proposed for accelerator applications. The move to volumetric structures increases the coupling impedance, as the beam is surrounded by the resonant unit cell on all sides and around the central hole for beam propagation there are coupling slots to further improve interaction. This volumetric structure is an interesting alternative to planar structures, however the space for the beam to propagate is small which could pose difficulties finding a suitable beam to excite the structure if it is physically realised for beam tests.

This has just been a short overview of existing metamaterial design proposals for accelerators, focusing on all metallic structures designed to be loaded into a waveguide as this is the type of structure developed within this thesis. A comprehensive review of metamaterials in accelerators is presented in Chapter 2. Though these designs are interesting, very few of them are physically realised and are based on simulations designed to improve performance only. No consideration has been made as to how the environment will affect the structure, whether it can be fabricated and loaded unsupported into a waveguide, and how this might affect the results. In the next Section, these effects and why they should be given further consideration if a novel metamaterial structure for accelerator applications is to be realised will be discussed.

1.2.4 Operational environment

One of the key motivating factors behind the work carried out within this thesis is that though the concept of integrating metamaterials into accelerator systems

has been considered in several different and novel ways, to date, published work on metamaterials for accelerators has been theoretical. Focusing on theoretical analysis of the metamaterials electromagnetic properties, considering either an infinite un-bounded form of the metamaterial or a very simple waveguide scheme, where only one layer or one row of metamaterial is used. Very little attention has been directed at alleviating some of the practical issues which will impair the use of metamaterials in active devices and high-power environments. In particular, metamaterials often require the use of complex geometries like SRRs and CSRR which have fine features, small gaps and sharp corners which are susceptible to damage or deformation via resistive heating. Even if the simple wire array to generate negative permittivity was considered, to reach interesting operating frequencies the wires would have to be thinned to a point where they too would be susceptible to damage [44]. There is also a challenge created by the over moded nature of many metamaterial based accelerating structures, making it difficult to couple RF into the structure and ensure operation at the correct mode.

By not taking these factors into consideration, many proposed metamaterial based accelerating schemes and metamaterials for applications within accelerators will not make it past the theoretical and simulation stages of development. In some cases the suitability of the structure for a cold test measurement is presented but not how this will hold up in a beam based environment. It is the opinion of the author that though metamaterial physicists are proposing interesting and novel applications to metamaterials in accelerators, without a full consideration of practical limitations in high power environment many of these designs will not come to fruition. By approaching the design of these accelerator based metamaterials from an engineering perspective the aim is to create structures that perform as well as existing metamaterial schemes but have improved robustness that allows for proper fabrication and integration.

The focus of thesis was to design a metamaterial structure for reverse Cherenkov applications, suitable for fabrication and operation within an accelerator environment. This work aims to address some of these practical issues in current schemes and to investigate design considerations that should be made to make the metamaterial structure more suitable to high power operation without compromising the electromagnetic performance. The initial proposed design is based on a CSRR metasurface structure similar to those presented by Shapiro and Temkin [40] [41]. Unlike the efforts of other groups this work was undertaken with the integration of the final structure taken into account, therefore minimal studies are performed on an infinite unbounded structure, and more focus is put on the bounded loaded

waveguide structure. Emphasis is placed on the modes that are formed in a loaded structure and how the truncation of a metamaterial by metallic walls leads to the generation of hybrid modes which can complicate coupling. One of the key aims of this work was to identify how these hybrid modes can be reduced.

The interaction between such structures and electron beams is often discussed either only in terms of simulations or in terms of small commercial beams. With the intention of many of these schemes to be used at existing accelerator sites, more consideration needs to be put on the interaction of the structure with a high power high intensity beam. It is for this reason that the final more robust design was simulated being excited by not only a standard commercial beam but also the beam available on VELA at Daresbury and a high intensity beam. In addition to the interaction between the particle and the beam it is key to understand how the structure will be excited, as stated before, many of these metamaterial based accelerator structures are over moded, with the operational mode often not being a fundamental mode of the structure. Using a conventional coupler to excite these structure would likely result in them operating outside their active frequency and thus the effects that they are designed to harness such as left handed behaviour and backward propagation will not occur, therefore thought needs to be put into designing a coupler that allows for operation at the correct mode.

1.3 Layout of thesis

In this thesis the aim is to investigate how best to integrate metamaterials into accelerators, focusing on;

- Designing a left handed metamaterial structure that can be loaded into a waveguide and used to generate backward propagating Cherenkov radiation.
- The key design considerations required to take such a design from a theoretical concept into a structure that can be fabricated and implemented in an accelerator environment.
- How metamaterials and other forms of dispersion engineering could be integrated into future accelerator designs that operate at high frequencies and smaller scales.

The structure of this thesis is as follows. Chapter 2 presents an in depth background into metamaterials and how such structures can be integrated into accelerators, including a description of the mechanisms behind left handed media and

how metallic resonator elements can be used to create such media. Chapter 3 presents the initial design for a metamaterial loaded waveguide, providing electromagnetic analysis of the unit cell and the loaded waveguide structure, with discussions on beam coupling and wakefields. Chapter 4 follows on from Chapter 3 and presents the design considerations made to increase fabrication suitability and robustness of the structure. Details of how these changes affect the structure are given and electromagnetic, beam coupling and wakefield analysis is provided for several modifications. A final design is proposed as a result of the modifications and discussed. In Chapter 5, the final design is considered within a beam based environment and simulations of the structure, for a number of known beams are given. An in depth analysis of the beam coupling within the structure is provided and the most suitable beam for operation is discussed. In Chapter 6, the work is extended from the microwave frequency range into high frequency accelerator schemes, operating at THz or optical frequency ranges. Three separate design concepts for high frequency operation are discussed and a background to each structure is provided. Finally, in Chapter 7, conclusions are presented and a discussion of potential further work is given.

Chapter 2

An introduction to metamaterials

In this Chapter an introduction to the topic of metamaterials is provided, to give background and context to the work within this thesis. A brief history of metamaterials is given in Section 1 focusing on how the field developed after Veselagos idea of left handed media, and in recent years. In Section 2, left handed media are discussed at length through mathematical analysis of Maxwells equations. Wave propagation in left handed media, negative refraction and the unique applications of backward propagating waves are discussed. In Section 3 the different types of metamaterial elements are covered, with a focus on metallic resonator elements particularly the split ring resonator and its complementary form. The equivalent circuit models of these two resonators are given and a mathematical analysis of the mechanism that gives rise to their unique electromagnetic effects is provided. In Section 4 an in depth discussion of existing metamaterial schemes for accelerators is presented detailing the different structures designed for accelerator applications. Finally an overview of effective parameter retrieval methods is given and an analysis of accuracy is provided.

2.1 History of metamaterials

The term metamaterial is relatively recent terminology for artificial materials which is more commonly used, when discussing older metamaterial designs. The first reference to an artificially designed material is from the late 19th century (1898), when the first microwave experiment on twisted structures, similar to those called chiral metamaterials in today's terminology were performed by J. C. Bose [45]. In later years artificial dielectrics formed by wire arrays were used to mimic plasmas, as the array of thin wires exhibits a negative effective permittivity

like a plasma and were used to study microwave propagation in the ionosphere in the 50's [46] and 60's [47]. This type of artificial dielectric, later became a key element in the realisation of left handed media [23] [20], due to the $\varepsilon < 0$ behaviour below the plasma frequency.

2.1.1 The modern era of metamaterials

The behaviour of metamaterials can be characterised by distinct electromagnetic properties, and the unique property that led to the initial growth of the field was the creation of materials with simultaneously negative ε and μ, in which the refractive index is negative. Materials with simultaneously negative ε and μ were first put forward by V. G. Veselagos in 1968 [24], who discussed the theory of electrodynamics in such media, focusing in particular on the backward propagation of electromagnetic waves and how this results in negative refraction. These materials are often referred to as Left Handed Media (LHM), due to behaviour of the **E**, **H** and **k** vectors in such materials. In the late 60's only $\varepsilon < 0$ values were achievable using certain metals below their plasma frequency. $\mu < 0$ materials were hard to find due to the weak magnetic interactions in most solid state materials, thus no material with simultaneously negative ε and μ had been experimentally observed, and would not be for over 30 years.

In 1999 J. B. Pendry et. al. [20] presented a method for obtaining values of μ previously not accessible by nature via microstructures fabricated from non-magnetic conducting sheets. The most notable value of μ obtained is that where $\mu < 0$, moving one step closer to materials with simultaneously negative ε and μ as predicted by Veselego. These microstructures have a unit cell size much shorter than the wavelength of radiation used, thus each microstructure can be considered like an atom in a conventional material and hence the term metamaterial refers to structures made up of these meta-atoms.

In a metamaterial the contents of the unit cell define the effective response of the material overall. The unit cell size p is constrained by

$$p \ll \lambda = 2\pi c_{\text{eff}} \omega^{-1}. \tag{2.1}$$

Where ω is the angular frequency and c_{eff} is the speed of light in the medium. This states that the unit cell must be much smaller than the wavelength of incident radiation to generate unique electromagnetic effects, hence such structures are often referred to as sub-wavelength. Resonant behaviours are exploited to obtain the

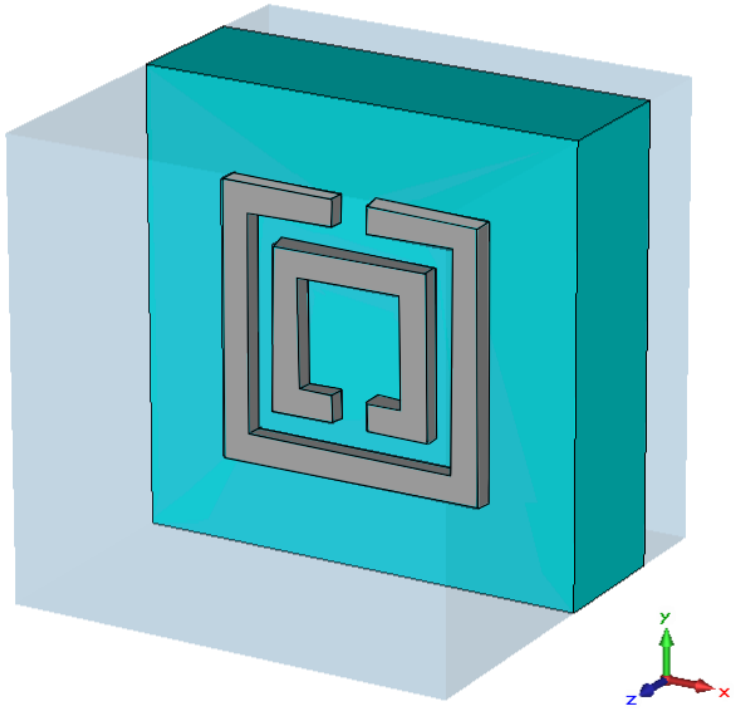

Figure 2.1: An illustration of a square Split Ring Resonator (SRR) used to achieve $\mu < 0$ in a set frequency range near resonance.

unique values of μ, via a number of designs. The most notable of these designs is that of the Split Ring Resonator (SRR) shown in Figure 2.1, which is the most well-known method for obtaining $\mu < 0$. The SRR is a resonant element, that exhibits a large positive μ below the resonant frequency and more interestingly a negative μ just above the resonant frequency. A more in depth discussion of the mechanisms behind metallic resonators and the SRR in particular will be given in Section 3 of this Chapter.

In 2000, the left handed medium theorised by Veselago was realised by D. R. Smith, S. Schultz et. al. [23], who presented a composite material comprising of a periodic array of split ring resonators with inter spaced continuous wires, see Figure 2.2. Here the SRR gives rise to $\mu < 0$ and the wire gives rise to $\varepsilon < 0$, therefore within a specific frequency range the media has simultaneously negative ε and μ. Thus thirty two years after Veselago theorised the existence of LHM, they were demonstrated and this marked the beginning of metamaterials as an entirely new research field.

Once the SRR and wire design was put forward as a method for obtaining simultaneously negative ε and μ, researchers began to explore alternative metamaterials that achieve the same effect. Most simultaneously negative ε and μ metamaterials

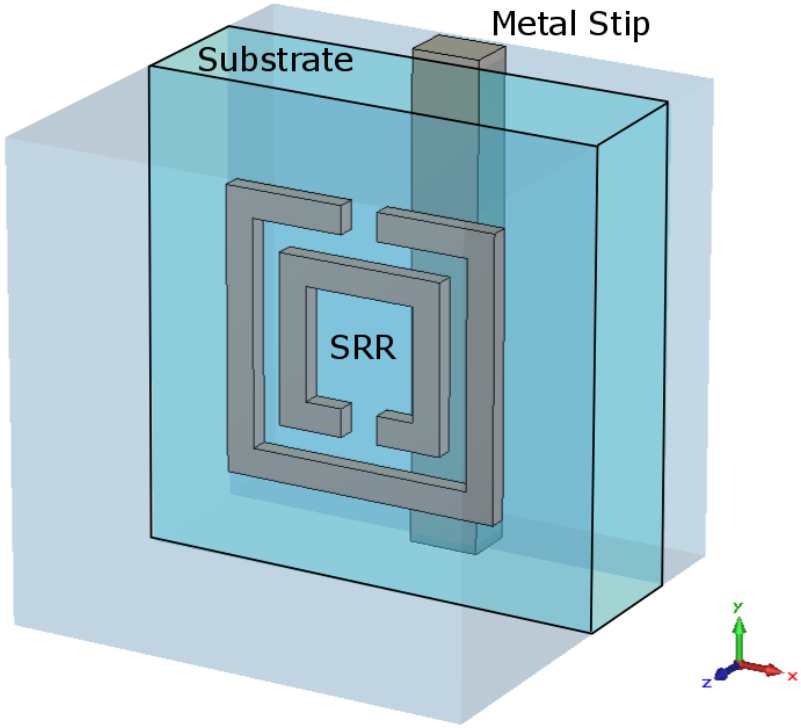

Figure 2.2: An illustration of the unit-cell of the LHM metamaterial, formed from an SRR and a split wire.

combine two elements, one which gives rise to $\varepsilon < 0$ within a frequency range and the other which gives rise to $\mu < 0$ in the same frequency range. For many years metamaterial research focused on creating new materials with simultaneously negative ε and μ, and how this property could be utilised. Research focused mainly on methods of cloaking [26] [48] using the negative refractive index created by such materials and on the design of super or hyper lenses [49] which also rely on the unique refractive properties of the material. This new research field had many branches of research to explore beyond those associated with left handed media, with new materials, unique effects and interesting applications yet to be discovered

2.1.2 Metamaterials for advanced electromagnetism

In previous years the emphasis in metamaterial research was on left handed media; new designs for materials with simultaneous negative ε and μ, new fabrication techniques, high frequency applications and significant effort towards the design and transform optics associated with electromagnetic cloaking [25]. However in recent years, research into metamaterials has expanded to encompass all aspects of advanced electromagnetism, such as the creation of active tuneable metamaterials [50], that incorporate elements that allows for tuning of the material, be that

mechanical methods [51], temperature sensitive elements for thermal control [52], or optical control [53]. These structures can then be tuned to behave in certain ways at certain frequency ranges to give a greater level of control to many applications.

In the area of advanced electromagnetism there is growing interest in materials with very low but still positive values of permittivity, Epsilon Near Zero (ENZ) materials [54]. These materials can be used to tailor the phase of radiation from sources [55], for coupling and energy squeezing [56]. Additionally ENZ materials can be used to cancel the scattering from dielectric or even conducting objects, drastically reducing their total scattering cross sections and making the covered objects practically undetectable to an external observer [57], similar to a negative index cloak. This area is growing rapidly and applications of this property are being considered for applications to accelerators, where the spacial dispersion in such media could be used as a method of to shape the propagating modes [58]. A possible application to accelerators is to flatten mode shape in an accelerating drift tube to enable higher acceleration for a given peak field.

In addition to the investigation of new electromagnetic effects, the research into the applications of left handed materials has expanded beyond cloaking [26] and subwavelength imaging [49] [27]. Where the conventional well studied left handed materials such as those using SRRs are used to explore novel applications in novel environments [59], [42], [60], this is particularly relevant to the research performed within the scope of this thesis. Thus in the near future the field of metamaterials can be expected to expand into further applications of electromagnetic LHM, novel electromagnetic metamaterials, further applications of acoustic metamaterials [61] [62] [63] and a growth in the field of mechanical [64] and elastodynamic metamaterials [65], as evidenced by the growth within the field in recent years [66].

2.2 Left Handed Media (LHM)

Throughout this thesis, materials with simultaneously negative valuesr of ε and μ are referred to as left handed media, to understand this the fundamentals of electromagnetism must be discussed. ε and μ are fundamental properties that govern the propagation of electromagnetic waves within a media, as they are the prominent parameters in the dispersion equation, which gives the relationship between the frequency ω of a monochromatic wave and it's wave vector k [24]. For

isotropic media this takes the form of

$$k^2 = \frac{\omega^2}{c^2}\varepsilon\mu = \frac{\omega^2}{c^2}n^2, \tag{2.2}$$

where n is the refractive index. From these equations it can be seen that a simultaneous change of the sign of ε and μ from positive to negative will have no effect on the relation. Thus to understand the effect of $\varepsilon < 0$ and $\mu < 0$ on the propagation of electromagnetic waves, relations in which ε and μ appear separately must be considered. The relations that fulfil this are the Maxwell equations and the constitutive relations

$$\bigtriangledown \times \mathbf{E} = -\frac{1}{c}\frac{\partial \mathbf{B}}{\partial t}, \tag{2.3}$$

$$\bigtriangledown \times \mathbf{H} = \frac{1}{c}\frac{\partial \mathbf{D}}{\partial t}, \tag{2.4}$$

$$\mathbf{B} = \mu\mathbf{H}, \tag{2.5}$$

$$\mathbf{D} = \varepsilon\mathbf{E}. \tag{2.6}$$

Where $\mathbf{E}$ is the electric field, $\mathbf{B}$ is the magnetic field, $\mathbf{D}$ is the displacement field and $\mathbf{H}$ is the magnetizing field. By using Gauss' law for a monochromatic plane wave proportional to $e^{i(kz-\omega t)}$ the above equations simplify to

$$\mathbf{k} \times \mathbf{E} = \frac{\omega}{c}\mu\mathbf{H}, \tag{2.7}$$

$$\mathbf{k} \times \mathbf{H} = -\frac{\omega}{c}\varepsilon\mathbf{E}. \tag{2.8}$$

From these equations it clear that having simultaneously negative values of ε and μ will give a different response than if they were simultaneously positive. For $\varepsilon > 0$ and $\mu > 0$ it can be seen from (2.7) and (2.8) that $\mathbf{k}$, $\mathbf{H}$ and $\mathbf{E}$ form a right handed triplet of vectors, where as if $\varepsilon < 0$ and $\mu < 0$ the three vectors form a left handed triplet [67]. Hence a medium with simultaneously negative ε and μ is referred to as a Left Handed Media (LHM) as shown in Figure 2.3

To understand wave propagation, it is important to understand energy flow as well as Maxwells equations, hence the Poynting vector $\mathbf{S}$ which gives the direction of the energy flux carried by a propagating electromagnetic wave is considered, this is given by;

$$\mathbf{S} = \frac{c}{4\pi}(\mathbf{E} \times \mathbf{H}), \tag{2.9}$$

which remains unaffected by simultaneously negative ε and μ. Therefore $\mathbf{S}$, $\mathbf{H}$ and $\mathbf{E}$ still form a right handed system and it is only the wave vector $\mathbf{k}$ and the Poynting vector $\mathbf{S}$ which propagate anti-parallel in a LHM as shown in Figure 2.3.

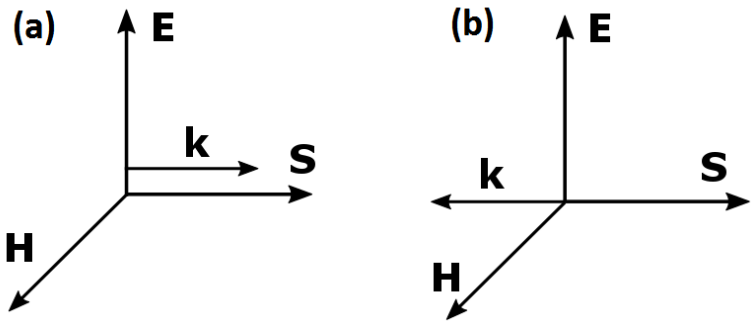

Figure 2.3: An illustration of the vector system of **E**, **H**, **k** and **S** for a plane wave in (a) an ordinary Right Handed Medium (RHM) and (b) a left handed medium.

With the wave vector **k** and the Poynting vector **S** propagating anti-parallel, the energy of the wave, the wave packets, and the wave-fronts will propagate in opposite directions, implying the phase and group velocities will have opposite signs indicating backward wave propagation, a unique property of LHM.

2.2.1 Negative refraction

LHM with simultaneously negative ε and μ, are often referred to as negative index materials, as the refractive index is less than zero. To illustrate this the behaviour of rays at an interface between a normal Right Handed Media (RHM) and a LHM, where negative refraction occurs will be discussed. When a ray of light passes from one medium to another Maxwells equations dictate that the boundary conditions on the fields are as follows;

$$E_{t_1} = E_{t_2}, \quad H_{t_1} = H_{t_2}, \tag{2.10}$$

$$\varepsilon_1 E_{n_1} = \varepsilon_2 E_{n_2}, \quad \mu_1 H_{n_1} = \mu_2 H_{n_2}. \tag{2.11}$$

Where subscript t indicates the tangential field and subscript n the normal field. These must be satisfied, independent of whether or not the media have the same handedness.

These boundary conditions impose continuity on the tangential (x, y) components of the wave-vector, independent of the handedness of the medium. The longitudinal z component of **E** and **H**, only maintains the same direction if both mediums have the same handedness, if the interface is between an RHM and an LHM then

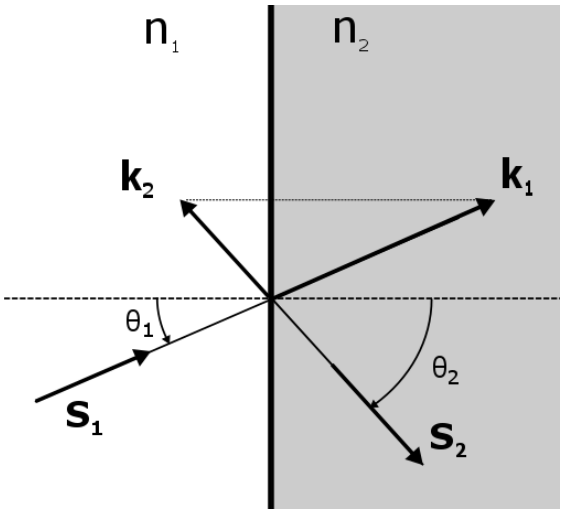

Figure 2.4: The path of wave vector **k** and Poynting vector **S** as an electromagnetic wave moves from an RHM to an LHM, the rays propagate along the direction of energy flow.

the z component will change its sign. Therefore when moving into an LHM the **E** and **H** vectors will not only experience a change in magnitude due to the change in ε and μ, but also undergo a reflection relative to the interface. A similar effect occurs for the wave vector **k**, which undergoes a reflection relative to the interface as shown in Figure 2.4. In an LHM the wave vector **k** and the Poynting vector **S** propagate anti-parallel, therefore a negative refraction of the poynting vector is observed in an LHM as shown in Figure 2.4, where $\theta_2 > \theta_1$. Since the rays follow the path of energy flow, a negative refraction of the light rays is observed as seen in Figure 2.5.

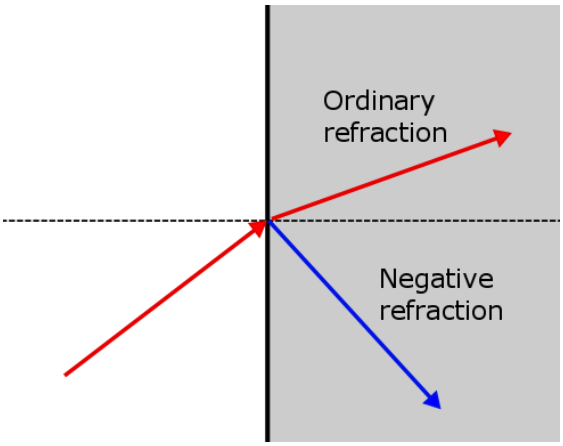

Figure 2.5: An illustration of the ordinary refraction (red) and negative refraction (blue) for a ray as moves from one media into another.

This can be described mathematically by Snells law

$$\frac{\sin\theta_1}{\sin\theta_2} = \frac{-|\mathbf{k}_2|}{|\mathbf{k}_1|} \equiv \frac{n_2}{n_1} < 0, \tag{2.12}$$

where n_1 and n_2 are the refractive indices of the RHM and LHM respectively, where $n_1 > 0$ implies that $n_2 < 0$ to satisfy (2.12). And thus n_2 can be written as;

$$n_2 \equiv -c\sqrt{\varepsilon_2\mu_2} < 0. \tag{2.13}$$

A negative refractive index hence why LHM are often referred to as negative index materials.

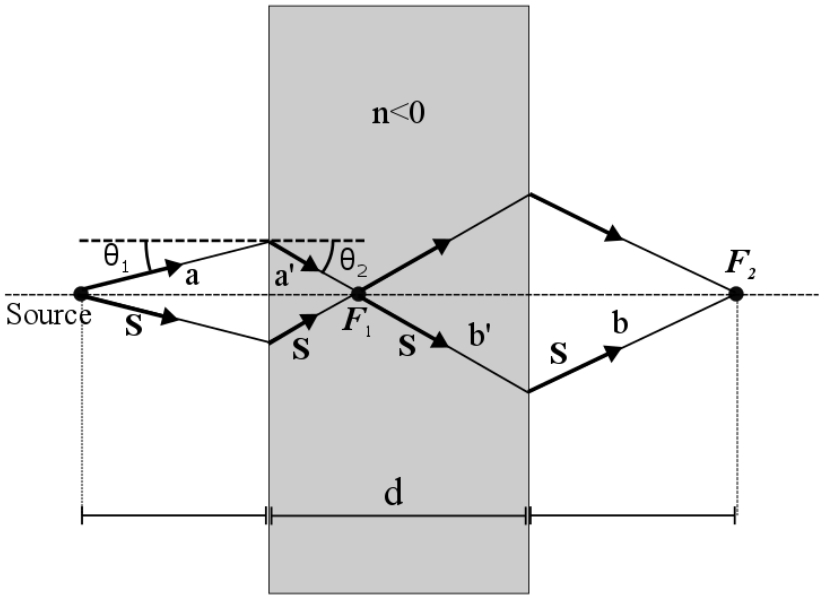

Figure 2.6: A graphical illustration of the focusing of paraxial rays from a point source by a left handed slab, there are two focussing points one inside and one outside the slab.

One interesting and commonly exploited effect of geometric optics in LHM is the focusing of energy from a point source by an LHM [24]. This effect is illustrated by Figure 2.6, and for paraxial rays this can be mathematically described by,

$$|n| = \frac{|\sin\theta_1|}{|\sin\theta_2|} \simeq \frac{|\tan\theta_1|}{|\tan\theta_2|} = \frac{a'}{a} = \frac{b'}{b}, \tag{2.14}$$

where n is the refractive index of the slab relative to the surrounding media. Thus it can be seen that the rays and the energy are focussed to two points, one inside and one outside the slab, the latter at a distance M from the source, which is

determined by,

$$M = a + a' + b' + b = d + \frac{d}{|n|}, \tag{2.15}$$

where d is the thickness of the slab as shown in Figure 2.6. If $n = -1$ then this effect will not be restricted to paraxial rays, as in that case $|\theta_1| = |\theta_2|$ regardless of angle of incidence. When $n = -1$ the rays coming from the source are again focused inside the slab and outside the slab, with the latter focussing point as given by (2.15) being a distance of $2d$ from the source. If $\mu = -1$ and $\varepsilon = -1$ and the impedance remains positive, then the medium can be considered a perfect match to free space and thus there is no reflection at the interface only refraction. This effect gives rise to the concept of a perfect lens [28], which can be used to restore the phase of propagating waves and the amplitude of evanescent states.

2.2.2 Reverse Doppler Shift

There are a number of consequences of the phase velocity propagating in the opposite direction to the energy density, namely the backward propagation of electromagnetic phenomena. One such effect of backward propagation on electromagnetic phenomena is reverse Doppler shift. The Doppler effect is the change in frequency of radiation for an observer moving relative to the source of the radiation, the frequency shift depends on the relative velocity of the source and the observer. In a RHM, when the observer moves towards the source, the wave-fronts and the observer move in opposite directions. For the observer moving towards the source the radiation appears at a higher frequency than to an observer at rest as seen in Figure 2.7a.

In a LHM this behaviour is different, since there is backward propagation, the wave-fronts move towards the source. Therefore if an observer is moving towards the source, then the observer and source are moving in the same direction, and since the observer is moving slower than the radiation, it will appear at a lower frequency to the moving observer than it would for a stationary observer, as seen in Figure 2.7b. The equation for the frequency shift due to Doppler effect is given by

$$\Delta\omega = \pm\omega_0 \frac{v}{v_p}, \tag{2.16}$$

where ω_0 is the frequency of the emitted radiation, v is the velocity at which the observer moves towards the source, v_p is the phase velocity of the emitted radiation and the sign denotes whether it is a RHM or an LHM. This can be written more

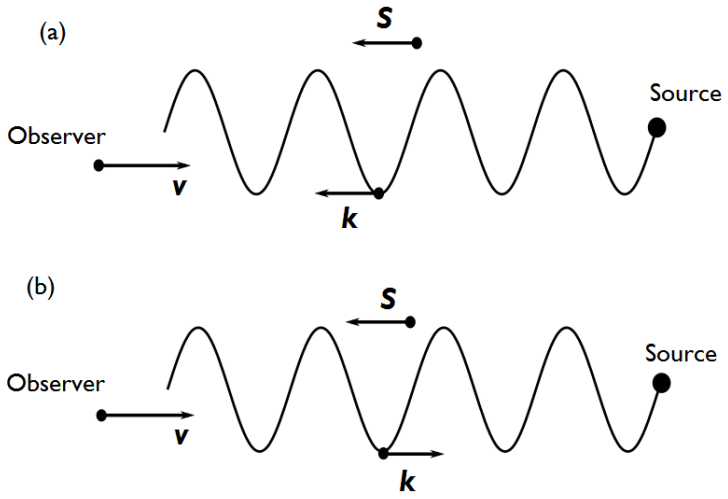

Figure 2.7: An illustration of the Doppler shift in (a) an ordinary right handed medium and (b) in a left handed medium.

compactly if the refractive index is used as an indication of the type of media,

$$\Delta\omega = \omega_0 \frac{nv}{c}. \tag{2.17}$$

It should be noted as $d|k|/d\omega < 0$ in LHM, then a negative frequency shift implies an increase in $|k|$, thus a shift towards shorter wavelengths is seen when the observer moves towards the source in both an RHM and an LHM.

2.2.3 Reverse Cherenkov Radiation

In addition to the reverse propagation of the Doppler effect, backward propagation of electromagnet waves results in the backward propagation of Cherenkov radiation. When a charged particle travels through a medium at a higher velocity than the phase velocity of light in that medium, Cherenkov radiation [68] occurs. It is commonly observed as the blue glow in the water surrounding fission reactors, where the emitted beta particles move faster than $0.75c$ the speed of light in water. If the particle does not decelerate too rapidly, it's motion can be considered as constant over many wave periods, and the spherical wave-fronts emitted by the particle are delayed with regards to the particle motion giving rise to a shock wave or wake travelling forward making an angle θ with the particle velocity as shown in Figure 2.8. The angle at which this radiation is emitted is given by

$$\cos(\theta) = \frac{c}{vn} \tag{2.18}$$

where θ is the angle of emission, v is the speed of the particle and n is the refractive index of the medium in which the particle is propagating.

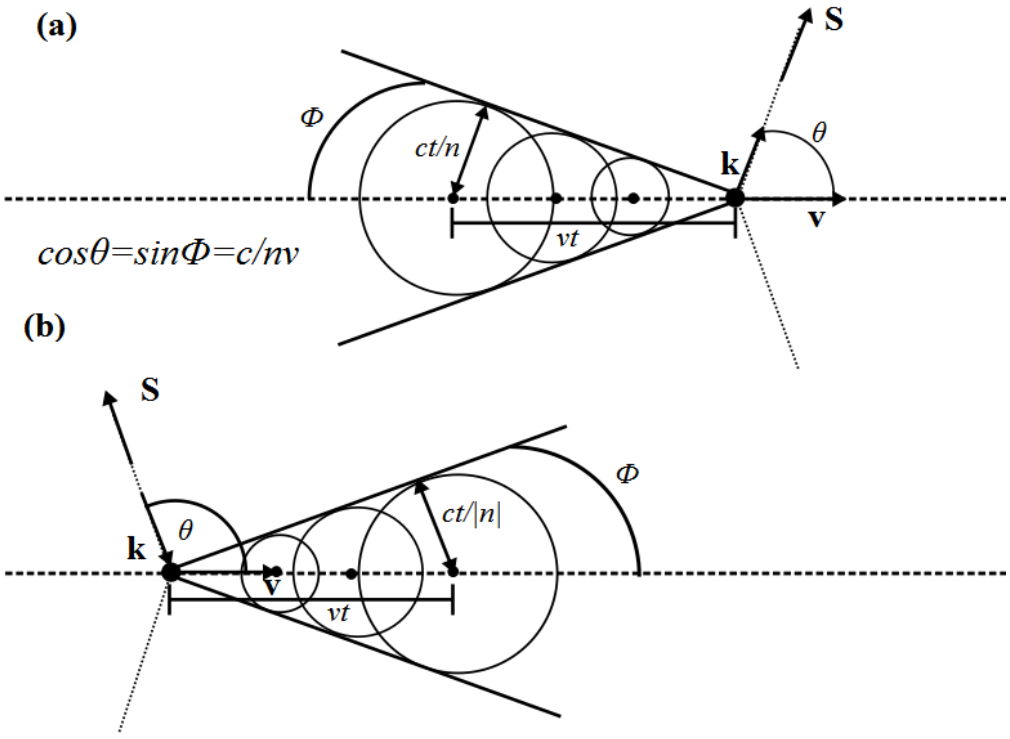

Figure 2.8: An illustration of Cherenkov radiation in (a) an ordinary right handed medium and (b) in a left handed medium.

If the medium is left handed and thus has a negative refractive index, then the wave propagation is backwards and the spherical wave-fronts move inwards towards the source, yet the equation for the angle remains (2.18). This means that each wave-front collapses when it reaches the position of the particle as shown in Figure 2.8b. In this case the resulting shock wave propagates backwards creating an obtuse angle from the particle motion. As all LHM are highly dispersive, the left handed behaviour is restricted to a certain frequency range. Since the particle will radiate at all frequencies, the Cherenkov radiation spectra will show wave-fronts moving both forwards and backwards [69]. It is this effect created by left handed media that is utilised in the majority of work in this thesis, where reverse Cherenkov is considered as a method for creating a non-destructive particle detector, coherent radiation sources or a means of wakefield acceleration.

2.3 Metamaterial elements

In this Section a brief overview is given of the different types of elements or unit cells which can be used to form a bulk metamaterial. The focus will be on metallic metamaterials due to their increased suitability for applications in an accelerator environment. Their increased suitability stems from the large range of low cost vacuum compatible materials available and the relative simplicity of the structures, often requiring only one type of element to form a metamaterial. Though dielectric metamaterials perform similarly in terms of their unique response they present further challenges in an accelerator environment. Additionally the electromagnetic response of metallic metamaterials has been extensively characterised and therefore only the wave beam interaction needs to be characterised in these studies. Dielectric metamaterials are a newer field and therefore present greater uncertainty, in terms of design, electromagnetic response and interaction with the beam. Each type of metamaterials will be discussed briefly in terms of how it gives rise to a unique electromagnetic effect, and a more mathematical analysis will be provided for the SRR and CSRR.

Though metamaterials are considered complex structures, they rely on resonances to generate the unique electromagnetic response, be that the LC resonance of metallic elements or the Mie resonance of dielectric structures, thus all structural designs must evolved from a basic resonator element. For example the split ring resonator evolved from two concentric metallic sheets which formed a capacitor, by adding the ring gaps, an inductance was introduced, and hence an LC resonator was created. Many metallic designs are modifications on this structure, looking at way to tweak the amount of inductance or capacitance to change the response. For the dielectric structures these rely on Mie resonances which have a clear mathematical rules dictating how parameters such as the elements size, shape and separation affect the resonance and therefore new designs are created by the modification of these parameters. Thus despite some of the designs appearing to have been created by trial and error, they have in fact evolved systematically from simple cylindrical capacitors.

2.3.1 Metallic metamaterials

Most metallic metamaterials are based on a resonant structure and when not a simple array of split wires, often take the form of a modified split ring resonators

seen in Figure 2.9. These structures rely on inductance and capacitance to drive a unique electromagnetic response just after the resonant frequency.

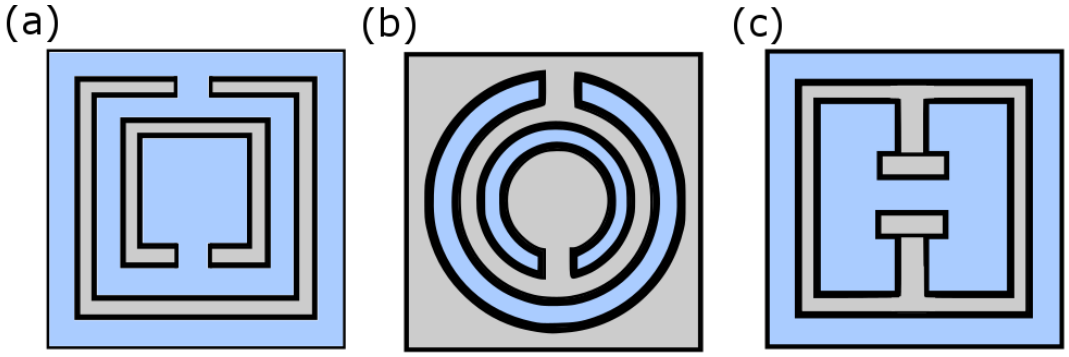

Figure 2.9: An illustration of the different types of SRRs. (a) The square split ring resonator, (b) the complementary split ring resonator, (c) and electric LC resonator.

Wire arrays

The most common element for obtaining negative permittivity is that of an array of thin wires, which exhibit $\varepsilon < 0$ below the plasma frequency, often these are combined with SRRs to create a LHM. The array of thin wires exhibits behaviour like a plasma and was initially used to study microwave propagation in the ionosphere in the 50's [46] and 60's [47], however in recent years this set-up has been studied due to its unique electromagnetic properties such as low frequency plasmon propagation [70]. In the metallic wire array if the spacing between the wires is significantly smaller than the wavelength then it behaves like a dispersion free media, and when the electric field propagates parallel to the wires, exhibits $\varepsilon < 0$ below the plasma frequency. This permittivity can be simply given by;

$$\varepsilon_{\text{eff}} = 1 - \frac{\omega_p^2}{\omega^2}, \tag{2.19}$$

where ω_p is the plasma frequency for the wire array. Though split wires are the most common way of achieving the $\varepsilon < 0$ component of an LHM, they are not the only method, and in certain situations alternative methods can be more suitable. One of the main drawback of wire media is they require continuous connections between the unit celsl therefore any deformation or damage that breaks this connection will change the properties of the bulk material. This provides motivation to seek alternative $\varepsilon < 0$ materials.

The electric LC resonator

Figure 2.9c), shows an electric LC resonator [71], so named as it strongly couples to the electric field, this resonator is comprised of a central capacitive gap connected to two inductive loops. The electric LC resonator poses an alternative method to generate $\varepsilon < 0$ and has been demonstrated in both the microwave frequency range [71] and at higher frequencies [72] where more complex geometries pose fabrication issues and wire media would need to be unphysically thin. Unlike the split ring resonator this structure gives rise to $\varepsilon < 0$ rather than $\mu < 0$ due to its coupling to the electric field. It is considered an alternative to split wires when an electric connection between unit cells is required to maintain bulk properties. It is often used in place of the CSRR at high frequencies as printing this structure onto circuit boards is simpler to fabricate than cutting rings out of a material.

The Split Ring Resonator (SRR)

The Split Ring Resonator (SRR) was the first metamaterial element designed to exhibit negative permeability $\mu < 0$, which until this point was only possible with a limited number of ferrite materials, which are unsuitable at GHz frequencies and lacking in mechanical stability [20].

The SRR is a resonant structure that relies on inductance and capacitance to drive the resonance that gives rise to the unique effect of $\mu < 0$. The most common form is the double split ring where a smaller split ring lies inside a larger split ring on a substrate with the ring gaps at opposite sides as shown in Figure 2.10. For higher frequency operation, where scales are much smaller the double SRR is often reduced to a single split ring or staple like structure [73], which is simpler to fabricate. When excited by an external time varying magnetic field, the gaps in the rings prevent current flow around any one ring, however the capacitance between the two rings forces the current to flow from one ring to the other across the space between them. For this structure the effective permeability as given by Pendry in 1999 [20] can be calculated as

$$\mu_{\text{eff}} = 1 - \frac{F_i}{1 + \frac{2\rho i}{\omega r \mu_0} - \frac{3}{\pi^2 \mu_0 \omega^2 C r^3}}, \tag{2.20}$$

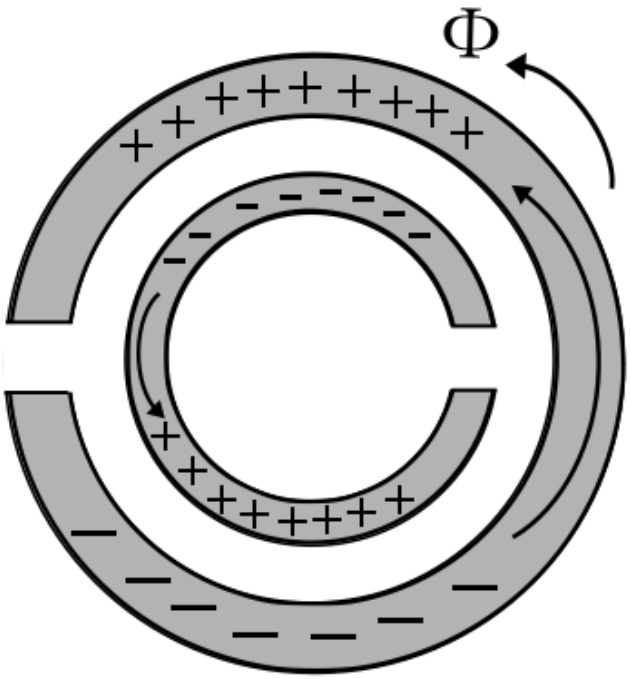

Figure 2.10: An illustration of the SRR showing the charge build up on the rings and the flow of flux.

where ρ is the conductivity and F_i is the fractional volume of the unit cell occupied by the interior of the inner ring defined as

$$F_i = \frac{\pi r^2}{p^2}, \tag{2.21}$$

where p is the unit cell size and r is the radius of the inner ring. C is the capacitance per unit area between the two rings,

$$C = \frac{\varepsilon_0}{w} = \frac{1}{wc_{\text{eff}}^2\mu_0}, \tag{2.22}$$

where w is the ring separation. By substituting (2.21) and (2.22) into (2.20), the equation for effective permeability can re-written as

$$\mu_{\text{eff}} = 1 - \frac{\frac{\pi r^2}{p^2}}{1 + \frac{2\rho i}{\omega r \mu_0} - \frac{3wc_{\text{eff}}^2}{\pi^2\omega^2 r^3}}. \tag{2.23}$$

However, since there is a capacitance within the system then there must also be a balancing inductance in the system, giving μ_{eff} a resonant form.

If a generic case is considered where the structure is highly conductive i.e. $\rho \approx 0$,

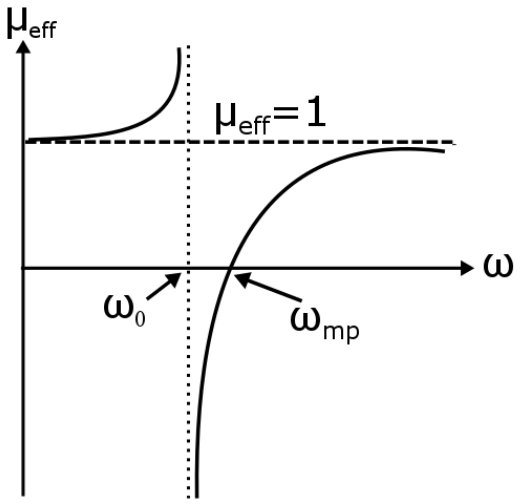

Figure 2.11: A sketch the typical form of μ_{eff} for an SRR made of a highly conducting material. Below the resonant frequency μ_{eff} is enhanced, but above resonance μ_{eff} is less than unity and can be negative close to resonance. The region between ω_0 and ω_{mp} is the active region of the resonator.

then below the resonant frequency μ_{eff} is enhanced and above the resonance μ_{eff} is less than unity, and may be negative close to the resonance. An illustration of this behaviour is given in Figure 2.11, which shows the behaviour of μ_{eff} around the resonant frequency ω_{mp}. If ω_0 is the frequency at which μ_{eff} diverges then it can be defined as

$$\omega_0 = \sqrt{\frac{3}{\pi^2 \mu_0 C r^3}} = \sqrt{\frac{3wc_{\text{eff}}^2}{\pi^2 r^3}}, \tag{2.24}$$

and ω_{mp} is defined as the magnetic plasma frequency,

$$\omega_{\text{mp}} = \sqrt{\frac{3}{\pi^2 \mu_0 C r^3 (1 - F_o)}} = \sqrt{\frac{3wc_{\text{eff}}^2}{\pi^2 r^3 \left(1 - \frac{\pi r^2}{p^2}\right)}}, \tag{2.25}$$

where F_o is the fraction of the structure not inside the ring,

$$F_o = 1 - \frac{\pi r^3}{p^2}. \tag{2.26}$$

The separation between ω_0 and ω_{mp} as seen in Figure 2.11, gives the active region of the resonator in which unique values of μ_{eff} are observed, from this it is possible to obtain the frequency at which the structure is active,

$$f_{\text{mp}} = (2\pi)^{-1} \omega_{\text{mp}} \tag{2.27}$$

which then gives

$$f_0 = f_{\text{mp}}\sqrt{\left(1 - \frac{\pi r^2}{p^2}\right)}. \tag{2.28}$$

This is the active frequency of the medium and can be used to determine the wavelength which excite the medium via $c = f\lambda$, which for an effective SRR will be much greater than the unit cell size.

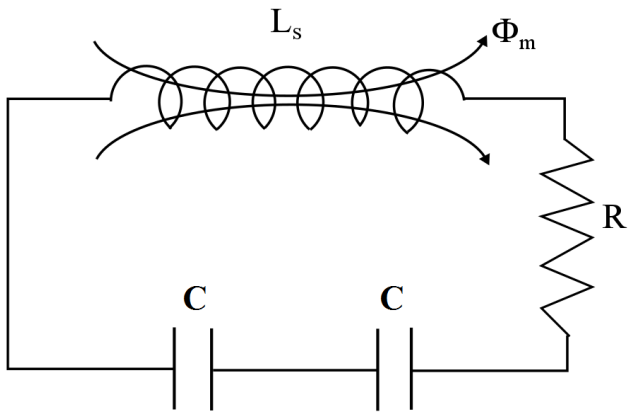

Figure 2.12: The equivalent circuit model of the split ring resonator.

Another way to describe the behaviour of the SRR, is to consider an equivalent LC circuit [74], as shown in Figure 2.12. In the LC equivalent circuit, the inductance L is the self-inductance of the structure and C is the capacitance associated with each ring, given by $C = \pi r C_{\text{pul}}$, where r is the mean radius of the double ring and C_{pul} is the capacitance per unit length of along the space between the rings. The total capacitance of this system is defined by the series connection between both rings thus is $C/2$. From this it is possible to determine the total current I flowing within the system when an external excitation Σ is incident on the structure.

$$\left(\frac{2}{i\omega C} + i\omega L\right) I = \Sigma. \tag{2.29}$$

This circuit model is valid if the following conditions are obeyed;

- The perimeter of the ring is considered small in comparison to half a wavelength of the incident excitation.
- The capacitance at the split in the ring is negligible compared to the capacitance between the rings.

If these conditions are met then it can be assumed that the current on each ring vanishes at the cuts and thus the angular dependence of the currents on each ring

can be considered to be linear such that the total current on each ring is constant. This also implies that the voltage across the slots is constant in both rings.

The resonant frequency ω_0 of the double SRR can be derived from (2.29) by setting $\Sigma = 0$,

$$\omega_0^2 = \frac{2}{LC} = \frac{2}{L\pi r C_{\text{pul}}}. \tag{2.30}$$

Near resonance the current flows across the spacing between the rings and thus the self-inductance can be modelled as the inductance of a ring with average radius r and ring width c. As with the capacitance, the inductance that gives rise to the resonant frequency ω_0 is the average of the inductances of both rings, ignoring the gaps. If the double split ring is excited by an external magnetic field, as is required to obtain the unique values of μ_{eff}, the Σ becomes $\Sigma = -i\omega\Phi_m$ where Φ_m is the external magnetic flux across the double split rings, this makes the equation for total current.

$$I = \frac{\Phi_m}{L}\left(\frac{\omega_0^2}{\omega^2} - 1\right)^{-1}. \tag{2.31}$$

The Complementary Split Ring Resonator (CSRR)

The Complementary Split Ring Resonator (CSRR) is the complement or the dual of the SRR, formed by cutting two concentric split ring out of a metal sheet. The CSRR provides the opposite unique electromagnetic effect to the SRR, when excited by an incident field it gives rise to negative permittivity, providing a planar fabrication alternative to split wires.

Where the SRR can be considered a resonant magnetic dipole that can be excited by an axial magnetic field, the CSRR behaves as an electric dipole, that can be excited by an axial electric field. The CSRR is often used when thin wires would be an unsuitable choice for the $\varepsilon < 0$ component, such as in an accelerator system [75] [40]. The added appeal of the CSRR is that when used to form evenly spaced metasurface sheets, it mimics a narrow patterned waveguide [30], which when a transverse magnetic field propagates between the layers becomes a LHM. Like the SRR the CSRR can be excited by both an electric and magnetic field, and thus when a magnetic field is applied across the surface parallel to the ring gaps it exhibits a resonant magnetic polarizability in that direction.

The CSRR was first put forward by Falcone et. al. in 2004 [29] as a design of planar negative permittivity metasurfaces, by applying the theory of diffraction and the Babinet principle to an SRR. Like the SRR, the CSRR has both induc-

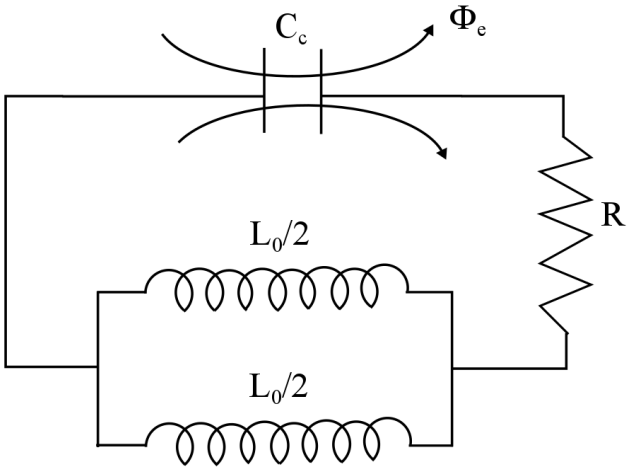

Figure 2.13: The equivalent circuit model of the complementary split ring resonator.

tance and capacitance, and thus can be modelled as an LC circuit as shown in Figure 2.13, where the equivalent circuit of the SRR had one inductance subject to magnetic flux and two capacitances, the CSRR has one capacitor subject to electric flux and two inductors. The inductance L_s of the CSRR is replaced by the capacitance C_c, of a disc with the radius of the inner ring. The series connection of the capacitors in the equivalent circuit model of the SRR is replaced by a parallel combination of inductances connecting the inner disk to ground. Each of these inductances is given by $L_0/2$ where $L_0 = 2\pi r_0 L_{\text{pul}}$, where r_0 is the radius of the inner ring, and L_{pul} is the inductance per unit length of the material connecting the inner disc to ground. In the absence of any dielectric substrate, for an infinitely thin perfect electrical conductor, it follows from duality that the parameters for the SRR and CSRR are related by

$$C_c = 4\left(\frac{\varepsilon_0}{\mu_0}\right) L_s \quad \text{and} \quad C_0 = 4\left(\frac{\varepsilon_0}{\mu_0}\right) L_0. \tag{2.32}$$

The factor of 4 arises from the symmetry properties to the electric and magnetic fields of both elements. From the above relations and duality, it can be deduced that the resonant frequency is the same for the CSRR and SRR when it is a true complement and when considering infinitely thin conducting sheets.

One of the reasons that the CSRR is of such great interest within the scope of this thesis, is the suitability of CSRR metamaterials for accelerator applications. The planar nature implies ease of fabrication and allows for good clearance for an electron beam to propagate parallel to the surface without any chance of collision. The all metallic nature of the CSRR makes it highly suitable for applications within a vacuum, as finding vacuum compatible substrates for SRRs can prove challenging.

In comparison to SRRs and wires, these structures are considered more robust with less resultant damage being observed when the structure is within a high power environment. In additional to this the structure is well studied, with numerous reviews on the topic allowing for easy analysis of the unique effects generated by a propagating electron beam.

Most appealing though is the capacity to create a left handed medium using only CSRRs an no other element, significantly simplifying both the fabrication and the overall structure. In the case of the CSRR the negative permittivity comes from the resonant behaviour but the negative permeability can be obtained by confinement of transverse magnetic modes propagating between metasurface layers [30].

2.3.2 Non-metallic metamaterials

In addition to metallic resonator elements, it is possible to generate negative permittivity and permeability via the Mie resonance of an array of dielectric elements as shown in Figure 2.14. Both $\varepsilon < 0$ and $\mu < 0$ can be obtained using Mie resonant elements, the first resonance gives rise to negative permittivity and the second resonance gives rise to negative permeability. It is possible to obtain simultaneously negative permittivity and permeability [76] by having Mie resonant dielectrics of different sizes as in Figure 2.14b where the first resonance of one coincides with the second resonance of the other. These structures take the form of ordered arrays of cubes, spheres or discs, and are fabricated via top down lithography or deposition techniques.

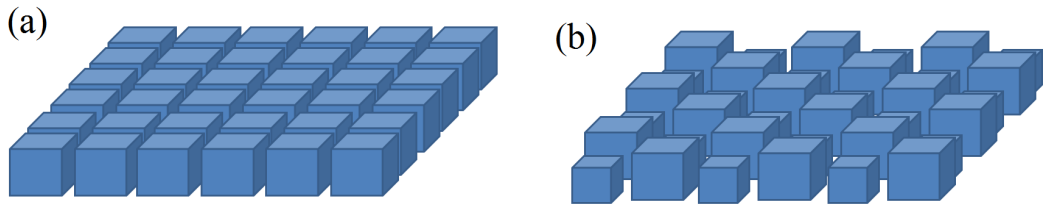

Figure 2.14: An illustration of Mie resonant dielectric cubes. (a) Array of same sized cubes used to generate $\varepsilon < 0$ or $\mu < 0$ via the first or second resonance. (b) An array of two different sized cubes, where the second resonance of the smaller cubes occurs at the same frequency as the first resonance of the larger cubes, creating an LHM where ε and μ are simultaneously negative.

Microspheres of TiO_2 are a good example of a Mie resonant metamaterial with a high dielectric constant, Rutile TiO_2 has also be used for ordered cube arrays [77] and disk arrays [78]. These microspheres exhibit a magnetic resonance giving rise to an effective magnetic response [79]. The response is characterised in three ways; the resonant frequency is determined by the mean size of the particles and permittivity of the microspheres, the bandwidth is determined by the dispersion of the particles on the substrate and the strength of the response is determined by the filling fraction. Therefore by tuning these parameters it is possible to obtain negative permeability, this is most likely with an ordered array of spheres but should also be possible with a random array. Random arrays of Mie resonant elements formed from bottom up fabrication techniques have been shown to give rise to negative values of ε and μ. The unique electromagnetic properties of these materials ensure that there is extensive discussion on these structures within the metamaterial community.

2.4 Metamaterials in accelerators

Conventional accelerator technology has reach saturation, where once the energy of accelerators was growing exponentially, it has now begun to plateau and an energy limit has been reached. To overcome this energy limit new accelerator technologies need to be explored. In addition to the energy the limit, these large scale accelerators are becoming increasing costly and thus to increase the applications of accelerators in industry and medical sectors as well as research facilities, compact accelerators with high accelerating gradients are needed. Metamaterials pose an interesting avenue for exploring novel compact accelerating technologies as they are easy to fabricate, relatively simple to integrate and provide control over the dispersion of electromagnetic waves.

Though other forms of dispersion engineering have been integrated into accelerator systems before, the integration of metamaterials into accelerators is a relatively new field. When intergrating metamaterials structures in accelerators a number of new factors need to be considered, due to the environment and associated strains that the metamaterial must operate under. This will often involve operating in a vacuum, requiring the use of vacuum compatible materials, at high powers and in the presence of an electron beam, which some metamaterials have been shown to be unable to withstand. All these factor pose significant challenges for integrating metamaterials into accelerators and it is for these reasons that the author believes the field has been slow to develop.

Within this Section the evolution of metamaterials in accelerators will be discussed, looking at the early metamaterial based accelerator schemes and moving on to new designs, then looking into the roles that metamaterials can play in such environments. Metamaterials also pose a strong avenue for alleviating problems such as higher order mode excitation in accelerating structures [80]. The focus of the this Section will be on metallic metamaterial elements and their integration into accelerators, though dielectric schemes exist, they lie closer to dispersion engineering than metamaterials at this time and will be discussed in Chapter 6. A metallic metamaterial structure is the focus of this thesis and therefore such schemes provide a strong background and motivation for this work.

2.4.1 Early split ring resonator based designs

Initial designs for incorporating metamaterials into accelerators focused on the use of a SRR and wire structure which used the backward propagation Cherenkov radiation in a LHM as a method of beam diagnostics [35]. The advantage of using a LHM to create a Cherenkov detector, is that the backward propagation dictates that the radiation is emitted in the opposite direction to the beam, thus making it easier to obtain a clean measurement. In this work the group focuses on a conventional LHM of SRRs and split wires as put forward by Smith in 2000 [23], this structure was designed for operation at 10 GHz. Results from this work showed that there exists a left-handed transmission band at 11.6-12.2 GHz. The final out come from these experiments is intended to be the observation of backward propagating Cherenkov radiation.

Once an infinite metamaterial structure had been characterised, the metamaterial needed to be loaded into a waveguide [36], as the dispersion characteristics of the waveguide are changed by the insertion of a metamaterial. The dispersion relation of a left handed waveguide is shown to have has several interesting frequency bands, including a region in which below cut of propagation can occur. Within such a loaded waveguide structures there is the appearance of several slow-backward wave bands, which indicate a possibility of applications in acceleration as well as detection. Through analysis of the permittivity and permeability tensors of a continuous anisotropic LHM it has been shown that it is possible to achieve synchronism between relativistic particles and the fundamental backward propagating accelerating mode, the TM_{11} mode. When such a mode propagates through the structure it supports these slow waves and allows for the acceleration

of particles, initial values for the characterisation of this structure have been reproduced in Table 2.1, the key parameters that indicate beam coupling are the shunt impedance and the R/Q, which give the net acceleration for a given amount of power loss and a given amount of stored energy respectively.

Table 2.1: A reproduction of the Table in [36], showing the parameters of the proposed left-handed accelerator.

Parameter	**Value**
Frequency, (GHz)	11.424
Quality factor (Q)	150
Shunt Impedance, (MΩ/m)	7
R/Q, (kΩ/m)	35
Group Velocity, c (m/s)	0.208
Accelerating Gradient, (MV/m)	$2.5\sqrt{P}$[MW]

In 2007, early designs and experimental work on the loaded waveguide structure were presented, the initial set-up for the left handed medium of SRRs and split wires comprised of three printed circuit boards [37], one with the wire strips alone, one with only SRRs, and then one with SRRs and wires combined. This allowed for testing of the negative permittivity and permeability elements, both separately and combined. Two types of measurement were performed to verify the left handed behaviour; a direct measurement of the refraction angle of incident radiation to observe the effect of negative refraction, [81], and measurement of the transmitted and reflected power [82], both methods verified the structure is left handed in the desired frequency range. The design of the SRR and wire array is reconsidered to improve the robustness of the structure and alternative configurations for improved response is investigated. The design changes from the wire array running along-side the SRRs, to a more symmetric geometry with the wires penetrating the centres of the SRRs. Before fabricating the structure a method to simulate wakefield coherent radiation generation in metamaterial loaded waveguides, where the medium is both dispersive and anisotropic is explored, so that different waveguide cross sections, different transverse beam distributions and different dispersive media can be analysed [83]. This improved design is fabricated and used in the investigation into the verification of backward propagating Cherenkov radiation via preliminary wakefield results [38] [39].

In 2008 experimental verification of backward propagating Cherenkov radiation in a left handed medium [38] was undertaken. Beam line experiments were performed with a 6 MeV, 1.4 nC, electron beam propagating through the metamaterial-loaded

waveguide. This electron beam generates a wakefield via the Cherenkov radiation mechanism, and a signal is detected in the left-handed frequency band around 10 GHz, corresponding to the left handed region found in cold tests, since the frequency bands matched this was considered an indirect demonstration of reverse Cherenkov radiation as predicted by Veselago. However explicit verification of direct backward propagation of the wakefield was not performed. The coinciding frequency band were sufficient for the group to believe that there had been backward propagating Cherenkov even if it had not been directly observed.

2.4.2 Complementary split ring resonator based designs

Though the design with SRRs and split wires showed promising results, the structure formed was very closed and ideally a more open structure is desirable to aid beam propagation. One such design is that of stacked CSRR metasurface sheets, which exhibit left handed behaviour when a transverse magnetic mode propagates below its magnetic plasma frequency [30].

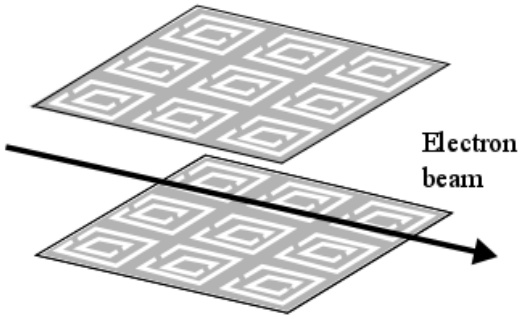

Figure 2.15: An illustration of the proposed metamaterial linear accelerator, showing two parallel sheets of CSRR and the path of the electron beam.

In 2009 an initial design for a CSRR metamaterial based accelerating structures [41] was proposed, the structure created a left handed media from sheets of CSRR set parallel to each other to form an infinite set of patterned waveguides as shown in Figure 2.15. The CSRRs give rise to negative permittivity [29] and the confinement of propagating transverse magnetic waves gives rise to the negative permeability [30], making the structure left handed at the operational frequency of around 5.5 GHz. This infinite structure is shown to have strong beam coupling parameters with an R_s/Q of 6.2 $k\Omega/m$. Some consideration of the potential configuration of this structure in an accelerator is made however simulations are performed for an unbound form with periodic boundaries in all directions and no consideration is made for the metallic walls, which will have an effect on the behaviour of the

structure.

The structure has the ability to support a negative-index transverse magnetic mode, which resonantly interacts with a relativistic electron beam, leading to applications in coherent sources and acceleration. The planar nature, makes it easy to fabricate and scalable to higher frequencies, an improvement on previous designs [40]. The spacial dispersion of the longitudinal field is strongest centrally between the sheets leading to improved interaction with the beam. Compared to the SRR and wire design and the fishnet [84] accelerating structures this is considered a better option as the beam propagates parallel to the sheets and is therefore un-obstructed. In these designs the issues of high power operation and RF-breakdown are not addressed, thus further providing motivation for this thesis.

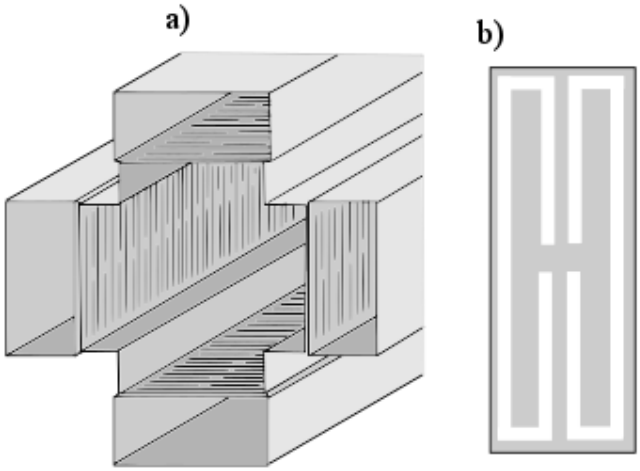

Figure 2.16: An illustration of the modified CSRR waveguide, showing a) the cross waveguides with CSRR like metasurfaces cut into the internal faces and b) the modified CSRR unit cell.

The CSRR design is developed further for wakefield applications with a cross formation of four rectangular waveguides [42] with the inner walls formed from modified CSRRs as shown in Figure 2.16. The modified CSRRs are elongated rings, side by side with the ring gaps centrally facing and a unit cell period of 7 mm leading to left handed behaviour at 2.7 GHz. Wakefield simulations of the structure identify narrowband longitudinal wake excitations at the operational frequency and when excited by a beam in the PIC solver it is shown to gain energy from the beam and emit coherent radiation. Simulating the CSRRs in a waveguide below cut off rather than as an infinite array shows that the fabrication of

the structure and applications in accelerators have been considered however still no move has been made to address the issues of a high power environment.

2.4.3 Alternative metamaterials for acceleration

Though the CSRR metasurface sheet loaded waveguide design shows a strong performance, suitability for accelerator applications, and is pursued in greater depth within this thesis, further alternative designs should be discussed to provide further context. The same group that developed the initial CSRR design have moved on to design a volumetric metallic metamaterial structure for interaction with a relativistic electron beam [43]. This work introduces a new volumetric structure, as shown in Figure 2.17, this forms a three dimensional unit cell rather than a 2D sheet. The structure is designed for operation at 17 GHz for applications in particle beam diagnostics, acceleration and microwave generation. The structure is all metallic and self-supporting, thus does not require any substrate which pose challenges to vacuum compatibility.

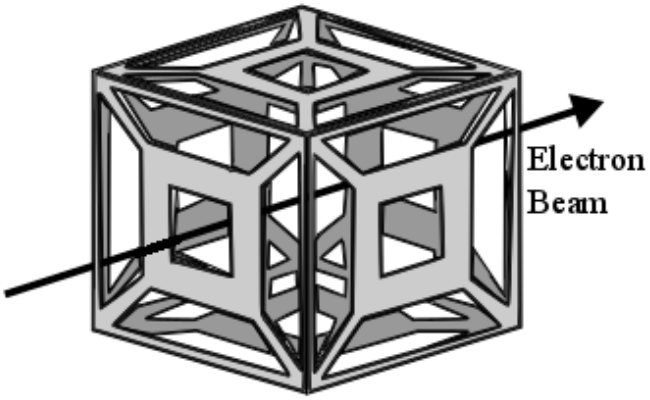

Figure 2.17: An illustration of a volumetric unit cell similar to the one proposed by the MIT group, here the beam line can be seen to pass through the centre of the cell.

The move away from planar structures into volumetric structures increases the coupling impedance, in planar structures the fields are concentrated on the plates a set distance from the beam, whereas in the volumetric structure the beam is surrounded by the resonant unit cell on all sides. The volumetric unit cell is an empty cube with capacitive and inductive resonators on the faces, and a central hole for beam propagation. Around the beam hole are coupling slots, to improve the interaction between the beam and the fields of the structure. Due to the 3D nature the

structure exhibits negative group velocity around the operational frequency for all propagation directions independent of geometry. In wakefield simulations a strong longitudinal wake impedance is excited around the operational frequency further indicating strong coupling. In particle in cell simulations, reverse Cherenkov is observed in the vacuum surrounding the volumetric structure. A modified version of the unit cell, with a two faced cube rather than a six faced cube is proposed for insertion in a waveguide for wakefield acceleration applications and in simulation is shown to behave like a dielectric wakefield accelerator.

The move from two dimensional planar sheet to a volumetric structure is interesting, and shows that methods to improve the wave beam interaction and the coupling have been considered. However there is still little consideration to the practical aspects of creating such a structure for applications within an accelerator. This continues to provide motivation for the work presented within this thesis, where the design consideration required to increase the suitability of metamaterials in accelerators is investigated.

2.4.4 Metamaterials for coherent sources

Another interesting application of metamaterials within accelerator environments is that of using the energy from a highly localized free-electron-beam to excite a planar plasmonic metamaterial to emit coherent light [85]. This experimentally demonstrates that a scalable, optical source can be constructed using a collectively oscillating optical nanoantenna array, driven by the injection of free electrons. The emission is determined by the collective interaction of the metamaterial made from the plasmonic nanoantennas. The dominant TM_{11} mode is of particular interest: it is frequency-matched to the metamaterial absorption resonance, has a highly uniform phase profile, launches a plane wave propagating perpendicular to the metamaterial plane and, uses a dominant proportion of the collective excitation energy of the metasurface. This excitation can be seen in Figure 2.18, the metasurface used to generate the light is a square arrays of Asymmetrically Split Rings (ASRs) which possess a plasmonic resonance from the interaction of large numbers of metamolecules in the array. This is an interesting and unique application that could be used for a threshold-free light source.

An alternative method to generate coherent radiation from a metamaterial structure is to use a negative index material to generate Smith-Purcell radiation [86]. Smith-Purcell radiation is normally generated via an electron beam passing close

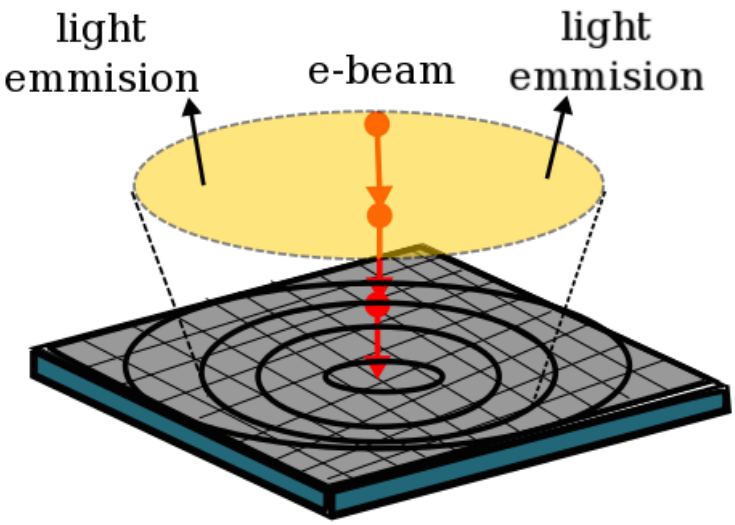

Figure 2.18: An illustration of the excitation of light from a metasurface excited by a free electron laser, the light emission is over a much larger area than the excitation spot.

to the surface of a metallic grating, however in this work a negative index material of SRR penetrated by split wires is used formed into a simple stepped grating [87]. This is formed into a periodic array of alternating media of RHM and LHM. In the designed structure, the reflection and transmission coefficients for the waves generated by the beam at the interface between a positive and a negative-index medium have larger magnitude than those generated from a conventional Smith-Purcell grating. The radiation is enhanced as the change in handedness of the grating leads to a coupling between the incident beam and all diffractive beams. This is an interesting design for a Smith-Purcell grating, using metamaterials however until the fabrication of resonators at small scales is improved this structure will be limited in frequency.

2.4.5 Metamaterials to alleviate existing challenges in accelerators

Not all applications of metamaterials in particle accelerators focus on structures to accelerate particles or to generate coherent sources, some applications look to alleviate existing challenges in accelerators. Such as reducing resistive wall impedance in beam pipes [59], which occurs due to the finite electrical conductivity of the beam pipe walls. This effect can constitute a significant percentage of the maximum acceptable impedance. The use of negative permittivity or negative

permeability material to reduce or nearly cancel the resistive wall impedance has been investigated, by inserting a layer of metamaterial between the vacuum and the beam pipe walls.

In simulations of metamaterial lined beam pipes, both $\varepsilon < 0$ and $\mu < 0$ layers lead to a major decrease of the real part of the longitudinal impedance above a characteristic frequency, dependent on constitutive parameters and layer thickness. The influence on the imaginary part of the impedance is the opposite with the $\mu < 0$ layer changing the imaginary part from inductive to capacitive, and the $\varepsilon < 0$ layer increasing the imaginary longitudinal impedance up to a constant above the characteristic frequency. For transverse impedance the effect is also evident, the $\mu < 0$ layer increases the real part and decreases the imaginary one, down to negative values and the $\varepsilon < 0$ layer significantly decreases the real part and increases the imaginary. In both cases though, the imaginary parts are approaching zero above the characteristic frequencies.

To understand how a real metamaterial would affect the impedance a rectangular waveguide loaded with SRRs a $\mu < 0$ material was studied [80]. In this set-up metallic SRRs on loss free substrate are used to coat the inner faces of a rectangular waveguide, these exhibit negative permeability between 4 GHz and 4.5 GHz. The longitudinal wake impedance of a beam propagating through the lined waveguide is compared to the results of an empty metallic waveguide, and though the overall longitudinal impedance is increased, in the negative permeability band the impedance is slightly lowered. The width of this band can be increased by changing the geometric parameters of the SRR however unless operation within this band can be ensured then the addition of SRR lining is not significantly beneficial.

Metamaterials have also been considered as a method to damp higher order modes in parasitic accelerator cavities [88]. Any discontinuity in the geometry of a beam pipe can represent serious issues for the stability of the beam in a particle accelerator. Many devices installed along the accelerator introduce undesirable parasitic cavities which give rise to wakefields and resonances, which destabilize the beam. These resonance could be damped by the insertion of simple SRR metamaterials into the parasitic cavities, the effect of this is studied by considering a simple cylindrical pill box cavity with SRR sheets inserted every 90°. The metamaterial insertions modify the resonant frequencies as expected, and bring down the shunt impedance and R/Q of the secondary mode within the cavity. This effect is also present for the first mode but is less significant. In field profile studies of the modes within the structure, the field strength is significantly lower for the

secondary mode when the metamaterial is present.

There is interesting work being done to integrate metamaterial elements into RF accelerator schemes, for bending and focusing applications [89] [90]. The design for a novel deflecting structure consists of a pair of elliptical CSRRs etched into a copper rectangular waveguide along with outer rectangular cavities to maintain the vacuum. The CSRR magnifies the electric field and the two CSRR on either side of the cavity create transverse deflection. The elliptical shape rather than the conventional circular shape allows the deflecting field to be "stretched" in one plane and the total deflecting voltage to be increased. A disadvantage of the structure is that the set-up of the deflector does not lend itself to multiple-cell operation, as the RF power flows transversely to the direction of particle propagation. Within this work, consideration onto how these structures can be integrated and will work in a high power environment has been made and it is noted that the structure is only compatible with low excitation powers owing to the high surface E-fields which will generate heating and deform the resonators. To alleviate potential heating problems the structure would have to be operated with low duty cycles. This work is interesting as it considers similar practical issues to those addressed within the scope of this thesis, however by using only two resonators it cannot full be considered a metamaterial structure.

2.5 Effective parameter retrieval methods

There are several methods for the retrieval of the effective parameters ε and μ such as the Drude Lorentz method, however S-parameter retrieval methods are considered the most accurate methods for effective parameter retrieval of metamaterials at microwave frequencies. These methods use the reflection and transmission coefficients of a plane wave incident on a slab of material to characterise the electromagnetic behaviour. As metamaterials have been shown to interact with electromagnetic radiation in the same way as a bulk material with equivalent material parameters these S-parameters retrieval methods can be used. S_{11} corresponds to the reflected wave and S_{21} to the transmitted wave as shown in Figure 2.19, using these S-parameters it is possible to obtain the effective parameters of the metamaterial.

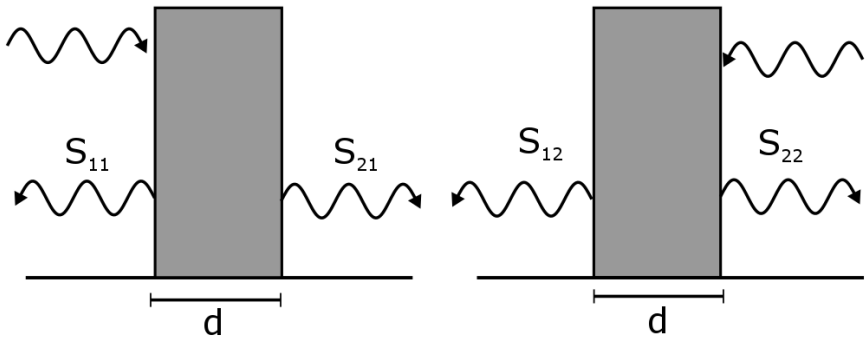

Figure 2.19: S-parameter measurements on a homogeneous slab of thickness d, showing both the reflection and transmission coefficients of a wave incident from either side of the slab.

2.5.1 Nicholson-Ross-Weir method

The use of S-parameter retrieval is first discussed by Nicholson and Ross in 1970 [91] and extended by Weir in 1974 [92], for the measurement of intrinsic properties of materials. Using S_{21} and S_{11}, it is possible to determine the real and imaginary parts of ε and μ as a function of frequency.

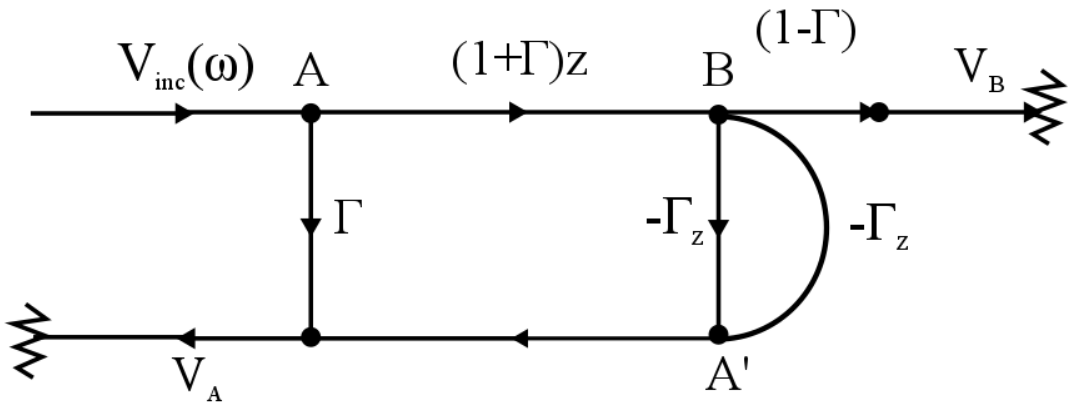

Figure 2.20: The signal flow graph of a slab of material width d in air.

Consider a slab of material characterised by $\varepsilon = \varepsilon_0\varepsilon_r$ and $\mu = \mu_0\mu_r$ where r denotes the relative permittivity (ε) and permeability (μ). This slab has a thickness d and an impedance of $z = \sqrt{\varepsilon_r\mu_r}z_0$ where z_0 is the impedance of the surrounding air. If d the thickness of the slab were infinite, then the reflection coefficient of a wave incident on the slab would be given by

$$\Gamma = \frac{z - z_0}{z + z_0} = \frac{\sqrt{\mu_r/\varepsilon_r} - 1}{\sqrt{\mu_r/\varepsilon_r} + 1}. \tag{2.33}$$

For finite slab width d, the transmission coefficient between faces the slab A and B, may be written,

$$\tau = \exp(-i\omega\sqrt{\mu\varepsilon}d) = \exp[-i(\omega/c)\sqrt{\mu_r\varepsilon_r}d] \tag{2.34}$$

By considering a signal flow graph of the slab in air as shown in Figure 2.20 the scattering coefficients S_{21} and S_{11} may be obtained,

$$S_{21}(\omega) = \frac{V_B}{V_{\text{inc}}} = \frac{(1+\Gamma)(1-\Gamma)\tau}{1-\Gamma^2\tau^2} = \frac{(1-\Gamma^2)\tau}{1-\Gamma^2\tau^2}, \tag{2.35}$$

$$S_{11}(\omega) = \frac{V_A}{V_{\text{inc}}} = \frac{(1-\tau^2)\Gamma}{1-\Gamma^2\tau^2}. \tag{2.36}$$

The sum and difference of the scattering coefficients gives

$$V_1 = S_{21} + S_{11}, \tag{2.37}$$

$$V_2 = S_{21} - S_{11}, \tag{2.38}$$

and if

$$\chi = \frac{1 - V_1V_2}{V_1 - V_2} = \frac{1-(S_{21}^2 - S_{11}^2)}{2S_{11}}, \tag{2.39}$$

then it can be shown that Γ may be obtained from the scattering coefficients, since

$$\Gamma = \chi \pm \sqrt{\chi^2 - 1}, \tag{2.40}$$

where the sign is chosen such that $|\Gamma| \leq 1$. The transmission coefficient can also be written as

$$\tau = \frac{V_1 - \Gamma}{1 - V_1\Gamma} = \frac{S_{11} + S_{21} - \Gamma}{1 - (S_{11} + S_{21})\Gamma}. \tag{2.41}$$

Here is where the method as defined by Nicholson and Ross differs from the method presented by Weir, in Nicholson and Ross's work the next step is to define the ratio of the relative permittivity and permeability as,

$$\frac{\mu_r}{\varepsilon_r} = \left(\frac{1+\Gamma}{1-\Gamma}\right)^2 = c_1, \tag{2.42}$$

then from (2.34) define

$$\mu_r\varepsilon_r = -\left\{\frac{c}{\omega d}\ln\left(\frac{1}{\tau}\right)\right\}^2 = c_2. \tag{2.43}$$

Then

$$\mu_r = \sqrt{c_1c_2}, \tag{2.44}$$

$$\varepsilon_r = \sqrt{\frac{c_2}{c_1}}. \tag{2.45}$$

Thus the complex permittivity and permeability can be obtained from measurements of the transmission and reflection scattering coefficients of a slab of material.

In 1974 William Weir changed this method slightly [92], in his work a propagating factor P is used in place of the transmission coefficient τ, this propagating factor is defined as

$$P = e^{-\psi d} = e^{-(\alpha + i\eta)d}. \tag{2.46}$$

Where ψ is the propagation constant, α is the attenuation constant and η is the phase constant equal to

$$\eta = \frac{2\pi}{\lambda_g}, \tag{2.47}$$

where this λ_g is the guide wavelength of the transmission line the slab sits in. As in the Nicholson and Ross method, the reflection coefficient Γ is defined in terms of χ by (2.39) and(2.40), and the propagation constant becomes

$$P = \frac{S_{11} + S_{21} - \Gamma}{1 - (S_{11} + S_{21})\,\Gamma}. \tag{2.48}$$

The same form as in (2.41). The complex dielectric constant and permeability can be determined from P and Γ;

$$\frac{1}{\Lambda^2} = \left(\frac{\varepsilon_r \mu_r}{\lambda_0^2} - \frac{1}{\lambda_c^2}\right) = -\left[\frac{1}{2\pi d} \ln\left(\frac{1}{P}\right)\right]^2, \tag{2.49}$$

$$\mu_r = \frac{1 + \Gamma}{\Lambda\,(1 - \Gamma)\sqrt{\frac{1}{\lambda_0^2} - \frac{1}{\lambda_c^2}}}, \tag{2.50}$$

where λ_0 is the free space wavelength, and λ_c is the cut-off wavelength and

$$Re\left(\frac{1}{\Lambda}\right) = \frac{1}{\lambda_g}. \tag{2.51}$$

Equation (2.49) has an infinite number of roots and is ambiguous as the phase of the propagation constant does not change when the length of the material d is changed by a multiple of the wavelength. The phase ambiguity can be resolved by finding a solution for ε and μ in which the group delay is a function of the total length of the material [92].

Hence from analysis of the S-parameters of a slab of material it is possible to determine the effective parameters ε and μ, which can be used to determine the

loss tangent and attenuation of the material, any ambiguity in the results for the parameters may be eliminated by taking the into account the group delay and computing this for measured values at small frequency increments. The combined method is known as the Nicholson-Ross-Weir method, it is used extensively to characterise the effective parameters of media within the microwave frequency range. Though used by some groups to calculate the effective parameters of metamaterials it does not take inhomogeneity into account and has ambiguity associated with the results.

2.5.2 S-parameter based retrieval method for metamaterials

A more technical approach to this method is given in Smiths 2002 paper [93], and was shown to give reasonable material parameters for split wires, SRRs and a the two combined. In this method the material properties are not classified by the permittivity ε and permeability μ but by the refractive index n and impedance z of the material. The four parameters can be related to each other by

$$\varepsilon = \frac{n}{z} \quad \text{and} \quad \mu = nz. \tag{2.52}$$

These parameters are frequency dependent complex functions that have to satisfy certain requirement based on causality. For passive materials $Re(z) > 0$ and $Im(n) > 0$. Generally if a material supports only one propagating mode then it will exhibit a well-defined refractive index, whether material is continuous or not. However it is generally not possible to assign an impedance to a no-continuous material, except in the cases where the wavelength in the material is much larger than the dimensions and spacing of the constituent scattering element i.e. in a metamaterial.

As with the Nicholson-Ross-Weir methods these charactering parameters can be determined from the transmission (S_{21}) and reflection (S_{11}) coefficients for a 1D slab of continuous material with waves incident normally on the face of the slab. The thickness of the slab d used for parameter retrieval is irrelevant to the retrieval method, therefore it is advantageous to use as thin a sample as possible such that $kd \ll 1$. Since metamaterials are formed from discreet elements or unit cells it makes sense to set d equal to the length of the unit cell. The transmission

coefficient is related to the impedance z and refractive index n by

$$\tau^{-1} = \left[\cos(nkd) - \frac{i}{2}\left(z + \frac{1}{z}\right)\sin(nkd)\right] e^{ikd}, \tag{2.53}$$

where d is the thickness of the slab and $k = \omega/c$ is the wavenumber of the incident wave. The incident wave is assumed to travel rightward into the slab along the x axis. The normalised form of the transmission coefficient is given as

$$\tau' = \exp(ikd)\tau. \tag{2.54}$$

The reflection coefficient is related to z and n by

$$\frac{\Gamma}{\tau'} = -\frac{i}{2}\left(z - \frac{1}{z}\right)\sin(nkd). \tag{2.55}$$

Equations(2.54) and (2.55) can be inverted to find n and z as a function of t' and r. This leads to the following expression

$$\cos(nkd) = \frac{1}{2\tau'}\left[1 - \left(\Gamma^2 - \tau'^2\right)\right] = Re\left(\frac{1}{\tau'}\right) - \frac{1}{2|\tau'|^2}(A_1\Gamma + A_2\tau'), \tag{2.56}$$

where $A_1 = \Gamma^*\tau' + \tau'^*\Gamma$ and $A_2 = 1 - |\Gamma|^2 - |\tau'|^2$ are both real valued functions that go to zero when no material is present. The equation for the impedance is given as

$$z = \pm\sqrt{\frac{(1+\Gamma)^2 - \tau'^2}{(1-\Gamma)^2 - \tau'^2}}. \tag{2.57}$$

Though these expressions for n and z are relatively uncomplicated they are complex functions, with real and imaginary components and multiple branches which can lead to ambiguity in determining the final expressions for ε and μ. To a certain extent these ambiguities can be resolved by utilising additional knowledge about the material. For example, in a passive medium, the requirement $Re(z) > 0$ fixes the choice of sign in (2.57), just as $Im(n) > 0$ leads to an unambiguous result for $Im(n)$;

$$Im(n) = \pm Im\left(\frac{\cos^{-1}\left(\frac{1}{2\tau'}[1 - (\Gamma^2 - \tau'^2)]\right)}{kd}\right). \tag{2.58}$$

When the right hand side of (2.58) is solved, the root which results in a positive solution for $Im(n)$ is chosen. The real component $Re(n)$ which will identify whether a material is left handed or not, is more complicated as it holds additional

branches as a result of the arccosine function;

$$Re(n) = \pm Re\left(\frac{\cos^{-1}\left(\frac{1}{2\tau'}[1-(\Gamma^2-\tau'^2)]\right)}{kd}\right) + \frac{2\pi m}{kd}, \tag{2.59}$$

where m is an integer. When d is large, the branches lie arbitrarily close to one another making the choice of the correct branch difficult in dispersive media. To confirm the correct branch of the solution has been chosen, more than one thickness must be measured to confirm that all sample thicknesses result in the same value of n.

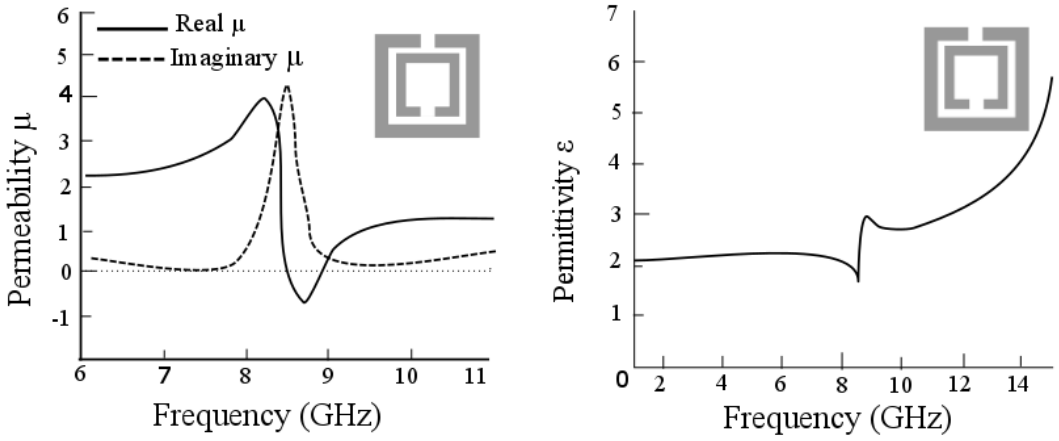

Figure 2.21: Plots of the effective parameters of a split ring resonator, as found using the S-parameter retrieval method in [93].

In their 2002 paper [93] on this method Smith and Schultz show the plots of the real and imaginary components of both the permittivity and permeability of a combination of SRRs and wires deigned to form a left handed media, and each element separately. A reproduction of the SRR plots can be found in Figure 2.21, there is a clear region in which the real part of the permeability is negative, as expected from an SRR. This method is also used to find the effective parameters for the plasmonic material SRRs discussed in the high frequency Chapter of this thesis. Though this method is shown to be reliable in some cases it still results in inconsistent artefacts that relate to a metamaterials inhomogeneous nature, thus in 2005 a modified method was proposed.

2.5.3 Smiths update S-parameter analysis

Though the original method of S-parameter retrieval applied to metamaterials results in physically reasonable material parameters [93] and is consistent with

experimental results from fabricated metamaterial samples [94] [77]. The inherent inhomogeneous nature of metamaterials results in ambiguities and artefacts that reduce the accuracy of this method, thus a modified method is required [95].It should be noted that these anomalies and artefacts are more sever for metamaterials with resonant elements, as large fluctuations in the impedance and refractive index can occur for these materials, such that the wavelength within the material can be on the order of the unit cell or even smaller, which breaks down assumptions made for this method.

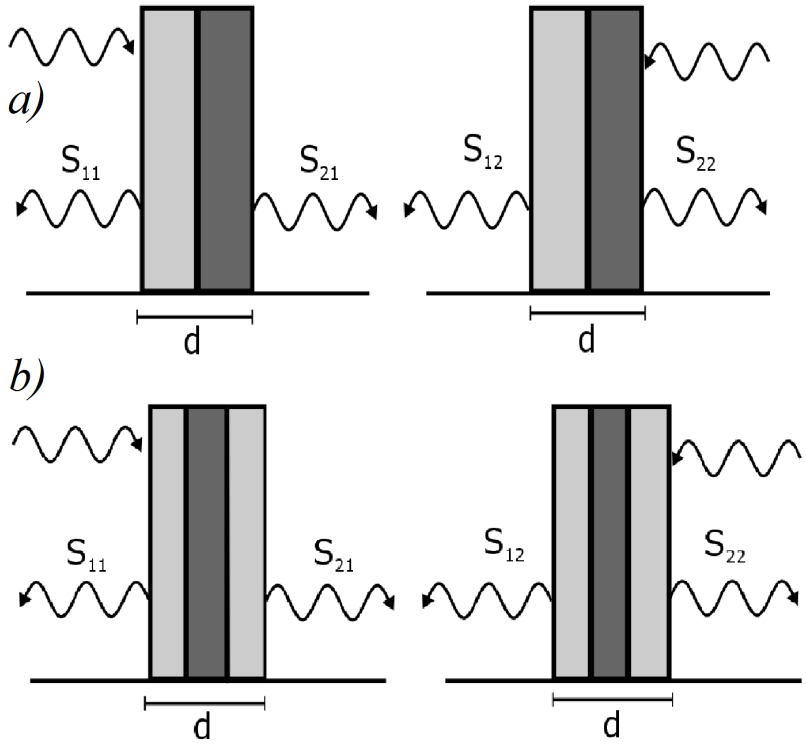

Figure 2.22: S-parameter measurements on inhomogeneous slabs of thickness d showing a) an asymmetric inhomogeneous slab and b) a symmetric inhomogeneous slab.

The most prominent issue with this method of parameter retrieval for metamaterials is that often the structure is not conceptually reducible to a model of a slab of continuous media, more often the unit cells must be considered like inhomogeneous asymmetric slabs or inhomogeneous symmetric slabs as shown in Figure 2.22, in which there are two or more distinct materials with differing material properties. This makes the equivalent one dimensional model of the material inhomogeneous as well, thus the retrieval method must be analysed for such structures to understand the limitations.

To identify the limitations of the method, the general approach to S-parameter retrieval must be analysed, by defining a one dimensional transfer matrix, relating the fields on one side of a planar slab to those on the other.

$$\mathbf{F}' = \mathbf{T}\mathbf{F}, \tag{2.60}$$

where

$$\mathbf{F} = \begin{pmatrix} E \\ \\ H_{\text{red}} \end{pmatrix}. \tag{2.61}$$

E and H_{red} are the complex electric and magnetic field amplitudes on the different sides of the slab, unprimed denotes the right hand side and primed denotes the left hand side. H_{red} is the normalised magnetic field and is given by $H_{\text{red}} = (i\omega\mu_0)H$. The transfer matrix $\mathbf{T}$ for a homogeneous 1D slab is given by

$$\mathbf{T} = \begin{pmatrix} \cos(nkd) & -\frac{z}{k}\sin(nkd) \\ \\ \frac{k}{z}\sin(nkd) & \cos(nkd) \end{pmatrix}, \tag{2.62}$$

where n is the refractive index and z is the impedance, which relate to the permittivity ε and permeability μ by;

$$\varepsilon = n/z \quad \text{and} \quad \mu = nz. \tag{2.63}$$

The scattered field amplitudes and phases can be measured in a straight forward manner and are therefore used to find the constituent parameters. A scattering matrix relates the incoming and outgoing field amplitudes and can be related directly to experimentally measured quantities. The elements of the scattering matrix can be found from the elements of the $\mathbf{T}$ matrix as;

$$S_{21} = \frac{2}{T_{11} + T_{22} + \left(ikT_{12} + \frac{T_{21}}{ik}\right)}, \tag{2.64}$$

$$S_{11} = \frac{T_{11} - T_{22} + \left(ikT_{12} - \frac{T_{21}}{ik}\right)}{T_{11} + T_{22} + \left(ikT_{12} + \frac{T_{21}}{ik}\right)}, \tag{2.65}$$

$$S_{22} = \frac{T_{22} - T_{11} + \left(ikT_{12} - \frac{T_{21}}{ik}\right)}{T_{11} + T_{22} + \left(ikT_{12} + \frac{T_{21}}{ik}\right)}, \tag{2.66}$$

$$S_{12} = \frac{2\det(\mathbf{T})}{T_{11} + T_{22} + \left(ikT_{12} + \frac{T_{21}}{ik}\right)}. \tag{2.67}$$

For a slab of homogeneous material, the transfer matrix (2.62) shows that $T_{11} = T_{22} = T_s$ and $\det(\mathbf{T}) = 1$ and the $\mathbf{S}$ matrix is symmetric. Thus,

$$S_{21} = S_{12} = \frac{1}{T_s + \frac{1}{2}\left(ikT_{12} + \frac{T_{21}}{ik}\right)}, \tag{2.68}$$

$$S_{11} = S_{22} = \frac{\frac{1}{2}\left(\frac{T_{21}}{ik} - ikT_{12}\right)}{T_s + \frac{1}{2}\left(ikT_{12} + \frac{T_{21}}{ik}\right)}. \tag{2.69}$$

By substituting in the T-matrix elements this gives

$$S_{21} = S_{12} = \frac{1}{\cos(nkd) - \frac{i}{2}\left(z + \frac{1}{z}\right)\sin(nkd)}, \tag{2.70}$$

$$S_{11} = S_{22} = \frac{i}{2}\left(\frac{1}{z} - z\right)\sin(nkd). \tag{2.71}$$

Equations (2.70) and (2.71) can be inverted to find n and z in terms of the scattering parameters as follows

$$n = \frac{1}{kd}\cos^{-1}\left[\frac{1}{2S_{21}}(1 - S_{11}^2 + S_{21}^2)\right], \tag{2.72}$$

$$z = \sqrt{\frac{(1 + S_{11})^2 - S_{21}^2}{(1 - S_{11})^2 - S_{21}^2}}. \tag{2.73}$$

This provides a complete material description of a homogeneous slab of material. However as established in the previous Section, there are several branches to the arccosine in the definition of the refractive index, leading to ambiguity in the determination of the material parameters, unless the wavelength within the media is much larger than the slab length. In addition to this, resonant metamaterials will always have a frequency region where the branches associated with the inverse cosine in the definition of the refractive index, will lie very close together making it difficult to determine the correct branch, thus methods to alleviate this must be used.

In periodic systems no matter what the scale of the unit cell relative to the wavelength, there exists a phase advance α per unit cell that can be defined based on the periodicity, this allows the periodic structure to be defined by an index at all scales. The properties of a periodic structure can be determined from the $\mathbf{T}$ matrix of a unit cell corresponding to a periodic structure where the fields on either side are related by a phase factor α such that

$$\mathbf{F}' = \mathbf{TF} = e^{i\alpha d}\mathbf{F}, \tag{2.74}$$

this allows for the dispersion relation of the periodic structure to be determined via knowledge of the transfer matrix, by solving

$$|\mathbf{T} - e^{i\alpha d}\mathbf{I}| = 0, \tag{2.75}$$

from which

$$T_{11}T_{22} - \xi(T_{11} + T_{22}) + \xi^2 - T_{12}T_{21} = 0, \tag{2.76}$$

can be found, in which $\xi = exp(i\alpha d)$. By using $\det(\mathbf{T}) = 1$ this can be simplified to

$$\xi + \frac{1}{\xi} = T_{11} + T_{22}, \tag{2.77}$$

or

$$2\cos(\alpha d) = T_{11} + T_{22}. \tag{2.78}$$

Thus the phase factor can be given in terms of the transfer coefficients.

When the fundamental unit cell is inhomogeneous, the validity of the equations for impedance and refractive index is not clear. In a symmetric inhomogeneous material the results presented by this retrieval method are questionable and in an asymmetric inhomogeneous material it is more complex. In the case of an inhomogeneous medium, where the unit cell is not symmetric in the direction of propagation $\varepsilon(z) \neq \varepsilon(-z)$ and $S_{11} \neq S_{22}$ then the standard retrieval process fails to provide a unique answer for n, and the results will depend on the direction of propagation. Depending on the direction of incident radiation, the refractive index is defined by either

$$\cos(nkd) = \frac{1}{2S_{21}}(1 - S_{11}^2 + S_{21}^2), \tag{2.79}$$

or

$$\cos(nkd) = \frac{1}{2S_{21}}(1 - S_{22}^2 + S_{21}^2). \tag{2.80}$$

However, if the unit cell is repeated infinitely then (2.78) shows a unique value of refractive index can be recovered. By expressing the S-matrix in terms of the T-matrix it is possible to compare the above two equations for refractive index to that of phase advance.

$$T_{11} = \frac{(1 + S_{11})(1 - S_{22}) + S_{21}S_{12}}{2S_{21}}, \tag{2.81}$$

$$T_{12} = \frac{(1 + S_{11})(1 + S_{22}) - S_{21}S_{12}}{2S_{21}}, \tag{2.82}$$

$$T_{21} = \frac{(1 - S_{11})(1 - S_{22}) - S_{21}S_{12}}{2S_{21}}, \tag{2.83}$$

$$T_{22} = \frac{(1 - S_{11})(1 + S_{22}) + S_{21}S_{12}}{2S_{21}}. \tag{2.84}$$

Using these equations in (2.78) yields

$$\cos(\alpha d) = \frac{1 - S_{11}S_{22} + S_{21}^2}{2S_{21}}. \tag{2.85}$$

Which shows that regardless of the wavelength to unit cell ratio, an effective index can be recovered using the modified S-parameter retrieval method which uses all elements of the S-matrix. Comparing (2.85) to (2.79) and (2.80) shows that the standard retrieval process can be applied to find the index of an inhomogeneous structure if using an averaged S_{av} of

$$S_{\text{av}} = \sqrt{S_{11}S_{22}}. \tag{2.86}$$

The analysis that led to the solution (2.85) does not require any assumption that the unit cell size must be negligible in comparison to the optical path length. Thus the retrieved index will be valid beyond the regime that tradition effective media theory is valid [93] [92].

To determine values for ε and μ it is also necessary to determine the impedance z_{red}, for a homogeneous material this is an intrinsic parameter that describes the ratio of the electric and magnetic fields for a plane wave. For an inhomogeneous material though, this will vary through the unit cell leading to an unavoidable ambiguity in defining the impedance. In such a medium z_{red} can be found from (2.74) as

$$z_{\text{red}} = \frac{T_{12}}{T_{11} - \xi}, \tag{2.87}$$

or equivalent

$$z_{\text{red}} = \frac{T_{22} - \xi}{T_{21}}, \tag{2.88}$$

solving (2.76) for ξ yields

$$\xi = \frac{(T_{11} + T_{22})}{2} \pm \sqrt{\frac{(T_{22} - T_{11})^2 + 4T_{12}T_{21}}{4}}, \tag{2.89}$$

which can be substituted into either definition of z_{red} to obtain two results corresponding to the two eigen values of (2.76);

$$z_{\text{red}} = \frac{(T_{22} - T_{11}) \mp \sqrt{(T_{22} - T_{11})^2 + 4T_{12}T_{21}}}{2T_{21}}. \tag{2.90}$$

The two roots of this equation correspond to the two directions of wave propagation. Inspection of this equation reveals that for a reciprocal structure, $T_{11} = T_{22}$ and the impedance has the form

$$z_{\text{red}}^2 = \frac{T_{12}}{T_{21}}. \tag{2.91}$$

Using the T-matrix defined by the S-matrix z_{red} becomes

$$z = \sqrt{\frac{(1+S_{11})^2 - S_{21}^2}{(1-S_{11})^2 - S_{21}^2}} \tag{2.92}$$

as in the standard retrieval method for homogeneous structures.

Although an inhomogeneous periodic structure does not have a well-defined impedance as the ratio of electric field to magnetic field E/H_{red} varies periodically through the structure, this variation becomes negligible for very small unit cell sizes relative to the wavelength. However with no unique definition of z_{red}, the values of ε and μ retrieved are not generally assignable, though can be applied in an artificial manner if the metamaterial is always terminated in the same location of the unit cell. Despite the modified version taking into account the inhomogeneous nature of metamaterials the ambiguity in the determination of the effective parameters via S-parameter retrieval is still present.

Though there is some ambiguity in this method, a version is used to characterise the high frequency plasmonic metamaterials discussed in Chapter 6. This provides an insight into the left handed behaviour of the structure, however is increasingly complex and thus for the loaded waveguide structure presented in Chapters 3-5, the left handed behaviour will only be discussed in terms of mode polarization.

2.6 Conclusions

This Section has focused on the key metamaterials, unique electromagnetic effects and applications of metamaterials that are most relevant to the work done within this thesis. A brief history of metamaterials was provided focusing on the discoveries that led to the creation of left handed media, which will be used in this work to generate backward propagating Cherenkov radiation. The mechanisms that govern electromagnetic behaviour in such left handed media were discussed

to clarify what is meant by backward propagating Cherenkov radiation. An in depth analysis of the complementary split ring resonator a metallic metamaterial was provided to highlight why this metamaterial was used for accelerator applications. The applications of metamaterials in accelerators was discussed and a clear gap in the research was highlighted, notably the lack of research into how to realise these metamaterial structures and make them robust for high power operation. Finally, methods for retrieving the effective parameters of metamaterials were presented and the reasons for using them in only one of the subsequent chapters is discussed.

Chapter 3

The Complementary Split Ring Resonator loaded waveguide

In this Chapter the first design of the Complementary Split Ring Resonator (CSRR) loaded waveguide is presented. An overview of the proposed structure and layer spacing constraints is given, and the choice of four metasurface layers over two metasurface layers is discussed. The unit cell is investigated in detail to understand the electromagnetic behaviour of an unbounded structure, the TM-like modes are identified, and dispersion analysis is performed. This is done for the ideal four layer case and the simplified two layer case. The structure is then truncated to fit inside a s-band waveguide 34 mm by 72 mm and the electromagnetic analysis of this structure is provided. The beam coupling parameters are calculated and analysed for comparison to conventional structures and existing metamaterial designs. Finally, the wakefield analysis is given to further confirm the existence of a mode to which an electron beam will couple to.

3.1 The waveguide structure

The waveguide structure was designed to be operational in the same frequency range as many conventional RF systems, as this would aid with initial cold tests and make it compatible with technology on-site at Daresbury. The CSRR metamaterial was loaded into an S-band waveguide (WR-284 if using American notation) with a cross section of approximately 34 mm by 72 mm, as shown in Figure 3.1. This allows for up to four layers of metamaterial sheets to be loaded with sufficient space for a beam of up to 5 mm in diameter to propagate between the metasurface sheets, and more layers if the structure was to be used with a beam of smaller

radius.

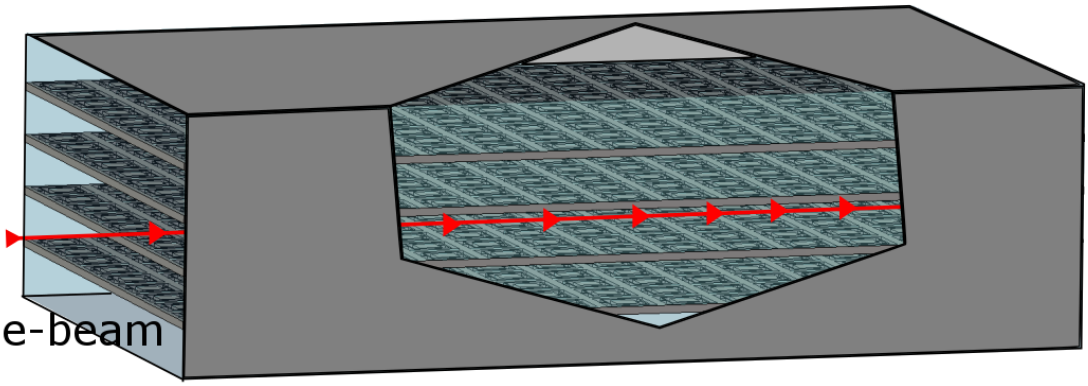

Figure 3.1: Cutaway of the loaded waveguide structure, showing the path of the beam through the waveguide.

The metasurface comprises of a sheet of metal with square CSRRs milled out of it, the geometry of which is shown in Figure 3.4, with the ring gap lying in the direction of propagation, along z. The CSRR is the complementary form of the split ring resonator and allows for the creation of a left handed material using only metallic elements, which increases the vacuum compatibility of the design and reduces the probability of charge build up and subsequent breakdown associated with dielectrics. The CSRRs have a negative effective permittivity when operated at resonance, and the metasurface sheets act as narrow, patterned waveguides which confine transverse magnetic modes leading to negative permeability below cut off [30]. Therefore for operation as a LHM, a TM or TM-like mode with strong longitudinal component of the electric field is required. The CSRR is compatible with conventional planar fabrication techniques and is easily scaled for high frequency applications, which due to recent developments in plasmonic materials could reach terahertz or optical frequencies [96], [97].

In terms of the modes discussed in this chapter, modes in which the field is only orientated in the longitudinal or transverse directions are classified as TM or TE modes respectively. TM-like modes are those in which the majority of the field is in the longitudinal direction, with non zero components of the transverse field, and TE-like modes are those in which the majority of the field is orientated in the transverse direction with a non zero longitudinal component. Hybrid modes where the fields are of the same order of magnitude in both the longitudinal and transverse directions. To illustrate this consider the TM-like mode found in the loaded waveguide structure, there is a clear TM_{31} structure for the E_z component of the

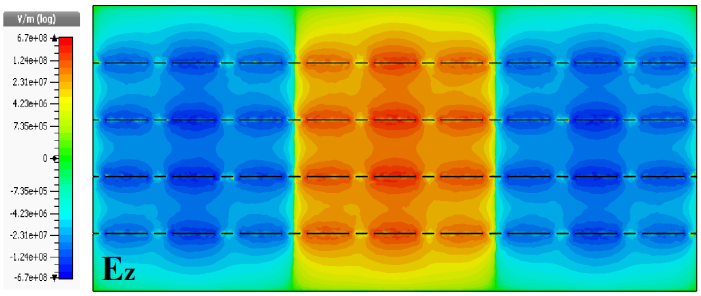

Figure 3.2: The E_z component of the field for a TM-like mode, showing a clear TM_{31} field profile.

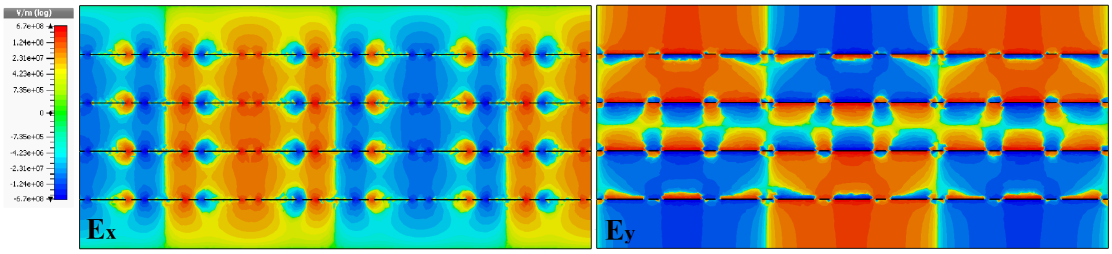

Figure 3.3: The E_x, E_y components of the field for a TM-like mode, showing clear non zero transverse fields.

field ash shown in figure 3.19 but also clear field profiles for E_x and E_y as shown in Figure 3.3. Hybrid modes are those in which the field is evenly distributed in both the transverse and longitudinal directions, and no clear mode profile can be determined.

Table 3.1: The frequencies of the three fundamental modes of the unit cell for layer spacing ranging from 6 mm to 14 mm.

Spacing (mm)	Mode 1 (GHz)	Mode 2 (GHz)	Mode 3 (GHz)
6	1.041	5.870	10.534
7	1.041	5.837	10.314
8	1.041	5.816	10.040
9	1.041	5.787	9.684
10	1.041	5.749	9.161
11	1.041	5.715	8.703
12	1.041	5.682	8.285
13	1.041	5.642	7.893
14	1.041	5.601	7.536

The loading of this structure into an S-band waveguide means consideration need to be put on how the finite size of the metamaterial and the spacing between the metasurface sheets affect the overall electromagnetic behaviour. The waveguide

was loaded with either two or four sheets to provide clearance for the beam whilst forming a bulk metamaterial. The four layer design can be seen in Figure 3.1. In previous studies of a CSRR metamaterial for accelerator applications the spacing used was 12.8 mm [40], however to load the metamaterial into a S-band waveguide this must be reduced to 11.3 mm and 6.76 mm for two layers and four layers, respectively. The eigenmode solver of CST Microwave Studio [98] has been used to investigate how the spacing of the metasurface layers affects the frequency at which modes occur. The fundamental three modes of the structure were considered with spacing varying from 6 mm to 14 mm. Table 3.1 shows the frequencies at which the three fundamental modes occur.

By comparing the values in Table 3.1, it can be seen that the first mode does not vary with the changing of the layer spacing and remains a TE mode. As the spacing between the layers increases, the frequency at which the second and third modes occur decreases, with the frequency of the third mode decreasing at a faster rate. These modes are TM or Hybrid, and change with the changing frequencies. Thus, increasing the spacing between the layers decreases the frequency of the modes and reduces the frequency gap between modes. A reduction in spacing between the layers results in an increase in capacitance between the layers, and increased deformation of the fields around the sheets, and so set-ups with closely lying metasurface sheets will exhibit more hybrid modes than those with a greater separation between layers. Although minor frequency shifting of the modes occurs as the metasurface layer spacing changes, this variation is sufficiently small that a reduced spacing may be chosen.

Initially, both the four layer and two layer designs were considered. The four layer design has a spacing of 6.76 mm and is thought to behave more like a bulk metamaterial, however due to the increased amount of metasurface which alters the field profile, this design is believed to lead to an increased number of hybrid modes which will make coupling complex. Alternatively, two simplified two layer designs were considered, the first with a larger sheet separation of 11.3 mm for beam propagation, and the second with the same spacing as the four layer structure (6.76 mm). Both two layer designs will disrupt the field less and thus result in fewer hybrid modes. However in the case of the increased spacing of 11.3 mm the performance may be reduced in terms of beam interaction, as the fields in a metasurface structure are generated on the sheets, and thus greater separation between the beam and the metasurface will reduce interaction.

3.2 The CSRR unit cell

The CSRR unit cell comprises of two split rings, one inside the other, cut out of metal, as seen in Figure 3.4. The dimensions are taken as those used by the MIT group [40]; this design is chosen as it is suitable for operation around 5 GHz and allows for nine resonators to fit into the S-band waveguide. In this set-up the ring gap lies in the direction of beam propagation and the sheets lie parallel to the beam. The CSRR has been chosen as the resonator element for this LHM as it can be fabricated from one continuous metallic sheet and thus this is vacuum compatible and suitable for bulk machining, as well as being considered more robust than other LHMs such as SRR and wire media.

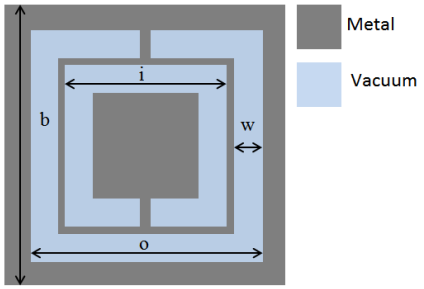

Parameter	Symbol	Value (mm)
Unit Cell	b	8
Outer Ring	o	6.6
Inner Ring	i	4.6
Ring Width	w	0.8
Gap width	g	0.3
Thickness	t	0.05

Figure 3.4: The unit cell and corresponding geometrical parameters.

3.2.1 Electromagnetic analysis of the unit cell with spacing 6.76 mm

In this Section the result of the electromagnetic analysis of the unit cell, and hence the unbounded infinite metamaterial with layer spacing 6.76 mm, are discussed. The first five modes will be discussed in terms of frequency, polarisation, and dispersive behaviour. This spacing was used for simulations of the four layer, truncated waveguide structure and the reduced spacing two layer structure.

Through electromagnetic analysis, the dominant field components and hence the polarisation of the first five modes of the CSRR-based MTM were identified in order to select those suitable for interaction with an electron beam. Table 3.2 shows the polarization and frequency of the first five modes of the CSRR-based metamaterial. A TM mode with a strong longitudinal component of the electric field is required to excite left handed behaviour, however, with the close lying metasurface sheets causing field deformation, this mode is likely to be a TM-like mode with strong longitudinal electric field and non-zero transverse components.

Table 3.2: The mode frequency and polarization of the unit cell with layer spacing 6.76 mm at a phase of 10°

Mode polarization	Frequency (GHz)
TE	1.041
TM-like	5.845
Hybrid	10.369
TE-like	10.872
TE-like	15.856

Figure 3.5 shows the E-field of the fundamental TM-like mode of the unit cell at 5.85 GHz. A longitudinal electric field was observed for this mode at the top and bottom edges of the unit cell corresponding to the mid-plane between the metasurface layers, where the electron beam propagates. This field distribution indicates that the TM-like mode will exhibit strong interaction with the beam.

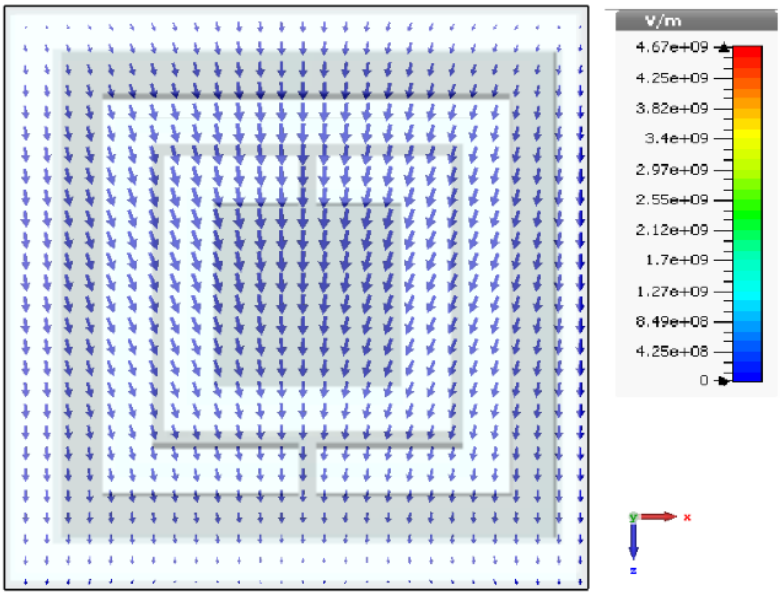

Figure 3.5: A top down view of the electric field distribution of the fundamental TM-like mode in the unit cell occurring at 5.85 GHz for a phase advance of 10° in z.

Dispersion analysis of the modes was performed to identify whether the TM-like mode exhibited a negative dispersion which would indicate left handed behaviour. The mode frequency is plotted as a function of phase, and the gradient of this was analysed. The gradient of the dispersion curve gives the nature of the mode: a negative gradient corresponds to a negative index mode (NIM) and a positive

gradient corresponds to a positive index mode (PIM). In a negative index mode permittivity and permeability are simultaneously negative and therefore a LHM is observed. Figure 3.6 shows the first four modes of the infinite MTM, there exists a clear fundamental PIM shown in red, and a clear fundamental NIM shown in blue. The remaining modes both have positive gradient and correspond to a hybrid mode and a TE-like mode, respectively.

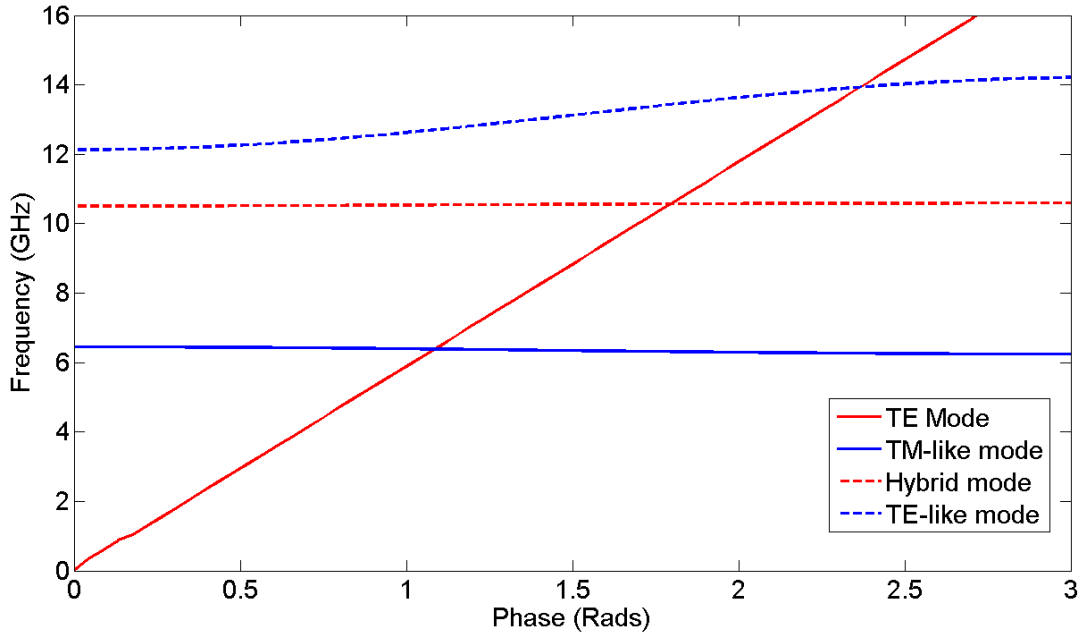

Figure 3.6: The dispersion of the fundamental modes of the infinite MTM with layer spacing 6.76 mm, showing modes with both positive and negative dispersion gradient.

To further investigate how this structure will interact with an electron beam, the dispersion of the TM-like mode was plotted with a relativistic beam line with velocity

$$v_b = 0.9c \tag{3.1}$$

where c is the speed of light in vacuum. It can be seen from Figure 3.7 that the beam line intersects the TM-like mode at 6.4 GHz and a phase advance of 1.192 radians. Thus a relativistic beam will interact with the TM-like mode indicating that this structure is suitable for beam-wave interaction based devices and will exhibit left handed behaviour when excited by an electron beam.

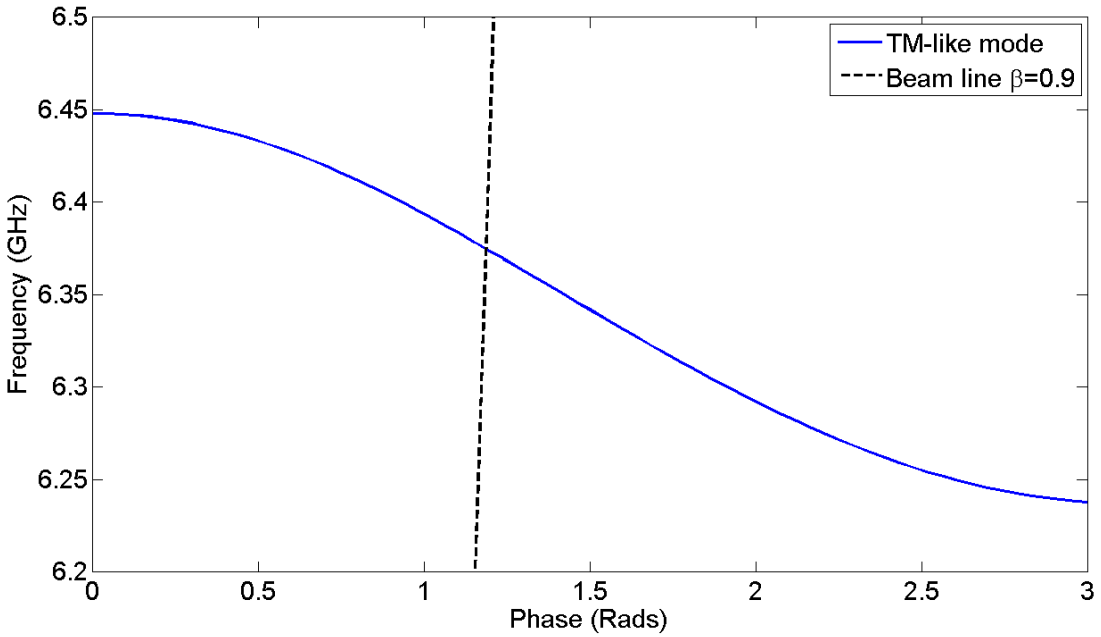

Figure 3.7: The dispersion of the TM-like mode shown in greater detail, the intersecting dashed line represents an relativistic electron beam, and shows the interaction point between the structure and a beam.

3.2.2 Electromagnetic analysis of the unit cell with spacing 11.3 mm

In the following Section, the spacing of 11.3 mm is analysed in terms of unit cell results. The results are compared to the response of the unit cell with the reduced spacing. This spacing is almost twice as large as the spacing for the four layer set-up and therefore a reduction in the number of hybrid modes and the frequency at which the modes occur is expected.

Table 3.3 gives a comparison of the fundamental mode polarisations and frequency for the first five modes of the infinite metamaterial with two different layer spacings. The fundamental TE mode occurs at the same frequency, 1.041 GHz, in both set-ups, and the fundamental TM-like mode shifts only slightly to the lower frequency of 5.715 GHz for the two layer structure. This TM-like mode is still the second mode in the system and take the same form as in the set-up with 6.76 mm spacing as seen in Figure 3.8. There is longitudinal field orientated along the top and bottom or the unit cell boundary corresponding to strong longitudinal field in the region of the beam. Beyond the TM-like mode it can be seen that there is a significant reduction in frequency for subsequent modes for the 11.3 mm spacing which is as expected. The nature of these higher order modes is harder to determine and thus it cannot be seen whether there is a reduction in hybrid modes here.

Table 3.3: A comparison of the first five modes in the unit cell with a layer spacing of 6.76 mm and 11.3 mm for the four and two layer systems respectively.

	Four layer		Two layer	
Mode order	Polarization	Frequency (GHz)	Polarization	Frequency (GHz)
1	TE	1.041	TE	1.041
2	TM-like	5.845	TM-like	5.715
3	Hybrid	10.369	TE-like	8.547
4	TE-like	10.872	Hybrid	9.059
5	TE-like	15.85	Hybrid	13.529

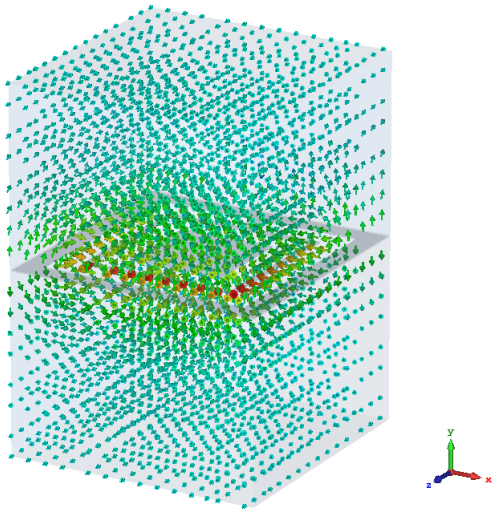

Figure 3.8: The TM-like mode of the unit cell for the two layer structure occurring at 5.715 GHz.

As with the spacing of 6.76 mm, dispersion analysis was performed for the fundamental modes in the structure to determine if the TM-like mode exhibits negative dispersion and can therefore be considered to have left handed behaviour. The dispersion plot of the first four modes in the structure is shown in Figure 3.9, again the TM-like mode exhibits a negative dispersion gradient, indicating the left handed nature of this mode.

The change in spacing has minimal effect in infinite metamaterial structure but it is believed to have a significant effect on the response of the truncated structure. As with two layers and more spacing, there will be less disruption to the beam and therefore less hybrid modes. As such, the TM-like mode is likely to occur at a lower mode order and frequency.

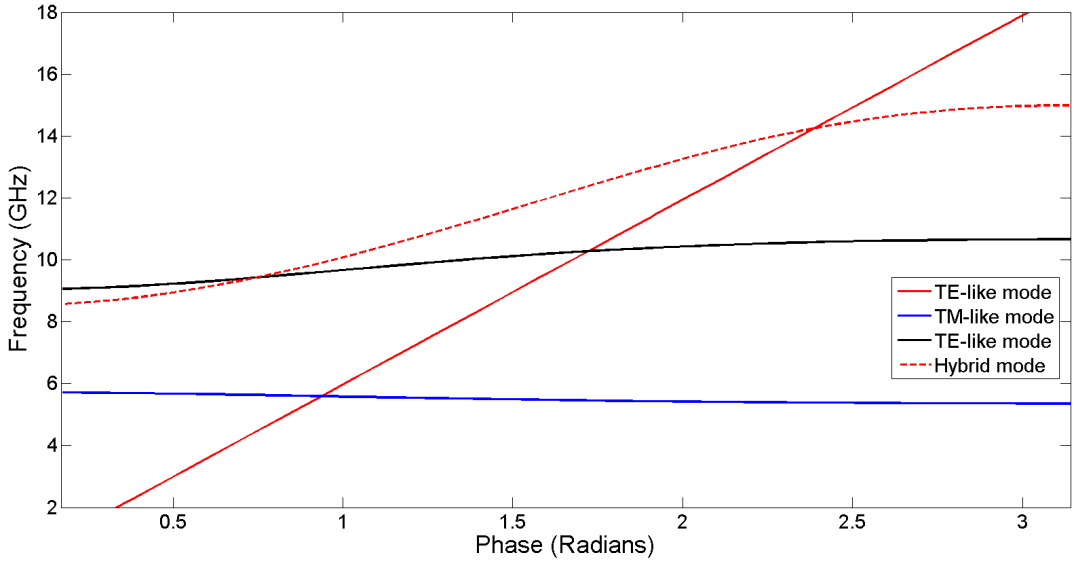

Figure 3.9: The dispersion of the first four modes of the unit cell with 11.3 mm spacing.

3.3 The CSRR Loaded waveguide

Having analysed the infinite metasurface structure by considering only the unit cell, the effect of truncating the infinite metamaterial is now discussed, by investigating how the addition of metallic walls and reductions of layers affects the electromagnetic response. It is also important to understand how the addition of metamaterial affects the behaviour of the empty metallic waveguide. In this Section the electromagnetic response of the empty waveguide is considered, then the electromagnetic behaviour and beam coupling parameters are analysed for the four layer structure, the two layer structure (11.3 mm spacing) and finally the reduced spacing two layer structure (6.76 mm spacing). The mode cut-off of the empty and loaded waveguides are compared to each other and below cut off operation is discussed. The three loaded waveguide structures are compared in terms of operating mode order, frequency, number of hybrid modes, and beam coupling parameters, R/Q and shunt impedance.

3.3.1 The empty S-band WR-284 waveguide

To understand how the metamaterial alters the response of the waveguide, the empty S-band WR-284 waveguide was analysed first, focusing on the cut-off frequencies of the different TE and TM modes. Table 3.4 shows the cut off frequency and polarisation of modes within the empty waveguide. Two TM modes are observed: TM_{11} at 4.99 GHz, and TM_{31} at 7.72 GHz. Both modes exhibit strong

longitudinal electric field in the region of beam propagation; therefore, they are suitable for left handed applications. A TM_{31}-like is found in the metamaterial loaded waveguide, as the addition of metamaterial damps the TM_{11} mode and leads to hybridization of the modes, the TM_{31}-like mode exhibits strong longitudinal field components in the region of the beam. In the loaded structure, more hybrid modes are expected due to the closeness of the sheets, and a reduction in cut off frequency for all modes is also expected as the layers create an increase in impedance.

Table 3.4: Cut-off frequencies of the modes in the empty WR-284 waveguide, showing the fundamental TE and TM modes and two hybrid modes.

Mode Polarization	Frequency (GHz)
TE_{10}	2.37
TE_{20}	4.29
TE_{01}	4.53
TM_{11}	4.99
TE_{11}	4.99
TE_{21}	6.15
Hybrid	6.15
TE_{30}	6.33
TM_{31}	7.72
Hybrid	7.72

3.3.2 The four layer loaded waveguide

When performing electromagnetic analysis on the loaded waveguide, a single transverse strip of the waveguide with periodic boundaries in the longitudinal direction was considered as shown in Figure 3.10. The first 25 modes of the structure are identified in the range of 1.772 GHz to 5.474 GHz, and the mode polarisation of these is considered. Straight away two things can be noted about the loaded waveguide structure: the first is that the addition of metamaterial has increased the number of modes over a set frequency range and the second is that there the cut off frequency for the modes is reduced. As expected, the metallic walls and closeness of the metasurface sheets gave rise to an increased number of hybrid modes, which explains the number of modes in the frequency range.

When considering the modes of this structure it should be noted that below 5.45 GHz TE-like or hybrid modes dominate. These modes show little or no longitudinal E-field; thus they are unsuitable for beam interaction. Above 5.45 GHz the

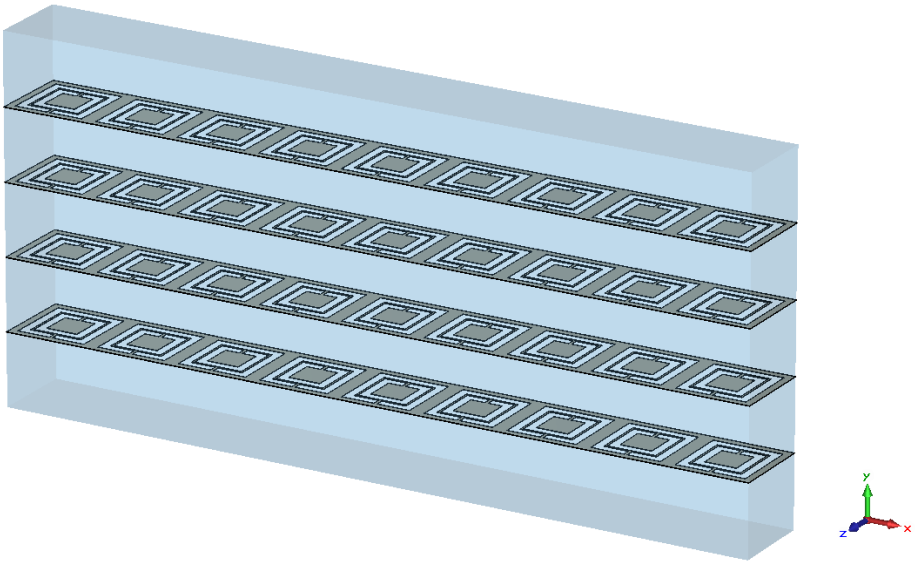

Figure 3.10: A transverse segment of the four layer set-up showing the 6.76 mm spacing and the truncation created by the waveguide walls.

modes begin to show stronger longitudinal components of the electric field; these are predominately hybrid modes with strong longitudinal and transverse components. A TM-like mode with suitable longitudinal field is found at the top of this frequency range.

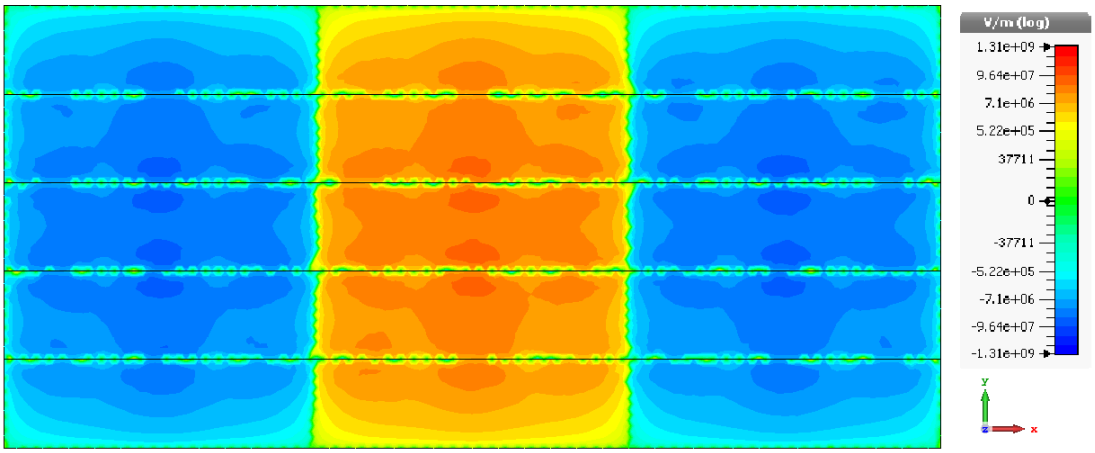

Figure 3.11: A transverse slice of the waveguide showing the longitudinal field component at 5.47 GHz, for a phase advance of 10°. There is a strong and centrally localised distribution of the field suitable for interaction with a cylindrical beam.

A TM-like mode was found at 5.47 GHz for a phase advance of 10° the field profile of this mode is shown in Figure 3.11 and it was the 24th mode in the waveguide. This mode corresponds to TM_{31}-like mode, when the frequency of this mode is compared to the frequency of the TM_{31} mode in the empty waveguide shown in

Table 3.4, a reduction in cut-off frequency is observed. Therefore the addition of metamaterial to the waveguide allows for below cut off operation. This mode has a strong electric field on axis, with field distribution ideal for interaction with a cylindrical beam of radius up to 3 mm, and thus suitable for both acceleration and Cherenkov source applications.

Though there exists a suitable TM-like mode the majority of modes within the structure are hybrid and therefore are unsuitable for applications based on beam-wave interactions. An example of the longitudinal field component of one of these hybrid modes is given in Figure 3.12, this corresponds to a hybrid mode close in frequency to the suitable TM-like mode.

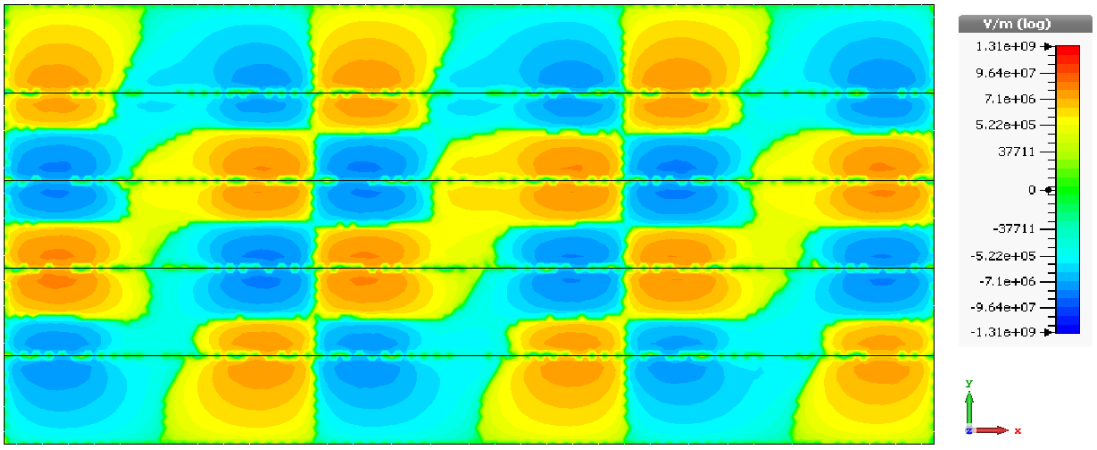

Figure 3.12: A transverse segment of the waveguide showing the distribution of the longitudinal electric field for the hybrid mode occurring at 5.32 GHz, for a phase advance of 10°.

In comparing the loaded and empty waveguide, two main differences are observed: the first is a reduction in cut off frequency for the TM modes and the second is a significant increase in hybrid modes. The increase in hybrid modes is due to the truncation of the MTM in the x and y planes and the addition of metallic interfaces around it, which increases the impedance of the structure. The increased number of hybrid modes makes the identification of TM-like modes for accelerator and negative index applications more complex. Ideally these modes should be eliminated or reduced to improve coupling capabilities and aid mode identification, a detailed discussion of the possible design modifications is presented in Chapter 4.

To confirm the suitability of the fundamental TM-like mode shown in Figure 3.11 for interaction with an electron beam, analytical analysis of R/Q and the shunt impedance (R_{SH}) was performed to determine the strength of coupling between

the beam and the mode. For accelerator applications, it is important to understand how the accelerating voltage of the structure relates to the energy stored via R/Q and how the accelerating voltage is linked to power loss via shunt impedance (R_{SH}) [99].

R/Q gives the net acceleration for a given amount of stored energy [100], and is given by;

$$\frac{R}{Q} = \frac{|V|^2}{\omega U}. \tag{3.2}$$

Where V is the accelerating voltage and U is the stored energy, which oscillates between the electric E and magnetic H components of the field which are out of phase with one another; therefore it can be stated that at a given time all the stored energy is either in the electric or magnetic field. For a resonant field, U the stored energy is given by

$$U = \frac{1}{2}\mu_0 \int |H|^2 dV = \frac{1}{2}\varepsilon_0 \int |E|^2 dV, \tag{3.3}$$

where ε_0 is the permittivity of free space and μ_0 is the permeability of free space. For energy efficient acceleration R/Q should be maximized, so as to have the greatest accelerating voltage for the smallest amount of stored energy.

R_{SH} gives the net acceleration for a given amount of power loss [100]. R_{SH} is given by

$$R_{\mathrm{SH}} = \frac{|V|^2}{P_S}, \tag{3.4}$$

where V is the accelerating voltage and P_s is the power lost within the structure. The main source of power loss within any accelerating structure is Ohmic heating. Both the input power and the power lost within the structure define the accelerating performance. A high R_{SH} means a greater amount of accelerating voltage for a smaller amount of power which is again the most efficient accelerating set-up.

It is possible to gain both these parameters by analysis of the electric and magnetic fields, however this process is lengthy and it is possible to calculate R/Q, and the shunt impedance through post processing steps in CST microwave studio [98], which was the method used for the analysis in this thesis. The beam coupling parameters per meter were calculated for the first 25 modes in the structure. Very few modes showed significant values of R/Q and R_{SH}, particularly at low frequencies where the modes were TE-like with little or no longitudinal field components. Modes that showed significant values of R_{SH} and R/Q correlated with the modes that exhibited a strong longitudinal E-field in the region of beam propagation. The

TM-like mode at 5.47 GHz exhibited the largest values of both R/Q (6.6 kΩ/m) and R_{SH} (10.94 MΩ/m) as shown in Table 3.5. This TM-like mode also exhibits the strongest and most widely distributed longitudinal E-field.

Table 3.5: The R_{SH} and R/Q of the TM-like mode and the surrounding hybrid modes.

Mode	Frequency (GHz)	R/Q (Ω/m)	$R_{\mathrm{SH}}(k\Omega/m)$
Hybrid	5.41	3	3.6
Hybrid	5.42	0	0.2
Hybrid	5.42	5	7.2
Hybrid	5.43	55	64.8
TM-Like	5.47	6600	10938
Hybrid	5.48	8	9.8

As it can be seen from Table 3.5, the fundamental TM-like mode is the only mode in this range to show significant response in terms of R/Q and R_{SH}. This result indicates that strong coupling to the TM-like mode in comparison to the surrounding hybrid modes can be achieved. These values are of the same order of magnitude as the parameters found for conventional RF accelerators, however these values require enhancement if the structure is to outperform conventional RF structures. Comparing these parameters to those obtained from previous metamaterials schemes for accelerators, discussed in Chapter two, it can be seen that compared to the SRR and wire structure from [36] the R/Q of this structure (6.6 kΩ/m) is significantly lower than the value of 35 kΩ/m, however the shunt impedance obtained from the CSRR structure (10 MΩ/m) is a significant improvement on the value of 7 MΩ/m in [36]. In comparison to the CSRR structure in [41], there is a slight increase in R/Q from 6.2 kΩ/m to 6.6 kΩ/m for the design presented here.

3.3.3 Two layer loaded waveguide with 11.3 mm layer spacing

The two layer structure presents a much simpler loaded waveguide in comparison to the four layer structure, with significantly more space for the beam to propagate, shown in Figure 3.13. The increased spacing in this truncated version of the infinite metamaterial should result in a reduction in modes in comparison to the four layer structure which will simplify coupling, however the increased spacing

between beam and metasurface may result in reduced interaction.

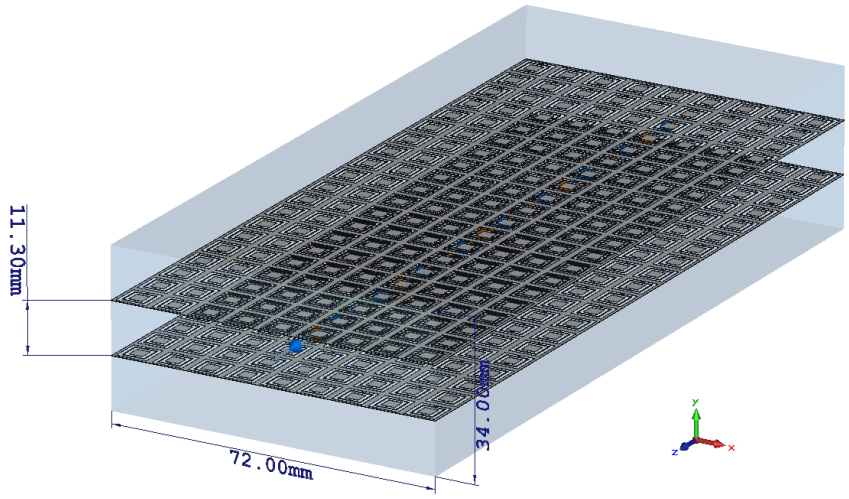

Figure 3.13: The two layer loaded waveguide structure, showing layer spacing of 11.3 mm and dimensions of the transverse segment.

Table 3.6 shows the results of the electromagnetic analysis for the two layer loaded waveguide structure with 11.3 mm spacing, only 10 modes are considered rather than 25 as a TM-like mode is found much earlier for this set-up. The TM-like mode at 5.269 GHz represents a slightly hybrid version of the TM_{31} mode as in the four layer set-up. This mode occur at a lower frequency than both the four layer structure and the empty waveguide, where it occurs at 5.47 GHz and 7.72 GHz, respectively, therefore the structure is operational below cut off.

Table 3.6: The mode polarization, frequency and beam coupling parameters for the first 10 modes in the two layer loaded waveguide structure with spacing 11.3 mm.

Polarization	Freq (GHz)	R/Q $(k\Omega/m)$	R_{SH} $(M\Omega/m)$
TE-like	1.99	0	0
TE-like	2.193	1.23	5.46
TE-like	2.327	0	0
TE-like	3.556	0	0
Hybrid	3.964	3.87	17.00
TE-like	4.292	0	0
Hybrid	4.783	0	0
TM-like	5.269	9.59	19.57
TE-like	5.312	0	0
Hybrid	5.475	0	0

The beam coupling parameters of R/Q per meter and shunt impedance per meter

were calculated using CST and are presented in Table 3.6. The TM-like mode is found to have very high beam coupling parameters values of 9.59 kΩ/m for R/Q and 19.57 MΩ/m for shunt impedance. This is a significant increase in response compared to the 4 layer structure which exhibited values of 6.6 kΩ/m for R/Q and 10.94 MΩ/m for R_{SH}. This shows a significant improvement in beam coupling and indicates that as well as being simpler to fabricate this structure will exhibit improved response.

The hybrid mode at 3.964 GHz represents a very weak version of the TM_{11} mode not found in the four layer set-up and has a strong shunt impedance of 17 MΩ/m and a R/Q of 3.87 kΩ/m which implies better coupling than the TM_{31} mode in the 4 layer structure. This mode occurs below the cut off frequency of the mode in the empty waveguide indicating below cut off operations. If the hybrid nature of this mode could be reduced and the R/Q value enhanced then this would represent a desirable operating mode, as the longitudinal electric field component is present for almost the full transverse plane. More interestingly this mode will be simpler to couple to via a conventional coupler, reducing the complexity of the device.

3.3.4 Two layer loaded waveguide with 6.76 mm layer spacing

The second possible two layer design maintains the initial reciprocal sheet spacing of 6.76 mm resulting in a spacing of 13.57 mm between the sheets and the outer walls as shown in Figure 3.14. Table 3.7 shows the results of the electromagnetic analysis of the first 10 modes in the two layer structure with 6.76 mm spacing. For this structure, the desired TM-like mode was found at 5.366 GHz with a R/Q of 8.925 kΩ/m and a shunt impedance of 18.45 MΩ/m, which shows and increase in mode order and frequency when compared to the two layer structure with larger layer spacing and a slight reduction in beam coupling parameters. The increase in mode order and frequency are to be expected as the closer lying metasurfaces result in more hybrid modes thus making the desired TM-like mode a higher order mode. The reduction in beam coupling is undesirable however expected as the four layer structure which also utilises this spacing has reduced beam coupling parameters too.

In comparison to the four layer structure, a significant reduction in the mode order of the desirable TM-like mode is once again observed from 24 to 10. This mode occurs at a slightly lower frequency than in the four layer structure and signifi-

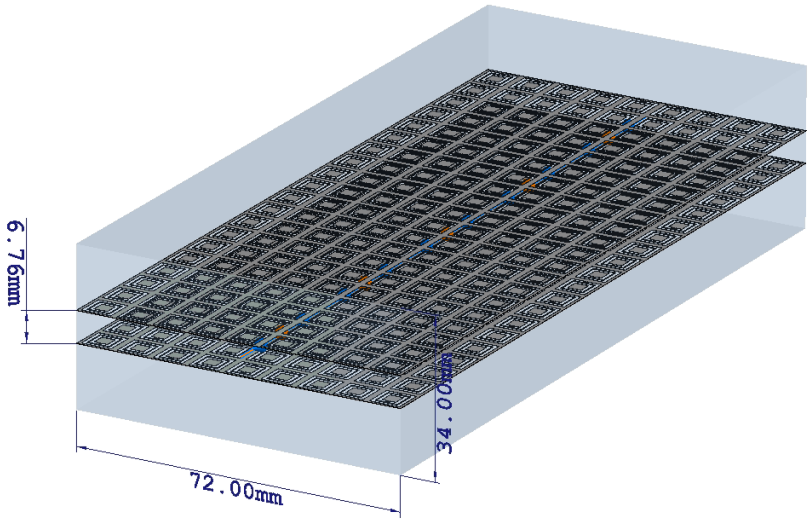

Figure 3.14: The two layer loaded waveguide structure, showing layer spacing 6.76 and transverse dimensions of the waveguide.

cantly lower than in the empty waveguide, thus below cut off. The beam coupling parameters obtained show improvement on the four layer structure, with significant improvement of the shunt impedance and slight improvement of the R/Q value. In order to verify the suitability of this structure as simplified alternative of the nominal CSRR loaded waveguide, wakefield simulations were performed and compared in the next Section.

Table 3.7: The mode polarization, frequency and beam coupling parameters for the first 10 modes in the two layer structure with spacing 6.76 mm.

Polarization	Frequency (GHz)	R/Q (kΩ/m)	R_{SH} (MΩ/m)
TE-like	1.895	0	0
TE-like	2.214	0.87	4.47
TE-like	2.327	0	0
Hybrid	3.375	0	0
Hybrid	4.015	2.85	14.38
TE-like	4.292	0	0
Hybrid	4.549	0	0
Hybrid	5.133	0	0
Hybrid	5.35	0	0
TM-like	5.366	8.93	18.46

3.4 Wakefield analysis

Wakefield analysis was performed to investigate electromagnetic interaction of the CSRR loaded waveguide with an electron beam. The wakefield solver cannot give a full characterization of the wave-beam interaction within the structure but provides an efficient method to estimate the coupling between the beam and the modes. Coupling between the beam and TM-like modes with strong longitudinal components is indicated by strong excitation in the longitudinal wake impedance. Ideally, a mode that excites strong longitudinal wake impedance with little to no transverse wake impedance is required for the applications. The hybrid nature of the modes within the structure implies there will be transverse excitations in addition to the longitudinal wakes, which if too large could lead to disruption of the beam.

For the wakefield simulations a section of the loaded waveguide 25 periods long in z is simulated as this is found in Chapter 5 to be sufficient to represent the behaviour of a loaded waveguide without excessive computing time. In Chapter 5 a study relating the peak wake impedance to the length of the waveguide is performed and it was found that the peak value of longitudinal wake impedance scaled with length via a linear relation, therefore simulations can be performed for a shorter structure and the response of the longer structure determined through extrapolation. The simulated Gaussian beam has a standard deviation of the bunch length σ=1.5 mm, a charge of 1 nC and an offset of 0.5 mm in x and y for calculation of the transverse wakes, this simulation ran for 2000 wake lengths. Through mesh convergence studies, it is found that numerical accuracy of the wakefield simulations is ensured by using a mesh density of 20 cells per wavelength. It needs to be noted that although convergence is reached, the hexahedral mesh of the wakefield solver leads to a slight shift in frequency if compared with the tetrahedral mesh of the eigen mode solver. However, this shift is not significant, with $< 1\%$ difference in frequency between the hexahedral and tetrahedral meshes at 20 cells per wavelength.

3.4.1 Four layer loaded waveguide

Figure 3.15 shows the longitudinal wake impedance excited within the four layer loaded waveguide structure when an electron beam with the defined parameters propagates between the central two layers. A strong longitudinal excitation occurs at 5.67 GHz a slightly higher frequency than the TM-like mode is found in the elec-

tromagnetic analysis and close in frequency to the interaction frequency between the beam and the TM-like mode of this unit cell. The excitation at 5.67 GHz, has a strength of 13.3 kΩ significantly stronger than any of the surrounding peaks. The dominance of this peak over the smaller surrounding excitations indicates clear single mode operation. The smaller peaks surrounding this central peak, correspond to hybrid modes of the system with equal strength longitudinal and transverse field components.

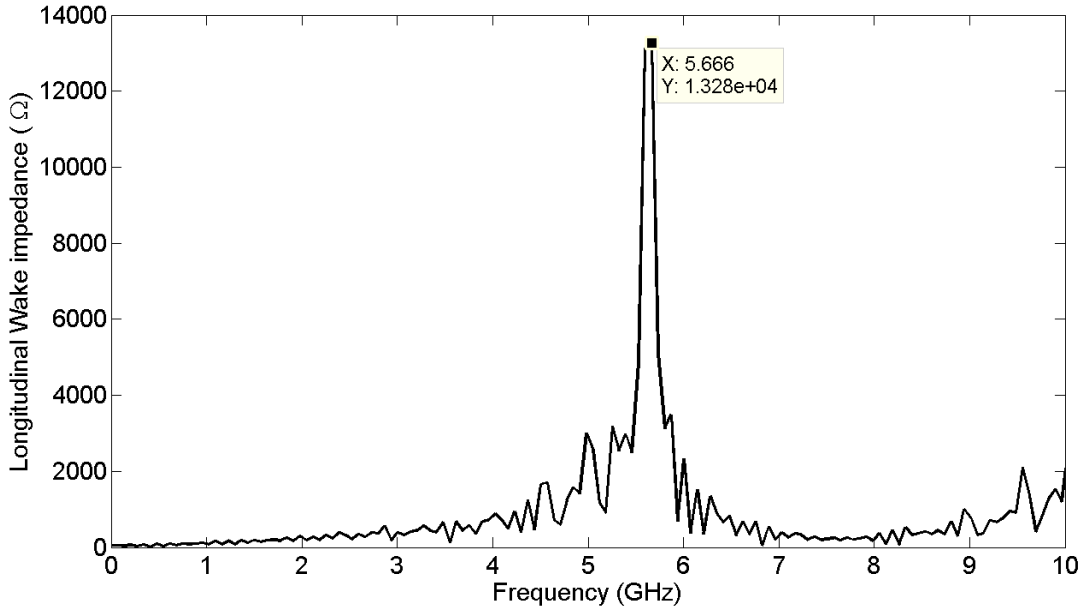

Figure 3.15: The longitudinal wake impedance for the four layer loaded waveguide structure within the frequency range of interest.

Figure 3.16 shows the transverse components of the wake impedance, with the strongest excitation occurring at the same frequency as the longitudinal wake 5.68 GHz, this is a clear indication that the mode of operation is a TM-like hybrid mode. It can be seen that both the x and y peaks are significantly smaller than the longitudinal excitation at only 6 kΩ. This is weak enough to ensure negligible effects on the beam transport. Further analysis via PIC simulations is required to fully understand how the structure and a realistic electron beam interact, and what mode is excited in the structure.

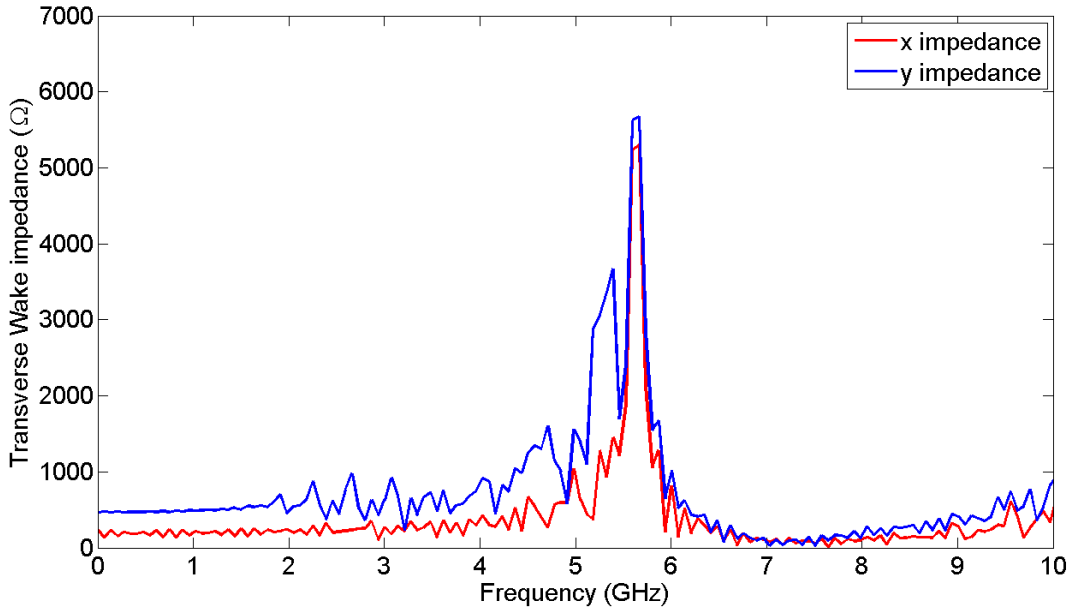

Figure 3.16: The transverse wake impedance for the loaded waveguide structure within the frequency range of interest, it can be seen the these excitations are much weaker than the longitudinal excitations.

3.4.2 Two layer loaded waveguide with 11.3 mm spacing

The initial wakefield analysis of the two layer structure was performed using the larger spacing of 11.3 mm, the increased spacing of the sheets increases the separation between the beam and metasurface which is likely to result in reduced interaction. Figure 3.17 shows the longitudinal wake response of the two layer structure with the 11.3 mm spacing, it can be seen that there is a strong excitation peak at 5.46 GHz which corresponds to the TM-like mode found at 5.268 GHz is much weaker than the excitation found for the four layer structure only 5.4 kΩ compared to 13.3 kΩ.

Figure 3.18 shows the transverse wake impedance of the structure, this is observed to be much weaker than the longitudinal wake response with peaks of less than 2.5 kΩ. The main peak in all directions occurs at the same frequency which indicates the hybrid nature of the desired mode, however the secondary transverse peaks do not correspond to the secondary longitudinal peaks which is another indication of the reduction of hybridization in this structure.

The weakened longitudinal wake response is due to the increased separation between the beam and the metasurface sheet, therefore the simulation will be run with the initial reciprocal separation of 6.76 mm to see if stronger wakes are observed there.

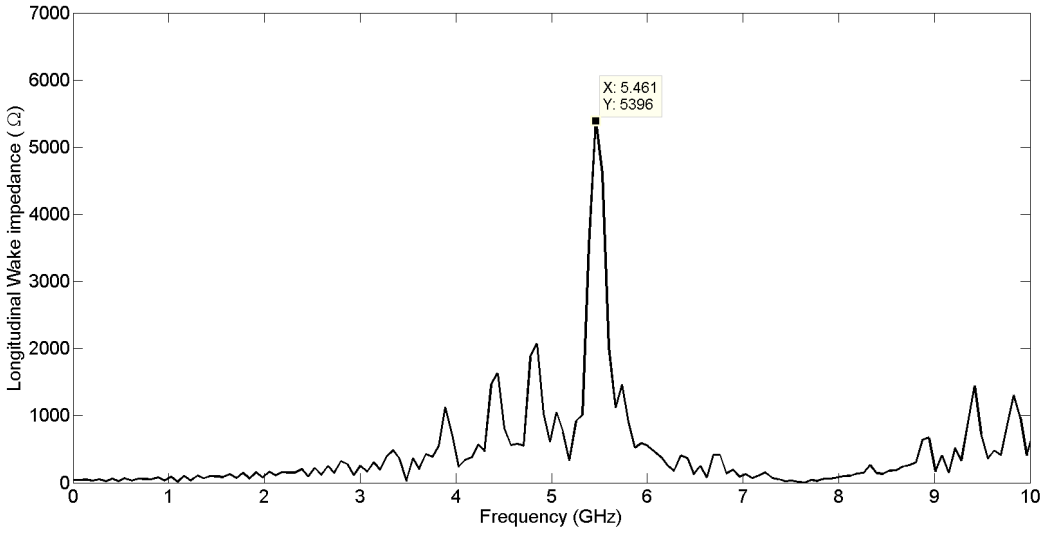

Figure 3.17: The longitudinal wake impedance of the two layer structure with a central layer spacing of 11.3 mm.

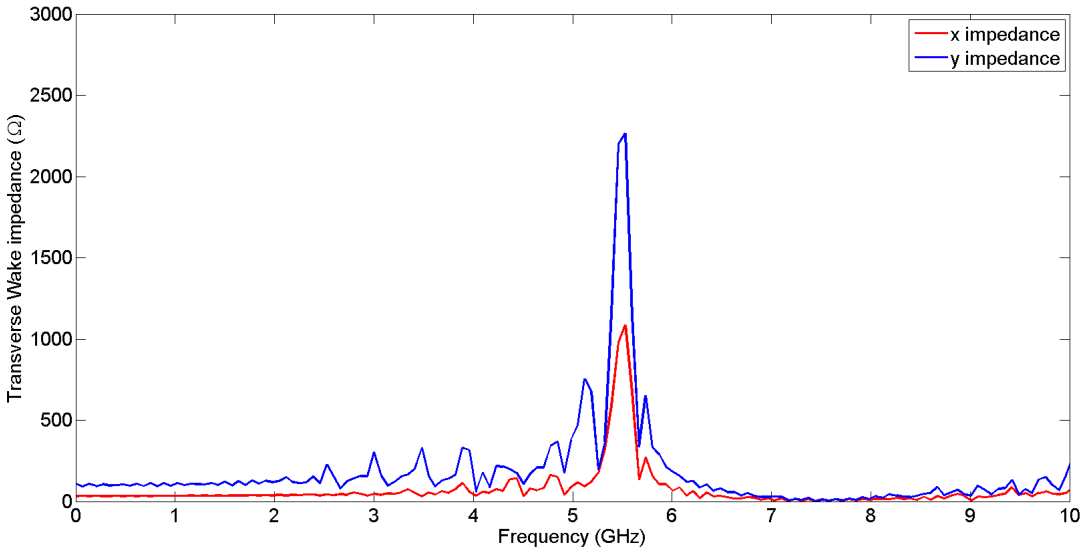

Figure 3.18: The transverse wake impedance of the two layer structure with a central layer spacing of 11.3 mm.

3.4.3 Two layer loaded waveguide with 6.76 mm spacing

The second two layer structure with spacing 6.76 mm is analysed using the same wakefield simulations details given above. This reduction in spacing to that of the four layer structure should increase the wake response as the beam now propagates close to the metasurface sheets.

Figure 3.19 shows the longitudinal wake impedance excited by an electron beam within the reduced spacing two layer system, a strong excitation peak of 11.9 kΩ

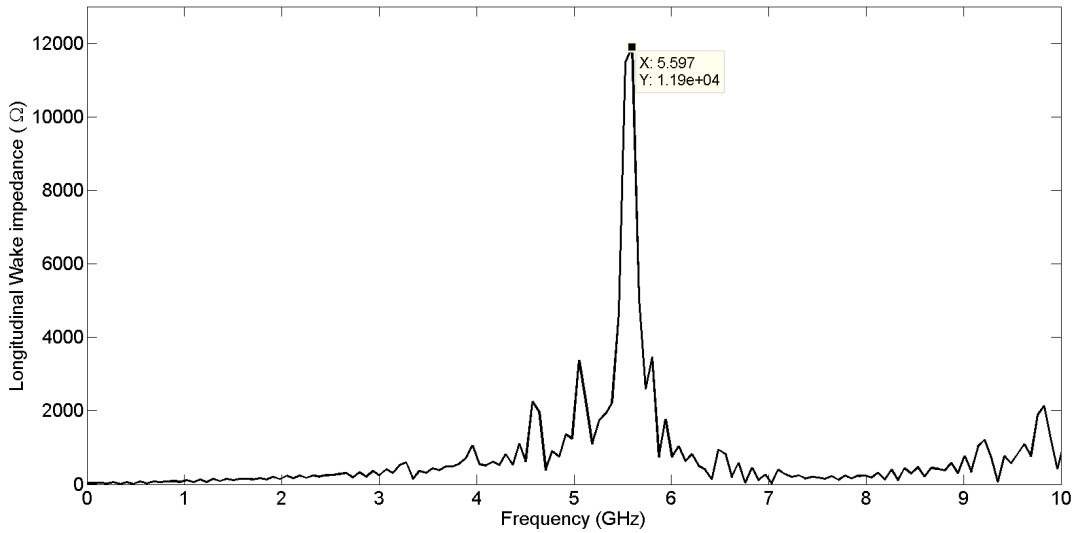

Figure 3.19: The longitudinal wake impedance of the two layer structure with a central layer spacing of 6.76 mm.

is observed at 5.6 GHz. This response is significantly stronger than that of the two layer set-up with 11.3 mm spacing, yet still not as strong a response as the four layer set-up. Though there is an increase in frequency, this excitation is believed to correspond to the desired TM-like mode found at 5.4 GHz, with the frequency shift being due to the change in mesh.

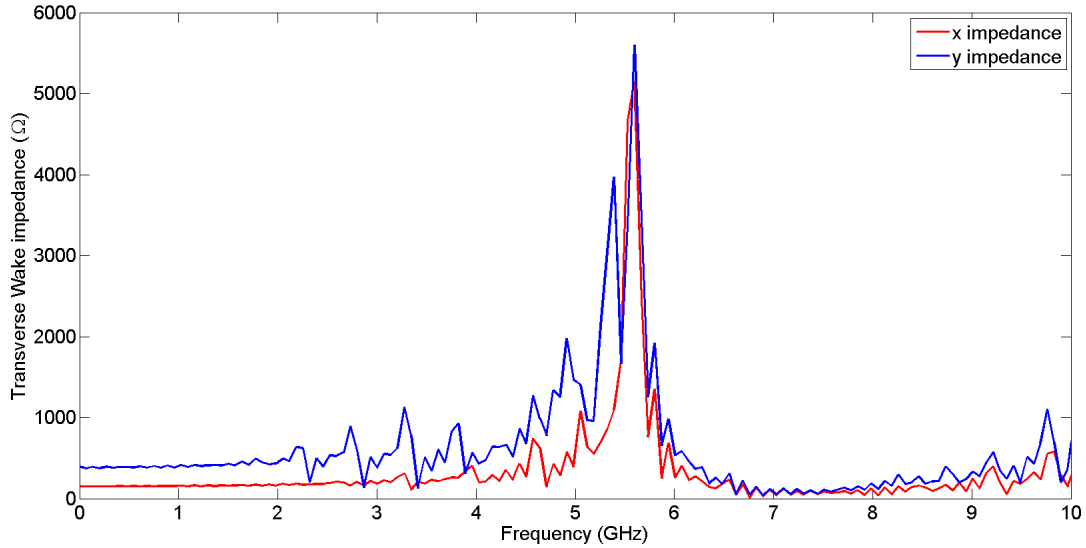

Figure 3.20: The transverse wake impedance of the two layer structure with a central layer spacing of 6.76 mm.

Figure 3.20 Shows the transverse wake excited within the two layer structure with reduced spacing. The transverse excitations occur at the same frequency as the longitudinal peak indicating the hybrid nature of the TM-like mode, these peaks

at 5.6 GHz have a strength of 5.2 kΩ in x and 5.6 kΩ in y. These excitations are almost half the strength of the longitudinal response and may cause disruption to the beam.

The response from the two layer structure with the reduced spacing is significantly stronger than that of the two layer structure with the increased spacing, indicating that the beam metasurface spacing plays a part in the response. However this response is still weaker than that of the four layer structure and so, the number of metasurface layers also factors into the behaviour of the structure.

3.5 Comparison of structures

Table 3.8 shows the results from both the electromagnetic and wakefield analysis of each loaded waveguide structure, with the different spacings. Focusing on the electromagnetic results the two layer structures significantly reduce the number of hybrid modes without significantly affecting the frequency, with this being most significant for the two layer set-up with increased spacing of 11.3 mm. This is also reflected by the beam coupling parameters, which are significantly higher for both two layer set-ups, with the shunt impedance of the two layer structures being nearly twice as high as the four layer set-up. This and the reduced number of hybrid modes is due to the fact that two layers do not disrupt the field as much as the four layer set-up. Based on this alone, a set-up with two layers appears to be the best option, however when the wakefield response is considered it can be seen that this is not the case.

Table 3.8: A table comparing the electromagnetic and wakefield results from all the set-ups.

Structure	Spacing (mm)	Mode order	Frequency (GHz)	R/Q (kΩ/m)	R_{SH} (MΩ/m)	Wake impedance (kΩ)
Four layer	6.76	24	5.47	6.6	10.9	13.3
Two layer	11.3	8	5.27	9.6	19.6	5.4
Two layer	6.76	10	5.37	8.9	18.5	11.9

The wakefield response indicates the level of interaction between the beam and the field interaction in the structure. It can be seen that the four layer structure performed better than the two layer set-ups, particularly the increased spacing set-up. Since the field generated in the structure originates on the metasurface

sheets, if the spacing between the beam and the metasurface is too large then the interaction will be significantly reduced. The four layer set-up additionally appeals as the additional layers make the structure more similar to a bulk 3D metamaterial which implies a greater level of interaction. For applications involving beam-wave interactions, which is the intended outcome for this structure, the four layer set-up is the best option.

3.6 Conclusions

The first CSRR loaded waveguide design considered in this work was discussed in this Chapter and a suitable electromagnetic mode for left-handed applications such as reverse Cherenkov radiation applications was identified. Through analysis of the unit cell, it has been shown that a change in layer spacing has minimal effect on the behaviour of the system in terms of mode frequencies. To gain full electromagnetic analysis of the design the finite form, where metallic waveguide walls confine the structure, was analysed extensively.

An empty S-band waveguide was analysed to provide a bench mark to compare the loaded waveguide structures to. The loaded waveguide exhibits more modes over a smaller frequency range, due to the increased number of hybrid modes created by the metasurface sheets, with less hybrid modes generated by the set-ups with fewer metasurfaces. In all the loaded waveguide cases there is a significant drop in cut off frequency of the desired TM_{31}-like mode from 7.72 GHz in the empty waveguide, to around 5 GHz for the loaded waveguide set-ups. The addition of the metamaterial to the waveguide damped the TM_{11} mode that was found in the empty waveguide.

The two layer set-ups were proposed as a simpler alternative to the four layer set-up in terms of fabrication and were shown to perform better in terms of the electromagnetic behaviour and beam coupling results. For the two layer set-ups there is a significantly lower number of hybrid modes and higher values of shunt impedance. For the set-up with increased spacing of 11.3 mm the TM-like mode occurs at 5.269 GHz and is the 8th mode, with R/Q of 9.6 kΩ/m and a shunt impedance of 19.6 MΩ/m. For the two layer set-up with 6.76 mm spacing the TM-like mode is the 10th mode with R/Q of 8.9 kΩ/m and shunt impedance of 18.46 MΩ/m, an increase in mode order and a reduction in beam coupling. In comparison the four layer set-up has the TM-like mode at 5.47 GHz the 24th mode with shunt impedance of 10.94 MΩ/m and R/Q of 6.6 kΩ/m, a higher mode

order and weaker beam coupling than the two layer set-ups. These beam coupling parameters are comparable to those found in conventional accelerators and an improvement on the SRR and wire design in terms of shunt impedance and previous CSRR designs in literature in terms of R/Q.

The excitations of the longitudinal wake impedance were analysed for all the set-ups, a strong excitation in the longitudinal wake impedance indicates strong beam coupling, which is desirable. Unlike the electromagnetic response, the four layer structure exhibited the strongest wakefield response with a longitudinal wake excitation of 13.3 kΩ corresponding to the TM-like mode found in the electromagnetic analysis. Despite strong electromagnetic performance in both two layer structures, the wakefield response is weak, especially for the set-up with 11.3 mm spacing. Increased spacing indicates a significant drop in performance, due to the increase beam metasurface spacing, which will significantly reduce interaction with the field. The four layer set-up is chosen as the best design, for wave-beam interaction applications.

The results from the initial design for the loaded waveguide structure presented in this Chapter illustrate that metamaterial loaded waveguide can be used generate backward propagating mode for reverse Cherenkov radiation. However this structure is not realisable, and the aim of this thesis is to form a design for a metamaterial loaded waveguide that can be fabricated and then tested on an existing electron beam. The current structure has several fabrication challenges associated with it and is susceptible to damaged and deformation from resistive heating as a results of high power operation. In the subsequent Chapter design considerations will be made to take this design from theoretical to practical, an aspect of metamaterials in accelerators that has previously been neglected in the literature.

Chapter 4

Design considerations of the CSRR loaded waveguide

In this Chapter, the design considerations made on the metamaterial loaded waveguide structure to improve fabrication suitability and robustness for high power operation are discussed. The focus of this Chapter is to address the challenges posed by realising a metamaterial structure for accelerators and investigate modifications to the metamaterial geometry which could make them more suitable to high power operation without compromising electromagnetic performance. Starting from the unit cell of the four layer structure discussed in the previous Chapter, a number of design modifications are investigated within the unit cell, and those that show promising results are carried through to be analysed as a full structure, both in terms of electromagnetic and wakefield response.

4.1 Motivation for modification

To date, published work on metamaterials for accelerators has mainly focused on theoretical analysis of the metamaterial electromagnetic properties [40] [43], whereas little attention has been dedicated to alleviating the practical issues which could impair their use in active devices and high-power environments. In particular, metamaterials often require the use of complex geometries with fine features/gaps and sharp corners which are susceptible to damage or deformation via resistive heating [44]. The incident magnetic field from the RF input induces a current in the metasurface which builds resistance leading to resistive heating. For thin sheets or small areas this is a significant issue that can lead to deformation or destruction of the elements [44]. It is these effects that the work within this

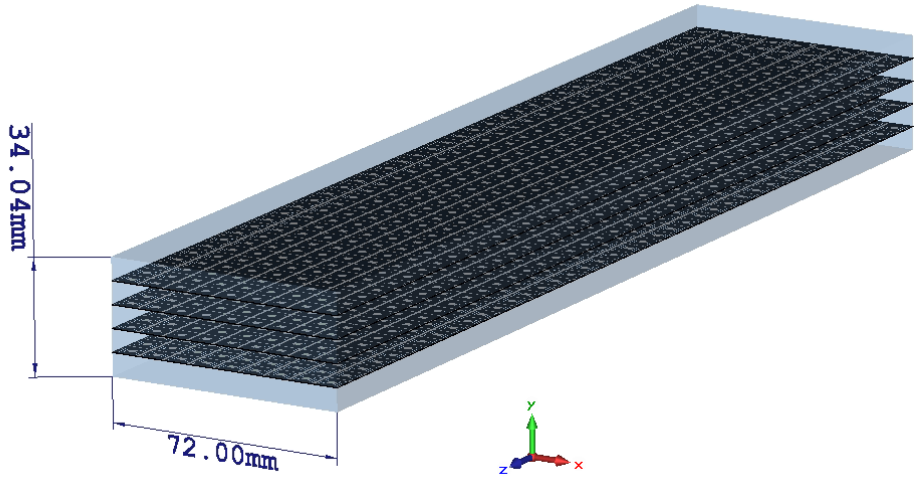

Figure 4.1: The four layer loaded waveguide structure showing dimensions.

chapter aims to mitigate.

In Chapter 3, the initial design of a loaded waveguide structure was presented, this took the form of a metallic 34 mm by 72 mm, WR-284 waveguide loaded with four CSRR-metasurfaces separated by 6.76 mm [75], this can be seen in Figure 4.1. This metamaterial loaded waveguide structure is a left handed medium, the Complementary Split Ring Resonator (CSRR) metasurfaces [40] give rise to left handed behaviour. The negative permittivity and permeability arise from the resonance of the CSRRs and the confinement of transverse magnetic modes respectively [30]. The use of an all metallic metamaterial structure is preferred as it can prevent typical issues associated with the use of dielectrics, such as accumulation of charge, breakdown at the vacuum/dielectric gaps where the fields are enhanced [34] and thermal management issues. The CSRR unit cell and parameters for this initial set-up can be seen in Figure 4.2. Throughout the rest of the Chapter this unit cell as presented in the initial design will be referred to as the nominal unit cell and the related loaded waveguide will be referred to as the nominal structure.

The nominal structure exhibits a TM_{31}-like mode with strong longitudinal electric field in the center of the structure, the profile of which is shown in Figure 4.3. This TM_{31}-like mode occurs at 5.5 GHz below the cut off frequency of this mode in a conventional waveguide. For this mode, beam coupling parameters of 6.6 kΩ/m for R/Q and 10.9 MΩ/m for shunt impedance are found, along with a longitudinal wake impedance of 13.3 kΩ. The aim of this work is to investigate modifications of this geometry to allow for increased fabrication suitability, a reduction in hybrid modes and a reduction in surface current while maintaining the electromagnetic

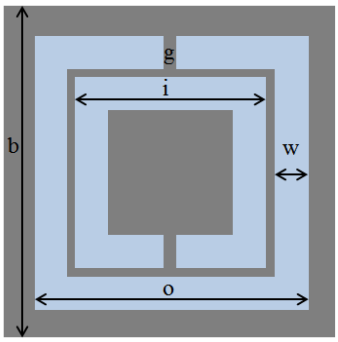

Parameter	Value (mm)
Unit Cell (b)	8
Outer Ring (o)	6.6
Inner Ring (i)	4.6
Ring Width (w)	0.8
Gap width (g)	0.3
Thickness (t)	0.05

Figure 4.2: The nominal unit cell and corresponding geometrical parameters.

and wakefield performance.

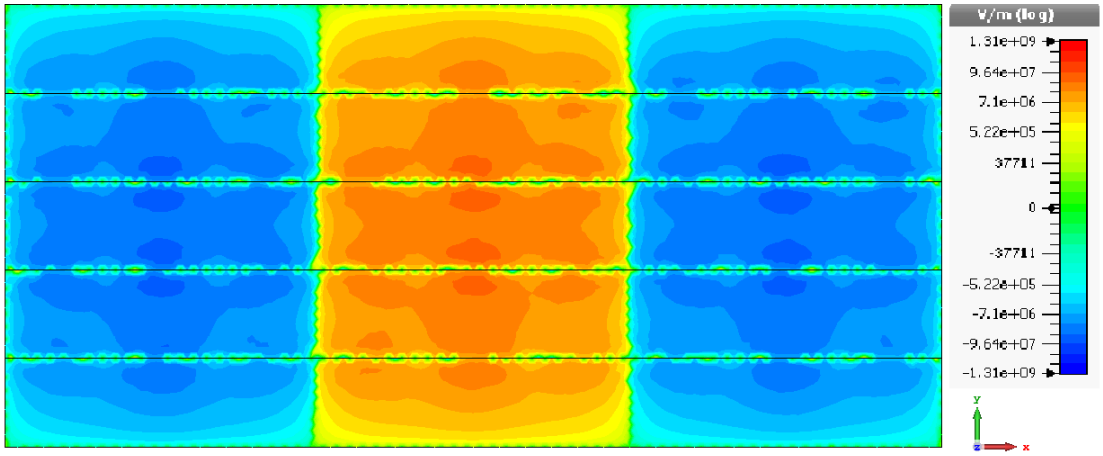

Figure 4.3: E_z field distribution of the fundamental TM-like mode supported by the CSRR-loaded waveguide, shown for a transverse segment of the waveguide.

To address the practical issues that can impair the use of metamaterials in accelerator systems, the initial design must be analysed to identify what modifications are required. In the case of the nominal unit-cell, resistive heating is likely to occur around the ring gap g, and on the strip separating the inner and outer rings. Therefore an increased sheet thickness t, an increased ring separation i and the introduction of curvature c will be considered to reduce this effect. In addition to resistive heating, a sheet thickness much smaller than transverse dimensions poses issues for fabrication and structural integrity, being unable to maintain the desired reciprocal separation unsupported. Therefore an increased sheet thickness and increased ring gap will also address challenges in fabrication.

The above stated parameters have been investigated for the unit cell via accurate numerical simulations, by considering the peak surface current, modal frequency

and hence dispersion properties of the five lowest order modes. Then, combinations of these parameters have been analysed for the loaded waveguide structure via accurate numerical simulations, in terms of field polarization, beam coupling parameters and wakefield response.

The modified geometries are labelled alphabetically such that waveguide A is loaded with metasurfaces formed from unit cell A. Cases A-D are formed from values chosen as a result of the parameter analysis performed on the unit cell, and that the optimal parameters found from this analysis have been used both separately and in come cases in combination to form the full waveguide test cases. The cases considered are as follows:

- Case A: increased sheet thickness of 1 mm and no other changes.
- Case B: increased ring separation changing i from 4.6 mm to 4 mm, increased ring gap g=0.8 mm and no other changes.
- Case C: increased sheet thickness of 1 mm, increased ring separation i=4 mm and increased ring gap g=0.8 mm.
- Case D: the addition of ring curvature with a radius of curvature 0.5 mm and increased sheet thickness of 1 mm.

Full structure electromagnetic analysis is provided for waveguides A-D and the beam coupling parameters are found for the longitudinal mode in each of these structure. Wakefield analysis is performed for waveguides A-C and the response of this analysed to decide on the best design considerations, to fit the specified criteria.

4.2 Unit cell analysis

The results gained from the nominal structure were sufficient to prove the suitability of a loaded waveguide structure for accelerator applications, however there are several challenges relating to fabrication and prolonged exposure to the high power RF that this structure possess. These challenges are discussed in the previous Section and have not been addressed in previous literature. Increased values of sheet thickness, ring separation and ring curvature, are investigated using the eigen mode solver of CST Microwave Studio [98]. The effects of changing these parameters on mode frequency and peak surface current are monitored for the first five modes. The design criteria for the unit cell is to maintain the dispersion

relation, increase fabrication suitability and reduce the surface current. To ensure the accuracy of the simulations a hexahedral mesh of 20 cells per wavelength was used which ensures a numerical accuracy of < 1 %. This mesh took into account curvature with order 2 curved elements and normal tolerances of 22.5 degrees.

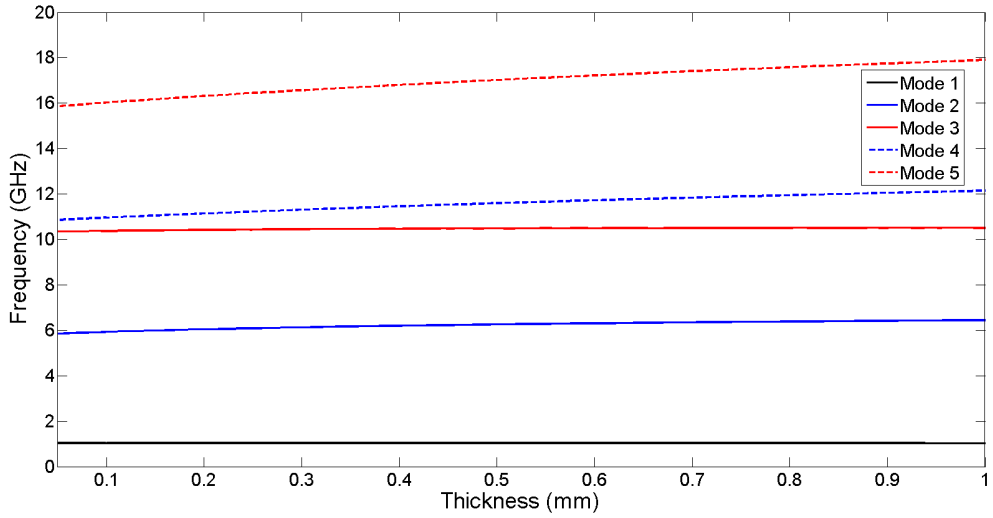

Figure 4.4: Frequency change in the first five modes of the unit cell with increasing sheet thickness.

The first design consideration was to increase the thickness of the unit cell and metasurface sheets from 0.05 mm to 1 mm by 30 linear steps. Increasing the thickness of the sheets results in a change of spacing between the metasurface layers from 6.76 mm to 5.81 mm, this varies the capacitance between layers and the frequency at which modes occur. The change in the frequency and peak surface current of the first five modes are shown in Figure 4.4 and Figure 4.6 respectively. In these figures the modes are labelled by the order in which they occur rather than the field polarization they exhibit which changes with the thickness.

Figure 4.4 shows a slight decrease in the frequency of the fundamental mode and a small increase in frequency for subsequent modes with increasing sheet thickness. Since there is little change in frequency, the effect on the dispersion will also be small. The results of this study indicate that an increase in thickness to 1 mm and a reduction in layer spacing to 5.81 mm has minimal effect on the frequency of the modes, changing the frequency of the desired mode by 7.3 %. In terms of dispersion Figure 4.5 shows the dispersion of the desired TM-like mode for both the nominal unit cell and the t=1 mm unit cell, it can be seen that the dispersion profile for both modes is near identical with the increase in thickness causing only a slight decrease in frequency. Therefore increased sheet thickness can be used with minimal effect on the dispersion of the operational mode.

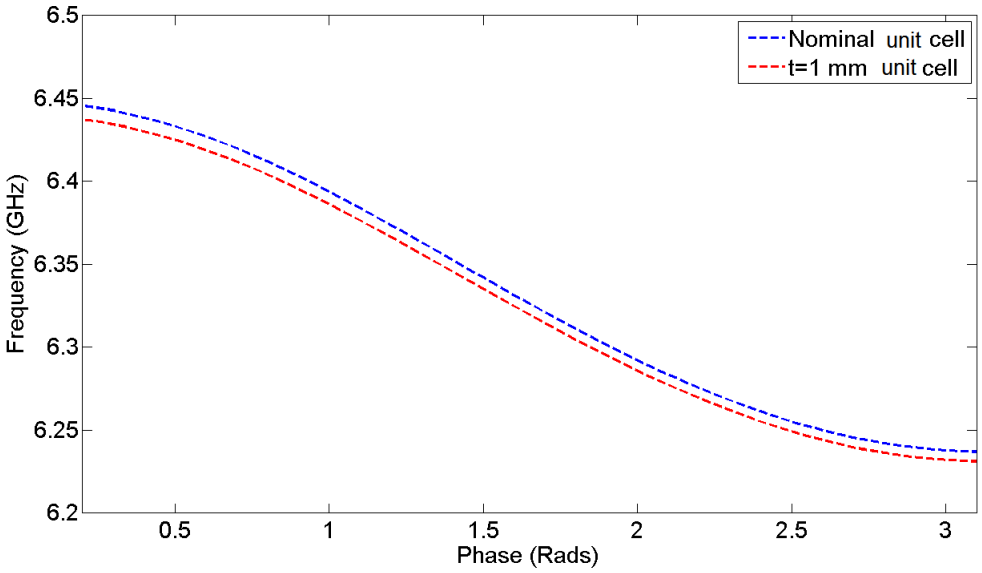

Figure 4.5: A comparison of the dispersion of the TM-like mode for the nominal unit cell and a unit cell of thickness 1 mm.

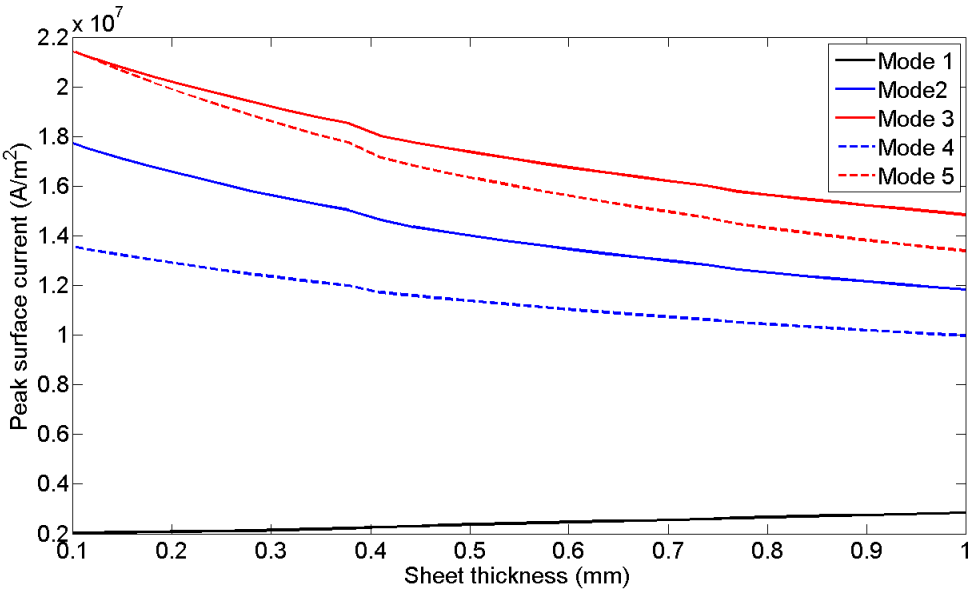

Figure 4.6: Change in simulated peak surface current for the first five modes of the unit cell with increasing sheet thickness.

In Figure 4.6, the effect of increased sheet thickness on the peak surface current is observed, with no change for the fundamental mode, but a significant drop ($0.4\times10^7(\mathrm{A/m^2})$) in peak surface current for the subsequent modes is observed as the sheet thickness increases. It is clear from Figure 4.6 that an increased thickness reduces the peak surface current significantly, this coupled with improved fabrication possibilities gained, indicate that an increased thickness of 1 mm is a good compromise for this parameter.

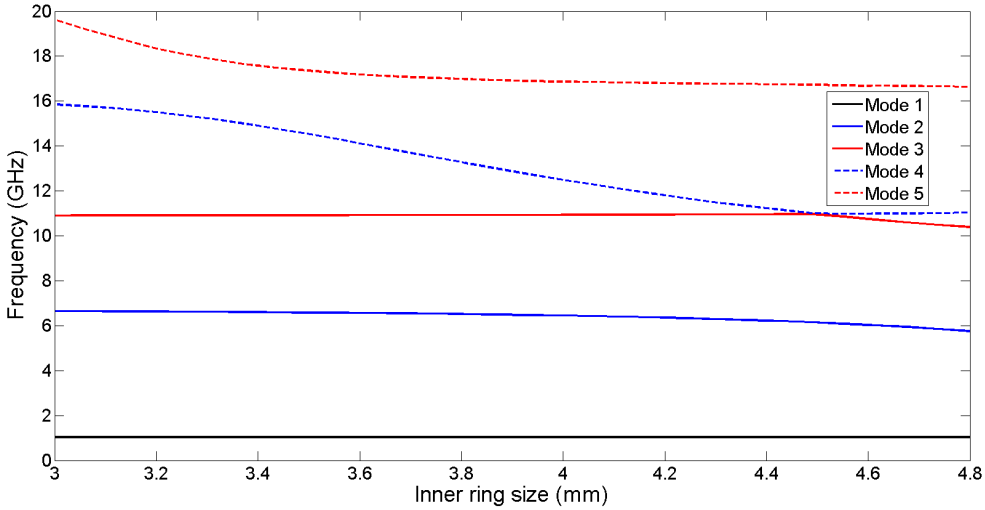

Figure 4.7: Modal frequency change with increasing inner ring width i and decreasing ring separation, for the unit cell.

The thickness of the metal separating the two rings was the next design consideration analysed, by changing the inner ring radius i while maintaining the original sheet thickness. The inner ring width i was varied from 3 mm to 4.8 mm in 30 linear steps, this allowed for both an increased ring separation and a decreased ring separation to be investigated as for the nominal unit cell $i = 4.2$ mm. It can be seen from Figure 4.7 that changing the inner ring radius does not significantly change the localization in frequency of the CSRR modes. By varying i, the ring separation is changed but the ring thickness w=0.8 mm is maintained, thus there is no change in inductance and capacitance of the system which maintains the dispersion and resonant response of the structure.

Thicker ring separation is thought to reduce the peak surface current that builds on the thin strips of metal separating the rings i, however it can be seen in Figure 4.8 that the change in peak surface current is minimal with no consistent trend. It is possible to identify a region of least variation between $i = 3.8$ mm and $i = 4.2$ mm therefore the optimal value of inner ring diameter lies within this region. An increase in ring separation and reduction of i greatly improves fabrication and structural integrity therefore $i = 4$ mm has been identified as a good compromise for the value of inner ring radius.

Finally, the addition of curvature to the split rings with no change in thickness or inner ring radius was studied. The addition of curvatures reduces sharp points for charge to build on and thus should reduce the damage to the resonator via resistive heating. The radius of curvature on the corners of the rings is increased

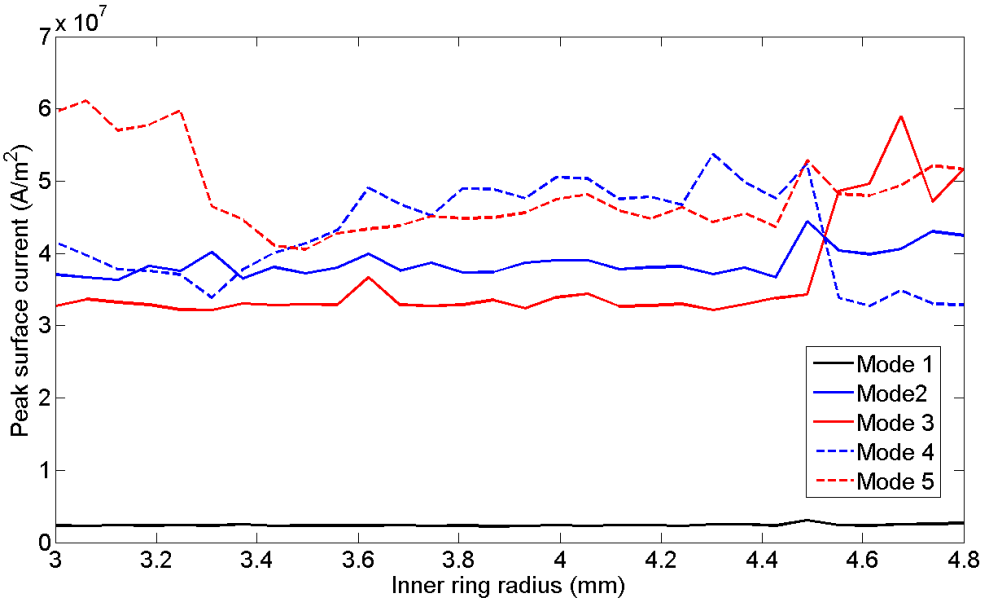

Figure 4.8: Change in simulated peak surface current with changing inner ring width i, for the unit cell.

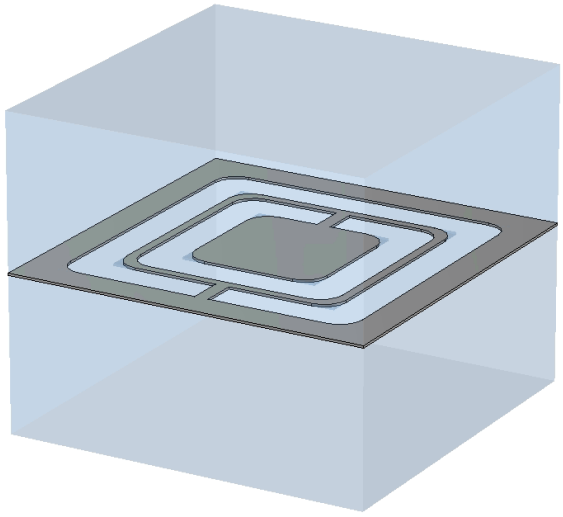

Figure 4.9: Modified unit cell with added curvature, using a radius of curvature of 0.5 mm and i of 4.6 mm.

from 0 to 0.65 mm in 30 linear steps, to identify an optimal parameter choice. This parameter sweep would ideally run to a radius of curvature of 1 mm however beyond 0.65 mm the number of suspicions elements at which the CST code is not able to handle the calculations as accurately as in the rest of the structure, is so high that the data cannot be considered accurate.

Figure 4.10 shows that the localization in frequency of the CSRR modes remains effectively unchanged with an increase in ring curvature, with only a slight increase

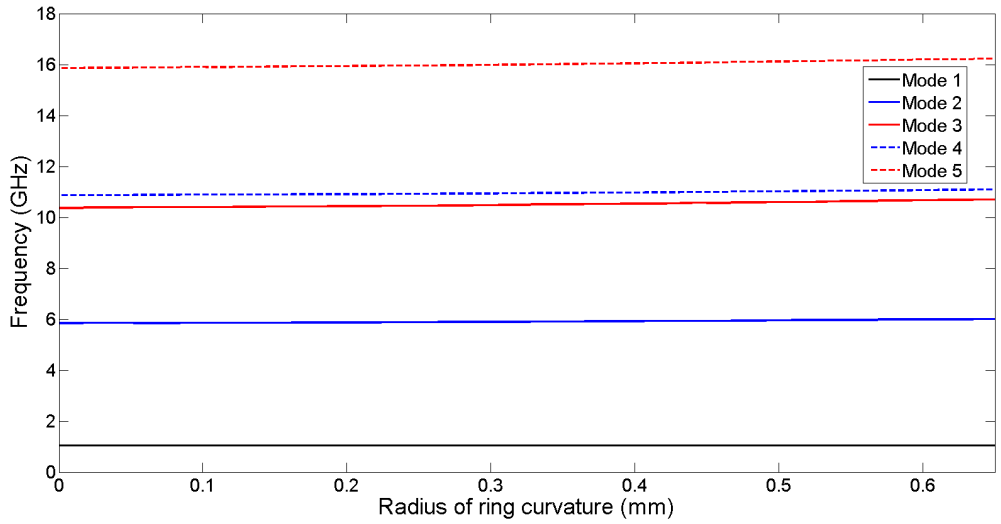

Figure 4.10: Change in frequency of the first five modes with increasing ring curvature, for the unit cell.

in frequency being observed. This also indicates that curvature arising from fabrication tolerances results in little change to the dispersive behaviour of the system.

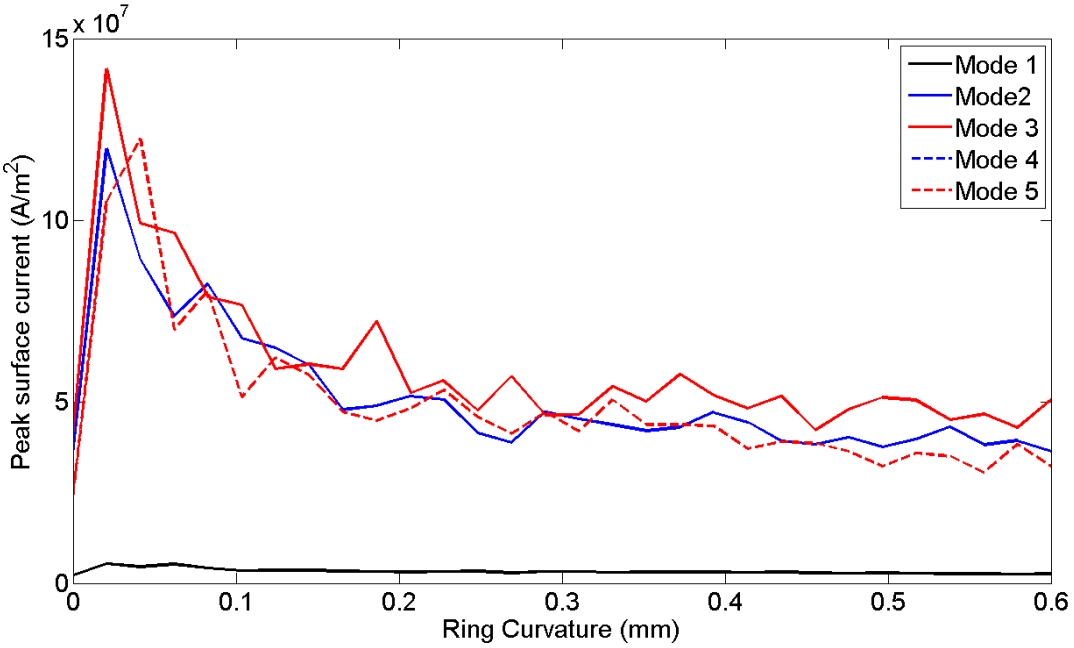

Figure 4.11: Change in simulated peak surface current with increasing ring curvature, for the unit cell.

Figure 4.11 shows a significant increase in peak surface current up to 0.05 mm and then reduces down to a constant between 0.4 mm and 0.6 mm. However at 0.6 mm the peak surface current is no lower than it was for zero radius of curvature, therefore increasing curvature does not reduce the peak surface current

on the rings. Though the overall surface current may be reduced by the addition of curvature, the benefits in reducing peak surface currents do not outweigh the added complexity of fabricating curved rings. Figure 4.12 shows a comparison of surface current build up on the nominal unit cell and a unit cell with ring curvature radius 0.5 mm, in both unit cells there is build up on the metal separating the rings and on the ring gap, the addition of curvature shows some reduction of the build-up on the metal separating the rings, however there is still significant build up. Therefore, the introduction of curvature is not necessary.

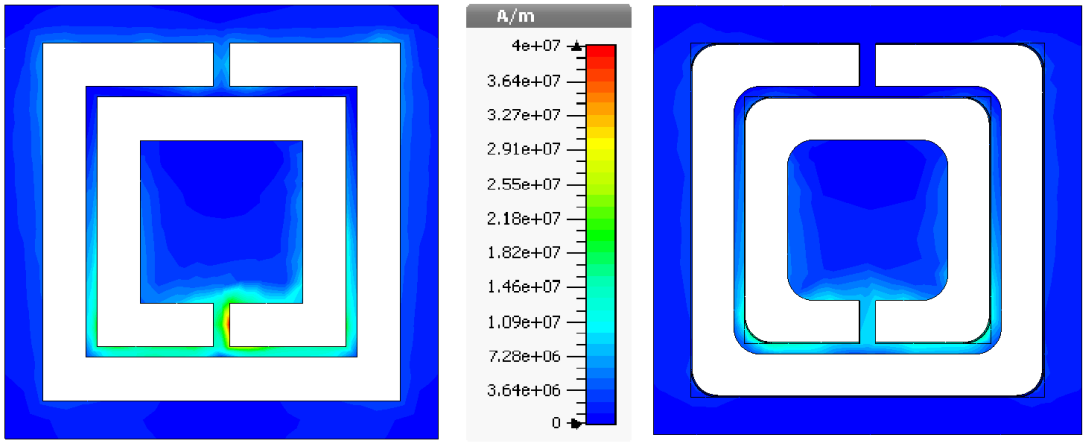

Figure 4.12: Simulation results showing, surface current build up on the two unit cells, a) the nominal unit cell and b) the unit cell with ring curvature radius 0.5 mm.

Throughout these investigations, a modified geometry of the CSRR unit cell to minimize some of the practical issues of MTMs in particle accelerators has been identified. Specifically this allows for increased sheet thickness t=1 mm and an inner ring radius i=4 mm resulting in an increased ring separation.

Table 4.1, summarizes the results obtained from four modified unit cells as compared to the nominal structure. It can be seen that the geometry modifications investigated on the unit cell have an effect on the modal frequency and for certain set-ups it can be expected that the TM-like accelerating mode will occur at a higher if not significantly higher frequency than in the original set-up. However, further analysis of the loaded structure is required to form conclusions on how these modifications affect the beam coupling parameters and the number of hybrid modes which arise when the metasurfaces are loaded into the metal waveguide.

Table 4.1: The frequency and mode type of the first five modes of each modified unit cell (UC).

Nominal Unit cell		Unit cell A Thickness t=1 mm		Unit cell B i=4 mm		Unit cell C i=4 mm t= 1mm		Unit cell D c=0.5 mm t= 1 mm	
Mode	**Freq** (GHz)	**Mode**	**Freq** (GHz)	**Mode**	**Freq** (GHz)	**Mode**	**Freq** (GHz)	**Mode**	**Freq** (GHz)
TE-like	1.041	TE-like	1.028	TE	1.040	TE-like	1.029	TE	1.028
TM-like	5.845	TM-like	6.446	TM-like	6.451	TE-like	6.767	TE-like	6.499
Hybrid	10.369	Hybrid	10.509	TE-like	10.934	TM-like	12.329	TM-like	10.629
Hybrid	10.872	TE-like	12.142	TE-like	12.487	Hybrid	13.037	TE-Like	12.235
TE-like	15.856	TM-like	17.905	TM-like	16.871	Hybrid	18.55	TE-Like	18.031

4.3 Electromagnetic analysis of the modified designs

In this Section, the effects of the proposed design modifications are investigated for the CSRR loaded waveguide. The infinite set-up created by the unit cell simulations is truncated to 4 layers within a metallic waveguide WR-284, 72 mm by 34 mm, and is infinitely long in the longitudinal direction as described in Chapter 3. This is achieved by simulating 4 layers of a single row of 9 CSRRs to form a single strip of the loaded waveguide, with periodic boundaries in the longitudinal direction of propagation. For each of the unit cells, a single strip form is produced to mimic the behaviour of the loaded waveguide and electromagnetic analysis is performed at a phase of 10 degrees. The modal frequencies, field polarization and number of hybrid modes are investigated. The aim of this investigation is to identify TM-like modes with strong longitudinal field suitable for reverse Cherenkov radiation. Through convergence analysis, it is found that a tetrahedral mesh of 10 cells per wavelength ensures a numerical error of $< 0.01\%$. These simulations were performed to an accuracy of 1×10^{-6}, with curved elements of order two, to aid with the meshing of fine features which occur within the CSRR.

Figure 4.13 shows the structures investigated, which are as follows;

- Waveguide A: increased sheet thickness of 1 mm and no other changes.
- Waveguide B: increased ring separation changing i from 4.6 mm to 4 mm, increased ring gap g=0.8 mm and no other changes.
- Waveguide C: increased sheet thickness of 1 mm, increased ring separation i=4 mm and increased ring gap g=0.8 mm.

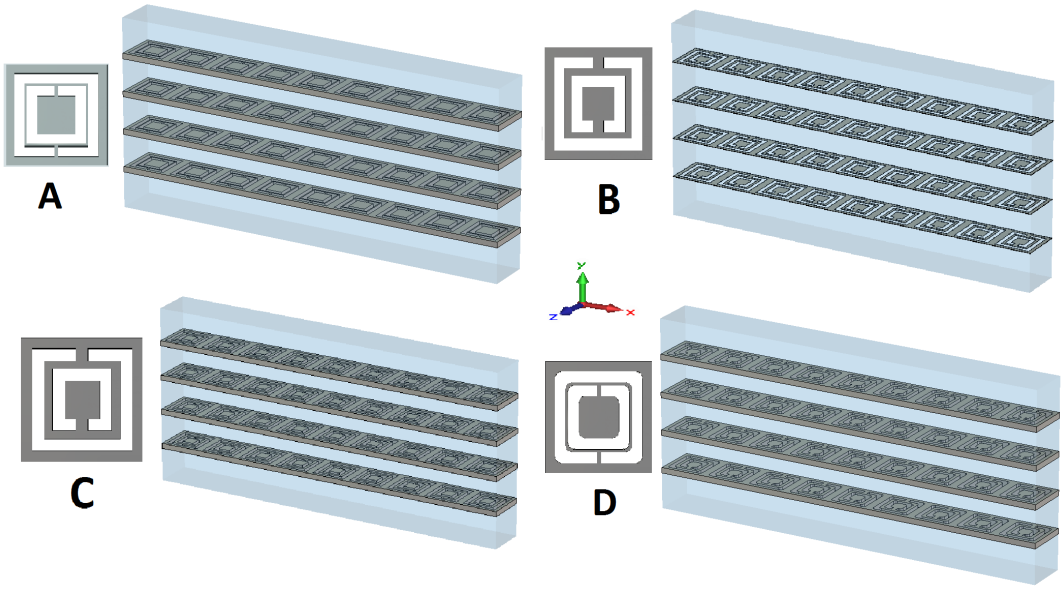

Figure 4.13: The Unit cell and respective single longitudinal period of the four loaded waveguides considered for the electromagnetic analysis, showing increased layer thickness (A), increased ring separation (B), increased ring separation and increased thickness combined (C) and increased sheet thickness and added curvature (D).

- Waveguide D: the addition of ring curvature with a radius of curvature 0.5 mm and increased sheet thickness of 1 mm.

These structures were compared to the nominal structure, with focus on the frequency of the TM_{31}-like mode, the number of modes in the structure, and the beam coupling parameters R/Q and R_{SH} [100]. In the nominal structure the TM_{31}-like mode is the 24th mode of the system occurring at 5.467 GHz with a shunt impedance of 11 MΩ/m and R/Q of 6.5 kΩ/m.

4.3.1 Waveguide A: Increased sheet thickness of 1 mm

For waveguide A, shown in Figure 4.14, there exists a TM_{31}-like mode at 5.86 GHz, which exhibits the same field profile shown in Figure 4.3 and occurs at a lower mode order than that of the nominal structure, indicating a reduction of hybrid modes. Table 4.14 shows that the TM_{31}-like mode at 5.86 GHz exhibits a high shunt impedance of 22.6 MΩ/m, an R/Q of 4.5 kΩ/m and occurs at a slightly higher frequency than in the nominal structure. This mode exhibits a significantly stronger shunt impedance than the nominal structure but no improvement in R/Q. In terms of both fabrication and performance this is a good candidate for the final structure.

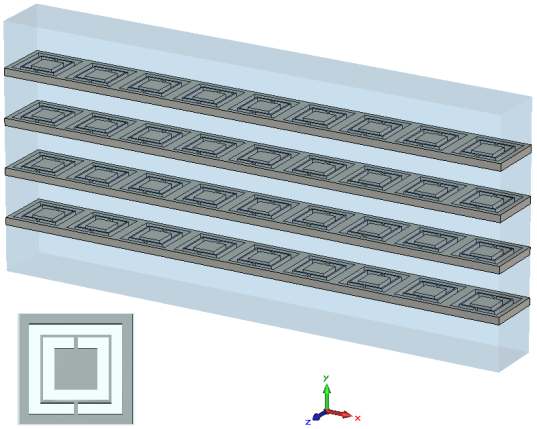

Mode	Frequency (GHz)	R/Q (kΩ/m)	R_{SH} (kΩ/m)
10	4.24	0	0
11	4.74	0	0
12	4.99	1.87	831.1
13	5.38	0	0
14	5.58	0	0.1
15	5.80	0.89	3445.1
16	**5.86**	**4.5**	**22683.2**
17	5.94	0	0.2
18	6.08	0	1.3
19	6.08	0	1.7
20	6.09	0	1.5

Figure 4.14: The unit cell and a segment of waveguide A showing the increased sheet thickness and no further modifications, and the beam coupling parameters of the TM-like mode and surrounding modes.

4.3.2 Waveguide B: Increased ring separation i=4 mm

For waveguide B shown in Figure 4.15, there exists a TM_{31}-like mode at 5.80 GHz, with field profile as shown in Figure 4.3. Table 4.15 shows that in comparison to the nominal structure, there is a slight increase in mode frequency and a clear reduction of mode order. For this mode the shunt impedance is 29.5 MΩ/m and R/Q is 7.73 kΩ/m, showing significant improvement on the nominal structure, and a slight improvement on waveguide A.

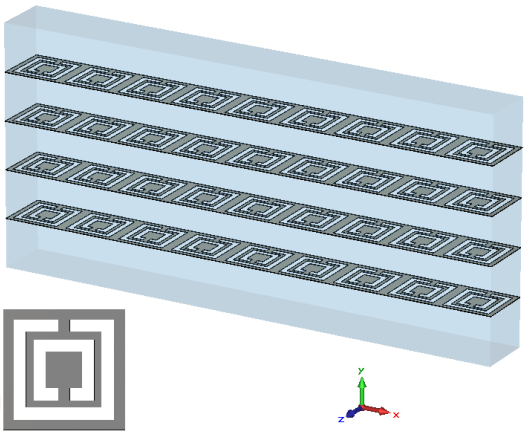

Mode	Frequency (GHz)	R/Q (kΩ/m)	R_{SH} (kΩ/m)
10	4.29	0	0
11	4.52	0	0.2
12	4.78	2.26	6380.7
13	5.22	0	0.1
14	5.45	0	0
15	5.69	0.99	2411.2
16	**5.80**	**7.73**	**29483.3**
17	5.95	0	0
18	6.06	0	0.4
19	6.12	0	11.0
20	6.19	0	0.6

Figure 4.15: The unit cell and a segment of waveguide B showing the increased sheet thickness and no further modifications, and the beam coupling parameters of the TM-like mode and surrounding modes.

4.3.3 Waveguide C: Increased ring separation i=4 mm and increased sheet thickness

The design modifications of waveguide A (t=1 mm) and waveguide B (i=4 mm) are combined to form waveguide C, this structure is shown in Figure 4.16. For waveguide C, there exist two TM-like modes with strong beam coupling parameters shown in Table 4.16. The first suitable TM-like mode occurs at 5.97 GHz, and corresponds to a TM_{31}-like mode, at a slightly higher frequency than the nominal structure and a reduction of mode order to the 15th mode. This mode exhibits a shunt impedance of 10.21 MΩ/m slightly lower than the nominal structure and an R/Q of 3 kΩ/m weaker than the nominal structure and both waveguides A and B.

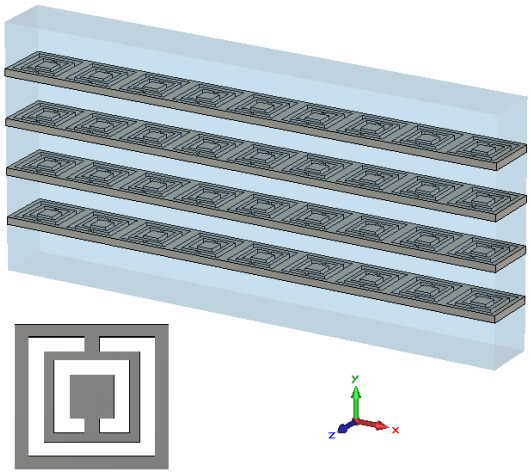

Mode	Frequency (GHz)	R/Q (kΩ/m)	R_{SH} (kΩ/m)
14	5.92	0	0
15	**5.97**	**3.05**	**10212.5**
16	6.15	1.29	218.7
17	6.26	0	0
18	6.44	0	0
19	6.50	0	0
20	6.57	0.03	41.2
21	6.70	0	0.1
22	6.73	0.11	157.2
23	**6.73**	**5.01**	**7440.4**
24	6.74	0.39	563

Figure 4.16: The unit cell and a segment of waveguide C showing the increased sheet thickness and no further modifications, and the beam coupling parameters of the TM-like mode and surrounding modes.

The second TM-like mode has the filed polarization as shown in Figure 4.17 similar to a TH_{51}-like mode, is the 23rd mode, thus a small reduction in mode order compared to the nominal structure. This mode occurs at 6.73 GHz, an increase in frequency of over 1 GHz compared to the nominal structure. It exhibits a shunt impedance of 7.44 MΩ/m and R/Q of 5 kΩ/m, significantly weaker beam coupling parameters than the nominal structure and waveguides A and B. Unexpectedly the results of combined increased ring separation and sheet thickness are worse than either modification performed separately, which despite the significant improvement in fabrication makes this structure unsuitable for the desired applications.

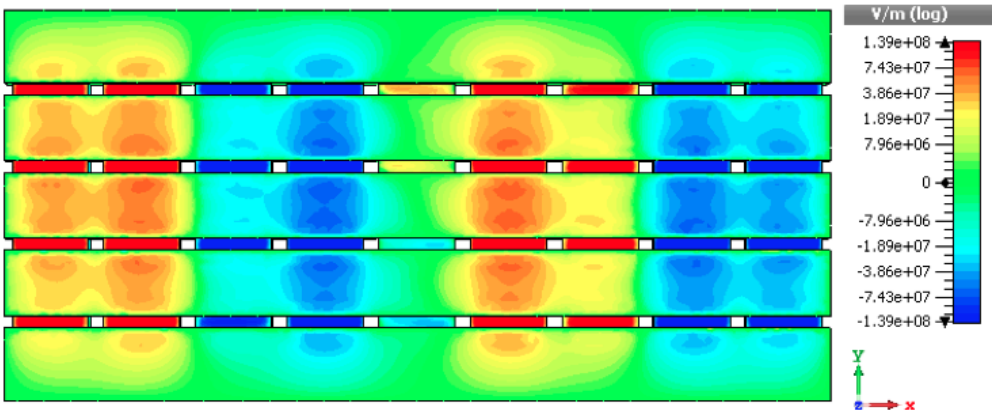

Figure 4.17: The alternative found TM-like mode at 6.73 GHz in waveguide C.

4.3.4 Waveguide D: addition of ring curvature 0.5 mm and increased sheet thickness

Finally, in order to perform an exhaustive study, a set-up with both increased surface thickness of 1 mm and ring curvature of 0.5 mm, as shown in Figure 4.18, was studied. Table 4.18 shows two TM-like modes are also found in waveguide D, one at 5.931 GHz and a second at 6.88 GHz. Both these modes occur at a higher frequency than the TM_{31}-like mode of the nominal structure, with a reduction in mode order.

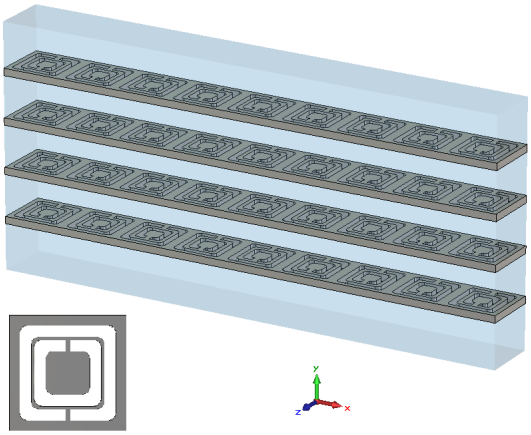

Mode	Frequency (GHz)	R/Q (kΩ/m)	R_{SH} (kΩ/m)
13	5.49	0	0.02
14	**5.93**	**2.50**	**12150.31**
15	5.99	0	0
16	6.18	0	0
17	6.24	1.39	3947.1
18	6.58	0	0
19	6.59	0	0.1
20	6.74	0.07	174.7
21	6.85	0	0.7
22	**6.89**	**5.95**	**14913.4**
23	6.91	0	2.7

Figure 4.18: The unit cell and a segment of waveguide D showing the increased sheet thickness and no further modifications, and the beam coupling parameters of the TM-like mode and surrounding modes.

The initial TM-like mode at 5.93 GHz is the 14th mode of the system and corresponds to a TM_{31}-like mode. This mode has an R/Q of 2.5 kΩ/m which is significantly lower than the nominal structure, and a shunt impedance of 12.15 MΩ/m which is slightly higher the nominal structure. The higher order TM-like

mode at 6.88 GHz is the 22nd mode of the system. This mode has a R/Q of 5.95 kΩ/m which is of the order of the nominal structure and a shunt impedance of 14.91 MΩ/m which is significantly higher than the nominal structure but weaker than the response of waveguides A-C.

4.3.5 Summary of results from electromagnetic simulations

Table 4.2 shows a comparison of the electromagnetic response of the desired TM-like mode in the different modified structures and the nominal waveguide. This compares the fundamental TM-like mode order, frequency, R_{SH} and R/Q, of all the structures considered. The mode order was considered as a reduction in mode order indicates a reduction in the number of hybrid modes. In the case of waveguides C and D a second TM-like mode was found at a higher frequency, shown in Figure 4.17, in addition to the TM_{31}-like mode. This mode is hybrid in nature and shows less defined longitudinal field in the central region.

Table 4.2: The frequency, mode order and beam coupling parameters of the modified set-ups. It should be noted that for set-ups C and D there are values for two suitable TM-like modes.

Waveguide	Mode order	Frequency (GHz)	R/Q (kΩ/m)	Shunt impedance (MΩ/m)
Nominal	24	5.467	6.5	11
t= 1mm (A)	16	5.86	4.5	22.6
i=4 mm (B)	16	5.8	7.75	29.5
i=4 mm t=1 mm (C)	15	5.97	3	10.25
i=4 mm t=1 mm (C)	23	6.73	5	7.5
c=0.5 mm t=1 mm(D)	14	5.93	2.38	12.13
c=0.5 mm t=1 mm(D)	22	6.89	5.88	14.85

To summarize the results of the electromagnetic and beam coupling analysis shown in Table 4.2, the best results in terms of performance were obtained from waveguide B with increased ring spacing as a result of setting i=4 mm. This set-up exhibited strong beam coupling parameters for a suitable TM-like mode at a lower mode order, indicating a reduction in hybrid modes. However, with no increased sheet thickness, this structure does not solve for the highlighted practical limitations of the nominal structure and is susceptible to damage at high power. Waveguide A with increased sheet thickness of 1 mm resulted in a reduced number of hybrid

modes while maintaining a strong TM-like mode with good beam coupling parameters; shunt impedance slightly higher than the nominal structure and a R/Q value on a similar level, indicating this set-up is a good compromise in terms of both fabrication and performance. Combining the modifications of waveguide A and B, waveguide C reduces the strength of the beam coupling parameters and introduces a secondary TM-like mode. Though this set-up has the highest fabrication suitability, results indicate that performance is significantly affected. The addition of curvature in waveguide D shows high shunt impedances but low R/Q meaning no significant improvement in beam coupling compared to the nominal structure or the other modifications, therefore this structure will not be investigated further.

4.4 Wakefield analysis of the modified designs

In this Section a comparison of the longitudinal wakefield response observed for waveguides A-C is presented using data simulated by CST [98]. A total length in z of 25 periods was considered for these investigations. The simulated Gaussian beam has a radius of 2.5 mm, a standard deviation of the bunch length of σ=1.5 mm, a charge of 1 nC and an offset of 0.5 mm in x and y for the transverse wakes, for 2000 wake lengths. Through mesh convergence studies, it is found that numerical accuracy of the wakefield simulations is ensured by using a hexahedral mesh density of 20 cells per wavelength. It needs to be noted that although convergence is reached, the hexahedral mesh of the wakefield solver leads to a $< 1\%$ shift in frequency if compared with the tetrahedral mesh of the eigen mode solver. However, with the introduction of the beam a shift to higher frequencies is also observed, this results in the wake excitations being observed at a higher frequency than the modes were found in electromagnetic simulations.

Wakefield analysis does not give full characterization of the wave beam interactions however strong coupling between the beam and a mode of the structure is indicated by a strong excitation of the longitudinal wake impedance. Ideally, a mode that excites strong longitudinal wake impedance with little to no transverse wake impedance is required for the applications. However, the hybrid nature of the modes within the structure implies there will be weak excitations to the transverse impedance in addition to the longitudinal wakes.

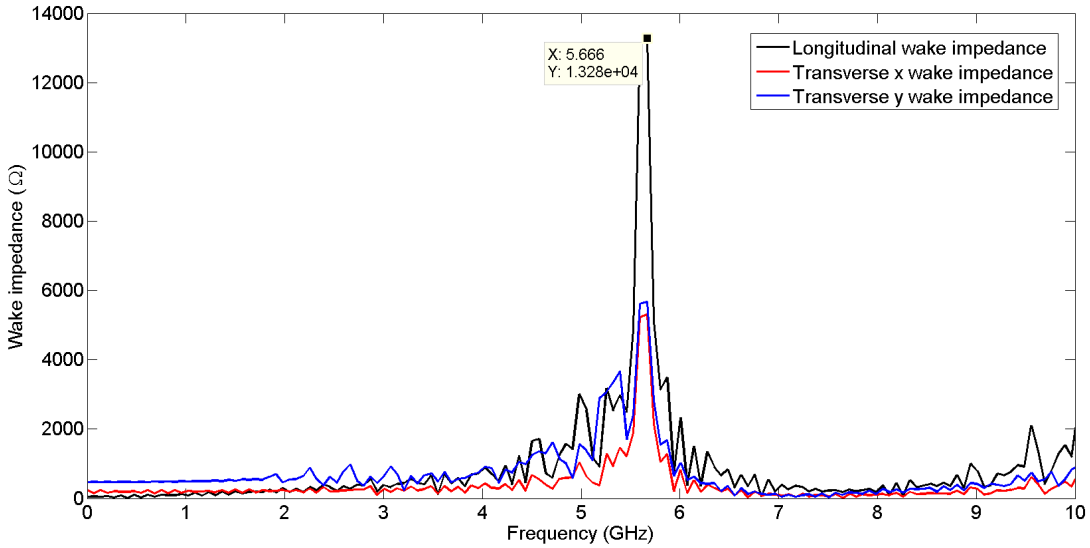

Figure 4.19: The wake impedance of the nominal structure in the region of the TM-like mode showing an excitation of 13.3 kΩ at 5.67 GHz.

4.4.1 The Nominal structure

In Figure 4.19, the longitudinal and transverse wake impedance for the original nominal structure is shown, with excitations occurring in the region of 5.5 GHz, where the TM_{31}-like mode is found. Figure 4.19 shows the excitation that corresponds to the TM_{31}-like mode found at 5.67 GHz with a strength of 13.3 kΩ. The transverse wake excitations occur at the same frequency as the longitudinal wakes due to the hybrid nature of modes in the structure, these excitations reach 5.3 kΩ and 5.7 kΩ for x and y respectively. The transverse excitations for the nominal structure are less than half the strength of the longitudinal excitations, thus there will be minimal disruption to the beam.

4.4.2 Waveguide A: Increased thickness

Figure 4.20, shows the longitudinal and transverse wake excitations of waveguide A, in which the TM_{31}-like mode occurs at 5.86 GHz. In this frequency range, there is an excitation of the longitudinal wake impedance, at 6.42 GHz with an impedance of 10.6 kΩ corresponding to the TM_{31}-like mode found in electromagnetic simulations, significantly weaker than the excitation identified for the nominal structure. Figure 4.20 shows the transverse wake impedance excitations occur at the same frequency as the longitudinal response with strengths of 4.6 kΩ and 5.8 kΩ for x and y respectively. These excitations are half the strength of the longitudinal response so they may cause disruption to the beam.

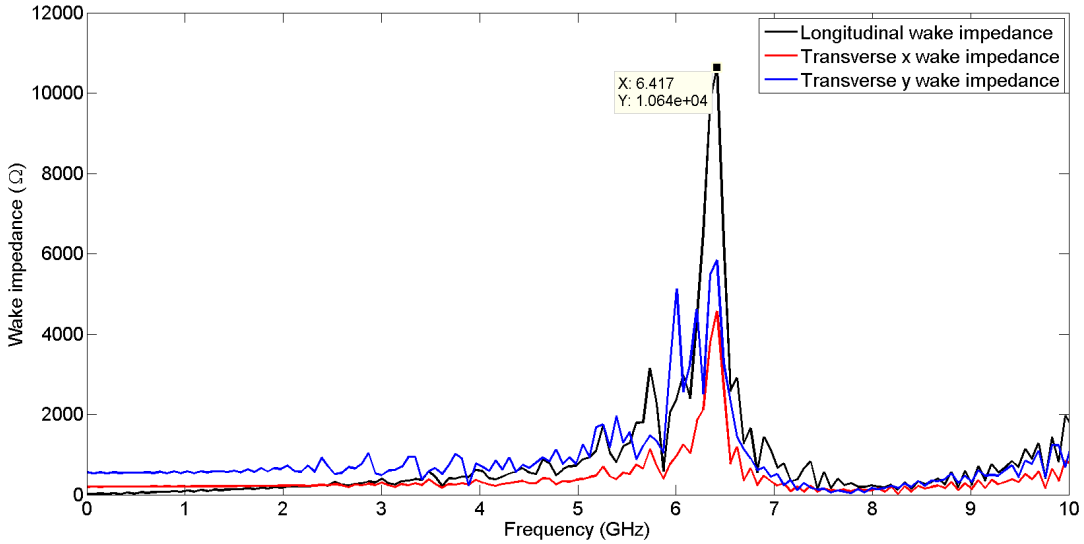

Figure 4.20: The wake impedance of waveguide A in the region of the TM-like mode showing an excitation of 10.6 kΩ at 6.42 GHz.

4.4.3 Waveguide B: Increased Ring separation

Figure 4.21 shows the transverse and longitudinal wake impedances for waveguide B, in this structure the TM_{31}-like mode occurs at 5.80 GHz. In Figure 4.21 two strong excitations of the longitudinal wake impedance are observed around this frequency, the first has a strength of 10.8 kΩ at 6.28 GHz and corresponds to the TM_{31} like mode and the second with a magnitude of 12.2 kΩ at 6.49 GHz corresponding to a higher order mode not found in electromagnetic simulations. This response is stronger than that of the nominal structure, making this waveguide a good candidate as the final structure although the significant drawbacks associated with thin sheets remain.

Figure 4.21 shows the transverse wake excitation of waveguide B, these excitation corresponds with the longitudinal excitations at 6.28 GHz, with a strength of 7 kΩ for y and a very small response for x. At 6.49 GHz transverse wakes are also observed with a strength of 4.9 kΩ and 6.5 kΩ for x and y respectively. These transverse wake excitations are very strong in comparison to those found in alternative set-ups and could cause disruption to the beam.

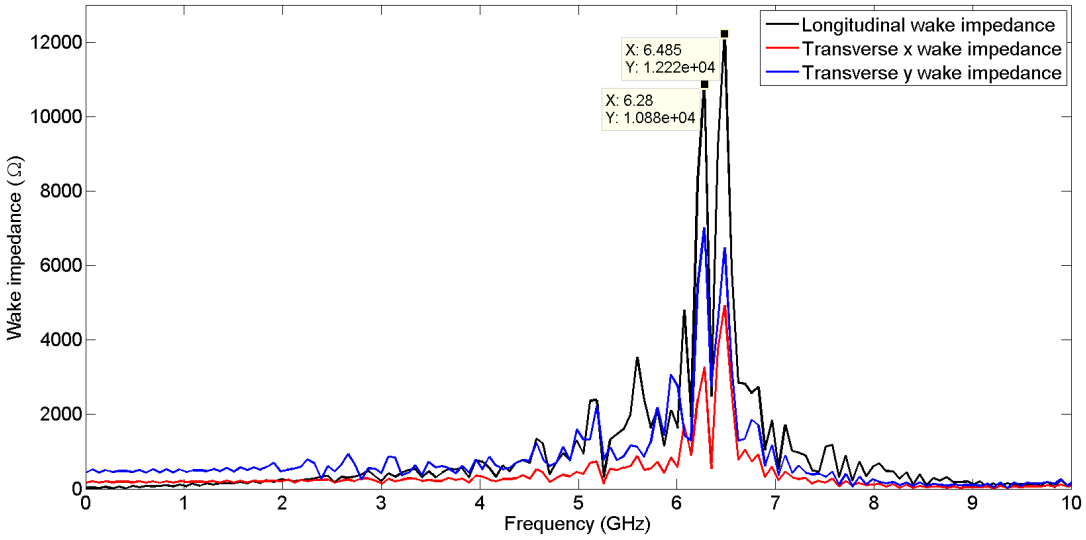

Figure 4.21: The wake impedance of Waveguide B in the region of the TM-like mode showing two longitudinal excitations of 10.8 kΩ at 6.28 GHz and of 12.2 kΩ at 6.49 GHz.

4.4.4 Waveguide C: Increased thickness and increased ring separation

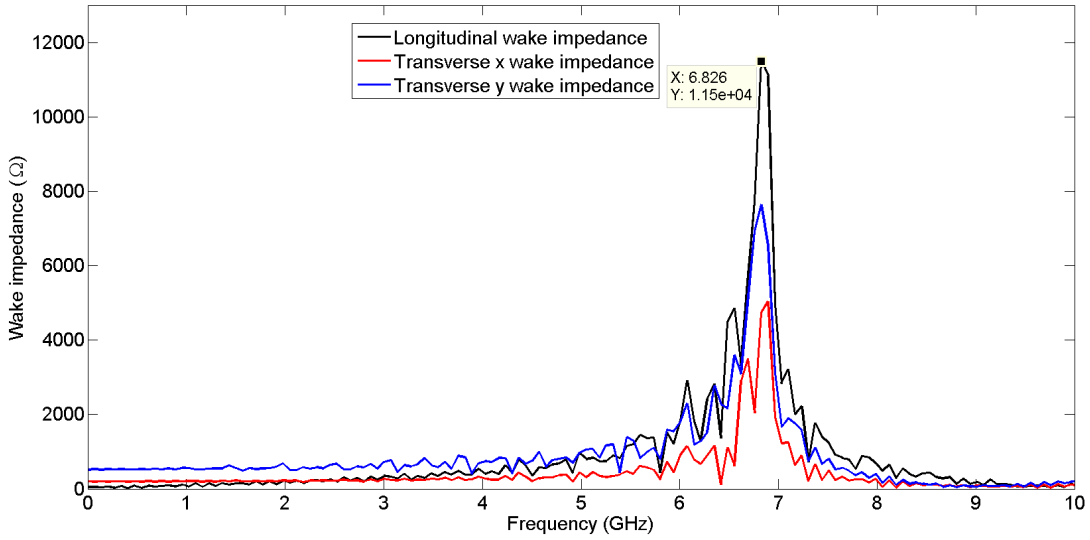

Figure 4.22: The wake impedance of waveguide C in the region of the TM-like mode showing a longitudinal excitation of 11.5 kΩ at 6.83 GHz.

Finally, the transverse and longitudinal wake impedance results of waveguide C are shown in Figure 4.22, for this structure two TM-like modes were found in the electromagnetic simulations at 5.97 GHz and 6.73 GHz. An excitation of the longitudinal wake impedance occurs at 6.83 GHz with a response of 11.5 kΩ this is a strong wakefield response and were it not for the weak beam coupling parameters this would be considered a strong candidate for design. Figure 4.22

shows the transverse wake excitations for waveguide C, these excitations occur at the same frequency as the longitudinal excitations with a strength of 5 kΩ and 7.7 kΩ for x and y directions respectively. These wakes are very strong especially the excitation in y of 7.7 kΩ which could cause significant disruption to the beam.

4.4.5 Summary of results from wakefield simulations

The results from the wakefield simulations are summarized in Table 4.3 and Figure 4.23. The strongest excitation of the longitudinal wake impedance for the modified set-ups corresponds to the second excitation peak found in waveguide B (the blue line) at 6.49 GHz with a strength of 12.2 kΩ, significantly stronger than the response of the other structure. However, this mode corresponds to a higher order mode which is complex to couple to. Comparing the excitations believed to correspond to the TM_{31} mode, it is clear that waveguide A (red line) and waveguide B perform similarly, and waveguide C provides the strongest response of 11.5 kΩ at 6.83 GHz. For waveguide A the excitation corresponding to the TM_{31}-like mode occurs at 6.42 GHz with a strength of 10.6 kΩ and for waveguide B this excitation is at 6.28 GHz with a strength of 10.8 kΩ, slightly stronger than waveguide A.

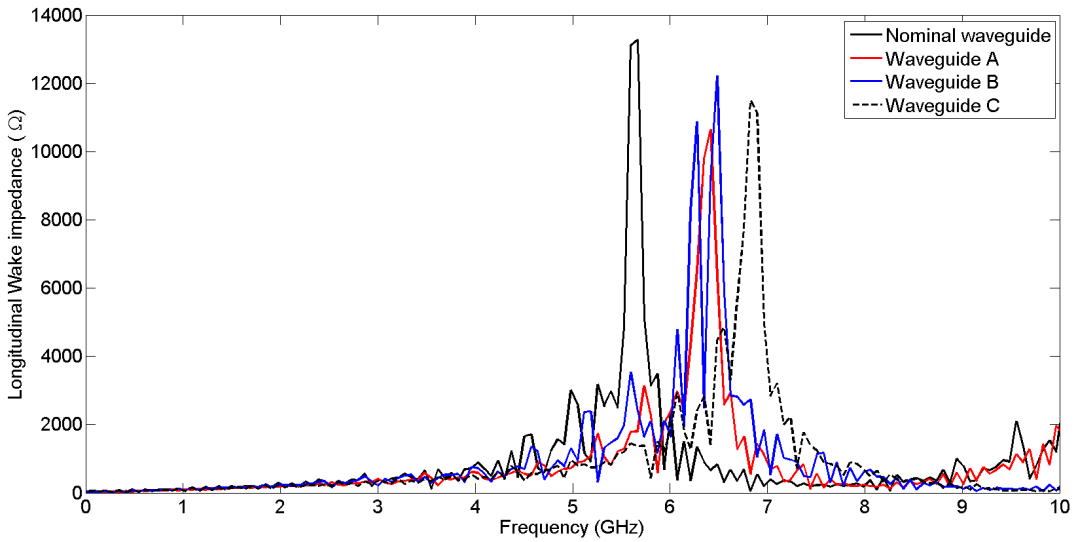

Figure 4.23: Comparison of the longitudinal wake impedance for the nominal structure and waveguides A-C.

Transverse wake excitations for all set-ups investigated are lower than the longitudinal wake excitation, however for waveguide B and C these are over half strength and may begin to disrupt the path of the beam which will significantly reduce performance. These high transverse peaks for waveguide B are another indication

that despite strong performance, this may not be the best option for the final set-up. Once again waveguide A provides a good compromise between fabrication suitability and performance, despite having the weakest longitudinal wake excitation. The reduced transverse wakes increase the suitability of this structure, make the behaviour of this structure most like the behaviour of the nominal structure.

Table 4.3: A summary of the longitudinal and transverse wake excitations for all set-ups.

	Longitudinal wakes		Transverse wakes x		Transverse wakes y	
	Freq (GHz)	Impedance (kΩ)	Freq (GHz)	Impedance (kΩ)	Freq (GHz)	Impedance (kΩ)
Nominal structure	5.67	13.3	5.67	5.3	5.67	5.7
Waveguide A	6.42	10.6	6.42	4.6	6.42	5.8
Waveguide B	6.28	10.8	-	-	6.28	7
	6.49	12.2	6.49	4.9	6.49	6.5
Waveguide C	6.83	11.5	6.83	5	6.83	7.7

4.5 Conclusions

In this Chapter, the geometrical features of a CSRR loaded waveguide have been investigated to address typical issues of MTMs for accelerators applications, such as robustness of the structure to high power environments and reduction in the number of hybrid modes in the frequency range of interest. In order to meet these criteria, increased thickness of the metasurface, increased ring separation and the addition of curvature have been thoroughly considered to identify the best compromise with performance of the design.

In terms of beam coupling parameters waveguide B, where ring separation was increased, performs best. Waveguide A with increased sheet thickness, $t = 1$ mm, and the original ring separation, $i = 4.6$ mm, is a suitable alternative but does not perform as well in terms beam coupling parameters. Both waveguide A and B perform similarly in wakefield simulations with the longitudinal excitation corresponding to the TM_{31} mode being very close in magnitude. With waveguide B performing slightly better than waveguide A, it appears to be the best choice for the final design, however fabrication challenges and the surface current issues associated with the thin sheet thickness still remain. The increase in thickness to 1 mm reduces peak surface current, while significantly increasing the fabrication suitability and robustness of the structure. Therefore considering that there is only a small drop in performance for waveguide A in terms of wakefield response,

it proves a good choice for the final design. Combining waveguides A and B to form waveguide C creates the structure with the highest fabrication suitability, however there is a very significant drop in performance in terms of beam coupling parameter for the desired TM-like mode.

In conclusion, there is a trade-off between strong beam-wave interaction and structural stability, which needs further analysis. Having reviewed the design considerations discussed within this Chapter it is possible to conclude that though Waveguide B performs best, the thinness of the metasurface limits applications to low power to avoid destruction of the structure. For high power applications and beam-based applications waveguide A can be considered the best design compromise, with a significant increase in fabrication suitability and reduction of susceptibility to resistive heating at minimal expense of performance in terms of both wakefield response and beam coupling.

Chapter 5

Particle in Cell Simulations of the CSRR loaded waveguide

In this Chapter the particle in cell simulations (PIC) of the loaded waveguide structure as performed using the CST particle studio PIC code are discussed to identify a beam suitable for wave-beam interactions. In Chapter 4, a final design of the loaded waveguide structure was presented, with a robust metasurface resistant to damage in a high power environment. Now consideration must be made on how the structure will interact with a realistic electron beam. The final structure designed in Chapter 4 is studied by means of Particle In Cell (PIC) simulations, where spectral analysis of the generated fields is used to identify strong interactions between the beam and the fields within the structure. The mode excited in the structure is identified via field monitors at the frequency of excitation, and the development of the field is observed as the beam propagates. The PIC simulations are performed for three realistic beams, the Versatile Electron Linear Accelerator (VELA) beam at Daresbury, the Facility for advanced Accelerator Experimental Tests (FACET) beam and a commercial low energy electron gun. These beams range in energy from 100 keV to 20 GeV and large (2 mm) and small (30 μm) spot sizes are considered for comparison. In addition to an analysis of the VELA beam simulated in the proposed waveguide, a discussion of how the simulated beam parameters will change with the CLARA upgrade is provided. Finally a brief description of the initial coupler designed for the proposed waveguide is presented, and the challenges of coupling to the TM_{31} mode are discussed.

5.1 Motivation for beam tests

In Chapter 4 a final design for the loaded waveguide structure was presented, this used metasurfaces with an increased sheet thickness of 1 mm to improve the fabrication suitability of the structure and make it more resistant to high power operation, this structure can be seen in Figure 5.1. The increased sheet thickness had the additional benefit of reducing the number of hybrid modes within the structure allowing for easier coupling to the desired TM-like mode [101]. With a robust final design simulated in terms of electromagnetic results and wakefield response, the next step is to perform Particle In Cell (PIC) simulations. These PIC simulations will be performed using the particle in cell solver of CST particle studio [98].

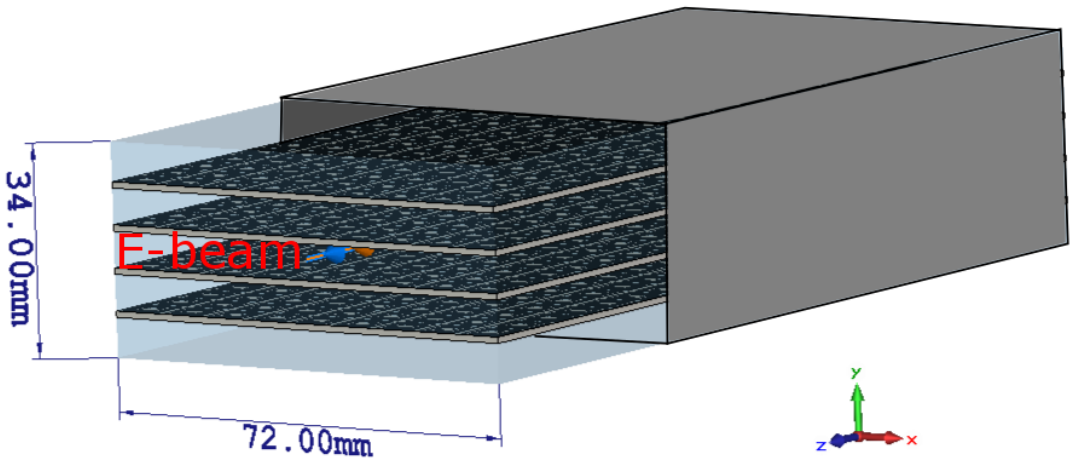

Figure 5.1: The loaded waveguide structure, showing the dimensions and the final metasurface design chosen in Chapter 4.

The structure is designed to generate backward propagating Cherenkov radiation, which has numerous applications including non-destructive beam position monitors, particle detection and coherent sources. The most common application is that of a Cherenkov detector, these use the emitted radiation created when a particle travels faster than the speed of light in that medium, to determine the type of particle that is propagating. These detectors are not only used for identifying particle in high energy physics experiments but also to determine particle types in astro-Particle physics. For beam line applications a differential Cherenkov detector is most suitable, and by using a negative index material as the radiator the resultant Cherenkov radiation can be detected behind the particle and therefore will not disrupt the beam, making this a good option for non destructive particle

detection. For backward Cherenkov to occur an electron beam must be travelling faster than light within the structure and couple to a left handed TM mode, which will result in backward propagation of the emitted radiation.

To investigate coupling between the beam and the structure the results of field probes throughout the structure were analysed and the frequency of excitations in the longitudinal field due to the propagating beam obtained. Three dimensional field monitors are then set up at the frequency of the excitation to identify the mode polarization of the field of the mode interacting with the beam. It is expected that these peaks of excited fields correspond to the TM-like mode found in the electromagnetic analysis of Chapter 4, and indicate strong beam coupling with the left handed mode which will result in backward propagating Cherenkov radiation.

In this Chapter three realistic electron beams are considered, the VELA beam, the FACET beam and the beam of a Kimball electron gun. This investigation is designed to not only give an overview of how a metamaterial structure behaves in an accelerator environment but to provide a precursor to tests performed when the structure is realised. Thus the beams used in these simulations need to be as close to the existing beams as possible.

The final aim of the structure is to perform beam test on site with the VELA/CLARA beam at Daresbury, as VELA is a facility designed for the testing of advanced accelerator components and applications. Throughout 2016 VELA is being upgraded to CLARA and this will affect the beam parameters on VELA, thus the parameters used within this chapter will change with the upgrade. A discussion is provided on the effects of the CLARA upgrade on the VELA beam, and whether operation on CLARA after completion may be an option. The electron beam at FACET is also discussed to provide a comparison to a high intensity beam, this facility has been used for a number of novel accelerator designs and applications. The commercial Kimball beam provides a means of analysing how the structure would interact with a low energy beam, while keeping the input power low, in real world beam tests this would allow for the investigation of particle beam interaction without risking structural damage.

5.2 Analysis structural length effects

In computationally heavy simulations such as wakefield simulations and particle in cell simulations, the structural length plays a key part in determining the complexity of the calculations, and consequently the run time. For these wakefield simulations, a distributed computing system was used to increase the speed of calculations, this system used two servers, both with 8 ports, one with 2x4 cores at 3.5 GHz with a 1 Tesla C2075 GPU, 511.9 GB of memory and 1.6 TB of disk space, the other with 2x8 cores at 2.6 GHz with 2 Tesla K40m GPUs, 256 GB of memory and 4471 GB disk space. When running the wakefield simulations the calculations were distributed over 4 ports and run with the GPU acceleration, this increased the speed of the calculations. However, depending on the complexity of the calculation, the simulations still took between one and five days to run. A longer structure means more mesh cells and therefore more calculations, increasing simulation run time and placing strains on the system used. Therefore methods to reduce the complexity of the calculations while maintaining the accuracy needed to be implemented.

There are a number of ways to reduce calculation complexity; the simulation run time can be reduced by considering fewer wakelengths when performing the calculations, however this significantly reduces the accuracy of the simulation. A better alternative which preserves validity of results, is to use a shorter structure with a fine mesh. In this Section, the relationship between structural length and wakefield response is analysed to determine if a shorter structure can be used while still giving accurate insight into how a longer structure would behave. The results of this analysis will then be used to determine the minimum length of the structure required to provide accurate results without overly complex computationally taxing calculations for subsequent particle in cell simulations. These results can then be scaled up to relate the results from the minimum length structure to a structure with the length needed for the applications.

Wakefield simulations were run using the wakefield solver of CST particle studio [98] increasing the length of the structure by 10 resonators (80 mm) with each run, data is collected for lengths of 10 to 90 resonators which corresponds to 80 to 720 mm. The final structure may well be larger than this however going beyond 90 resonators gives a run time of over 48 hours and can fail to run on the system. For simulations of a structure over 90 resonators, the simulations would have to be run on an external system, and an arrangement has been made with CST to run the larger structures on the MPI system at their European office.

Table 5.1: The increase of longitudinal wake impedance with increasing waveguide length, given both in the number of unit cells and in mm.

Number of Unit cells in z	longitudinal length (mm)	Frequency (GHz)	Wake Impedance (kΩ)
10	80	6.417	4.95
20	160	6.417	15.16
30	240	6.417	25.13
40	320	6.417	39.21
50	400	6.417	46.72
60	480	6.417	57.24
70	560	6.417	68.22
80	640	6.417	78.11
90	720	6.417	89.16

The wakefield simulations were set up in CST [98] as follows; a hexahedral mesh of 15 cells per wavelength was used and the simulations ran for 5000 wakelengths to ensure a high level of accuracy. The structure is then excited by an electron beam, the beam is Gaussian with a standard deviation of the bunch length of σ=1.5 mm, a charge of 1 nC and a 0.5 mm offset in x and y for the transverse wakes. The results from each run can be found in Table 5.1, and show that for all lengths the strongest excitation occurs at the same frequency of 6.417 GHz. It can also be seen that the longitudinal wake impedance increases with the length of the structure.

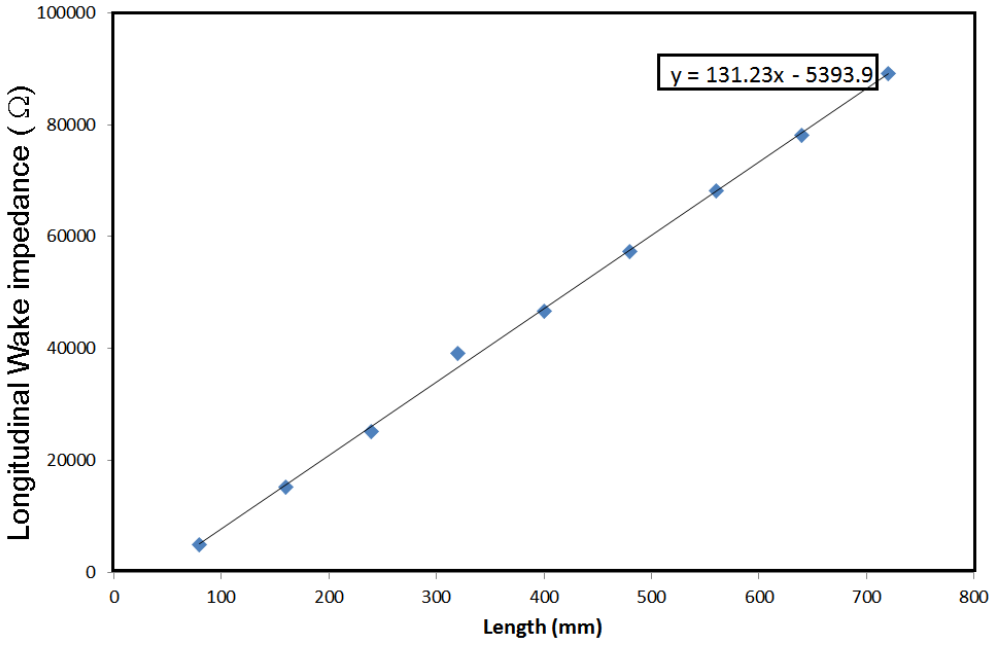

Figure 5.2: The relationship between longitudinal wake impedance and structural length, including the equation for the linear relationship.

Figure 5.2 relates the length of the structure to the longitudinal wake impedance obtained via the simulations, which indicates the strength of the coupling between the beam and the fields within the structure. From this plot it can be seen that a linear approximation can be used to describe the relationship between the structural length and the strength of the excitation. The gradient of this linear approximation is 131 kΩ/m, indicating the increase in response per unit length. The fit to the data is given by;

$$z = 131 \times 10^3 l - 5.39, \tag{5.1}$$

where z is the impedance in Ohms and l is the length in meters. There is a linear approximation that can be used to scale the results of simulations of a short structure to those of a longer structure to reduce the strain put on the computer systems. For further wakefield simulations and particle in cell simulations a structure with a length of 40 resonators is used to keep calculation complexity down while maintaining a good degree of accuracy and knowing that the results can be related to those of a longer structure via the linear approximation given in (5.1).

5.3 Results of Particle in Cell simulations

Through the particle in cell (PIC) simulations in this Section the aim is to obtain a comprehensive view of how the loaded waveguide structure and an electron beam interact. The spectral peaks of the field components generated by the beam will be compared to the frequency at which the structure is known to behave as a left handed medium. For these simulations, a transverse segment of final design of the 4 layer loaded waveguide as described in Chapter 4, was used, this segment is 40 resonators (320 mm) long, this length is sufficient to observe relevant excitation strength without excessive increase of the computational burden. All simulations were performed using a hexahedral mesh of 15 cells per wavelength in CST particle studio, which has shown convergence of the results and thus ensures numerical accuracy. The simulation time for each set-up is taken to be 25 ns.

A single bunch is simulated for both high and low energy beams, with large (2 mm) and small (30 μm) spot sizes, to determine and compare the proposed structure performance for different beams characteristics. Electric field probes are set up along the length of the structure for all simulations to analyse how the field develops down the structure. These probes are at positions of 80 mm, 160 mm and 240 mm down the length of the structure in z, corresponding to 10, 20 and 30 res-

onators down the longitudinal length of the structure. These probes measure the longitudinal field within the structure when a beam is present, a strong excitation of the longitudinal electric field indicates coupling between the structure and the beam at this frequency. Once excitation frequencies have been identified via the electric field probes, three dimensional field monitors are set at the frequency of the excitation to analyse the field polarization that excites a response. If the structure behaves as expected then the strong excitations will correspond to the transverse magnetic modes identified in the electromagnetic simulations of Chapters 3 and 4. In particular the TM_{31}-like mode found at 5.86 GHz which was identified as left handed and suitable for accelerator applications. These simulations will highlight any modifications needed for operation in conjunction with low energy and high energy beams and will inform the beam tests planned on this structure at the novel and compact accelerator development facility at Daresbury Laboratories.

5.3.1 VELA Beam excitation

The Versatile Electron Linear Accelerator (VELA) [102] is based on site at Daresbury laboratory and is run by ASTeC and the STFC, a schematic of the layout of VELA can be seen in Figure 5.3 and a lay out of the diagnostics can be seen in Figure 5.4. VELA [103] is designed to aid in the development and testing of novel and compact accelerator technology [104] and thus is an ideal beam for the testing of the novel metamaterial loaded waveguide proposed within this thesis. VELA aims to revolutionise the application of accelerators in healthcare, security screening, energy generation and industrial processing, whilst addressing underlying challenges in RF acceleration, beam diagnostics, magnet systems, optics, vacuum systems, and controls processes. VELA will also enable the development of a facility to explore the fundamental delivery capabilities of the next generation light sources as part of the Compact Linear Accelerator for Research and Applications (CLARA) programme [105].

VELA offers beams with energies of 4.5-5 MeV, with bunch length from 80 ps to 3 ps, with minimal energy spread of 0.1-5%, the beam parameters used in the simulation are given in Table 5.2 [108], and represent the current operation of VELA. The advantages of testing the structure on VELA are numerous, primarily VELA is a dedicated facility for testing novel accelerator technology. There is a dedicated test area with a vacuum sealed test box into which the structure could be loaded, thus the metamaterial loaded waveguide does not need to be made vacuum tight for preliminary tests. Secondly, the beam energy on VELA is sufficient enough to

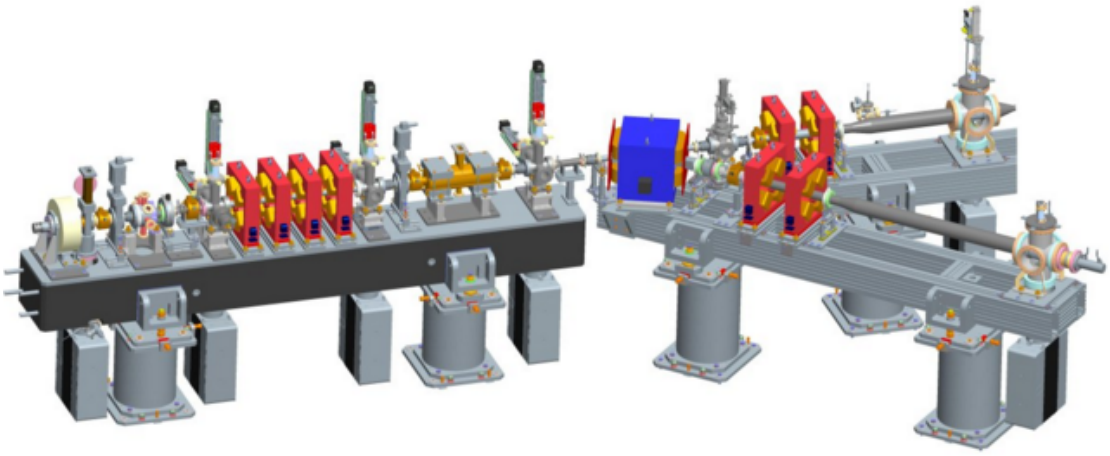

Figure 5.3: An overview of the VELA lay out, starting from just after the electron gun up to the diagnostics and showing the two user beam lines. [106] [107]

excite the left handed modes within the structure and generate backward propagating Cherenkov whilst being sufficiently low in energy so as to not damage the metasurfaces.

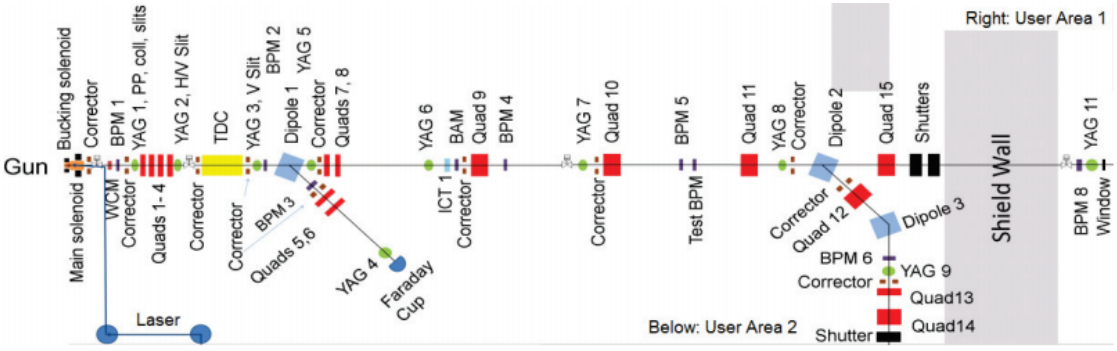

Figure 5.4: A general layout of the VELA beam line [109]

Table 5.2: The VELA beam parameters used to define the Gaussian beam in the PIC simulations. [108]

Beam Parameter	Value (Unit)
Beam radius (σ_{xy})	1.5 mm
Beam energy	4.5MeV
Energy spread	2%
Charge	250 nC
Sigma (σ_z)	2.5 ps
Cut off	5 ps

Simulation results

To analyse the amount of coupling between the beam and the structure, the excitation of the longitudinal electric field is considered. Strong excitations in the field indicate strong beam coupling between electron beam and the structure. Figure 5.5 shows the longitudinal excitations of the field at each probe down the length of the structure. For the VELA beam, the key excitations occur at the same frequency at each probe, the first excitation peak is strongest for the central probe and the second excitation peak is strongest for the first probe.

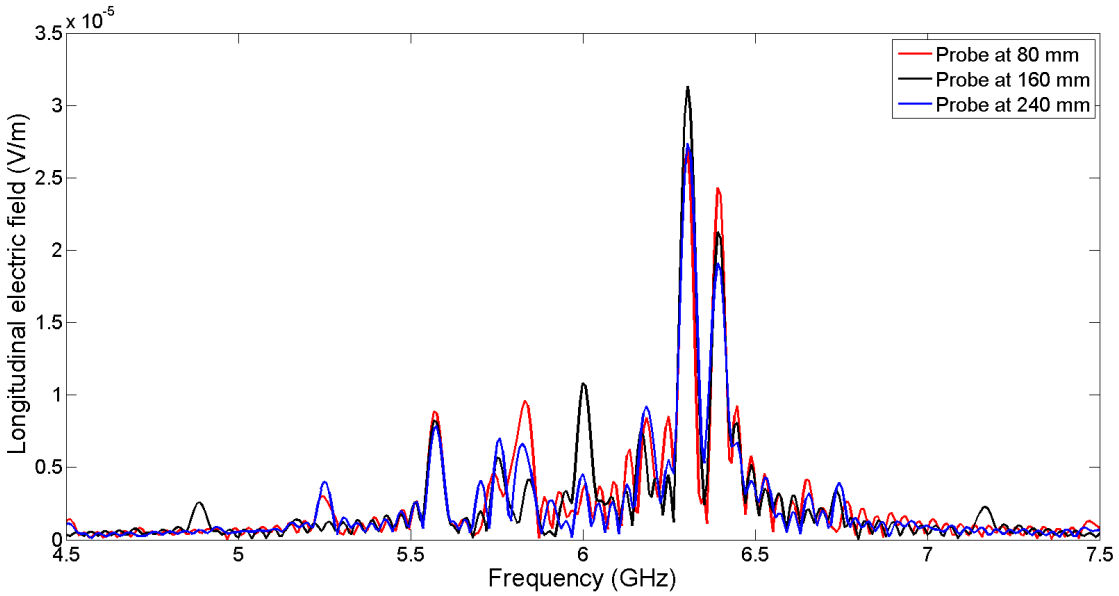

Figure 5.5: The longitudinal electric field generated by the VELA beam for the probes placed at 80, 160 and 240 mm down the structure, showing how the coupling changes as the beam moves down the structure.

Figure 5.6, shows the longitudinal field at the central probe, there are two clear strong excitations, the first at 6.304 GHz with a strength of 31 μV/m and the second at 6.392 GHz with a strength of 21.27 μV/m. These excitations occur at the same frequency for all probes within the structure. The excitation correspond to interaction with the field within the structure at that frequency and the field can be found from the three dimensional field monitors in place.

Figure 5.7 shows the longitudinal field component in a transverse section of the waveguide corresponding to the strong first excitation of the longitudinal field at 6.304 GHz as seen in Figure 5.6. The longitudinal field shown here has a clear TM_{31} structure, thus the beam couples to the left handed mode found within the electromagnetic analysis of the structure. Through the electromagnetic analysis performed in Chapter 4, this mode was found to occur at 5.86 GHz, thus there has

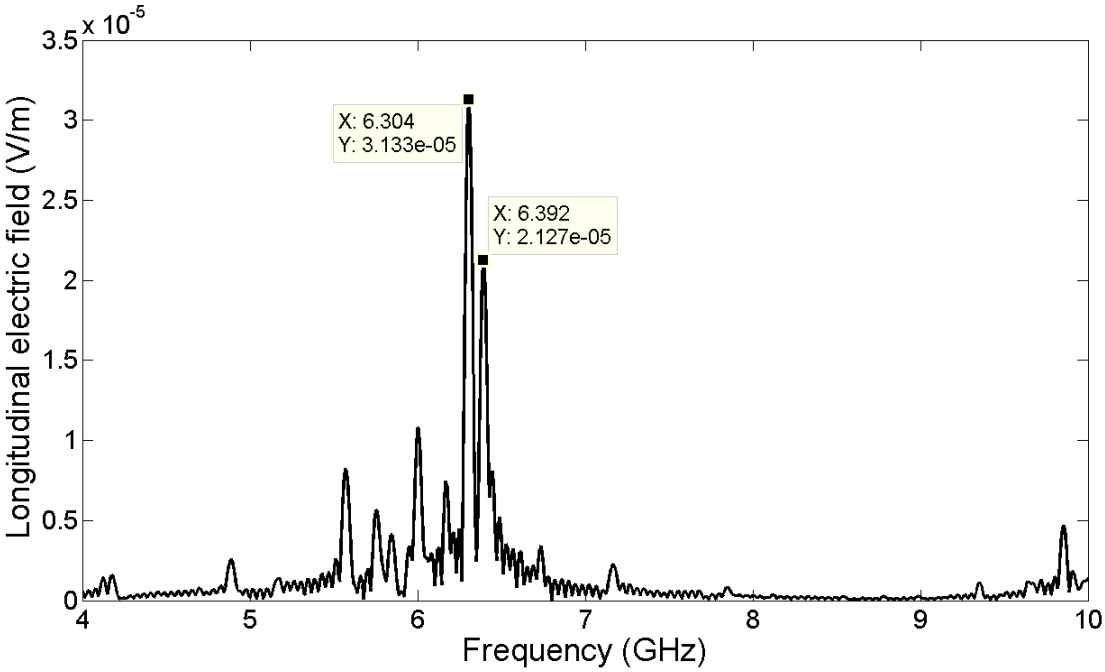

Figure 5.6: The longitudinal electric field at the probe in the centre of the waveguide for the VELA beam.

been a slight increase in frequency with the introduction of the beam. The change from tetrahedral mesh to hexahedral mesh is one of the factors that contributes to the frequency change. The strong clear filed profile and strong excitation in the longitudinal field show that the VELA beam will couple strongly to the desired mode and therefore this beam proves a good option for beam tests of the structure.

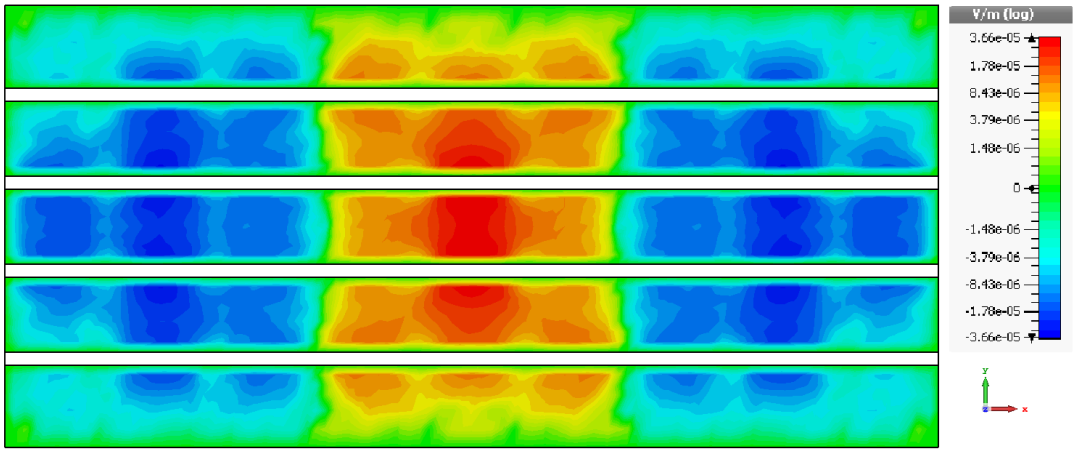

Figure 5.7: The longitudinal field profile in a transverse section of the waveguide corresponding to the excitation peak at 6.304 GHz when the structure is excited by the VELA beam. This mode has the form of a TM_{31}-like mode.

Figure 5.8, shows the longitudinal electromagnetic field profile for a transverse

section of the structure, this corresponds to the weaker excitation peak in the longitudinal electric field at 6.392 GHz. It can be seen that this excitation corresponds to a higher order longitudinal mode similar to the TM_{51} mode, which occurred at a much higher frequency for this structure in the electromagnetic analysis. Though this mode is a transverse magnetic mode, with strong longitudinal components in the region of the beam, it is not desirable to use this mode and thus there may be a need to find methods of damping higher order modes for certain applications within an accelerator.

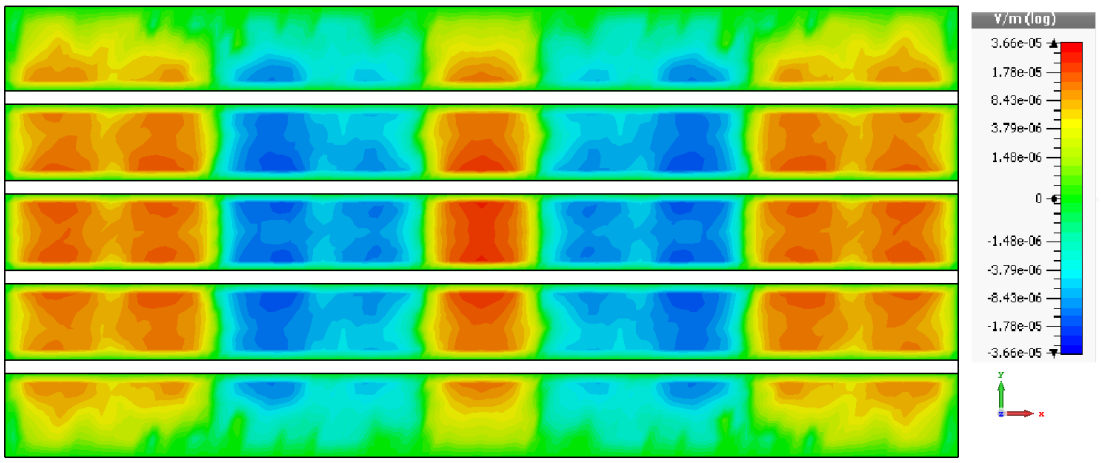

Figure 5.8: The longitudinal field profile in a transverse section of the waveguide corresponding to the excitation peak at 6.392 GHz when the structure is excited by the VELA beam. This mode has the form of a TM_{51} mode.

5.3.2 FACET Beam excitation

The Facility for advanced Accelerator Experimental Tests (FACET) [110] is based at the Stanford Linear Accelerator Center (SLAC) and is the only facility in world with the high intensity drive bunches necessary for high-gradient plasma and dielectric wakefield acceleration [111]. The FACET electron beam is high energy, up to 20 GeV and high density with a small spot size in the μm scales. The bunch length is given in terms of mm in the literature [112], and CST allows for parameters to be input as either a distance or a time, thus this can be used without conversion. Though research at FACET encompasses dielectric based wakefield acceleration, the focus is on plasma wakefield acceleration as the facility uses part of SLACs two-mile-long linear accelerator to provide the high peak current, high-energy electron and positron beams required for this type of acceleration. FACET aims to use electron and position beams to generate plasma wakefield acceleration, whereas AWAKE [16] the European collaboration based at CERN, is a proton

driven plasma wakefield accelerator.

Table 5.3: The FACET beam parameters used to define the Gaussian beam in the PIC simulations. [112]

Beam Parameter	Value and unit
Beam radius (σ_{xy})	30 μm
Beam energy	20 GeV
Energy spread	0.5%
Charge	1.6 nC
Sigma (σ_z)	0.125 mm
Cut off	0.25 mm

Though the metamaterial loaded waveguide structure discussed will not be tested at FACET, the beam provides an interesting insight into how the structure would operate on a beam line designed specifically for compact novel accelerator research. This can provide a comparison between a dielectric wakefield accelerator and the metamaterial structure. The beam parameters used within the simulations of this beam are given in Table 5.3. It should be noted that this beam is more suited to a smaller scale structure as the beam radius is significantly smaller than the spacing between the metasurface sheets. Since the field within the CSRR metamaterial structure are strongest closest to the sheet, there may not be a strong a field generation in this structure despite the high intensity of the beam.

Simulation Results

Figure 5.9 shows the longitudinal field excitation at the probes placed down the length of the loaded waveguide structure when excited by the beam at FACET. In this case the results from each probe are very similar, with the primary and secondary excitations occurring at the same frequency for all probes and exhibiting similar magnitude regardless of probe location. It is clear from the vertical axis in Figure 5.9 that all peaks are an order of magnitude higher than those found on VELA.

Looking specifically at the results of the central field probe, which are shown in Figure 5.10, it can be seen that the primary excitation at 6.312 GHz is the strongest with a magnitude of 234.2 μV/m and the secondary excitation at 6.4GHz has a

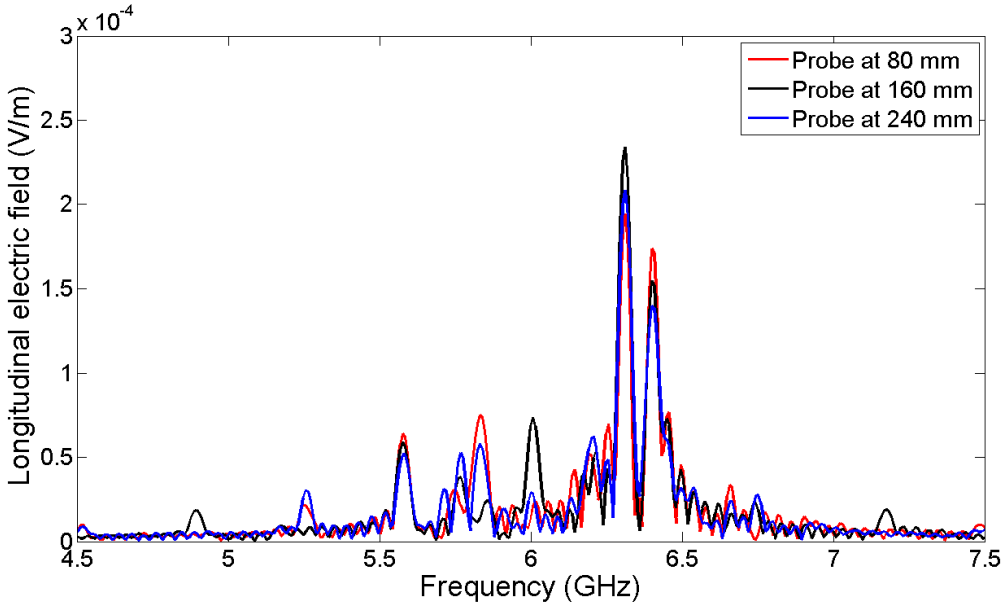

Figure 5.9: The longitudinal electric field for the probes placed at 80, 160 and 240 mm down the structure, showing how the coupling changes as the FACET beam propagates through the structure.

weaker magnitude of 154.8 μV/m. These excitations indicate strong coupling between the beam and the field within the structure at this frequency. These should correspond to transverse magnetic modes with a strong longitudinal field component in the region of the beam.

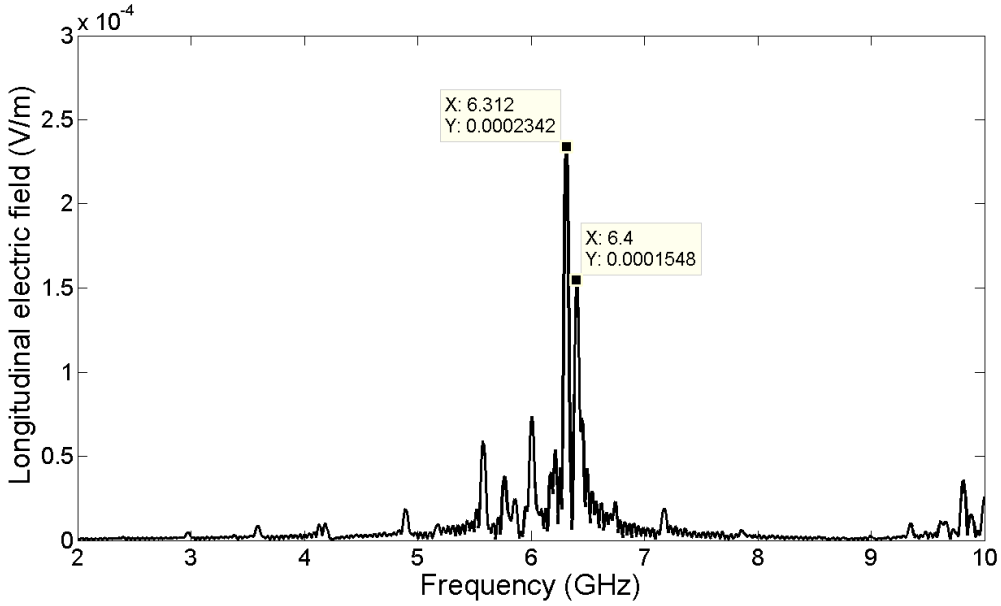

Figure 5.10: The longitudinal electric field at the probe in the centre of the waveguide for the FACET beam.

Figure 5.11 shows the longitudinal field profile of the primary excitation at 6.312 GHz

for a transverse section of the waveguide. This can be seen to correspond to a hybrid version of the TM_{31}-like mode found in electromagnetic simulations, with strong longitudinal field components in the region of the beam. This mode polarization is less defined than that of VELA, due to the small beam radius of the FACET beam which results in a larger spacing between the beam and the metasurface sheets. For the VELA beam the spacing between the metasurface and the beam was 1.405 mm, whereas for the FACET beam this is 2.89 mm, an increase in spacing by over a half. In a structure based on metasurface sheets, the field will be concentrated in the area closest to the sheet, so though the high intensity of the beam results in strong excitations of the electric field, the resultant mode profile is less well defined.

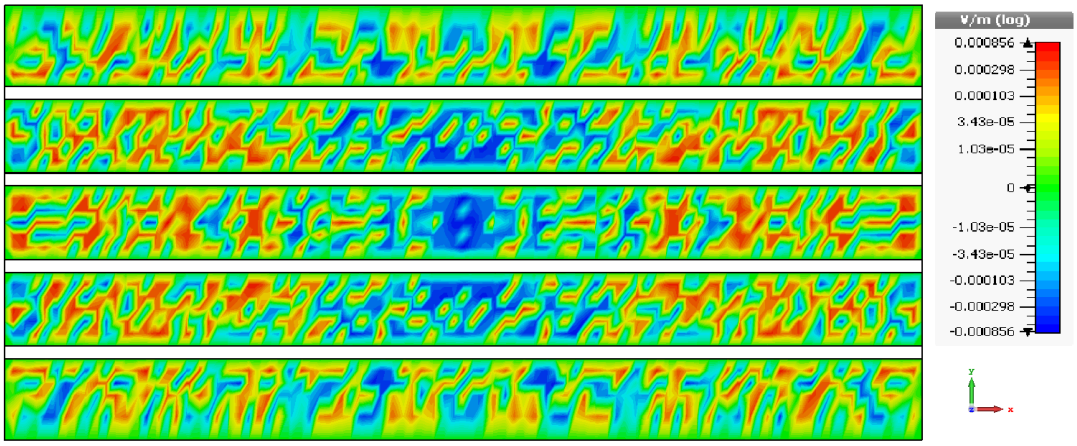

Figure 5.11: The longitudinal electric field generated by the FACET beam in a transverse segment of the waveguide corresponding to the peak at 6.312 GHz.

Figure 5.12 shows the longitudinal field profile corresponding to the secondary excitation at 6.4 GHz for a transverse section of the waveguide. This weaker excitation corresponds to a hybrid form of a higher order transverse magnetic mode, this mode is similar to the TM_{51} mode. As with the primary excitation, the mode polarization is less defined for the FACET beam than those generated by other beams due to the small spot size. Though the FACET beam generates very strong excitations of the longitudinal electric field when compared to the VELA beam, the small spot size and less defined mode profiles of the generated modes make this a less appealing option for beam tests, though an interesting case for comparison.

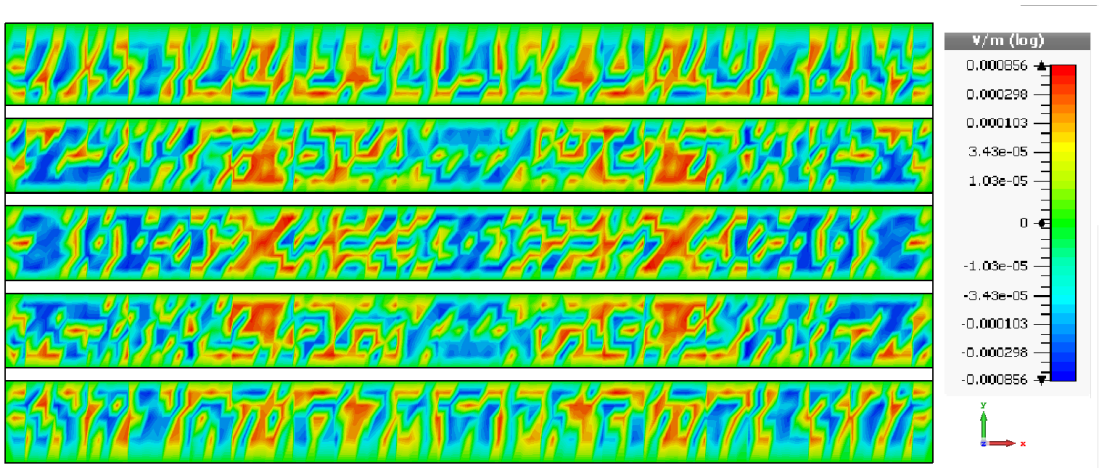

Figure 5.12: The longitudinal electric field generated by the FACET beam in a transverse segment of the waveguide corresponding to the peak at 6.4 GHz.

5.3.3 Kimball Beam excitation

The company, Kimball produces commercial electron guns with beams for a range of operations, with energy from 1 eV to 100 keV, beam current from 1 nA to 20 mA and spot sizes from 15 μm to over 500 mm [113]. The guns are designed for use in a wide variety of applications including; Ultra-High Vacuum (UHV) surface physics, space science, and surface processing. The beam can be focused to very small spot sizes for applications such as x-ray production, and welding. At the other end of the scale, the gun can be used to create flood beams, for use in charge neutralization, electron beam scrubbing, space simulation and radiation damage studies.

Table 5.4: The beam parameters used to define the Gaussian beam in the PIC simulations for the commercial Kimball gun. [113]

Beam Parameter	Value and unit
Beam radius (σ_{xy})	2 mm
Beam energy	100 keV
Energy spread	0.4%
Charge	10 nC
Sigma (σ_z)	1 mm
Cut off	2 mm

The beam from the electron gun with parameters as shown in Table 5.4 is referred to as the Kimball beam. The cut off and sigma are given in terms of length within

the literature and CST allows for parameters to be input as either a distance or a time, which means there is no need to convert the bunch length. The full specification of the beam are given in Table 5.4. For these PIC simulations the highest energy beam of 100 keV is used to provide comparison to alternative schemes, this is within the energy range of low energy beam test that could be performed at an other facilities in the UK. A beam radius of 2 mm is used for these simulations to improve the interaction between the beam and the structure and generate a suitable left handed mode.

Simulation Results

The excitation of the longitudinal electric field at each field probe down the structure is shown in Figure 5.13, it is clear that the primary and secondary excitations for this structure occur at the same frequency at each probe. However unlike the VELA and FACET beams simulated within this Chapter, there is a significant difference between the results obtain for the first probe 80 mm into the structure and the results from the second and third probes at 160 mm and 240 mm down the structure. The results from the first probe show a weak initial excitation at 6 GHz and then a strong second excitation at 6.232 GHz of 330 μV/m, significantly stronger than the excitations at the other probes. This peak is then followed by several diminishing higher frequency excitations that are not present for the other probes. Though the frequency of both excitations remains the same for each probe, the strength of the excitation at 6.232 GHz diminishes the further down the structure the probe is located, whereas the strength of the excitation at 6 GHz remains relatively constant for all probes.

Figure 5.14 shows the longitudinal field excitations for the probe located at the centre of the structure. Two clear excitations are present, the first at 6 GHz with a strength of 114.8 μV/m and the second at 6.232 GHz with a strength of 196.5 μV/m. This second excitation is significantly weaker than the response found at the first probe, this is expected as this beam has a significantly lower energy than the other beams studied and therefore begins to lose energy more notably as it travels down the structure. This is clear when the excitation at 6.323 GHz is considered, with the magnitude of the excitation dropping from 330 μV/m 80 mm down the structure to 149 μV/m 240 mm down the structure, decreasing by 54.85 % over a distance of 160 mm. To verify that the reduced response was not due to the low energy beam propagating slower and therefore not reaching the probe in the simulation time, the run time of the simulation was increased and no change in the response was observed.

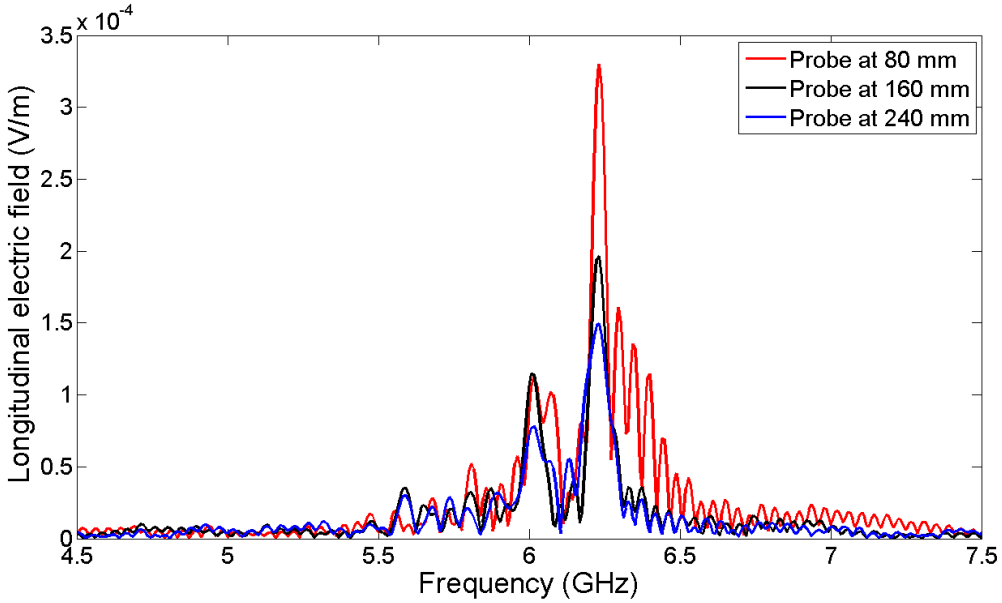

Figure 5.13: The longitudinal electric field for the probes placed 80, 160 and 240 mm down the structure, showing how the coupling changes as the kimball beam moves down the structure.

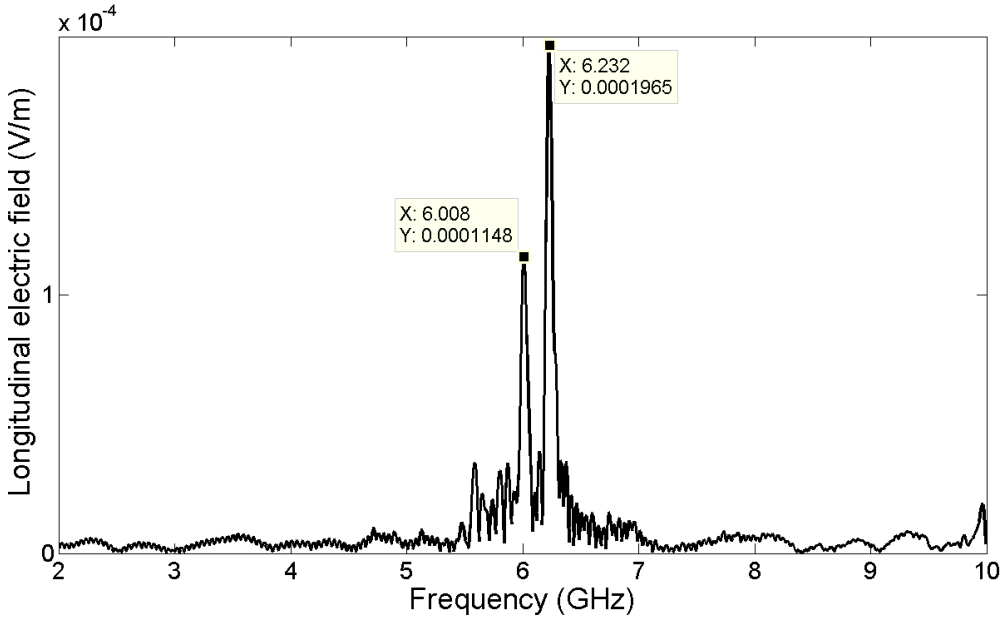

Figure 5.14: The longitudinal electric field at the probe in the centre of the waveguide for the Kimball beam.

Figure 5.15 shows the longitudinal field profile of the excitation at 6.02 GHz in a transverse slice of the waveguide. The field profile is clearly that of hybrid mode similar to TM_{33}, however since the higher frequency excitation corresponds to a TM_{11}-like mode, this cannot be considered to be a TM-like mode. Though this mode exhibits longitudinal field in the region of the beam, the profile is not well

defined leading to complex coupling and the strength of the excitation is significantly weaker than the second excitation this beam generates. Therefore this mode is unsuitable for wave-beam interaction applications.

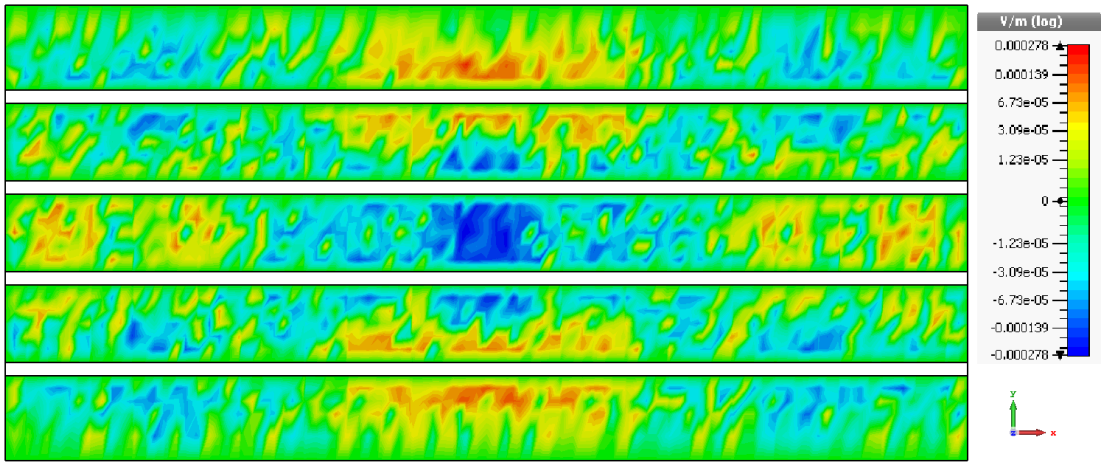

Figure 5.15: The longitudinal electric field corresponding to the excitation peak at 6.02 GHz when the structure is excited by the Kimball beam.

Figure 5.16 shows the longitudinal field profile corresponding to the strong excitation peak at 6.232 GHz in a transverse slice of the waveguide. Unlike the other beams simulated in this Chapter, the strongest excitation does not correspond to the TM_{31}-like mode but to the fundamental TM_{11} mode which is not supported by the structure, and was not found in any electromagnetic simulations. This mode is ideal for accelerator applications as it is considerably easier to couple this mode into the structure, however this mode was not found in the electromagnetic simulations in Chapters 3 and 4, therefore away from the gun coupling to this mode diminishes significantly. This effect is observed by the reduced peaks found at the field probe at 240 mm down the structure. This mode is not a propagating mode within the loaded waveguide structure and therefore is unsuitable for the wave-beam interaction applications that the loaded waveguide structure is designed for.

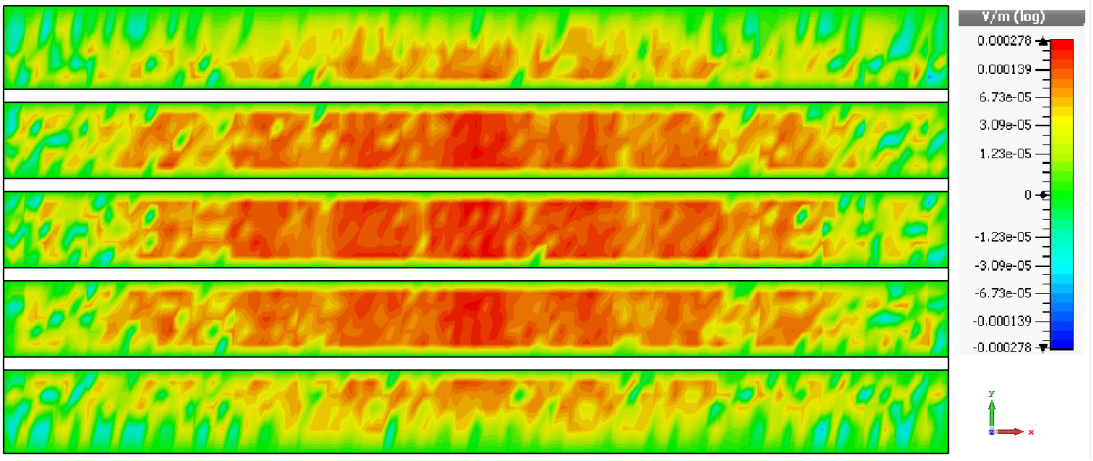

Figure 5.16: The longitudinal electric field corresponding to the excitation peak at 6.232 GHz when the structure is excited by the kimball beam.

5.4 Summary of PIC simulation results

Table 5.5 provides a summary of the results of the PIC simulations for each electron beam, the excitation frequencies and strength are taken from the results of the probe in the middle of the structure. From Table 5.5 it can be seen that the strongest response was generated by the FACET beam at 6.31 GHz with a magnitude of 234.2 μV/m, the Kimball beam was found to excite a stronger response at 6.232 GHz at the first probe 80 mm down the structure, however this has diminished below the response of the FACET beam by the second probe, 160 mm down the structure. Though the excitation as a result of the FACET beam is strong, the corresponding electric field exhibits a less defined TM_{31} profile than is desirable for the operation of this structure. This is due to the small spot size which implies a greater spacing between the beam and the metasurfaces on which the fields are generated. The beam would prove suitable for use with a scaled down version of the metamaterial loaded waveguide for high frequency applications, as this would reduce the metasurface beam spacing and hence improve the response.

Table 5.5: The frequency and magnitude of the primary and secondary excitations of the longitudinal electric field for each beam at the probe 160 mm down the structure.

			Primary excitation		*Secondary excitation*	
Beam	**Energy**	**Radius**	**Frequency**	**Strength**	**Frequency**	**Strength**
VELA	4.5 MeV	1.5 mm	6.304 GHz	31.33 μV/m	6.392 GHz	21.27 μV/m
FACET	20 GeV	30 μm	6.312 GHz	234.2 μV/m	6.4 GHz	154.8 μV/m
Kimball	100 KeV	2 mm	6.008 GHz	114.8 μV/m	6.232 GHz	196.5 μV/m

A well-defined form of the TM_{31} mode suitable for acceleration is found at 6.304 GHz when the structure is excited by the VELA beam as shown in Figure 5.7. This mode is clearly the mode found in the electromagnetic simulations of the structure, and will give rise to left handed behaviour within the structure. Though this mode is suitable for the accelerator based applications discussed, this excitation is an order of magnitude weaker than those observed for both the FACET and Kimball beams, implying weaker coupling.

The Kimball beam provides interesting results, with the secondary excitation as a result of this beam exhibiting a strong magnitude of 196.5 μV/m at 6.232 GHz, due to the reduced metasurface beam spacing of 0.905 mm. This mode corresponds to the fundamental transverse magnetic mode and thus would prove considerably simpler to couple to than the TM_{31} mode found for the strongest excitations of the other beams, which would simplify the coupler design. This mode, is not supported by the loaded waveguide, thus exciting the structure with this beam will result in inconsistent behaviour of the structure making the Kimball beam unsuitable for the designed applications.

5.5 The CLARA upgrade

CLARA is the Compact Linear Accelerator for Research and Applications, it is a dedicated flexible Free Electron Laser (FEL) test facility and installation began in 2015 at Daresbury. This facility is designed to test several of the most promising new FEL schemes, moving the UK closer to the goal of a UK X-ray Free Electron Laser (X-FEL). Figure 5.17 shows an overview of the proposed CLARA layout [114] and Figure 5.18 shows the layout of the CLARA front end [115] and how it will effect VELA. While current X-FEL schemes in the USA [116], Japan [117], Germany [118] and Switzerland [119] perform well there is significant potential for improvement. FEL experts have suggested numerous ways to improve the photon output in terms of temporal coherence, wavelength stability, increased power, intensity stability and ultra-short pulse generation. However the small number of available FEL facilities means that many of these improvements have not been developed and thus the role of CLARA is to provide research and development into the creation of high performance FEL, with a final goal of finding developments that allow for the creation of a UK X-FEL.

The main aim for CLARA is to produce ultra-short photon pulses of high-brightness coherent light, existing X-FELs are capable of generating pulses with a duration

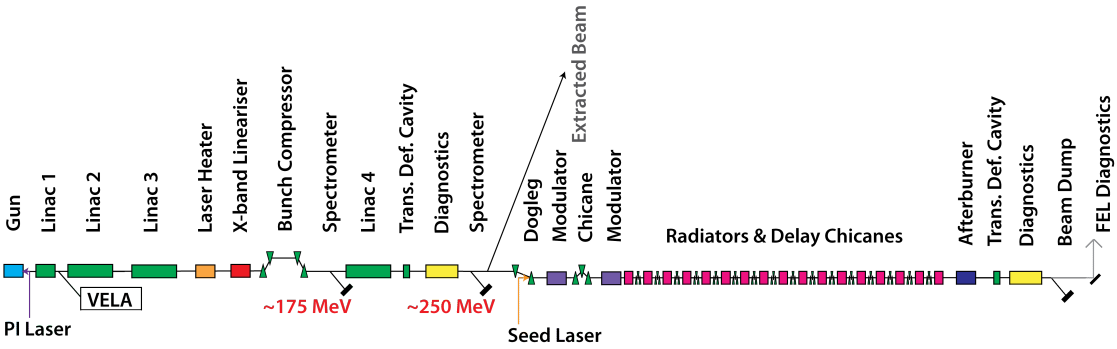

Figure 5.17: An overview of the CLARA lay out, from gun to output diagnostics. [114]

of tens of femtoseconds however several schemes have been proposed to produce schemes that generate pulses two to three orders of magnitude shorter than that. To achieve these ultra-short pulses, CLARA must utilise advanced techniques such as laser seeding, laser-electron bunch manipulation and femtosecond synchronisation. These techniques can only be implemented by developing a state of the art facility, which CLARA is design to be and therefore, CLARA has a direct impact on the wider FEL community and ensure that the UK is equipped with all the skills to develop its own facility in the future. The dynamic nature of FEL research means that not only should the facility be able to demonstrate and study the novel concepts of today but also be well equipped to prove future novel concepts. For this reason, there are a number of planned operating modes for CLARA as seen in Table 5.6, each designed for a different class of FEL experiment.

Table 5.6: A reproduction of the main parameters as presented in the CLARA conceptual design report [120].

	Operating modes			
Parameter	Seeding	SASE	Ultra-Short	Multibunch
Max Energy (MeV)	250	250	250	250
Macro pulse Rep Rate (Hz)	1100	1100	1100	1100
Bunches/macro pulse	1	1	1	16
Bunch Charge (pC)	250	250	20-100	25
Peak Current (A)	125400	400	∼1000	25
Bunch length (fs)	850250 (flat-top)	250 (rms)	<25 (rms)	300 (rms)
Norm. Emittance (mm-mrad)	≤ 1	≤ 1	≤ 1	≤ 1
rms Energy Spread (keV)	25	100	150	100
Radiator Period (mm)	27	27	27	27

The CLARA installation began in 2015, therefore the beam parameters for VELA as simulated will change to the 'post CLARA upgrade parameters' by the time the metamaterial structure is realised and tested. Figure 5.18 shows how the CLARA

upgrade will fit with the layout of VELA. Not only will this provide future opportunities for beam test on CLARA but it will mean operating on an upgraded VELA with enhanced beam parameters post CLARA installation. VELA will operate on an improved electron gun with a higher repetition rate of 400 Hz, and with higher energy electrons, with the upgrade delivering up to 25 MeV electrons compared to the current 4.5 MeV. This will increase beam power by a factor of 5 and the installation of the high repetition rate gun will increase the beam power by another factor of 40. Thus there will be a factor of 200 beam power increase on VELA following the CLARA upgrade.

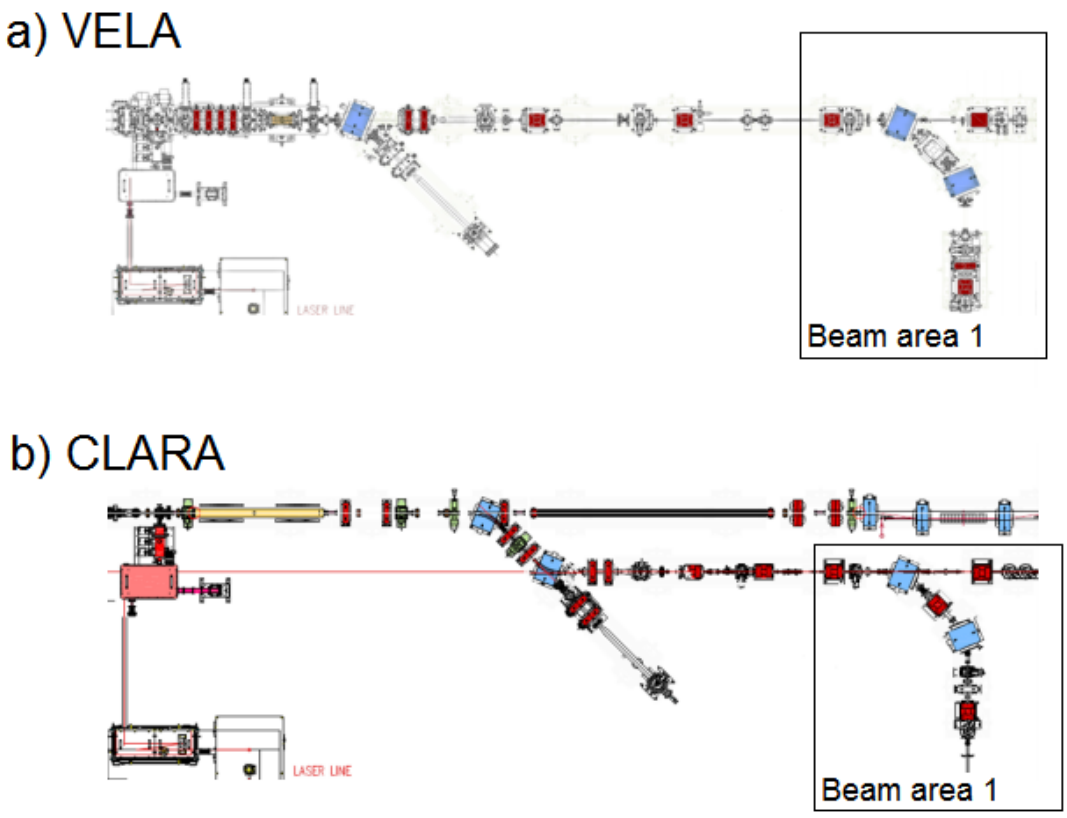

Figure 5.18: CLARA and VELA front end layouts. Showing how the beam can be directed from the gun to the rest of CLARA, down a diagnostic spectrometer line or into the existing VELA line with two user areas [115].

These upgrade will result in a more intense and energetic beam which will result in stronger coupling between the proposed metamaterial structure and the beam for the operating TM-like mode. This will result in a stronger excitation in the longitudinal beam coupling, and since the beam radius will remain the same, the clear field excitation of TM-like mode as was observed for the current VELA beam. Testing of the structure on CLARA will be done on the coffin and not the full FEL beam, however this will still be a more intense and energetic beam than the cur-

rent VELA beam, which will create a strong excitation of the left handed TM-like mode. The upgrade and operation on CLARA pose a good option for utilising the metamaterial loaded structure for backward propagating Cherenkov applications, as a source or a non-destructive detector, and in the multi bunch operating mode of CLARA there is the possibility of using the structure for accelerating purposes.

5.6 Coupler design

The proposed structure will need RF input and output, for applications in an accelerator environment, be that as a detector or an accelerator, therefore a coupler needs to be designed to get the RF into the loaded waveguide. Due to the nature of the operating mode of the loaded waveguide structure careful consideration must be put on how to couple this mode into the structure. The operating mode is the TM_{31} mode occurring at 5.86 GHz, this poses two clear challenges to coupling, firstly this is not the fundamental TM mode and therefore will be harder to couple to and secondly this mode occurs at a higher frequency than the standard operation of an S-band waveguide. Both of these challenges need to be addressed by the coupler design to ensure efficient coupling and hence efficient operation of the structure.

The initial design presented here uses a dual feed to improve the coupling to the TM_{31} mode, this design can be seen in Figure 5.19, here the dimensions of the two inputs and the location and depth of the notches on the side are modified to improve the coupling to the higher order mode. This design was simulated using the frequency domain solver of CST, with one input mode and up to 10 output modes to identify where the desired mode will be generated. This design generates the TM_{31} mode as the 6th output mode at 5.86 GHz the same frequency of the mode in the loaded waveguide structure. The correlation in frequency is good however the mode order is high and coupling may not be as strong as is needed. To identify how strong the strength of the coupling, the S-parameters need to be analysed, namely S_{11} and S_{21} of the desired mode.

Figure 5.20 shows the linear magnitude of the S-parameters of the desired TM_{31} mode in the coupler, S_{11} shows the reflection at port one, and S_{21} shows the transmission of the 6th mode at port 2. For strong coupling S_{11} should be minimal or close to zero at the desired frequency of 5.86 GHz and S_{21} should be maximal or close to 1. From Figure 5.20, it can be seen that S_{11} is minimal with a value of 0.014 at 5.869 GHz indicating very little reflection and S_{21} shows a value of

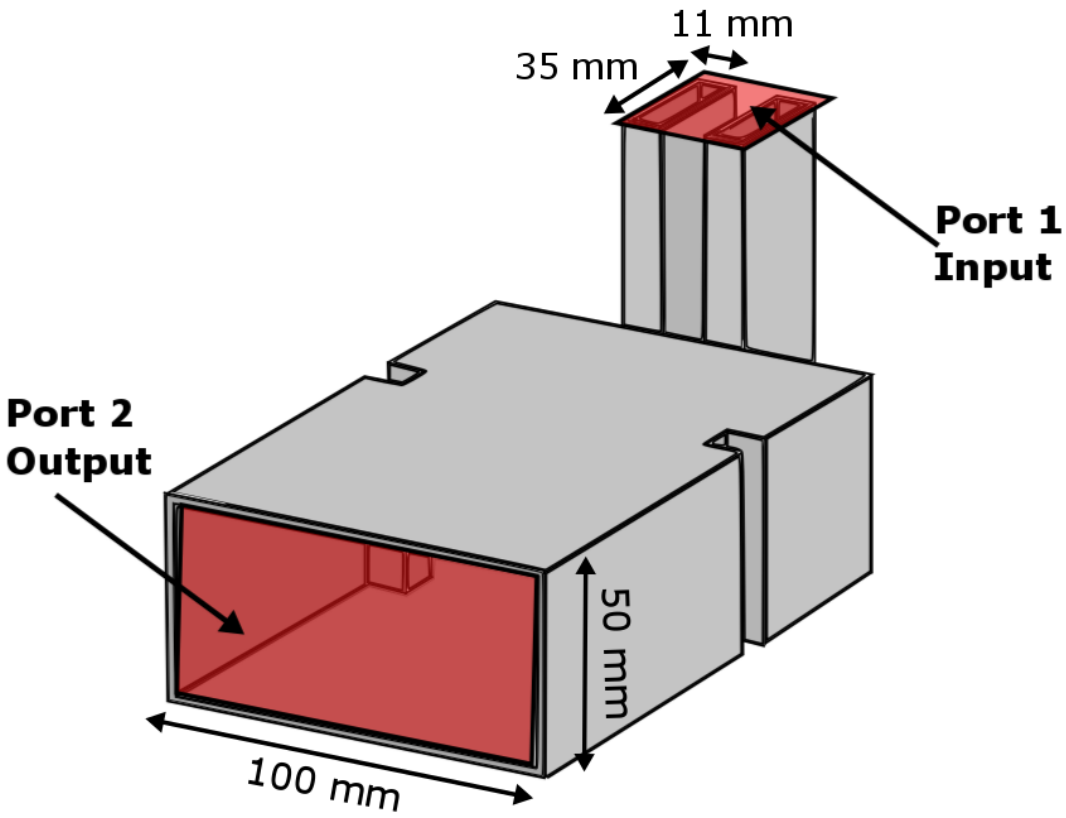

Figure 5.19: An initial design for the coupler for the metamaterial loaded waveguide designed to load the structure with the TM_{31} mode.

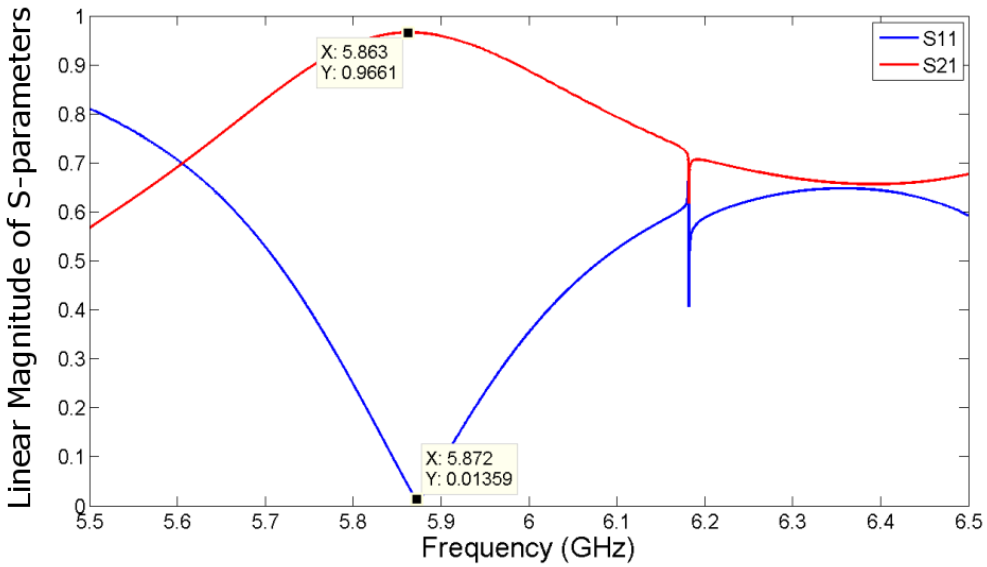

Figure 5.20: The linear plot of the S-parameters of the desired mode, showing S_{11} and S_{21} of the TM_{31} mode.

0.97 at 5.869 GHz indicating a strong amount of transmission thus strong coupling.

This coupler design has shown strong coupling to the TM_{31} mode at the correct

frequency of 5.86 GHz, however this coupler design is not the correct dimensions to launch straight into the loaded waveguide. To obtain the TM_{31} mode at the correct frequency, the output waveguide had the dimensions of 50 mm by 100 mm much larger than the dimension of the S-band loaded waveguide (34 mm by 72 mm). When using the correct waveguide size at the output port, the TM_{31} mode does not show as strong coupling or occur at the correct frequency. Thus, there either needs to be tapering between the current designed coupler and the loaded waveguide to ensure the correct mode is launched or a new coupler design needs to be found to launch straight into the waveguide without tapering. These challenges are discussed in the future work Section of the final Chapter.

5.7 Conclusions

In this Chapter the behaviour of the loaded waveguide structure within an accelerator environment is discussed and particle in cell simulation results are provided for three different electron beams, the current VELA beam, the electron beam at FACET and the beam from a commercial Kimball gun. The CLARA upgrade and the effect this will have on testing the structure at Daresbury laboratories is also discussed.

In terms of the particle in cell simulation results, the strongest excitation in the longitudinal electric field was observed for the FACET beam, with a strength of 234.2 μV/m at 6.312 GHz corresponding to a hybrid form of the TM_{31} mode. Though this strong excitation indicates strong coupling, the corresponding mode is not well defined and thus not ideal for the applications, however provides and interesting comparison between facilities and beam types. Since the field within the CSRR metamaterial structure are strongest closest to the sheets, the reduced definition in the modes is likely due to the small spot size which results in weak field generation despite the strong coupling the high intensity beam will generate. The commercial Kimball gun generates equally strong excitations which correspond to a TM_{11}-like mode. However the strength of the excitation corresponding to this mode diminishes down the length of the structure, thus a consistent response cannot be maintained. This mode is not supported by the waveguide, and was not found within the electromagnetic results, thus away from the gun coupling to this mode diminishes significantly, as illustrated by the reduced excitation found by the probe at 240 mm down the structure. Therefore, the mode generated by the Kimball beam is not a propagating mode within the loaded waveguide structure and is unsuitable for wave-beam interaction applications.

The response of the structure to the VELA beam is interesting, as though the excitations in the longitudinal electric field are an order of magnitude less than those generated by the other beams, the associated mode polarizations are the most defined. There is a clear generation of the TM_{31} mode which corresponds to the excitation at 6.304 GHz, which is suitable for the left handed accelerator applications this structure is designed for. The increase in energy as a result of the CLARA upgrade will increase the viability of the beam for this structure as it will improve the strength of the longitudinal field excitations whilst maintaining a clear field profile. Thus the decision to use the VELA/CLARA beam for the testing of this this structure, is not only valid as it fits the remit of VELA as a dedicated test facility for advanced accelerator technology but also in terms of the response it is expected to generate.

An initial coupler design was presented and the complexity of coupling to the TM_{31} mode was discussed. Though the initial design for a coupler looked promising generating the correct mode at 5.86 GHz, with over 95 % transmission, this design has several drawbacks. Firstly the output port on the coupler is larger than the loaded waveguide and therefore if this coupler is to be used then tapering is required. Secondly the TM_{31} mode is still the 6th mode at the output port and lower order modes may couple into the structure over this one. Therefore further thought needs to be made on the design of the coupler if the structure is used as an accelerating waveguide to ensure that the correct mode can be launched efficiently into the structure.

Chapter 6

High frequency artificial engineered materials for accelerators

Though the main focus of this thesis is metamaterials for accelerator applications within the microwave range, this is not the limit of metamaterial applications in this field. Working in the microwave range allows for larger length scales of the designed structures making a proof of concept model for experimental validation much more feasible. In addition this is also the frequency range of the conventional accelerators and RF systems at Daresbury. High frequency accelerators have increasingly gained attention in recent years and thus consideration must be put on how metamaterial elements might be scaled down for applications in high frequency small scale accelerators and how other methods of dispersion engineering can be used instead. This Chapter will focus on the motivation behind high frequency dispersion engineering for accelerators, how plasmonic materials can be used to overcome issues with high frequency operation and how both metamaterials and dispersion engineering can be used at THz frequencies.

6.1 High frequency dispersion engineering

There is a pressing demand within the accelerator community to move to higher gradients and more compact structures which often results in operating at a higher frequencies. In addition to this there is a move to generate coherent THz radiation as a method to fill the THz gap [121]. With emerging technologies such as the dielectric laser accelerating structure at SLAC [4], where one accelerating

structure is only 500 μm long, there is a push to create equally small elements for detection and as undulators and wigglers. Metamaterials and alternative forms of dispersion engineering are one way of achieving these applications as they are inherently small scale, moving research closer to a table top accelerator or the much discussed accelerator on a chip design.

Due to their subwavelength nature, metamaterials are an interesting candidate for miniaturising accelerator systems, however there are a number of limitations on metamaterials at THz and beyond. The metals used to commonly fabricate these metamaterial structures can be considered too metallic in the near IR and visible frequencies. The high carrier concentration of metals leads to large plasma frequencies and large losses limiting the efficiency of the structure. It is for this reason that alternative plasmonic materials are investigated within this Chapter for applications in both metamaterials and dispersion engineering. Alternative plasmonic materials are able to bridge the properties of both metals and dielectrics, where the carrier concentration can be tuned such that the material can behave like a metal and the typical losses of noble metals can be reduced. This is done either by doping semiconductors to control carrier concentration [122] or by reducing the carrier concentration of metals by mixing them with non-metals, to form intermetallics [97].

The second and most limiting drawback to metamaterials at high frequency is their subwavelength nature meaning that unit cells must be increasingly small for higher frequencies, with periods of tens of μm in THz [123], and at hundreds of nm for near IR and visible frequencies [124]. Though fabrication of simplified metamaterial geometries is possible at these frequencies and a good review of them was published in Nature Photonics in 2007 [125], the methods to do this can be expensive and the basic geometries limit the range of applications. Advances are being made to improve fabrication and durability of metamaterials at this scale, however when considered within an accelerator environment with high power and in the vicinity of particle beams, they remain unsuitable. Alternative methods of dispersion engineering that rely on wavelength scale structures rather than subwavelength structures are more desirable for accelerator applications, as they are larger, have a greater flexibility in geometries, and are easier and cheaper to fabricate.

These wavelength order structures provide an alternative method of dispersion engineering when working at scales in which subwavelength metamaterials currently prove challenging to fabricate. Examples of dispersion engineering for accelera-

tors include; THz Smith-Purcell gratings for diagnostic applications on small scale accelerators, dielectric lined waveguides for acceleration or coherent sources and Photonic Band Gap (PBG) structures, using Bragg reflectors for accelerator applications including particle detection and coherent source generation at THz.

This Chapter covers some examples of alternative plasmonic materials and how they can be used to overcome the limitations of conventional materials in both metamaterials and for Smith-Purcell gratings. For metamaterials applications new plasmonic materials are investigated as an alternative to metals when creating low loss split ring resonators for application in the NIR and visible frequency ranges. In terms of Smith-Purcell gratings the use of a highly doped semiconductor is investigated as an alternative to metals to increase the effectiveness of the interaction by allowing for an increased beam grating spacing. Finally the results of combining photonic band gap structures with dielectric lined waveguides are investigated in the form of a dielectric Bragg waveguide for THz applications.

6.2 Metamaterials based on new plasmonic materials

High frequency applications in near infra-red and visible frequency range have, for many years not only been limited by fabrication techniques but also the materials available. Metamaterial structures are commonly fabricated from metals which exhibit high losses in this frequency range and therefore new materials are desirable. Conventional plasmonic materials such as silver and gold have been popular for applications at high frequency but have drawbacks that limit their metamaterial applications. Conventional plasmonic structures based on noble metals exhibit large losses in the visible and Near-IR range, have large magnitudes of real permittivity, are non-tuneable and become even more lossy when patterned. It is for these reasons they have limited suitability for metamaterial applications and an alternative needs to be found. New plasmonic materials as put forward by Boltasseva [126, 122] pose the most promising alternatives to silver and gold, as they are compatible with Complementary metaloxidesemiconductor (CMOS) technology allowing for easy fabrication at smaller scales and integration into existing micro-structures which opens up a range of applications at higher frequencies. The key requirements of these materials are; low loss, tuneability and comparable values of real permittivity to both metals and dielectrics.

The main drawback to metals is that they are 'too metallic', the high carrier concentration leads to large plasma frequencies and large losses. The carrier concentration can be controlled in materials like semiconductors by doping, this creates new plamonics materials. An example of a type of new plasmonic materials is transparent conducting oxides where the plasma frequency can be tuned, these include materials like, Indium Tin Oxide (ITO) and Gallium doped Zinc Oxide (GZO) [122]. Intermetallics, another type of new plasmonic materials, are formed by reducing the carrier concentration of metals by mixing them with non-metals, they have higher carrier concentrations than transparent conducting oxides, and can be tuned by altering processing conditions. The most well used of the intermetallics is Titanium Nitride [97] which performs very well in the visible and near IR frequency range.

The new plasmonic materials focussed on in this work [96] are Gallium doped Zinc Oxide (GZO), a Transparent Conductive Oxide (TCO) which shows lower losses than silver and gold at the visible and Near Infra-Red range (NIR), and the intermetallic ceramics Titanium Nitride (TiN) and Zirconium Nitride (ZrN) which exhibit metallic properties in the optical and NIR range.

6.2.1 Design of Plasmonic Split ring resonators

Split Ring Resonators (SRRs) [20], give rise to negative permeability via a resonant response, when combined with thin metal wires they form a Negative Index Material (NIM). SRRs are commonly designed in the microwave frequency range as they are cheap and easy to fabricate in copper [23]. However, as discussed metals are too lossy for operation above THz frequencies and therefore alternative materials for fabricating metamaterials in this frequency range are required. Since metallic behaviour is required for resonant applications new plasmonic materials are proposed as they have metal like properties but are significantly lower in losses than metals within this frequency range.

The drawback of using plasmonic materials in SRRs is that the magnitude of real permittivity can be insufficient to drive a resonant response. This can be overcome by tuning the permittivity of the dielectric substrate to drive a resonant response. To investigate this the plasmonic SRRs will be simulated using CST Microwave Studio [98] on loss free substrates with set permittivity values and compared to a loss free version of the substrate FR-4 (ε=4.3).

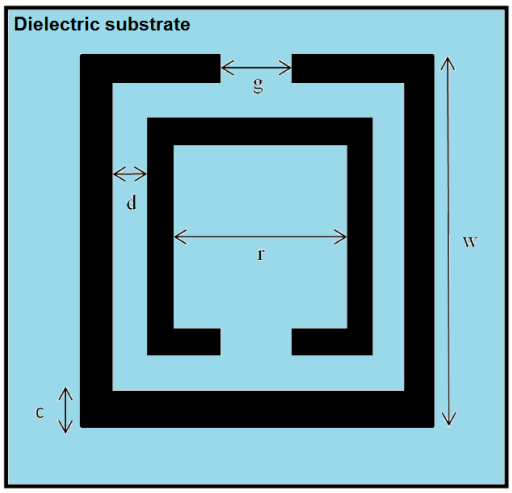

Figure 6.1: The unit cell of the plasmonic SRR on dielectric substrate, with a period of 500 nm. Parameters shown are outer ring width w=300 nm, gap width g=40 nm, ring thickness and spacing d=c=30 nm and inner radius r=120 nm. For operation around 100 THz.

The simulations focus on a periodic array of unit cells, each one comprising a single plasmonic SRR as shown in Figure 6.1, on a substrate 150 nm thick. The resonator lies in the xy plane with the electromagnetic radiation propagating in the z direction. The simulation was performed with unit cell boundary conditions in x and y and open boundary conditions in z, forming a single metasurface sheet of plasmonic SRRs to be studied. The SRR was simulated in vacuum, on the loss free form of the conventional substrates FR-4 (ε=4.3) and on a range of loss free substrates where permittivity is varied in steps of 5 from ε=5 up to ε=40. Thus a range of high and low permittivity substrates is studied.

6.2.2 Comparison of alternative Plasmonic materials

The new plasmonic materials TiN, GZO and ZrN, were simulated at THz frequencies, by inputting their parameters into CST by means of Drude dispersion model to fit the experimental curves published in literature [127]. The Drude dispersion model parameters are used to find the dielectric constant, via;

$$\varepsilon(\omega) = \varepsilon_\infty - \frac{(\omega_p)^2}{\omega^2 - i\omega\gamma}, \tag{6.1}$$

where ε_∞ is the dielectric constant at infinite frequency, ω_p is the plasma frequency, and γ is the damping frequency. Using this equation and the parameters given in Table 6.1, the real and imaginary components of the permittivity can be plotted for comparison.

Figure 6.2 shows the real component of the permittivity for each new plasmonic

Table 6.1: The Drude parameters of the three new plasmonic materials and silver as input into CST for the simulations [98].

Material	Dielectric constant ε_∞	Plasma frequency ω_p (Rad/s)	Damping frequency γ (Rad/s)
Ag	5.0	1.4433×10^{16}	1.0×10^{14}
TiN	4.017	0.7×10^{16}	9.0×10^{14}
GZO	4.0	2.9×10^{15}	1.5×10^{14}
ZrN	1.117	1.2×10^{16}	3.5×10^{14}

material compared to silver. From this plot it can be seen that ZrN has the real permittivity most similar to that of a metal, and thus at certain frequencies ZrN will drive its own resonance. Both TiN and GZO have much smaller values of real permittivity and so will require higher permittivity substrates to generate the appropriate resonant response.

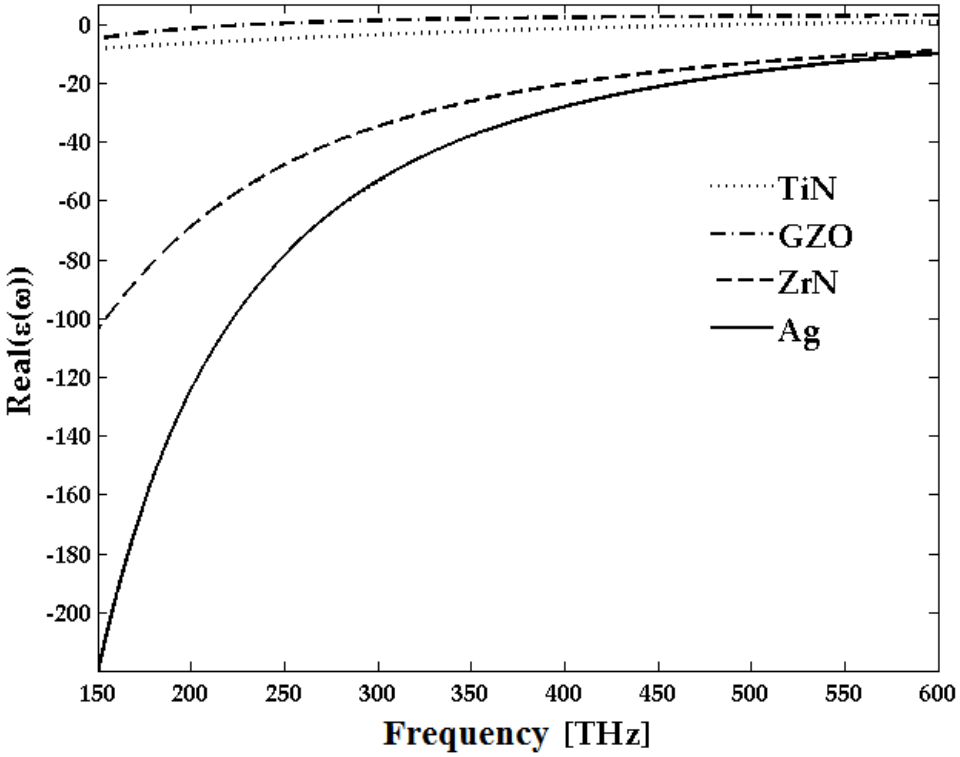

Figure 6.2: Real part of the permittivity for the new plasmonic materials compared to silver.

Figure 6.3 shows the imaginary component of the permittivity for each new plasmonic material compared to silver. Once again ZrN follows a very similar curve to

silver however it exhibits higher values than silver indicating higher losses which are not ideal. TiN also closely follows the curve of silver, however it's values of imaginary permittivity are weaker thus it exhibits lower losses. GZO exhibits the lowest imaginary component of permittivity making it a low loss material that exhibits dielectric like behaviour.

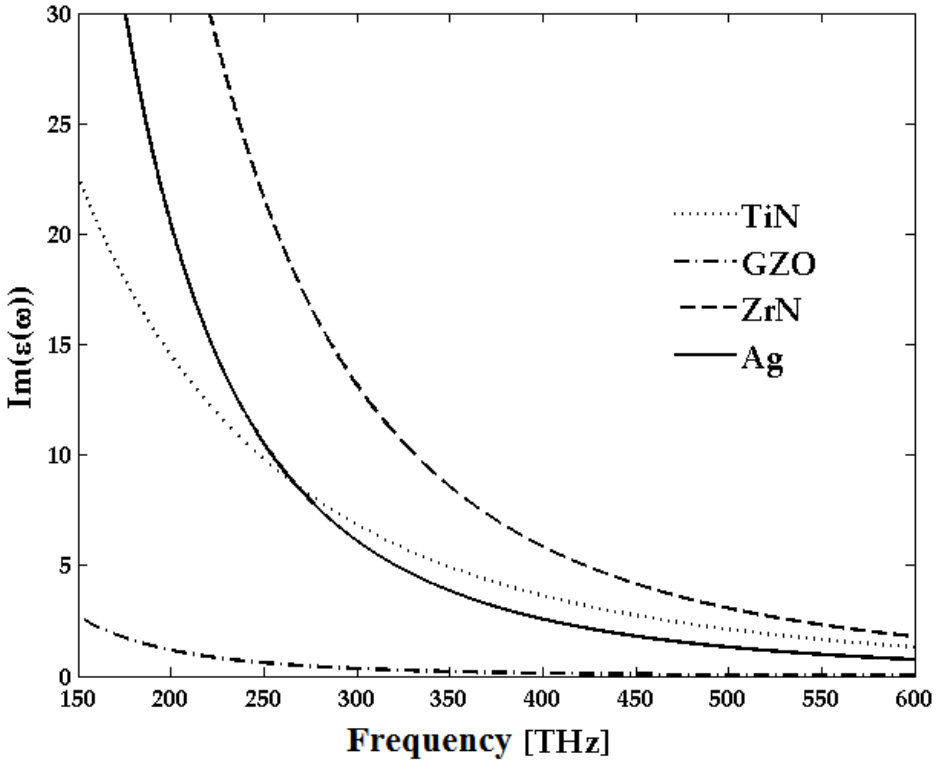

Figure 6.3: Imaginary part of the permittivity for the new plasmonic materials compared to silver.

6.2.3 Simulation Results

To investigate the nature of the electromagnetic response and identify resonances, the S-parameters are extracted with the magnitude and bandwidths of the resonant response being discussed. For each material the S_{11} results of the low permittivity substrates up to ε=15 are shown in one plot and the high permittivity substrates ε=20 to ε=40 are shown in another.

ZrN results

Figure 6.4 shows the S_{11} results of the ZrN SRR on low permittivity substrates. Figure 6.2 showed that ZrN has a real permittivity sufficient to drive a resonant response without a substrate, and therefore should perform well on low permittivity

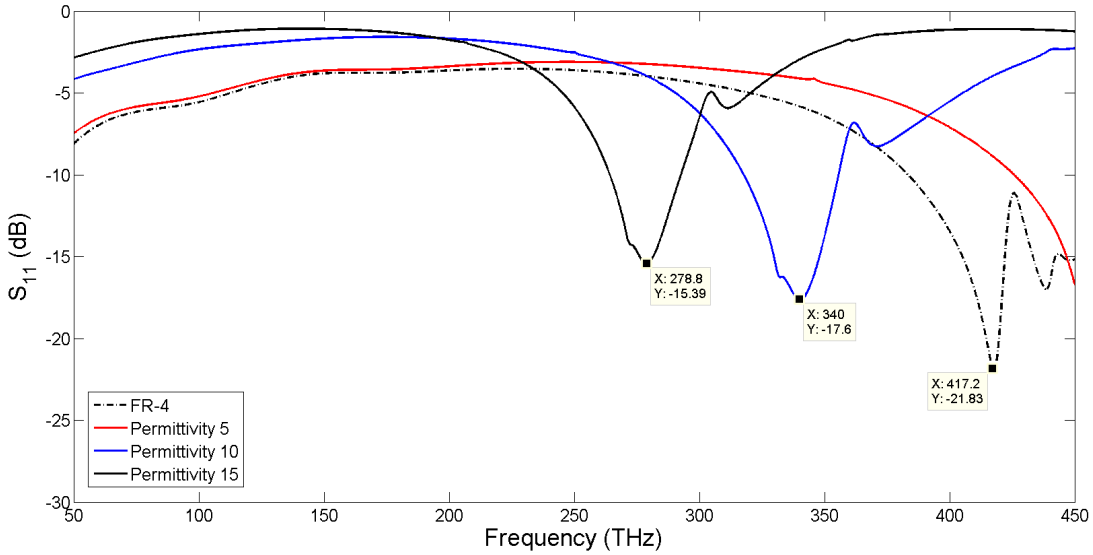

Figure 6.4: S_{11} variation for ZrN-based SRR on low permittivity substrates.

substrates. From Figure 6.4 it can be seen that the strongest resonant response is observed for the SRR on a substrate of FR-4 (dashed line), this reaches -21.83 dB at 417 THz. This resonant response is not only strong but broadband making it ideal for negative index applications.

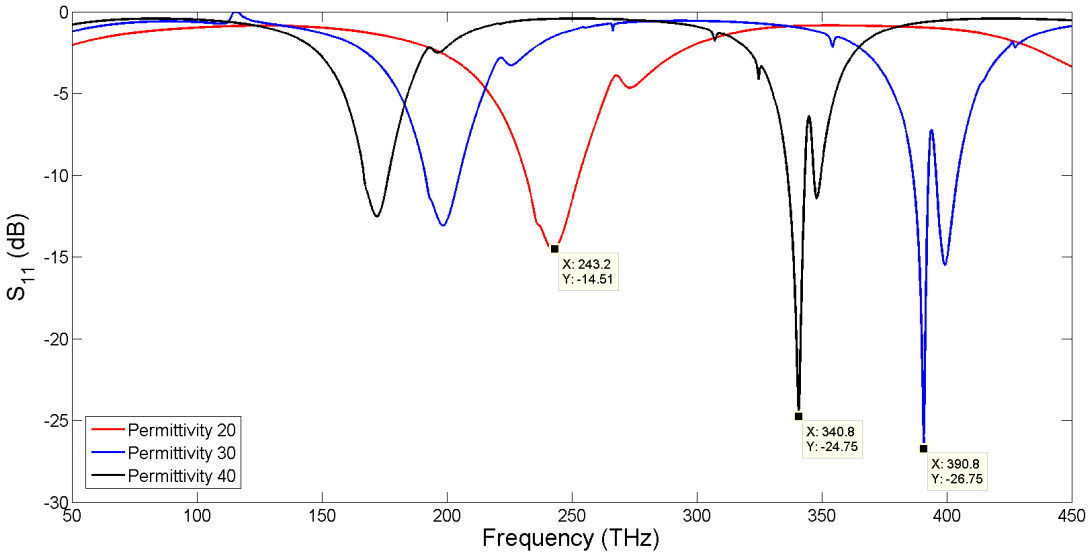

Figure 6.5: S_{11} variation for ZrN-based SRR on high permittivity substrates.

Figure 6.5 shows the S_{11} results of the ZrN SRR on high permittivity substrates, it is immediately apparent that for high permittivity values additional higher order resonances are observed. The strongest resonance for these simulations is the second resonance of the SRR on ε=30 substrate (shown in blue) this reaches -26.75 dB at 390 THz. This response though slightly stronger in magnitude to that

of the SRR on FR-4 substrate is much narrower in bandwidth and therefore less suitable for the applications.

TiN results

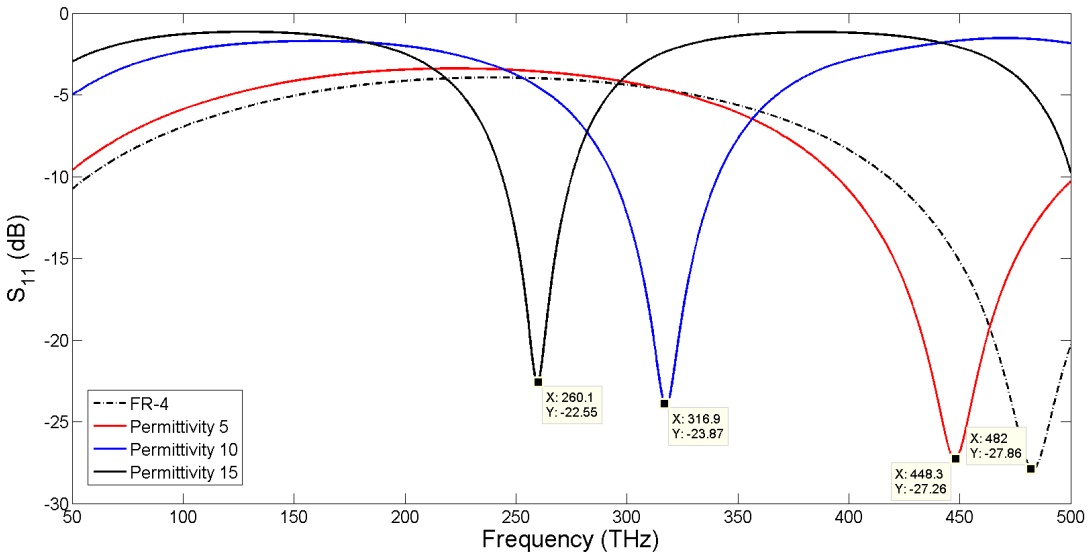

Figure 6.6: S_{11} variation for TiN-based SRR on low permittivity substrates.

Figure 6.6 shows the results of the TiN SRR simulated on low permittivity substrates, these resonances are broadband with clear noise free dips. TiN unlike ZrN has a weaker real component of permittivity and is therefore unable to generate a resonant response without a substrate to provide a permittivity gradient. The strongest resonant response on a low permittivity substrate is for FR-4 (dashed line) which shows a response of -27.86 dB at 482 THz, the response for the SRR on ε=5 (red line) is very similar with a magnitude of -27.26 at 448 THz. Both resonances are broadband and thus can be used for a number of applications.

Figure 6.7 shows the results of the TiN SRR simulated on high permittivity substrates, these resonances are sharper than those found on a lower permittivity substrate and show higher order resonances. Compared to ZrN these resonant peaks are more defined without the small secondary dip present in the ZrN results. The strongest response is observed for the third resonance of the SRR on the ε=40 at 474 THz with a strength of -27.16 dB, once again the high permittivity response is significantly more narrowband than those found on the low permittivity substrates. Though the resonant response has a similar magnitude on the high permittivity substrate, the lower permittivity responses are more suitable for accelerator applications as they are broadband fundamental resonances.

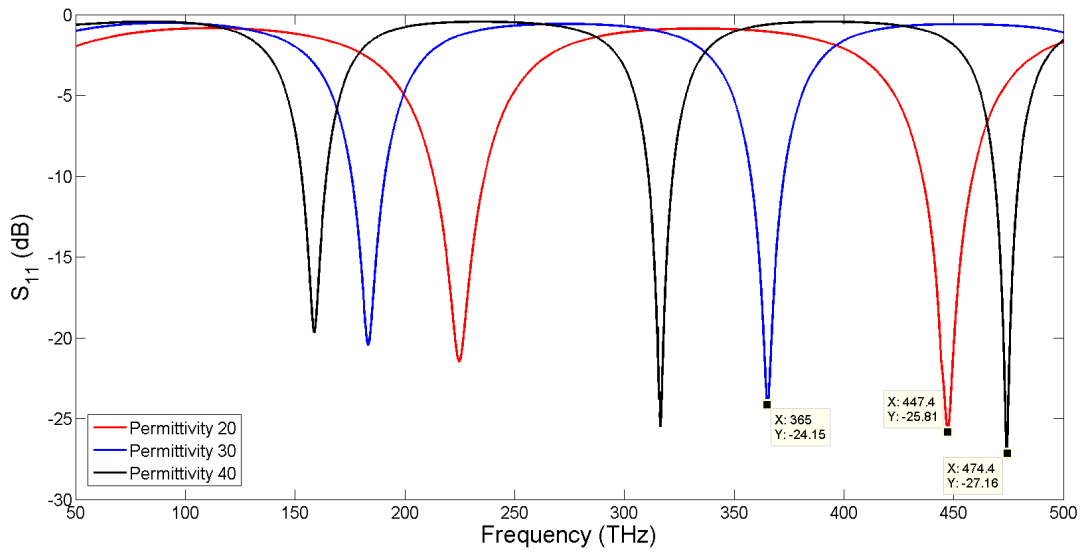

Figure 6.7: S_{11} variation for TiN-based SRR on high permittivity substrates.

GZO results

Figure 6.8 shows the results of the GZO SRR simulated on low permittivity substrates. The strongest resonances by far are observed for GZO on low permittivity substrates, with a response of -56.03 dB at 315 THz for the ε=10 substrate (shown in blue). This resonance, though strong and at a suitable frequency for many applications, is narrowband, unlike the low permittivity responses for the other new plasmonic materials.

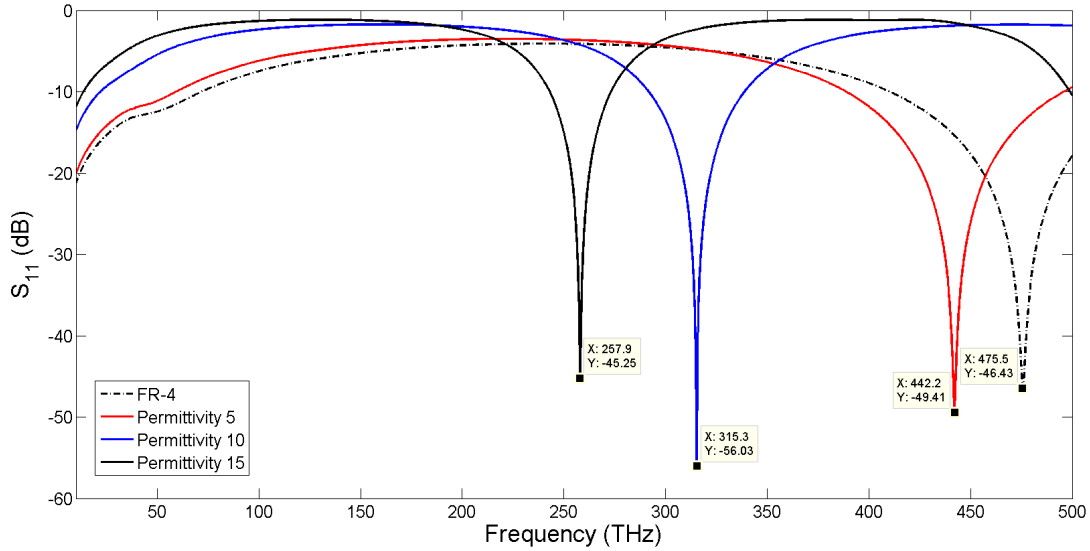

Figure 6.8: S_{11} variation for GZO-based SRR on low permittivity substrates.

Figure 6.9 shows the results of the GZO SRR on high permittivity substrates, once

again higher order excitations arise with increasing permittivity. The strongest resonant response is the second resonance of the SRR on the ε=40 substrate, with a resonance of -46.76 dB at 315 THz. Though this response is strong for GZO the narrow bandwidth and higher order nature of the responses limits applications.

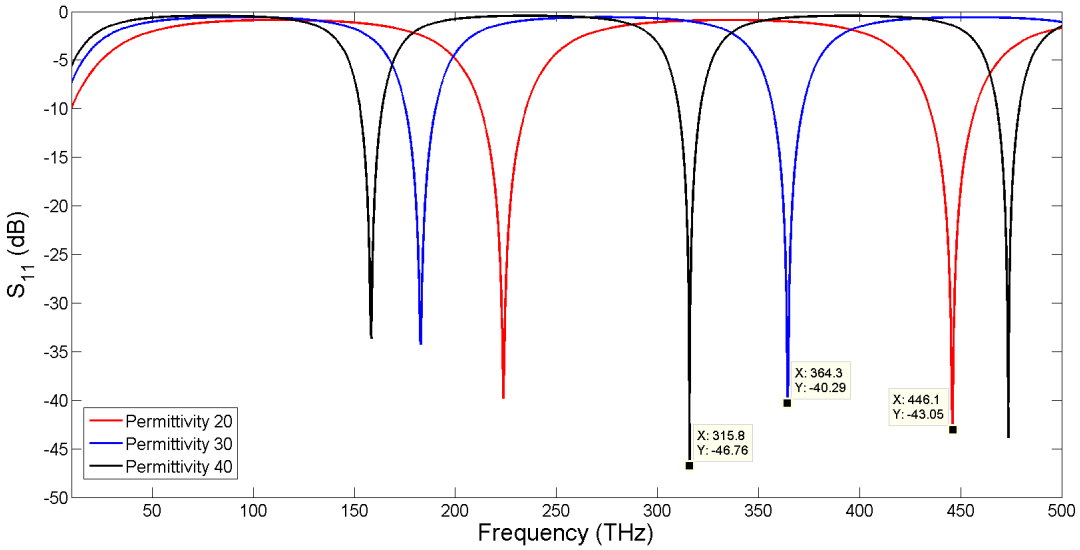

Figure 6.9: S_{11} variation for GZO-based SRR on high permittivity substrates.

6.2.4 Effective parameter retrieval for the plasmonic SRR

In Chapter 2, the different methods of effective parameter retrieval were presented, and the validity of these methods for retrieving metamaterial effective parameters was discussed. The method deemed most suitable for metamaterial effective parameter retrieval was the S-parameter retrieval methods put forward by Smith [23], which deals with the inhomogeneous nature of metamaterials to a certain extent. However, these methods still lead to significant ambiguity in the results due to the closeness of the arccosine branches used to determine the refractive index and metamaterials inhomogeneous nature which leads to ambiguity in the impedance.

In this Section, Smiths method of S-parameter retrieval is used to determine the effective permeability of the GZO SRR on a substrate with permittivity 10, as this design gave the strongest resonant response of all the structures. The S-parameters were found using the frequency domain solver of CST Microwave Studio [98]. To do this a single unit cell as shown in Figure 6.10, was simulated with an input port on the front face and an output port on the back face. The unit cell has boundaries such that is periodic in x and y forming a single metasurface sheet. The real and imaginary components of S_{11} and S_{21} were found, which correspond

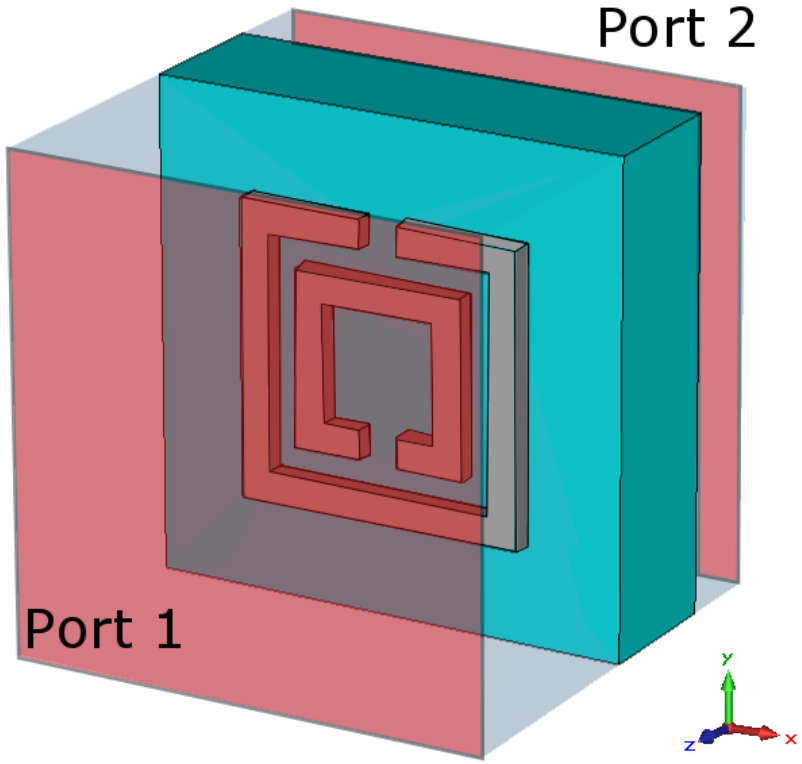

Figure 6.10: The GZO SRR on substrate, showing the input and output ports for parameter retrieval calculations.

to transmission and reflection. Transmission was given as

$$\text{trans} = Re(S_{21}) + iIm(S_{21}), \tag{6.2}$$

which is then normalised to

$$\tau = e^{ipk}\text{trans}, \tag{6.3}$$

where p is the unit cell size and k is the wave number. The reflection is given by

$$\Gamma = Re(S_{11}) + iIm(S_{11}). \tag{6.4}$$

The reflection and transmission can then be used to find the impedance

$$z = \pm\sqrt{\frac{(1+\Gamma)^2 - \tau^2}{(1-\Gamma)^2 - \tau^2}}, \tag{6.5}$$

where the positive sign is chosen to fulfil the requirement that $Re(z) > 0$. The refractive index is given as;

$$Re(n) = \pm Re\left(\frac{cos^{-1}\left(\frac{1}{2\tau}\left[1 - (\Gamma^2 - \tau^2)\right]\right)}{kp}\right) + \frac{2\pi m}{kp}, \tag{6.6}$$

$$Im(n) = \pm Im\left(\frac{cos^{-1}\left(\frac{1}{2\tau}\left[1-(\Gamma^2-\tau^2)\right]\right)}{kp}\right). \tag{6.7}$$

Both the refractive index and the impedance can then be used to find the real and imaginary components of the permeability via

$$Re(\mu) = Re[(Re(n) + iIm(n)) \times (Re(z) + iIm(z))], \tag{6.8}$$

$$Im(\mu) = Im[(Re(n) + iIm(n)) \times (Re(z) + iIm(z))]. \tag{6.9}$$

These values of real and imaginary permeability can then be plotted against frequency to show how the response of the structure develops through the frequency range.

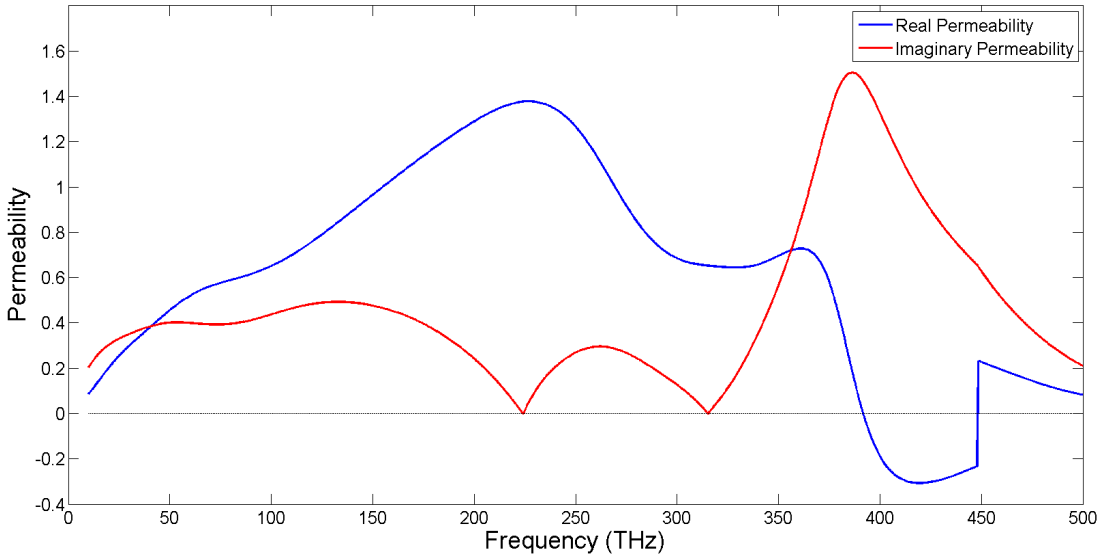

Figure 6.11: The real and imaginary permeability of the GZO SRR on the substrate with permittivity 10.

Figure 6.11 shows the real and imaginary components of permeability as calculated using S-parameter retrieval method detailed above. This plot shows how the permeability of the GZO SRR on the permittivity 10 substrate develops over the frequency range. Since the SRR is a metamaterial designed to give rise to negative permeability there is expected to be a region in which this is the case. In Figure 6.11 this region of negative permeability can be seen to occur between 390 and 450 THz. For an SRR, negative permeability is expected at in the frequency range between the resonant frequency and the magnetic plasma frequency as discussed in Chapter 2 Section 3. In Figure 6.8 the S_{11} resonance for GZO on permittivity 10 substrate occurs at 315 THz, therefore this negative permeability can be considered to occur at a frequency above resonance. However this could

be seen to occur at a significantly higher frequency and therefore potentially not correspond to the resonance.

To a certain extent the response shown in Figure 6.11 is in line with the expected response, the higher frequency of this response indicates that the retrieval method may not be accurate enough to fully determine the response of metamaterials. In the scope of this thesis, this methods accuracy cannot be ensured therefore cannot be used to fully determine the behaviour of the loaded waveguide structure. The ambiguity in the results provided by S-parameter retrieval methods cannot easily be resolved, due to the generation of multiple arccosine branches in the determination of the refractive index. This ambiguity may be easier to resolve when the s-parameters are obtained from experimental tests rather than simulations, when the mitigating factors detailed in Chapter 2 Section 5 can be applied.

6.2.5 Summary of plasmonic SRR results

The use of alternative plasmonic materials-based SRRs is newly proposed as a method to bring SRRs metamaterials into high frequency ranges. Compared to traditional noble metals, these new plasmonic materials offer a low loss, CMOS compatible, cheaper alternative. Each of the new plasmonic materials (ZrN, TiN, and GZO) showed strong resonance when placed on a dielectric substrate of high permittivity, with GZO showing the most promising results. It can be seen that higher substrate permittivity drives a stronger resonance however after a certain point these will lead to higher order resonances which reduce the strength and bandwidth of the resonant response. The strongest response was obtained by simulating GZO on the ε=10 substrate, with a resonance of -56.03 dB at 315 THz, however this response had a narrow bandwidth which can limit applications. In terms of real world applications, a GZO-based SRR on an alumina (ε=9.9) substrate would provide a strong resonance at NIR frequencies which could be tuned to visible frequencies by modification of the SRRs geometrical parameters. This strong response and the low loss nature of GZO make it an interesting option in high frequency application where broad bandwidths are not required. The second strongest response was for the TiN SRR on FR-4 substrate, this reached -27.86 dB at 482 THz and is very broadband which is desirable. Thus it can be concluded that new plasmonic materials form a strong, low loss alternative to conventional materials for metamaterial applications at high frequencies particularly at NIR and visible frequencies.

6.3 Plasmonic Smith-Purcell gratings

Metallic gratings are commonly used to generate Smith-Purcell radiation, when an electron passes close to the surface of the grating, it generates Smith-Purcell radiation [128] which is emitted in crescent shaped waveforms for every period of the grating passed. In this section a Smith-Purcell grating formed from a new plasmonic material indium antimonide (InSb), which is a doped semi-conductor, is proposed for improved Smith-Purcell radiation at approximately 0.35 THz [129]. InSb is most efficient below 1 THz therefore the structure is designed to operate within the THz gap. The plasmonic behaviour of InSb at THz frequencies enhances surface wave interactions allowing for an increased spacing between the beam and the grating. Structures like these could be used as detectors on the end of a small scale dielectric laser accelerator, to create another small scale element that helps reduce the overall size of the accelerator system, moving one step closer to the accelerator on a chip design.

Future particle accelerators for next generation light sources and wakefield accelerator will rely on short particle bunches and an accurate method for beam profile measurements is required. The coherent Smith-Purcell radiation generated by a particle bunch passing over a metallic like grating has already been used for multi-shot diagnostics [130], where non-destructive average time profile measurements are performed. Therefore developing a grating with greater separation of beam and grating will increase applications of these structures, as the current spacing requires a very small beam radius to operate without collisions.

6.3.1 Indium Antimonide

Indium antimonide has recently gained attention as a plasmonic material which can provide the characteristic plasma frequency at the THz frequency range, where natural metals do not exhibit any plasmonic behaviour. It is a doped semiconductor material that behaves like a metal within a set frequency range. The material is simulated in CST [98] by inputting material parameters into a Drude dispersion model that gives the dielectric constant;

$$\varepsilon(\omega) = \varepsilon_\infty - \frac{(\omega_p)^2}{\omega^2 - i\omega\gamma}, \tag{6.10}$$

where ε_∞ is the dielectric constant at infinite frequency, ω_p is the plasma frequency, and γ is the damping frequency.

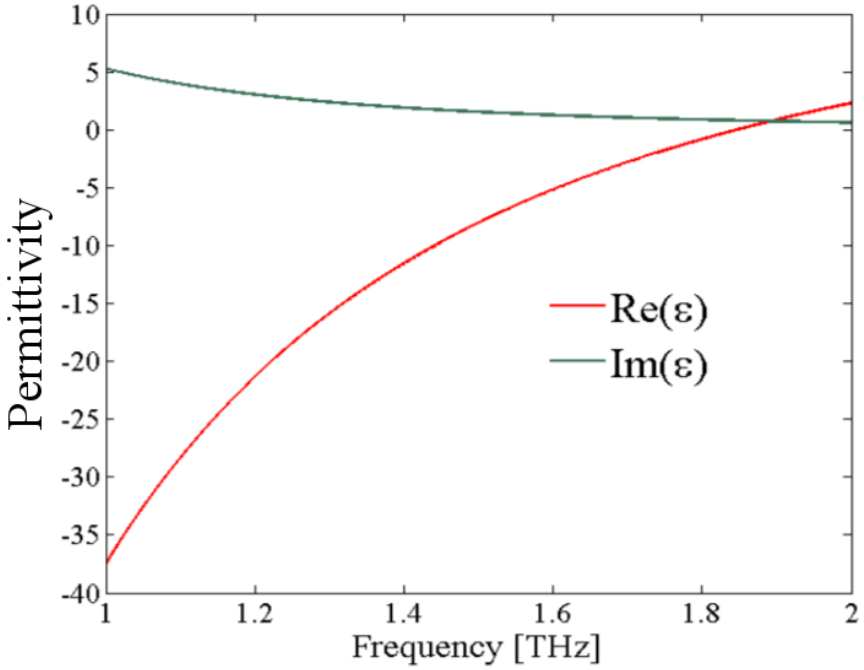

Figure 6.12: The Drude dispersion curve for InSB, showing the real and imaginary permittivity curves.

Figure 6.12 shows the real and imaginary components of the permittivity of InSb for the frequency range of 1-2 THz, it can be seen that the imaginary part of the permittivity has a small magnitude throughout the frequency range making this a low loss material. The plot of the real component of the permittivity shows that below the plasma frequency of 1.9 THz InSb exhibits metallic properties and thus is expected to increase the interaction of a THz Smith-Purcell grating with respect to conventional metal gratings.

6.3.2 Grating structure

When an electron passes close to the surface of a periodic metallic like grating, radiation known as Smith-Purcell radiation [128] is emitted in crescent shaped waveforms for every period of the grating passed. The wavelength of the emitted radiation is given by

$$\lambda = \frac{l}{|s|}\left(\frac{1}{\beta} - \cos\theta\right), \tag{6.11}$$

where l is the grating period, s is the spectral order of the radiation, $\beta = v/c$ the particle velocity with respect to the speed of light and θ is the angle of emission. By changing the grating period the wavelength of Smith-Purcell radiation can be tuned, for this set-up a grating period of 250 μm is used to ensure THz frequency

emission for all spectral orders.

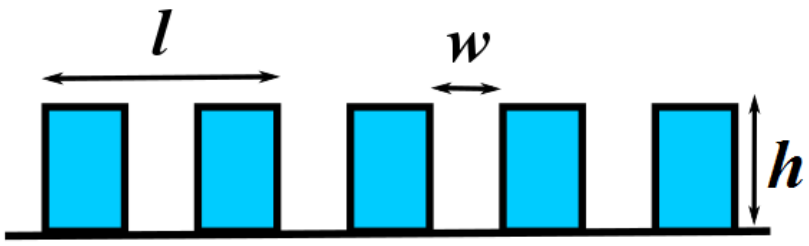

Figure 6.13: An illustration of the grating geometry for Smith Purcell generation, showing grating period, groove depth and groove width.

Figure 6.13 shows the configuration of the grating used for these simulations, the values of the grating geometry are given in Table 6.2 and are similar to those used by Dartmouth [87]. This structure is on the order of a wavelength, with a period on the order of 100 μm, for a metamaterial structure which is subwavelength this period would be much smaller on the order of 10 μm. At these frequencies, the period of a metamaterial structure would push the limit of fabrication and thus for these frequencies, dispersion engineering such as the Smith-Purcell grating are a more feasible option.

Table 6.2: Details of the grating geometry used for the Smith-Purcell simulations.

Parameter	Symbol	Value
Grating period	l	250 μm
Groove Width	w	87 μm
Grating height	h	200 μm
Period	p	30

Methods to improve the interaction of the grating and the beam have been proposed before, including the addition of a plasmonic coating to the grating [131] but grating made entirely from an alternative plasmonic material to enhance surface wave interactions has not been proposed until now [129].

6.3.3 Smith-Purcell radiation generation

To generate Smith-Purcell radiation the grating must be excited by a relativistic electron bunch propagating sufficiently close to the surface. Here an electron bunch passing 35 μm from the grating is simulated using CST Particle studio, this distance has been chosen as it is the distance used in the literature [87]. The

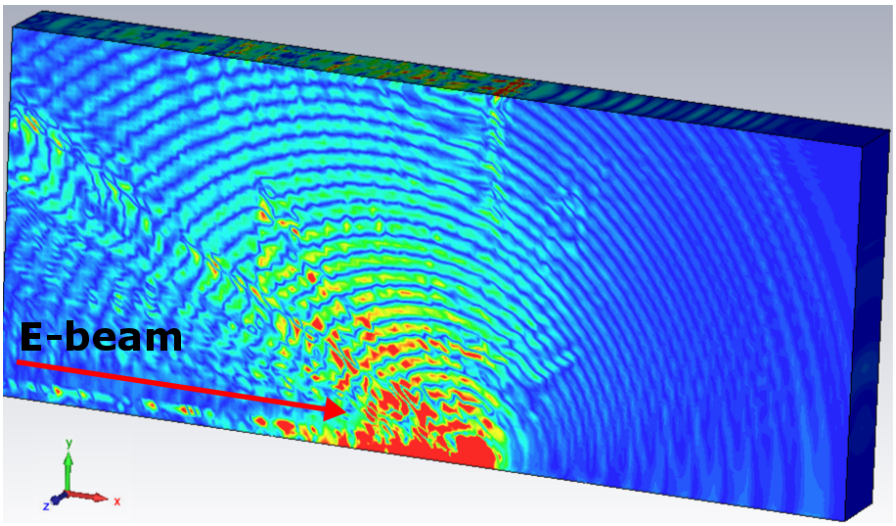

Figure 6.14: The crescents of Smith-Purcell radiation emitted as a relativistic particle passes over the Smith-Purcell grating.

single electron bunch used to excite the grating has an energy 40 KeV, thickness 24 μm, charge 0.048 pC and bunch length 0.1 ps. To monitor the response of the structure, field probes are placed 130° and 50° at a distance of 5250 μm from the centre of the grating. These probes monitor the development of the magnetic field over time allowing for the identification of generated Smith-Purcell and other radiation. A frequency response was obtained from the fast Fourier transform of the time dependent field probe results. In addition to the field probes, a 3D field monitor was used to identify how the field develops as the particle propagates down the structure, the results of this can be seen in Figure 6.14. Crescents of radiation generated as the particle passes over the grating are clearly seen in the field plot, one crescent for every period traversed.

Figure 6.15 shows the longitudinal magnetic field B_z obtained from the magnetic field probe at 130°, there are two clear types of radiation present in the plot. Clear Smith-Purcell radiation is evident between 75 ns and 125 ns, with thirty oscillations, one oscillation for every period of the structure, similar to the one crescent per period shown in Figure 6.14. The second type of excitation between 140 ns and 230 ns is sharper and more closely packed this corresponds to the evanescent waves. The two forms of radiation are distinct and clearly separate.

Figure 6.16 shows the fast Fourier transform of the time plot, giving the frequency response of the field. There is one strong clear excitation and a second smaller less defined excitation present. The stronger excitation centred at 0.355 THz corresponds to the Smith-Purcell radiation observed due to the beam passing the surface of the grating. The evanescent wave signal corresponds to the smaller peak

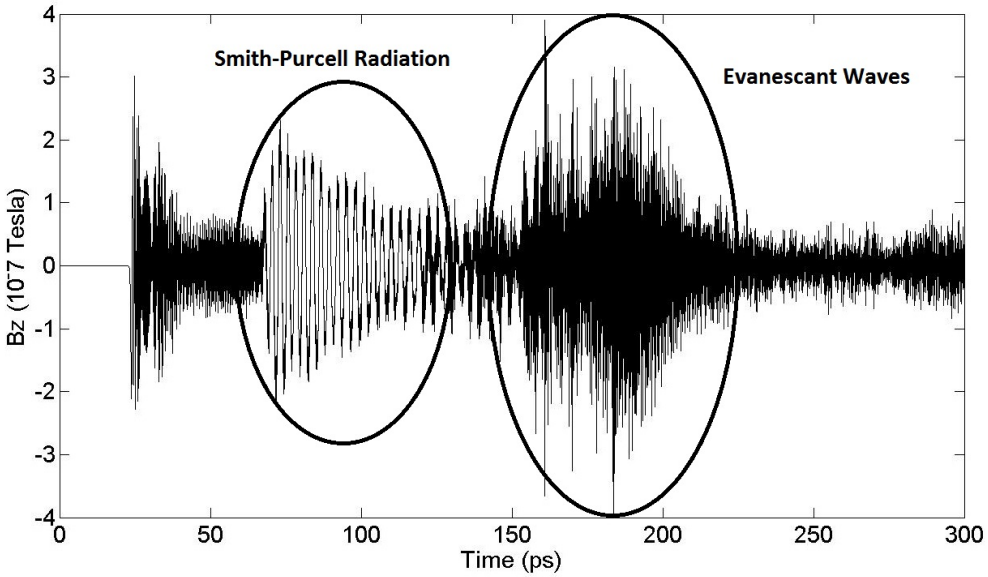

Figure 6.15: The longitudinal magnetic field component B_z at 130° from the centre of the grating, showing both the Smith-Purcell radiation with 30 oscillations and the evanescent waves generated by the bunch.

at 0.286 THz, is independent of radiation angle, and lower than the minimum allowed frequency of Smith-Purcell radiation. From these plots it is clear that the plasmonic material InSb can be used in place of a metal for a Smith-Purcell grating within the THz frequency range, the response observed is very similar to that of a standard metallic grating [132]. The next step is to see if the unique behaviour of plasmonic materials within this frequency range can enhance the interaction between the beam and the grating to increase the spacing, one of the key drawbacks to using these structure within conventional accelerators.

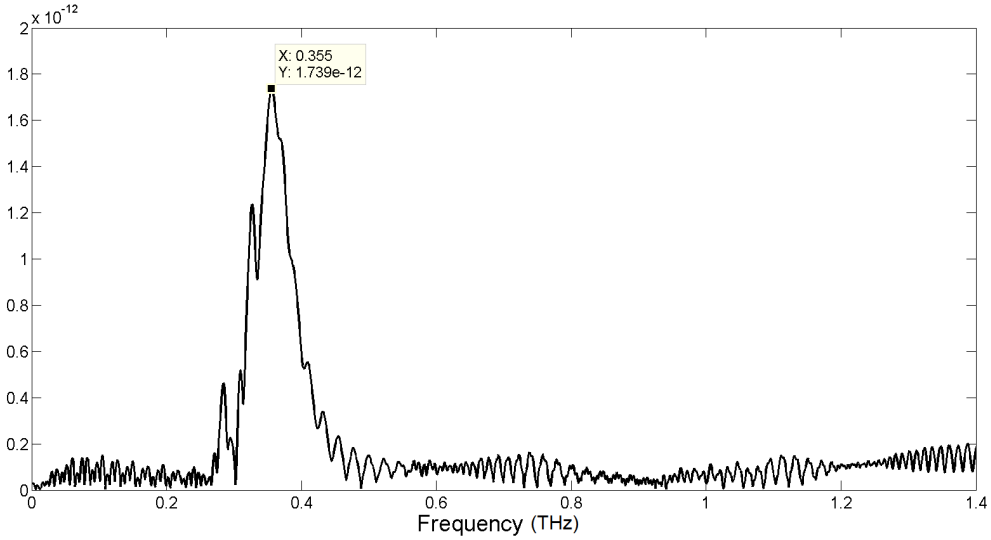

Figure 6.16: The Fourier transform of the time scale plot of magnetic field showing one single spike corresponding the Smith-Purcell.

6.3.4 Indium Antimonide grating for increased beam grating spacing

The beam grating spacing for initial investigations into the use of plasmonic materials for Smith-Purcell generation was set to 35 μm the standard spacing for many experiments [87]. This spacing is very small and can limit experiments as the mechanisms for propagating a beam so close to a structure without collisions are complex and thus simpler methods of particle detection exist. Plasmonic materials have enhanced surface wave interactions which means that the Smith-Purcell response should be enhanced allowing for an increase beam grating spacing, which would make this technique more attractive. To investigate this response an InSb grating was compared to a Perfect electric Conductor (PEC) grating at two increased spacing 55 μm and 75 μm to see if increase response is observed when a plasmonic material is used. To do this field probes were set up to measure the time development of the field at an angle of 130° and then the frequency response was analysed by taking the fast Fourier transform. It is the frequency response gained from the fast Fourier transform that was compared for each material.

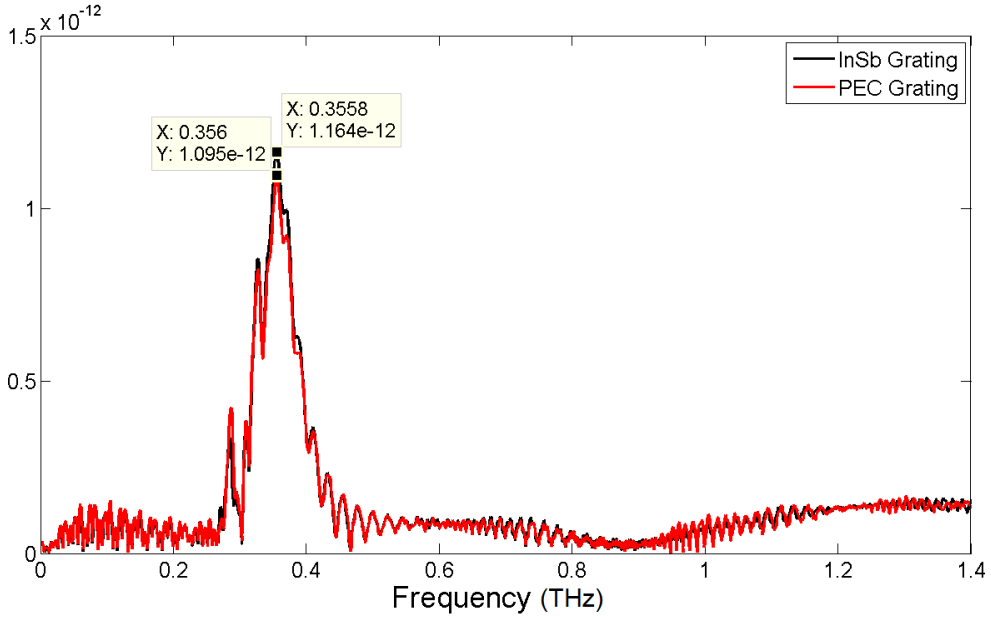

Figure 6.17: The fast Fourier transform results for an the InSb and PEC gratings with a beam grating spacing of 55 μm.

Figure 6.17 shows the frequency response of both InSb and PEC gratings with a beam grating spacing of 55 μm an increase of 20 μm from the standard spacing. At this point the difference between both materials is not very pronounced, the Smith-Purcell radiation is emitted at the same frequency 0.356 THz for both materials. The response for InSb is slightly stronger with a magnitude of 1.164×10^{-12}

compared to the value of 1.095×10^{-12} gained for PEC but at this spacing the difference is minimal. The evanescent response remains unchanged for InSb but slightly stronger for the PEC.

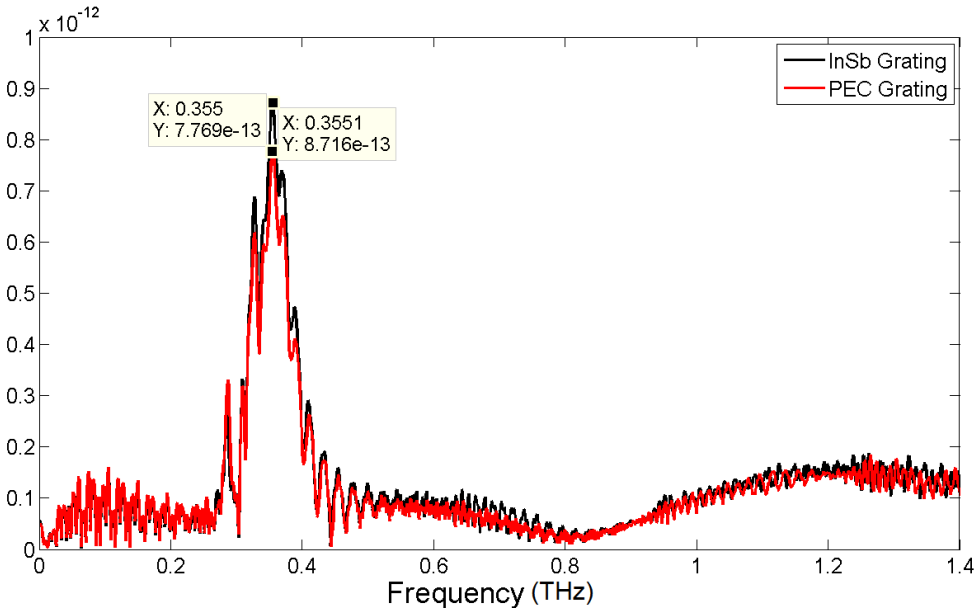

Figure 6.18: The fast Fourier transform results for an the InSb and PEC gratings with a beam grating spacing of 75 μm.

Figure 6.18 shows the frequency response of both InSb and PEC gratings with a beam grating spacing of 75 μm and increase of 40 μm from the standard spacing. At this spacing the difference in response between InSb and PEC is more evident, though the excitations occur at the same frequency 0.355 THz the response for InSb is stronger with a magnitude of 8.716×10^{-13} compared to 7.769×10^{-13} for PEC. It should be noted that PEC is an ideal loss free metal whereas the InSb simulated here exhibits losses, thus if this material were to be compared to a lossy metal, it would show even greater improved performance for increased separations. Though the response of InSb is greater than that of PEC there is still a reduction in strength in comparison to the closer spacing, and thus the spacing still limits the response, but not as significantly as with metallic gratings. The increased spacing of 55 μm obtained using the grating made from the new plasmonic material improves the suitability of this structure for detection purposes.

6.3.5 Conclusions

Here it has been demonstrated that plasmonic doped semiconductors such as InSb can be used to replace metals in Smith-Purcell gratings when used below their plasma frequency. Results from the field probe and the 3D field monitors show

clear crescents of Smith-Purcell radiation propagate when a bunch passes over the grating. Through field probe analysis, clear time development of Smith-Purcell radiation and evanescent wave signals can be identified, with thirty oscillations clearly present, one for each period of the grating passed. In the fast Fourier transform frequency analysis distinct excitations for Smith-Purcell and evanescent waves are identified. The use of InSb and plasmonic materials allows for an increase in the beam grating spacing which is not possible with a purely metallic grating. However as with the metallic grating there are still limitations in spacing and a drop in response magnitude is observed with increased spacing, however this is less pronounced than that of a metallic grating. The magnitude of this spacing has always been a limiting factor of these technologies and increased spacing could lead to easier applications and more development of these technologies.

6.4 The Dielectric Bragg waveguide

In this Section, a cylindrical Bragg waveguide is proposed as an alternative to conventional dielectric lined waveguides, for the generation of high power THz for acceleration applications [133]. The structure comprises of a cylindrical dielectric lined waveguide with the metallic coating replaced by a Bragg reflector comprising of alternating dielectric layers. Starting from the theory of planar Bragg reflectors, a new analytical approach to structural design is derived via numerical simulations. By adjusting the layer thickness condition and the number of layers, the dielectric Bragg waveguide is designed to give the strongest wakefield response. The wakefields can be used for the direct excitation of high-power THz radiation or for high-gradient acceleration.

6.4.1 Dielectric lined waveguides

High power THz sources driven by relativistic electron beams are of growing interest in the wider scientific community. Electron-beam driven devices are well developed for large scale synchrotrons [31] and Free-Electron Lasers (FELs) [32]. However, research is now pushing towards more efficient, compact and cost-effective devices. Dielectric Lined Waveguides (DLWs) are potential candidates for small scale THz generation [134]. Dielectric structures support the generation of Coherent Cherenkov Radiation (CCR) [135] with high peak power and very narrow line widths, for advanced radiation sources and applications in particle detection.

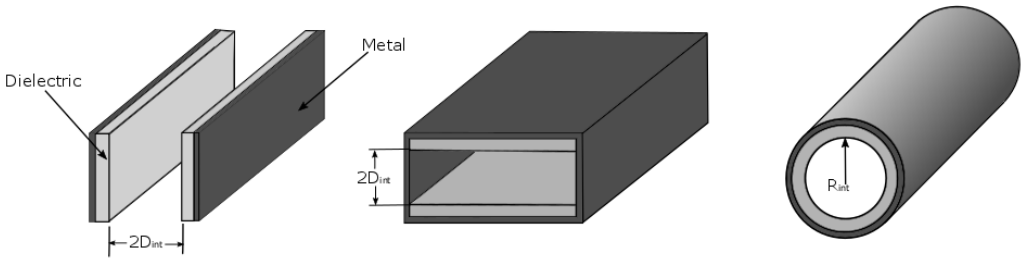

Figure 6.19: Conventional dielectric lined waveguides for accelerator applications, A) Planar slab symmetric, B) Rectangular and C) Cylindrical dielectric lined waveguides.

These Dielectric Lined Waveguides (DLWs) and Dielectric Bragg Waveguides (DBWs), act as small scale accelerators, fulfilling the basic requirement that they support the propagation of a longitudinal mode that will accelerate non relativistic particles. The dielectric coating slows the propagating electromagnetic waves such that the beam propagates at a higher phase velocity than the electromagnetic radiation and hence generates Cherenkov radiation which can be used for wakefield acceleration, it is through this mechanism that structures such as DLWs and dBWs accelerate particles.

In DLWs the dielectric wall thickness is optimised to only excite the fundamental mode, increased thickness results in the appearance of higher order modes which weaken the fundamental mode of operation. Figure 6.20 shows this effect for a simple diamond DLW with different dielectric thicknesses. The thickness is the difference between the inner radius a and the outer radius b, for these simulations the inner radius is set at a=40 μm. In Figure 6.20, the strongest response is obtained for a thickness of 10 μm (red line) however this is very narrowband, a broadband response is gained from a thickness of 5 μm (green) and secondary excitations are clear for a thickness of 30 μm (blue) which weaken the initial response, and optimal thickness is between 5 μm and 15 μm.

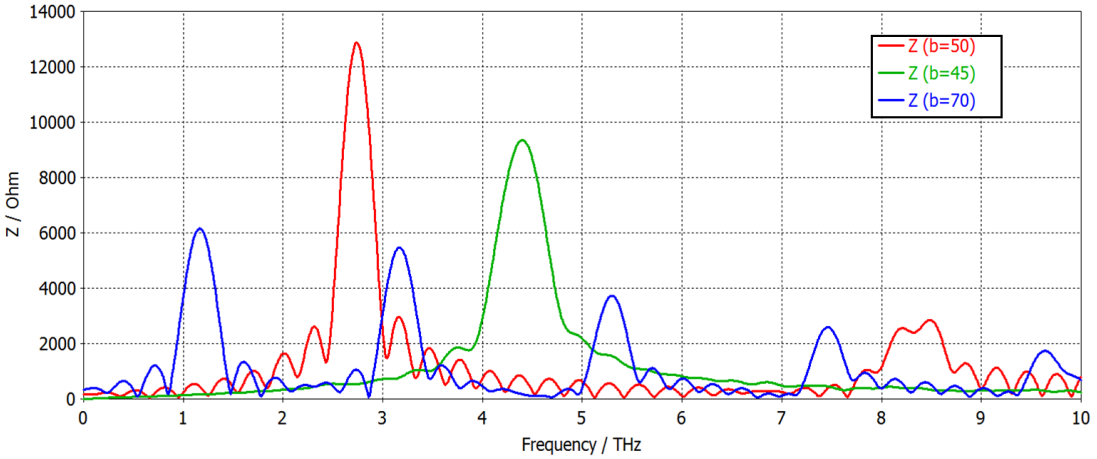

Figure 6.20: The longitudinal wake impedance as a function of frequency for a cylindrical dielectric lined waveguide with changing dielectric thickness.

6.4.2 Planar Bragg waveguide

Photonic Band Gap (PBG) structures, such as the Bragg waveguide [136] [137], have gained increasing interest due to their ability to support efficient Cherenkov radiation without metallic components. The introduction of PBG structures adds control over mode characteristics and damps unwanted higher order modes meaning GeV/m accelerating gradients are achievable. These Bragg structures have the ability to store higher energies for a given gradient making them desirable for high gradient structures. The use of dielectric multi-layers in place of the metallic coating in DLWs eliminates the associated dissipative losses in the THz regime. Figure 6.21 shows a planar Bragg waveguide which uses photonic structures for confinement instead of metallic coatings. The layers of dielectric with alternating low and high permittivity enhance the constructive interference to confine the mode; a higher contrast in permittivity between the layers will lead to a higher reflectivity and thus better confinement. The advantages of using Bragg reflectors in place of the metallic coating in conventional dielectric lined waveguides are numerous, they allow for higher energy operation, increase mode control, damp unwanted higher order modes and reduce coupling to transverse wakes.

The frequency of operation is dictated by both the matching layer thickness and it's permittivity. Once the wavelength of operation is defined it is then possible to determine the thickness of the subsequent layers if the permittivity of those layers is known. The thickness criteria used for planar structures is as follows;

$$d_i = \frac{\lambda}{4\sqrt{\varepsilon_i - 1}} \tag{6.12}$$

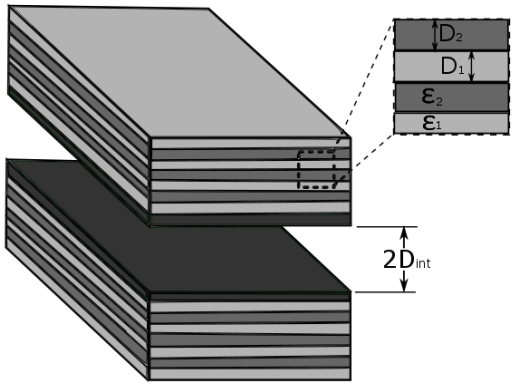

Figure 6.21: A planar Bragg accelerator, showing the matching layer and the alternating dielectric layers.

Where λ is the desired wavelength, ε_i is the permittivity of the layer and d_i is the thickness of the layer, this rule is known as the quarter-wavelength condition for constructive interference.

6.4.3 Material choices

The mechanism that makes a Bragg waveguide effective is the high contrast in permittivity between the two alternating dielectrics, a higher contrast implies better confinement and thus better performance. Ideally this would mean having a dielectric with very low permittivity and one with very high permittivity, however this is limited by the existing available dielectrics and those that are suitable for accelerator applications. The low permittivity dielectric is often chosen to be the same permittivity as the matching layer. The matching layer is determined by the performance of a dielectric layer on a conventional dielectric lined waveguide as the Bragg layers are effectively replacing the metal.

A number of different dielectrics conventionally used for dielectric lined waveguides were investigated and diamond with permittivity ε=5.68 performed best, thus is used as both the matching layer and the low permittivity material. To contrast the permittivity of diamond, a high permittivity material is needed, however the choice of this material is limited by thermal break down issues and vacuum compatibility. A commonly used material with a relatively high permittivity in comparison to diamond is Zirconia-Toughened-Alumina (ZTA) [137] which has a permittivity of ε=10.6, is low loss in the THz frequency range and has good thermal conductivity, therefore is a good choice of material. Due to these factors and the relative difference in permittivity between ZTA and diamond, the high permittivity material for the dielectric Bragg grating is taken to be ZTA.

6.4.4 The cylindrical Bragg waveguide

The cylindrical Bragg waveguide is attractive over the planar Bragg waveguide as it achieves higher values of interaction impedance [136], and allows for a greater aperture for the beam to propagate without compromising this interaction impedance. The planar Bragg waveguide remains relatively well studied, and yet despite the advantages of a cylindrical schemes, they are not as well developed, due to the complexity of fabrication and the complex mathematics required to determine the layer thickness to obtain confinement of the modes. In this Section of the Chapter a cylindrical Bragg waveguide for Cherenkov applications is considered and a simplified rule for determining layer thickness is developed for a proof of concept process rather than determining the electric field at each dielectric boundary.

The dielectric Bragg waveguide comprises of a cylindrical multilayer dielectric waveguide, as shown in Figure 6.22. It has a low permittivity diamond match-

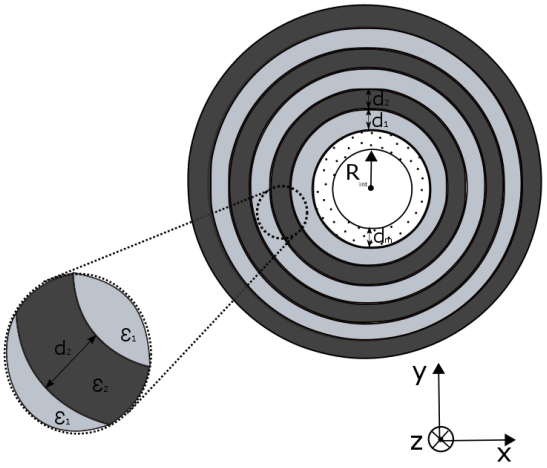

Figure 6.22: Schematic of the dBW showing matching layer and subsequent alternating dielectric layers. d_m is the thickness of the matching layer and d_1 and d_2 are the thicknesses of the alternating dielectrics.

Table 6.3: The geometrical parameters of the dBW and the parameters of the wakefield simulations.

Parameter	Symbol	Value
Charge	Q	200 pC
Length	l	1000 μm
rms bunch length	σ_z	10 μm
Inner Radius	R_{int}	40μm
Matching layer thickness	d_m	15 μm
ZTA permittivity	ε_{ZTA}	10.6
ZTA layer thickness	d_{ZTA}	9.6 μm
Diamond permittivity	ε_{di}	5.68
Diamond layer thickness	d_{di}	15.3 μm

ing layer determined by studies on a metallic coated dielectric lined waveguide. This matching layer is then surrounded by six alternating layers of dielectric that provide a high contrast of permittivity, ZTA with a permittivity of $\varepsilon_{\text{ZTA}} = 10.6$ and diamond with a permittivity of $\varepsilon_{\text{di}} = 5.68$. The matching layer thickness is determined from 3D numerical simulations of a diamond dielectric lined waveguide, through these studies the thickness of $15\mu m$ was determined to provide the strongest response without generation of secondary excitations. The fundamental frequency of the structure was found to be 2.918 THz giving the a fundamental wavelength of $\lambda_0 = 148.7\mu$m which can then be used to determine the thickness of the subsequent dielectric layers. The parameters of the structure can be found in Table 6.3.

6.4.5 Matching layer conditions

There exists a clear and well-defined rule for determining the thickness of the Bragg reflecting layers for a planar Bragg waveguide, however for the cylindrical Bragg waveguide this becomes more complex, requiring analysis of the electric field at each interface and within each layer. A simplified rule for determining the layer thickness which would allow for quick analysis of a cylindrical dBW needs to be developed. In this section a simplified rule to determine the layer thickness is discussed and used to provide a proof of concept design for a cylindrical Bragg waveguide for coherent THz generation, for testing on VELA/CLARA [138].

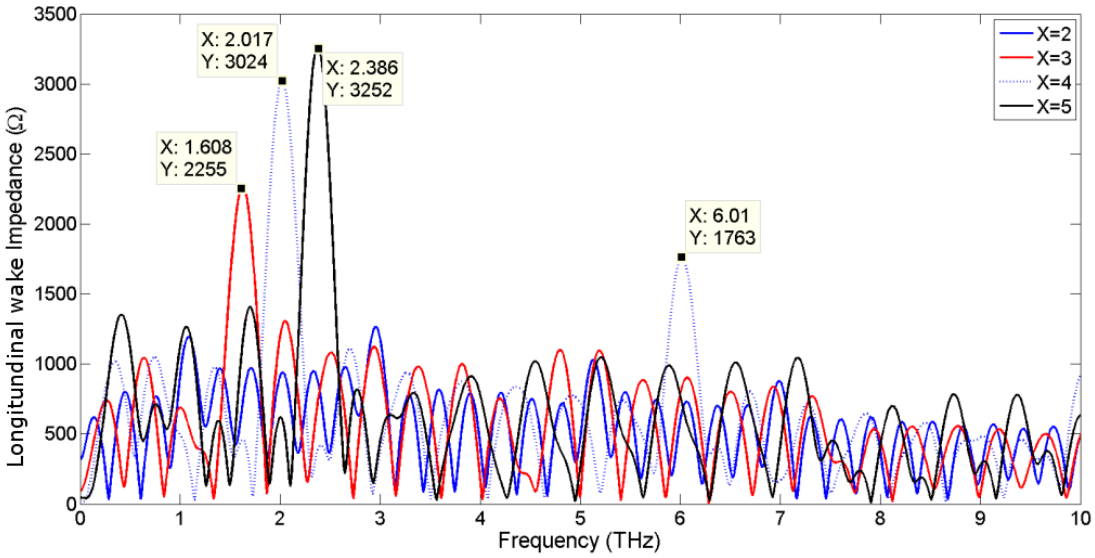

Figure 6.23: The change in longitudinal wake impedances of the dBW with changing X for the thickness conditions.

Using the fundamental wavelength $\lambda_0 = 148.7\mu$m of a 15 μm diamond DLW, it is possible to analytically determine the thickness of the subsequent layers, to provide optimal constructive interference. In a planar Bragg reflector, this thickness d_n follows the quarter wavelength rule [137], however, for cylindrical schemes this rule does not hold and more complex mathematics is generally used. In order to modify the planar rule for the cylindrical case, we investigated a number of different thickness criteria of the form,

$$d_i = \frac{\lambda}{X\sqrt{\varepsilon_i - 1}} \tag{6.13}$$

where X represents an integer ranging from 2 to 5, λ is the fundamental wavelength of the structure and ε_n is the permittivity of the layer. Each of these conditions is simulated for a six layer set-up. Wakefield simulations are performed using a

hexahedral mesh with 10 cells per wavelength in CST particle studio [98]. Excitations of the longitudinal wake impedance show interaction between the beam and the structure, the frequency and magnitude of these excitations is measured to quantify the interaction. Electrical boundaries which set the tangential electric field to zero are used in all directions and a magnetic symmetry plane is used in the YX plane to reduce simulation time without compromising numerical accuracy.

Figure 6.23 shows the longitudinal wake impedance excitations for each of the conditions from X=2 to X=5. It can be seen that the fifth wavelength condition provides the best results with an excitation of 3.25 kΩ at 2.39 THz, the half wavelength condition gives no clear excitation and the third wavelength condition shows only a weak excitation. For the quarter wavelength condition as used in a planar Bragg waveguide a response nearly as strong as the fifth wavelength condition is seen however a secondary excitation at 6 THz is observed and these higher order excitations are undesirable. Therefore for a simplified rule to determine layer thickness, the fifth wavelength rule has been chosen, this results in diamond layers with thickness $d_{\mathrm{di}} = 15.3$ μm and ZTA layers with thickness $d_{\mathrm{ZTA}} = 9.6$ μm.

Figure 6.23 shows no higher order modes except when X=4. A standard diamond DLW $d_{\mathrm{di}} = 15$ μm typically exhibits two higher order modes in this frequency range [134], thus the addition of Bragg layers damps the higher order modes leading to single mode operation. It can be noted that a significant amount of low level excitation is also present within the spectral range around the desired frequency. This is likely due to the condition resulting in the constructive interference being enhanced but not sufficiently so as to form a perfect reflector. One way to further improve confinement is to increase the number of dielectric layers, which is investigated in the next Section.

6.4.6 Optimisation of the dielectric Bragg waveguide

Figure 6.24 shows the results obtained by varying the number of layers from six to twelve, to investigate how this effects the confinement of the modes. It can be seen that for all set-ups with more than 6 layers this results in a reduction in peak impedance to 3.1 kΩ and a slight shift in frequency from 2.375 THz to 2.273 THz. There is also a slight reduction in the noise around these modes but it is not sufficient to say that an increase number of layers significantly improves performance. The 8 layer Bragg reflector shows the greatest reduction in spectral noise, however further investigation into reduction of this noise needs to be carried

out. This effect most likely originates from the thickness condition not resulting in a full Bragg reflector, as the thickness value determined by the simplified rule does not lead to fully enhanced constructive interference or a perfect reflector.

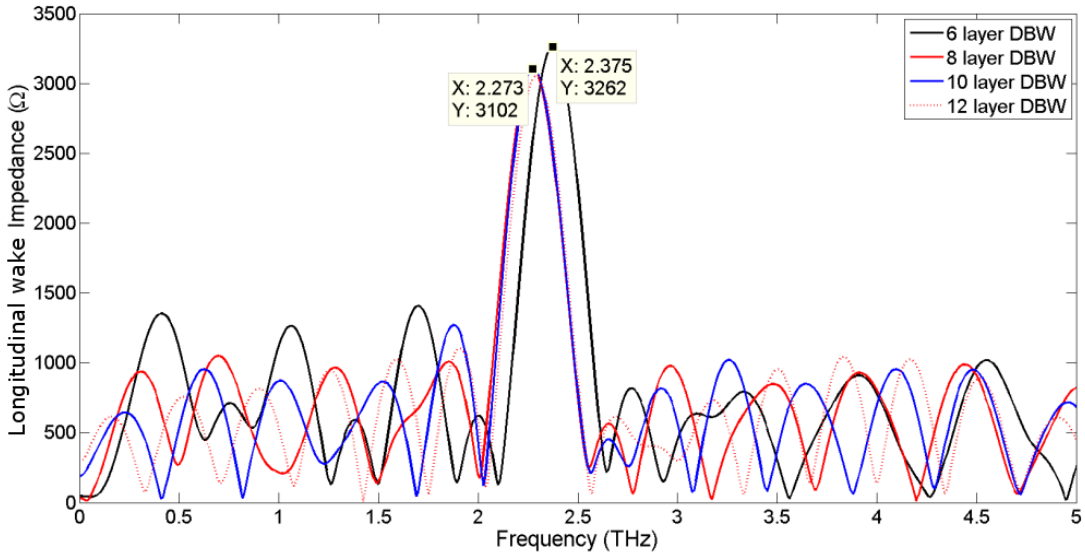

Figure 6.24: The change in longitudinal wake impedance with increasing number of Bragg reflector layers.

Figure 6.25 shows the field within an 8 layer Diamond-ZTA dielectric Bragg waveguide as a particle bunch propagates along the centre of the structure. It can be seen from Figure 6.25 that there is not full confinement of the radiation associated with the beam and it is clear that further study needs to be made into improving radiation confinement if this project were to be taken further.

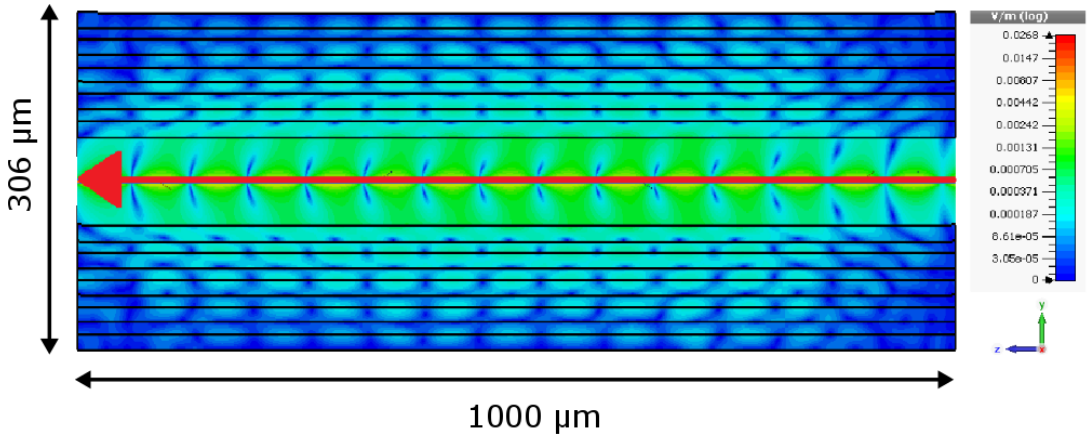

Figure 6.25: The absolute value of electric field for the optimised dBW showing the path of the electron beam.

The structure presented at the THz meeting for VELA was that of a diamond-ZTA

dielectric Bragg waveguide with a diamond matching layer of thickness 15 μm, a fifth wavelength thickness condition resulting in $d_{\mathrm{di}} = 13.8$ μm and $d_{\mathrm{ZTA}} = 9.6$ μm and 8 Bragg reflector layers. This set-up results in an impedance of 3.1 kΩ at 2.27 THz for a length of 1000 μm. However if this were to be fabricated a more rigorous mathematical method for defining the layer thickness would be required to fully confine the beam.

6.4.7 Conclusions

Within this Section it has been shown that dielectric Bragg reflectors can be used in place of the metallic coating on conventional dielectric lined waveguides, to form dielectric Bragg waveguides, for coherent Cherenkov radiation in the THz regime. By replacing the metallic coating of a dielectric lined waveguide with multi-layers of dielectric, high peak powers and single mode operation can be obtained, with a clear reduction in higher order modes being observed. A simple proof of concept mathematical model is presented to determine the matching layer thickness and it is clear that though this works to prove that a dBW can be used in the same way as a DLW, further rigorous mathematical analysis of the thickness condition is required to fully confine the radiation and thus have efficient operation.

6.5 Summary of dispersion engineering for high frequency operation

Recent advances in accelerator science have made high frequency operation desirable, this poses a number of challenges for metamaterial use within this range and has led to investigating methods to improve metamaterial operation at these frequencies and when needed, to explore alternative forms of dispersion engineering. This has focused on plasmonic materials and how they can be used to overcome the limits of metals, both in terms of loss at high frequencies for metamaterials and for improved surface wave interactions in Smith-Purcell gratings. In addition to this the intergeneration of PBG structures into accelerator design has been considered by investigating Bragg reflectors as a replacement for the metallic coating on dielectric lined waveguides to form dielectric Bragg waveguides. These methods have been investigated to provide novel alternatives to conventional accelerators and diagnostic techniques and aim to operate at small scales similar to those of the dielectric laser accelerator at SLAC, moving towards the accelerator on a chip design.

Alternative plasmonic materials provide a strong low loss alternative to conventional metals in both SRRs and Smith-Purcell gratings. The Smith-Purcell grating made from the new plasmonic material InSb successfully behaves like a conventional metallic grating, the expected enhancement of surface plasmons leading to increased beam grating spacing was not as significant as expected, however the comparison here was made to PEC, a loss free ideal conductor, and therefore a greater improvement would be seen for a comparison to a lossy metal. In terms of the SRRs, the response of the resonators made from new plasmonic materials is much more encouraging, GZO is one of the best performing materials exhibits narrow band resonances on an Alumina substrate reaching -56 dB, a strong response with the added benefit of this material being much lower in losses than the conventional plasmonic materials. For broadband operation the intermetallic TiN showed strong broadband resonances on low permittivity substrates reaching -27.86 dB on FR-4 substrate, which could lead to future high frequency applications for metamaterials in accelerators.

The dielectric Bragg waveguide shows potential as a good alternative to conventional DLWs at THz for both generation of radiation and acceleration, however requires further analysis of the matching layer condition to outperform conventional DLWs. The proof of concept mathematical method was sufficient to prove the suitability of such a structure as a replacement for conventional dielectric lined waveguides, however there is a need for a full mathematical analysis of the confinement formed by the Bragg layers. Without an improved matching layer condition, the Bragg waveguide does not provide enough confinement to perform to the standard of conventional dielectric waveguides. With full confinement being provided by the Bragg layers, this waveguide would form a good high power alternative to metal coated structures.

In summary, plasmonic materials prove to be a way towards considerable improvement of metamaterials at high frequencies as they effectively remove the material challenges posed by the frequency range, making fabrication methods the only limitation on the structure. While fabrication continues to limit metamaterials, wavelength scale dispersion engineering has been demonstrated to form a promising alternative when operating at these frequencies. These structures are expected to gain more interest in subsequent years and pave the way towards developing smaller scale high frequency accelerators with multiple miniaturised components.

Chapter 7

Summary

7.1 Conclusions

This thesis focused on the design of a metamaterial loaded waveguide for particle accelerator applications. The metamaterial loaded waveguide was designed to exhibit a left handed mode which can be used to generate backward propagating Cherenkov radiation. This structure utilises the generated backward propagating Cherenkov radiation for applications in; coherent sources, particle acceleration and as a non-destructive particle detector. The metamaterial loaded into the waveguide is comprised of Complementary Split Ring Resonator (CSRR) sheets which exhibit negative permittivity due to their resonant nature, and lead to negative permeability when formed into patterned waveguides which confine transverse magnetic (TM) modes. As a result of this, the fundamental TM-like mode shows left handed behaviour.

The emphasis of this work was to propose a realisable design for a metamaterial loaded waveguide in which the robustness of the metasurface in terms of both resistance to high power and structural integrity are taken into account. The initial design of the CSRR loaded waveguide investigated in this work is based on a well-known metamaterial unit cell for which a few proposals for accelerator applications can be found in the literature. In previous published work however, the metamaterial forms an unbounded infinite structure for the beam to propagate through, whereas here the realistic case of having the metallic walls of a waveguide truncating the metamaterial is considered. The initial design is simulated and found to exhibit a TM_{31}-like mode at 5.5 GHz which gives rise to left handed behaviour and is suitable for accelerator applications. This design is novel and could lead to a proof-of-concept experiment in the field. Nevertheless, the origi-

nal design presented important limitations which needed to be addressed before a prototype could be fabricated. First of all, the thin sheet thickness used, requires support to be loaded in the waveguide and is unlikely to withstand the high power environment associated with accelerator systems. Additionally the initial design exhibited a high number of hybrid modes which further increase the complexity of coupling the right RF mode to the structure, thus a reduction in the number of hybrid modes supported by the structure around operation is desirable. To alleviate these issues and to take the work of metamaterials in accelerators beyond merely simulation work, a number of design considerations on the original structure were investigated.

The aims of the design considerations are as follows; to reduce the surface current and number of hybrid modes, to increase the fabrication suitability and resistance to high power, while maintaining field strength and beam coupling parameters. The design considerations investigated to address these aims were;

- Waveguide A: increased sheet thickness of 1 mm and no other changes.
- Waveguide B: increased ring separation changing i from 4.6 mm to 4 mm, increased ring gap g=0.8 mm and no other changes.
- Waveguide C: increased sheet thickness of 1 mm, increased ring separation i=4 mm and increased ring gap g=0.8 mm.
- Waveguide D: the addition of ring curvature with a radius of curvature 0.5 mm and increased sheet thickness of 1 mm.

All these modifications address two or more of the above listed aims. The modifications were investigated via unit cell analysis and then full structure analysis both in terms of electromagnetic and wakefield response, via simulations. All the designs significantly reduced the number of hybrid modes within the waveguide structure, however some negatively impacted the overall performance of the structure. Both waveguide C, with increased sheet thickness and increased ring separation, and waveguide D, with ring curvature of 0.5 mm, showed significant reductions in performance both in terms of the beam coupling parameters and the wakefield response, despite improved fabrication and a reduction of hybrid modes.

The best response was given by the design with increased ring separation and no other change, which exhibited a strong TM_{31}-like at 5.79 GHz with an R/Q of 7.9 kΩ/m, a shunt impedance of 27 MΩ/m and a longitudinal wake excitation of 10.8 kΩ at 6.28 GHz which corresponds to the TM-like mode. The design with

increased sheet thickness and no other modification performed well but not as well as increased ring separation alone, exhibiting a strong TM_{31}-like at 5.86 GHz with an R/Q of 4.5 kΩ/m, a shunt impedance of 23 MΩ/m and a longitudinal wake excitation of 10.6 kΩ at 6.42 GHz. These values are strong but not quite as good as those found for the increased spacing. Focusing on improved performance only it is clear that the design with the increased ring separation and no other change is most desirable, however these modifications were not performed to enhance performance but rather maintain it while improving the structures resistance to a high power environment, which a design with no increased sheet thickness cannot provide. The final chosen design was that of increased sheet thickness alone, due to the improved fabrication suitability and increased resistance to damage from high power operation, additionally performance was well maintained as the electromagnetic performance was better than the nominal waveguide and the wakefield response of the same magnitude.

Once a final design was chosen, particle in cell simulations were performed to characterise the structure's interaction with a beam. Analysis of the excitation of the longitudinal electric field when a beam is present and the fields this generated were provided. This analysis was provided for three existing beam systems, a low energy commercial electron gun, the current beam on VELA and the high energy FACET beam at SLAC for comparison. Each beam generated an interesting response within the structure, the FACET beam generated the strongest excitations, however the generated field had a poorly defined mode polarization due to the small spot size and resultant increased separation between the beam and the metasurface sheets. The commercial gun resulted in the generation of a strong TM_{11} mode, however this mode is unsupported by the metamaterial loaded waveguide and thus away from the gun, the coupling to this beam diminishes significantly, making it unsuitable for accelerator applications. The VELA beam produced weak excitations in comparison to the other beams, however at 6.3 GHz it generates an excitation that corresponds to a well-defined form of the TM_{31} mode, indicating this beam would be ideal for the desired left handed applications. With the post CLARA installation upgraded VELA parameters leading to a higher power beam, with the aim to generate strong excitations and well defined fields. In addition to this an initial coupler design was presented and the challenges to coupling to the correct mode discussed. Therefore the structure is now at a stage where fabrication and testing can begin.

In the final Chapter of this thesis, methods of high frequency dispersion engineering are discussed for integration within high frequency compact accelerator

systems. These structures as discussed as current fabrication techniques limit the scales and hence the frequencies that metamaterials can reach and thus alternative designs are required. The use of plasmonic effects and emerging plasmonic materials as alternative to noble metals is discussed not only as a way to bring metamaterials into the optical and infra-red frequencies with reduced losses, but as an alternative to metals in Smith-Purcell gratings to enhance response. In addition to this an all dielectric Bragg structure was discussed as an alternative to dielectric lined waveguides for acceleration. These designs push metamaterials and dispersion engineering beyond the THz frequency range enabling advanced accelerator applications in the future.

7.2 Future work

The future plan for the loaded waveguide structure is to fabricate the metasurface sheets, perform cold tests to confirm left handed behaviour and then perform beam tests to confirm backward propagating Cherenkov radiation. If the proof-of-concept experiment on this structure is successful, then the incorporation of the loaded waveguide structure into an accelerator system can be considered. For example, the require length of the structure if it were to be used as a form of non-destructive detector, and where on the accelerating system should it be placed.

7.2.1 Challenges in realising the CSRR loaded structure

With the next step in the work being the fabrication of the structure for testing, there are two key challenges that need to be addressed and overcome. These relate to the physical systems involved, both the creation of metasurface sheets and the method for coupling RF into the structure.

Metasurface fabrication

The metasurface has a number of fine features to cut out, and so care must be taken when fabricating them to avoid damage and defects which can affect the overall electromagnetic behaviour of the structure. At the mm scales used for the metasurface, milling or laser cutting are the best options, as this can cut through the 1 mm thick copper. Since the metal separating the rings is only 0.2 mm the manufacturing tolerances need to be less than 0.01 mm, which means precision

machining is required. To find the best process the results from different machining techniques need to be considered and compared.

Another factor that needs to be considered is the vacuum compatibility of the metasurface sheets, as stated the CSRRs were chosen as they can be fabricated from metal and thus be made vacuum compatible. However, care needs to be taken that the cutting process does not create any rough edges that could lead to spikes in field emission and ultimately breakdown. Similarly, the braising used to fix the metasurfaces to the waveguide walls will need to be suitable for operation in a vacuum.

Coupler design

An initial coupler design was presented in Chapter 5, and the challenges facing the design discussed briefly, however the challenges and coupler design require further consideration. The desired mode of operation for the structure as identified in both the electromagnetic analysis of the structure and the particle in cell simulations at around 5.9 GHz, is the TM_{31} mode which is not straight forward to couple into the structure. Using the higher order mode requires a coupler to be designed such that the majority of the energy is coupled to this higher order mode, rather than the fundamental mode. Designs based on multiple inputs, resonant elements and the introduction of notches, are currently being investigated by Divya Unnikrishnan at Lancaster University to solve for this problem.

The second challenge to coupling the RF into this structure is the frequency at which this mode occurs 5.86 GHz, which is above the standard operational frequency for the S-band waveguide the metasurface is loaded into. Though this means that higher frequencies of operation are obtainable at larger length scales using a metamaterial structure, it adds complexity to the coupling. One way to overcome the frequency mismatch currently being investigated is to introduce a taper between the coupler and the loaded waveguide to provide frequency conversion.

7.2.2 Further Design considerations

A number of design considerations were considered to make the structure more robust in a high power environment and to reduce the surface current. Though these design modifications are a significant improvement on the unrealistic design

presented in previous work there are still factors that can limit the applications of the structure that can be improved on, these include;

Heating/thermal damage

Though the current design has shown to reduce the surface current build up on the sheets and thus reduce the restive heating, the structure will still present limitations in terms of operating power. The power limit on the structure needs to be quantified both through further simulations and then testing of the fabricated structure. Once a power limit has been determined, the aim should then be to raise this limit by mitigating the effects of the high power environment. As heating is the most detrimental effect of working in a high power environment, it is important to find way not only to reduce the build-up of heating in the structure but to cool the structure if heating occurs.

Using thermal analysis and observing where structural deformation occurs after testing, will aid in the identification of hot spots in the structure, where cooling will be required. One method of cooling would be to introduce thin water cooling pipes that run along the metasurface sheets, these could also be used as a method of further supporting the structure if needed. The introduction of these pipes could have an effect on the behaviour of the metamaterial and thus if they were to be implemented, further electromagnetic studies would be required.

Mechanical excitation

As the metasurface sheets and the metamaterial structure as a whole are very sensitive to deformation, therefore it is important to see if mechanical excitation will affect the metamaterial behaviour. If vibrations in the structure lead to mechanical resonances that result in the metasurface sheets moving, this could lead to an altered electromagnetic response as it could change the spacing between the layers or lead to damage to resonator elements the structure which will have an effect on the overall behaviour.

To investigate these effects, the structure should be mechanically excited to identify if it has any resonant eigen modes that will occur within the structures operation frequency, and if so how they affect the behaviour of the structure. If the effects are significant then methods of mitigation will be required to reduce the impact of mechanical resonances.

7.2.3 Cold measurements

The initial cold test, in which the structure is excited only by input RF and no electron beam are required to confirm the existence of a left handed mode suitable for the structures applications. To analyse the left handed behaviour of the structure, the S-parameters need to be obtained and analysed. Initial analysis requires only the S_{11} parameter, as a resonance dip around the simulated frequency of the TM-like mode would indicate the existence of such a mode. To fully characterise the behaviour of the structure full S-parameter analysis as detailed in Chapter Two of this thesis would be required, this would allow for the effective permittivity and permeability to be determined as well as the refractive index and impedance of the structure. To confirm the accuracy of the results, multiple parameter retrieval methods would be used and compared.

The s-parameter results would be obtained using standard waveguide to SMA couplers and a network analyser, the initial tests could be performed using standard waveguide to SMA couplers and should provide the information required to determine the behaviour of the structure. Tests with the coupler would provide the s-parameters of the interesting TM_{31}-like mode and would allow verification on its left handed nature.

7.3 The future of metamaterials in accelerator

The field of metamaterials in accelerators is ever growing, where once the work done in this thesis was one of the few projects on metamaterials in accelerator environment, this is no longer the case. The growth of metamaterials in accelerators comes from a need to have better control over the dispersion properties of accelerator systems. Not only are left handed media being considered for alternative methods of accelerator or diagnostics but they are being considered to create compact radiation sources, and as methods to control and manipulate the dispersion in accelerator schemes.

By considering how to make metamaterial structure for accelerator more realisable and creating designs that are resistant to high power environments and robust, this work has taken a step forward in the field by addressing important challenges in the design of metamaterials which could seriously impair their further development into high power applications. To advance the field these structures need to be fabricated, tested and analysed, so that methods that improve performance can

be found that do not limit the applications. By considering how the environment affects metamaterials, they can be adapted and used to alleviate existing issues within accelerator environments and to form novel methods of acceleration.

With a significant push in recent years towards more compact accelerators, developing metamaterials designs for high frequency operation provides a convenient way to scale down accelerator components. High frequency metamaterials are already a growing area of research, with numerous schemes in the optical and THz range. Significant effort is still required to make this technology and its countless possibilities suitable for high power, to enable future advancements in acceleration, however the work detailed in this thesis is the first step towards achieving this.

Bibliography

[1] M Stanley Livingston. *Advances in Electronics and Electron Physicst*, **50**.

[2] Wolfgang KH Panofsky. *SLAC Beam Line*.

[3] Alexej Grudiev, S Calatroni & W Wuensch. *Physical Review Special Topics-Accelerators and Beams*, **12**, 10 (2009) 102001.

[4] EA Peralta, K Soong, RJ England, ER Colby, Z Wu, B Montazeri, C McGuinness, J McNeur, KJ Leedle, D Walz et al. *Nature*, **503**, 7474 (2013) 91–94.

[5] M Litos, E Adli, W An, CI Clarke, CE Clayton, Sébastien Corde, JP Delahaye, RJ England, AS Fisher, J Frederico et al. *Nature*, **515**, 7525 (2014) 92–95.

[6] Wei Lu, M Tzoufras, C Joshi, FS Tsung, WB Mori, J Vieira, RA Fonseca & LO Silva. *Physical Review Special Topics-Accelerators and Beams*, **10**, 6 (2007) 061301.

[7] R. wideroe. *Arch. f. Elektrotech*, **21** (1929) 387.

[8] Alexander Wu Chao, Karl Hubert Mess, Maury Tigner & Frank Zimmermann. "Handbook of accelerator physics and engineering". World scientific (2013).

[9] Xiaoming Wang, Rafal Zgadzaj, Neil Fazel, Zhengyan Li, SA Yi, Xi Zhang, Watson Henderson, Y-Y Chang, R Korzekwa, H-E Tsai et al. *Nature communications*, **4**.

[10] T. P. Rowlands-Rees, C. Kamperidis, S. Kneip, A. J. Gonsalves, S. P. D. Mangles, J. G. Gallacher, E. Brunetti, T. Ibbotson, C. D. Murphy, P. S. Foster, M. J. V. Streeter, F. Budde, P. A. Norreys, D. A. Jaroszynski, K. Krushelnick, Z. Najmudin & S. M. Hooker. *Phys. Rev. Lett.*, **100** (2008) 105005. `http://link.aps.org/doi/10.1103/PhysRevLett.100.105005`

[11] T. P. A. Ibbotson, N. Bourgeois, T. P. Rowlands-Rees, L. S. Caballero, S. I. Bajlekov, P. A. Walker, S. Kneip, S. P. D. Mangles, S. R. Nagel, C. A. J. Palmer, N. Delerue, G. Doucas, D. Urner, O. Chekhlov, R. J. Clarke, E. Divall, K. Ertel, P. S. Foster, S. J. Hawkes, C. J. Hooker, B. Parry, P. P. Rajeev,

M. J. V. Streeter & S. M. Hooker. *Phys. Rev. ST Accel. Beams*, **13** (2010) 031301. http://link.aps.org/doi/10.1103/PhysRevSTAB.13.031301

[12] SPD Mangles, CD Murphy, Z Najmudin, AGR Thomas, JL Collier, AE Dangor, EJ Divall, PS Foster, JG Gallacher, CJ Hooker et al. *Nature*, **431**, 7008 (2004) 535–538.

[13] Pisin Chen, JM Dawson, Robert W Huff & Thomas Katsouleas. *Physical review letters*, **54**, 7 (1985) 693.

[14] Haiyang Lu, Mingwei Liu, Wentao Wang, Cheng Wang, Jiansheng Liu, Aihua Deng, Jiancai Xu, Changquan Xia, Wentao Li, Hui Zhang et al. *Applied Physics Letters*, **99**, 9 (2011) 091502.

[15] Allen Caldwell, Konstantin Lotov, Alexander Pukhov & Frank Simon. *Nature Physics*, **5**, 5 (2009) 363–367.

[16] A Caldwell, E Adli, L Amorim, R Apsimon, T Argyropoulos, R Assmann, A-M Bachmann, F Batsch, J Bauche, VK Berglyd Olsen et al. *Nuclear Instruments and Methods in Physics Research Section A: Accelerators, Spectrometers, Detectors and Associated Equipment*.

[17] GENNADY V Stupakov & MS Zolotorev. *Physical review letters*, **86**, 23 (2001) 5274.

[18] Xintian Eddie Lin. *Physical Review Special Topics-Accelerators and Beams*, **4**, 5 (2001) 051301.

[19] Benjamin M Cowan. *Physical Review Special Topics-Accelerators and Beams*, **11**, 1 (2008) 011301.

[20] J.B. Pendry, A.J. Holden, D.J. Robbins & W.J. Stewart. *Microwave Theory and Techniques, IEEE Transactions on*, **47**, 11 (1999) 2075–2084. ISSN 0018-9480.

[21] Kenneth S Cole & Robert H Cole. *The Journal of Chemical Physics*, **9**, 4 (1941) 341–351.

[22] SI Maslovski, SA Tretyakov & PA Belov. *Microwave and Optical Technology Letters*, **35**, 1 (2002) 47–51.

[23] D. R. Smith, Willie J. Padilla, D. C. Vier, S. C. Nemat-Nasser & S. Schultz. *Phys. Rev. Lett.*, **84** (2000) 4184–4187. http://link.aps.org/doi/10.1103/PhysRevLett.84.4184

[24] Victor Georgievich Veselago. *Physics-Uspekhi*, **10**, 4 (1968) 509–514.

[25] Ulf Leonhardt & Tomáš Tyc. *Science*, **323**, 5910 (2009) 110–112.

[26] David Schurig, JJ Mock, BJ Justice, Steven A Cummer, John B Pendry, AF Starr & DR Smith. *Science*, **314**, 5801 (2006) 977–980.

[27] Xiang Zhang & Zhaowei Liu. *Nature materials*, **7**, 6 (2008) 435–441.

[28] J. B. Pendry. *Phys. Rev. Lett.*, **85** (2000) 3966–3969. http://link.aps.org/doi/10.1103/PhysRevLett.85.3966

[29] F. Falcone, T. Lopetegi, M. A. G. Laso, J. D. Baena, J. Bonache, M. Beruete, R. Marqués, F. Martín & M. Sorolla. *Phys. Rev. Lett.*, **93** (2004) 197401. http://link.aps.org/doi/10.1103/PhysRevLett.93.197401

[30] M. Beruete, M. Aznabet, M. Navarro-Cía, O. El Mrabet, F. Falcone, N. Aknin, M. Essaaidi & M. Sorolla. *Opt. Express*, **17**, 3 (2009) 1274–1281.

[31] M. Abo-Bakr, J. Feikes, K. Holldack, G. Wüstefeld & H.-W. Hübers. *Phys. Rev. Lett.*, **88** (2002) 254801. http://link.aps.org/doi/10.1103/PhysRevLett.88.254801

[32] G. L. Carr, Michael C. Martin, Wayne R. McKinney, K. Jordan, George R. Neil & G. P. Williams. *Nature*, **420** (2002) 153–156.

[33] Ju Gao & Fang Shen. *Phys. Rev. A*, **73** (2006) 043801. http://link.aps.org/doi/10.1103/PhysRevA.73.043801

[34] M. C. Thompson, H. Badakov, A. M. Cook, J. B. Rosenzweig, R. Tikhoplav, G. Travish, I. Blumenfeld, M. J. Hogan, R. Ischebeck, N. Kirby, R. Siemann, D. Walz, P. Muggli, A. Scott & R. B. Yoder. *Phys. Rev. Lett.*, **100** (2008) 214801. http://link.aps.org/doi/10.1103/PhysRevLett.100.214801

[35] Sergey P Antipov, Wanming Liu, John Gorham Power & Linda K Spentzouris. "Left-handed metamaterials studies and their application to accelerator physics". In "Particle Accelerator Conference, 2005. PAC 2005. Proceedings of the", pages 458–460. IEEE (2005).

[36] S Antipov, W Liu, W Gai, JG Power & L Spentzouris. "Left-Handed Structures for Accelerator Applications". In "ADVANCED ACCELERATOR CONCEPTS: 12th Advanced Accelerator Concepts Workshop", volume 877, pages 815–822. AIP Publishing (2006).

[37] S Antipov, L Spentzouris, W Gai, W Liu & JG Power. *Nuclear Instruments and Methods in Physics Research Section A: Accelerators, Spectrometers, Detectors and Associated Equipment*, **579**, 3 (2007) 915–923.

[38] S. Antipov, L. Spentzouris, W. Gai, M. Conde, F. Franchini, R. Konecny, W. Liu, J.G. Power, Z. Yusof & C. Jing. *Journal of Applied Physics*, **104**, 1 (2008) 014901–014901–6. ISSN 0021-8979.

[39] Sergey Antipov, LK Spentzouris, M Conde, W Gai, W Liu, R Konecny, JG Power & Z Yusof. "Metamaterial-loaded waveguides for accelerator applications". In "Particle Accelerator Conference, 2007. PAC. IEEE", pages 2906–2908. IEEE (2007).

[40] M. A. Shapiro, S. Trendafilov, Y. Urzhumov, A. Alù, R. J. Temkin & G. Shvets. *Phys. Rev. B*, **86** (2012) 085132.

[41] MA Shapiro, JR Sirigiri, RJ Temkin & G Shvets. "Metamaterial-based linear accelerator structure". In "Proceedings Particle Accelerator Conference PAC", volume 9 (2009).

[42] JS Hummelt, BJ Munroe, MA Shapiro & RJ Temkin. "Simulation of Wakefields from an electron bunch in a Metamaterial waveguide". In "Particle Accelerator Conference, 2013. PAC", (2013).

[43] Xueying Lu, Michael A. Shapiro & Richard J. Temkin. *Phys. Rev. ST Accel. Beams*, **18** (2015) 081303. `http://link.aps.org/doi/10.1103/PhysRevSTAB.18.081303`

[44] D. Shiffler, R. Seviour, E. Luchinskaya, E. Stranford, W. Tang & D. French. *Plasma Science, IEEE Transactions on*, **41**, 6 (2013) 1679–1685. ISSN 0093-3813.

[45] Jagadis Chunder Bose. *Proceedings of the Royal Society of London*, **63**, 389-400 (1898) 146–152.

[46] RN Bracewell et al. *Wireless Engineer*, **31**, 12 (1954) 320–326.

[47] KE Golden & TM Smith. *Nuclear Science, IEEE Transactions on*, **11**, 1 (1964) 225–230.

[48] R Liu, C Ji, JJ Mock, JY Chin, TJ Cui & DR Smith. *Science*, **323**, 5912 (2009) 366–369.

[49] Zhaowei Liu, Hyesog Lee, Yi Xiong, Cheng Sun & Xiang Zhang. *science*, **315**, 5819 (2007) 1686–1686.

[50] Allan D Boardman, Volodymyr V Grimalsky, Yuri S Kivshar, Svetlana V Koshevaya, Mikhail Lapine, Natalia M Litchinitser, Vadim N Malnev, Mikhail Noginov, Yuriy G Rapoport & Vladimir M Shalaev. *Laser & Photonics Reviews*, **5**, 2 (2011) 287–307.

[51] Hu Tao, Andrew C Strikwerda, Kebin Fan, Willie J Padilla, Xin Zhang & Richard Douglas Averitt. *Journal of Infrared, Millimeter, and Terahertz Waves*, **32**, 5 (2011) 580–595.

[52] Jun-Yu Ou, Eric Plum, Liudi Jiang & Nikolay I Zheludev. *Nano letters*, **11**, 5 (2011) 2142–2144.

[53] Tom Driscoll, S Palit, Mumtaz M Qazilbash, Markus Brehm, Fritz Keilmann, Byung-Gyu Chae, Sun-Jin Yun, Hyun-Tak Kim, SY Cho, N Marie Jokerst et al. *Applied Physics Letters*, **93**, 2 (2008) 024101.

[54] Mário G Silveirinha, Andrea Alù, Brian Edwards & Nader Engheta. "Overview of theory and applications of epsilon-near-zero materials". In "URSI General Assembly", Citeseer (2008).

[55] Andrea Alù, Mário G Silveirinha, Alessandro Salandrino & Nader Engheta. *Physical Review B*, **75**, 15 (2007) 155410.

[56] Brian Edwards, Andrea Alù, Michael E Young, Mário Silveirinha & Nader Engheta. *Physical review letters*, **100**, 3 (2008) 033903.

[57] Andrea Alù & Nader Engheta. *Physical Review E*, **72**, 1 (2005) 016623.

[58] Jonathan Gratus & Matthew McCormack. *Journal of Optics*, **17**, 2 (2015) 025105.

[59] A Danisi, C Zannini, R Losito, A Masi & B Salvant. "Theoretical Analysis of Metamaterial Insertions for Resistive-Wall Beam-Coupling Impedance Reduction". In "Proceedings, 5th International Particle Accelerator Conference (IPAC 2014)", page TUPRI055 (2014). `http://cds.cern.ch/record/1749084/files/CERN-ACC-2014-0191.pdf`

[60] Emmy Sharples & Rosa Letizia. "Wakefield excitation via a metasurface-loaded waveguide". In "Proceedings, 5th International Particle Accelerator Conference (IPAC 2014)", page TUPME038 (2014). `http://jacow.org/IPAC2014/papers/tupme038.pdf`

[61] Shu Zhang, Leilei Yin & Nicholas Fang. *Physical review letters*, **102**, 19 (2009) 194301.

[62] Steven A Cummer, Johan Christensen & Andrea Alù. *Nature Reviews Materials*, **1** (2016) 16001.

[63] Steven A Cummer & David Schurig. *New Journal of Physics*, **9**, 3 (2007) 45.

[64] Jesse L Silverberg, Arthur A Evans, Lauren McLeod, Ryan C Hayward, Thomas Hull, Christian D Santangelo & Itai Cohen. *Science*, **345**, 6197 (2014) 647–650.

[65] Muamer Kadic, Tiemo Bückmann, Nicolas Stenger, Michael Thiel & Martin Wegener. *Applied Physics Letters*, **100**, 19 (2012) 191901.

[66] Muamer Kadic, Tiemo Bckmann, Robert Schittny & Martin Wegener. *Reports on Progress in Physics*, **76**, 12 (2013) 126501. `http://stacks.iop.org/0034-4885/76/i=12/a=126501`

[67] VG Veselago. *Fizika Tverdogo Tela*, **8** (1966) 3571–3573.

[68] Pavel A Cherenkov. *Doklady Akademii Nauk SSSR*, **2** (1934) 451.

[69] Jie Lu, Tomasz M. Grzegorczyk, Yan Zhang, Joe Pacheco Jr, Bae-Ian Wu, Jin A. Kong & Min Chen. *Opt. Express*, **11**, 7 (2003) 723–734. http://www.opticsexpress.org/abstract.cfm?URI=oe-11-7-723

[70] J. B. Pendry, A. J. Holden, W. J. Stewart & I. Youngs. *Phys. Rev. Lett.*, **76** (1996) 4773–4776. http://link.aps.org/doi/10.1103/PhysRevLett.76.4773

[71] D. Schurig, J. J. Mock & D. R. Smith. *Applied Physics Letters*, **88**, 4. http://scitation.aip.org/content/aip/journal/apl/88/4/10.1063/1.2166681

[72] Krzysztof Iwaszczuk, Andrew C. Strikwerda, Kebin Fan, Xin Zhang, Richard D. Averitt & Peter Uhd Jepsen. *Opt. Express*, **20**, 1 (2012) 635–643. http://www.opticsexpress.org/abstract.cfm?URI=oe-20-1-635

[73] T. F. Gundogdu, I. Tsiapa, A. Kostopoulos, G. Konstantinidis, N. Katsarakis, R. S. Penciu, M. Kafesaki, E. N. Economou, Th. Koschny & C. M. Soukoulis. *Applied Physics Letters*, **89**, 8. http://scitation.aip.org/content/aip/journal/apl/89/8/10.1063/1.2335955

[74] Ricardo Marqués, Ferran Martín & Mario Sorolla. "Metamaterials with negative parameters: theory, design and microwave applications", volume 183. John Wiley & Sons (2011).

[75] Emmy Sharples & Rosa Letizia. *Journal of Instrumentation*, **9**, 11 (2014) P11017.

[76] I Vendik, O Vendik, I Kolmakov & M Odit. *Opto-Electronics Review*, **14**, 3 (2006) 179–186.

[77] K. Takano, Y. Yakiyama, K. Shibuya, K. Izumi, H. Miyazaki, Y. Jimba, F. Miyamaru, H. Kitahara & M. Hangyo. *Terahertz Science and Technology, IEEE Transactions on*, **3**, 6 (2013) 812–819. ISSN 2156-342X.

[78] Riad Yahiaoui, U-C Chung, Catherine Elissalde, Mario Maglione, Valérie Vigneras & Patrick Mounaix. *Applied Physics Letters*, **101**, 4 (2012) 042909.

[79] H. Nemec, C. Kadlec, F. Kadlec, P. Kuzel, R. Yahiaoui, U.-C. Chung, C. Elissalde, M. Maglione & P. Mounaix. *Applied Physics Letters*, **100**, 6. http://scitation.aip.org/content/aip/journal/apl/100/6/10.1063/1.3683540

[80] A Danisi, M Grech, A Masi, R Losito & N Sammut. "FEM simulations of metamaterial impact on the longitudinal beam-coupling impedance of a rectangular beam pipe". In "Advanced Electromagnetic Materials in Microwaves and Optics (METAMATERIALS), 2015 9th International Congress on", pages 49–51. IEEE (2015).

[81] Andrew A Houck, Jeffrey B Brock & Isaac L Chuang. *Physical Review Letters*, **90**, 13 (2003) 137401.

[82] RA Shelby, DR Smith, SC Nemat-Nasser & Sheldon Schultz. *Applied Physics Letters*, **78**, 4 (2001) 489–491.

[83] S Antipov, L Spentzouris, W Liu, W Gai & JG Power. *Journal of Applied Physics*, **102**, 3 (2007) 034906.

[84] R Marqués, L Jelinek, F Mesa & F Medina. *Optics express*, **17**, 14 (2009) 11582–11593.

[85] G Adamo, JY Ou, JK So, SD Jenkins, F De Angelis, KF MacDonald, E Di Fabrizio, J Ruostekoski & NI Zheludev. *Physical review letters*, **109**, 21 (2012) 217401.

[86] Delmar L Barker & William R Owens. "Smith-Purcell radiation source using negative-index metamaterial (NIM)" (2008). US Patent 7,397,055.

[87] J. Urata, M. Goldstein, M. F. Kimmitt, A. Naumov, C. Platt & J. E. Walsh. *Phys. Rev. Lett.*, **80** (1998) 516–519. `http://link.aps.org/doi/10.1103/PhysRevLett.80.516`

[88] A Danisi, A Masi & R Losito. "Numerical analysis of metamaterial insertions for mode damping in parasitic particle accelerator cavities". In "Advanced Electromagnetic Materials in Microwaves and Optics (METAMATERIALS), 2015 9th International Congress on", pages 46–48. IEEE (2015).

[89] I McGregor, KM Hock et al. *Proc. IPAC*, pages 1286–1288.

[90] I. McGregor & K. M. Hock. *Phys. Rev. ST Accel. Beams*, **16** (2013) 090101.

[91] AM Nicolson & GF Ross. *Instrumentation and Measurement, IEEE Transactions on*, **19**, 4 (1970) 377–382.

[92] William B Weir. *Proceedings of the IEEE*, **62**, 1 (1974) 33–36.

[93] DR Smith, S Schultz, P Markoš & CM Soukoulis. *Physical Review B*, **65**, 19 (2002) 195104.

[94] AF Starr, PM Rye, DR Smith & S Nemat-Nasser. *Physical Review B*, **70**, 11 (2004) 113102.

[95] DR Smith, DC Vier, Th Koschny & CM Soukoulis. *Physical Review E*, **71**, 3 (2005) 036617.

[96] E. Sharples & R. Letizia. "New plasmonic material based split ring resonators for high frequency applications". In "Advanced Electromagnetic Materials in Microwaves and Optics (METAMATERIALS), 2013 7th International Congress on", pages 307–309 (2013).

[97] Gururaj V. Naik, Jeremy L. Schroeder, Xingjie Ni, Alexander V. Kildishev, Timothy D. Sands & Alexandra Boltasseva. *Opt. Mater. Express*, **2**, 4 (2012) 478–489.

[98] CST Computer Simulation Technology AG. "CST Microwave studio, 2014". CST Computer Simulation Technology AG, Germany (2014). http://www.cst.com

[99] R. Wanzenberg. "Monopole, Dipole and Quadrupole Passbands of the TESLA 9-cell Cavity". Technical report, DESEY, Hamburg, Germany (2001).

[100] Peter Tenenbaum. pages 13–19. Lecture notes from DESY.

[101] Emmy Sharples & Rosa Letizia. *IEEE transactions on plasma Science*.

[102] STFC. "ASTeC - The Versatile Electron Linear Accelerator (VELA)" (Acessed:2015-06-17). http://www.astec.stfc.ac.uk/ASTeC/Business/39928.aspx

[103] PA McIntosh, D Angal-Kalinin, N Bliss, R Buckley, S Buckley, JA Clarke, P Corlett, G Cox, GP Diakun, B Fell et al. *THPWA036, these proceedings*.

[104] PA McIntosh, D Angal-Kalinin, N Bliss, S Buckley, J Clarke, G Diakun, A Gallagher, A Gleeson, A Goulden, C Hill et al. *IPAC*, **12** (2012) 4074.

[105] JA Clarke, D Angal-Kalinin, R Bartolini, DJ Dunning, S Jamison, JK Jones, IPS Martin, JW McKenzie, BL Militsyn, NR Thompson et al. *IPAC*, **12** (2012) 1750.

[106] BL Militsyn, D Angal-Kalinin, AD Brynes, F Jackson, JK Jones, AS Kalinin, JW McKenzie, BD Muratori, TCQ Noakes, MD Roper et al. "Beam Physics Commissioning of VELA at Daresbury Laboratory". In "Proceedings, 5th International Particle Accelerator Conference (IPAC 2014)", page TH-PRO052 (2014). http://accelconf.web.cern.ch/AccelConf/IPAC2014/papers/thpro052.pdf

[107] Science ASTeC & Technology Facilities Council. "VELA Beam Diagnostics" (Acessed:2016-02-24). http://www.astec.stfc.ac.uk/ASTeC/Programmes/vela/38428.aspx

[108] J Jones & B L Militsyn. "VELA beam paramaters". private communication (2015).

[109] JW McKenzie, D Angal-Kalinin, JK Jones, BL Militsyn et al. "VELA (formerly EBTF) simulations and first beam commissioning". In "Proceedings, 4th International Particle Accelerator Conference (IPAC 2013)", page MOPFI065 (2013). http://accelconf.web.cern.ch/accelconf/IPAC2013/papers/mopfi065.pdf

[110] CI Clarke, FJ Decker, RJ England, R Erikson, C Hast, MJ Hogan, SZ Li, M Litos, Y Nosochkov, J Seeman et al. *Energy [GeV]*, **23** (2012) 20.

[111] National accelerator Laboratory SLAC. "Facility for Advanced Accelerator Experimental Tests" (Acessed:2015-06-24). https://portal.slac.stanford.edu/sites/ard_public/facet/newnav/Pages/tf/facet/whatis.aspx

[112] National accelerator Laboratory SLAC. "FACET beam parameters" (Acessed:2015-06-24). https://portal.slac.stanford.edu/sites/ard_public/facet/Documents/FACET%20Beam%20Parameters.pdf

[113] Kimball Physics KPI. "Kimball Physics, electron gun systems comparison charts" (Acessed:2015-06-17). http://www.kimballphysics.com/electron-gun-systems/comparison-charts

[114] Peter Williams. "CLARA layout". private communication (2016).

[115] PH Williams, D Angal-Kalinin, JA Clarke, BD Fell, JK Jones, JW McKenzie & BL Militsyn. "A FRONT END FOR THE CLARA FEL TEST FACILITY AT DARESBURY LABORATORY". In "Proceedings, 5th International Particle Accelerator Conference (IPAC 2014)", page THPRO029 (2014). http://accelconf.web.cern.ch/AccelConf/IPAC2014/papers/thpro029.pdf

[116] Paul Emma, R Akre, J Arthur, R Bionta, C Bostedt, J Bozek, A Brachmann, P Bucksbaum, Ryan Coffee, F-J Decker et al. *nature photonics*, **4**, 9 (2010) 641–647.

[117] Tetsuya Ishikawa, Hideki Aoyagi, Takao Asaka, Yoshihiro Asano, Noriyoshi Azumi, Teruhiko Bizen, Hiroyasu Ego, Kenji Fukami, Toru Fukui, Yukito Furukawa et al. *Nature Photonics*, **6**, 8 (2012) 540–544.

[118] Majed Chergui Winfried Decking Barry Dobson Stefan Dsterer Gerhard Grbel Walter Graeff Heinz Graafsma Janos Hajdu Jonathan Marangos Joachim Pflger Harald Redlin David Riley Ian Robinson Jrg Rossbach Andreas Schwarz Kai Tiedtke Thomas Tschentscher Ivan Vartaniants Hubertus Wabnitz Hans Weise Riko Wichmann Karl Witte Andreas Wolf Michael Wulff Mikhail Yurkov Massimo Altarelli, Reinhard Brinkmann. "The European X-Ray Free-Electron Laser". Technical report, DESY XFEL Project group, Hamburg, Germany (2007). http://xfel.desy.de/localfsExplorer_read?currentPath=/afs/desy.de/group/xfel/wof/EPT/TDR/XFEL-TDR-final.pdf

[119] Romain Ganter. "SwissFEL-Conceptual design report". Technical report, Paul Scherrer Institute (PSI) (2010).

[120] JA Clarke, D Angal-Kalinin, N Bliss, R Buckley, S Buckley, R Cash, P Corlett, L Cowie, G Cox, GP Diakun et al. *Journal of Instrumentation*, **9**, 05 (2014) T05001.

[121] Gwyn P Williams. *Reports on Progress in Physics*, **69**, 2 (2005) 301.

[122] P.R. West, S. Ishii, G.V. Naik, N.K. Emani, V.M. Shalaev & A. Boltasseva. *Laser & Photonics Reviews*, **4**, 6 (2010) 795–808. ISSN 1863-8899. http://dx.doi.org/10.1002/lpor.200900055

[123] Ta-Jen Yen, WJ Padilla, Nicholas Fang, DC Vier, DR Smith, JB Pendry, DN Basov & Xiang Zhang. *Science*, **303**, 5663 (2004) 1494–1496.

[124] Jason Valentine, Shuang Zhang, Thomas Zentgraf, Erick Ulin-Avila, Dentcho A Genov, Guy Bartal & Xiang Zhang. *Nature*, **455**, 7211 (2008) 376–379.

[125] Vladimir M Shalaev. *Nature photonics*, **1**, 1 (2007) 41–48.

[126] Gururaj V. Naik & Alexandra Boltasseva. *Metamaterials*, **5**, 1 (2011) 1 – 7. ISSN 1873-1988. http://www.sciencedirect.com/science/article/pii/S1873198810000538

[127] Gururaj V. Naik, Jongbum Kim & Alexandra Boltasseva. *Opt. Mater. Express*, **1**, 6 (2011) 1090–1099. http://www.osapublishing.org/ome/abstract.cfm?URI=ome-1-6-1090

[128] S. J. Smith & E. M. Purcell. *Phys. Rev.*, **92** (1953) 1069–1069. http://link.aps.org/doi/10.1103/PhysRev.92.1069

[129] Emmy Sharples & Rosa Letizia. "InSb grating for Smith-Purcell THz radiation". In "7th European/UK-China Workshop on Millimeter Waves and Terahertz Technologies (UCMMT 2014)", (2014).

[130] H. L. Andrews, F. Bakkali Taheri, J. Barros, R. Bartolini, V. Bharadwaj, C. Clarke, N. Delerue, G. Doucas, N. Fuster-Martinez, M. Vieille-Grosjean, I. V. Konoplev, M. Labat, S. Le Corre, C. Perry, A. Reichold & S. Stevenson. *Phys. Rev. ST Accel. Beams*, **17** (2014) 052802. http://link.aps.org/doi/10.1103/PhysRevSTAB.17.052802

[131] Zhang Ping, Zhang Ya-Xin, Zhou Jun, Liu Wei-Hao, Zhong Ren-Bin & Liu Sheng-Gang. *Chinese Physics B*, **21**, 10 (2012) 104102. http://stacks.iop.org/1674-1056/21/i=10/a=104102

[132] D. Li, Z. Yang, K. Imasaki & Gun-Sik Park. *Phys. Rev. ST Accel. Beams*, **9** (2006) 040701. http://link.aps.org/doi/10.1103/PhysRevSTAB.9.040701

[133] E. Sharples & R. Letizia. "THz Wakefield Radiation Generation Via Dielectric Bragg Waveguide". In "Advanced Electromagnetic Materials in Microwaves and Optics (METAMATERIALS), 2015 9th International Congress on", (2015).

[134] Yuancun Nie. *Radiation physics and chemistry*, **106** (2015) 140–144. ISSN 0146-5724. http://pubdb.xfel.eu/record/187368

[135] Elena P. Cherenkova. *Nuclear Instruments and Methods in Physics Research Section A: Accelerators, Spectrometers, Detectors and Associated Equipment*, **595**, 1 (2008) 8 – 11. ISSN 0168-9002. 2007 Proceedings of the Sixth International Workshop on Ring Imaging Cherenkov Detectors. http://www.sciencedirect.com/science/article/pii/S0168900208009297

[136] Amit Mizrahi & Levi Schächter. *Phys. Rev. E*, **70** (2004) 016505. http://link.aps.org/doi/10.1103/PhysRevE.70.016505

[137] G. Andonian, O. Williams, S. Barber, D. Bruhwiler, P. Favier, M. Fedurin, K. Fitzmorris, A. Fukasawa, P. Hoang, K. Kusche, B. Naranjo, B. O'Shea, P. Stoltz, C. Swinson, A. Valloni & J. B. Rosenzweig. *Phys. Rev. Lett.*, **113** (2014) 264801. http://link.aps.org/doi/10.1103/PhysRevLett.113.264801

[138] JA Clarke, D Angal-Kalinin, N Bliss, R Buckley, S Buckley, R Cash, P Corlett, L Cowie, G Cox, GP Diakun et al. *Journal of Instrumentation*, **9**, 05 (2014) T05001. http://stacks.iop.org/1748-0221/9/i=05/a=T05001

Chapter 8

List of Publications

A complete list of publications created through the course of this research, including journal papers, conference publications and publications under review or in preparation.

Journal Publications

- *Investigation of CSRR loaded waveguide for accelerator applications* Sharples, E. & Letizia, R. 11/2014 In : Journal of Instrumentation. 13 p., P11017

- *Design considerations of complementary split ring resonator loaded waveguides for wakefield generation* Sharples, E. & Letizia, R. 03/2016 In: IEEE Transactions on plasma Science, *Under review*

- *Relativistic beam interactions with metallic metamaterials structures* Sharples, E. & Letizia, R. under preparation for publication.

Conference Publications

- *Using CST to model metamaterials for particle accelerator applications*, Sharples, E. & Letizia, R. CST European user conference, Strasbourg, April 2016

- *Excitation of a Complementary Split Ring Resonator loaded waveguide for Cherenkov radiation by the VELA beam*, Sharples, E. & Letizia, R. National Vacuum Electronics Conference, Strathclyde, Novemeber 2015

- *THz Wakefield Radiation Generation Via Dielectric Bragg Waveguide*, Sharples, E. & Letizia, R. IEEE explore/ 9th International Congress on Advanced Electromagnetic Materials in Microwaves and Optics, September 12, 2015

- *Electron beam excitation of a CSRR loaded waveguide for Cherenkov radiation*, Sharples, E. & Letizia, R., In Metamaterials, Metadevices, and Metasystems 2015, Proceedings of SPIE Vol. 9544, September 1, 2014

- *Optimization studies on CSRR loaded waveguide for particle accelerator applications*, Sharples, E. & Letizia, R. 2015 Abstracts 2015 IEEE International Conference on Plasma Sciences (ICOPS). IEEE, 1 p.

- *InSb grating for Smith-Purcell THz radiation* , Sharples, E. & Letizia, R. 2014 2 p.

- *Wakefield excitation via metasurface-loaded waveguide*, Sharples, E. & Letizia, R. Proceedings of IPAC2014, Dresden, Germany. Geneva: JACoW, p. 1437-1439 3 p. May 2014

- *New Plasmonic Material Based Split Ring Resonators For High Frequency Applications*, Sharples, E. & Letizia, R. IEEE explore/ 7th international congress on Advanced Electromagnetic Materials In Microwaves and Optics, September 2013